Secondary Ion Mass Spectrometric Analysis of Oxygen Grain Boundary Diffusion in Magnesium-Oxide Bicrystals

by

Michael James Liberatore

Submitted to the Department of Materials Science and Engineering
in partial fulfillment of the requirements for the degree of

Doctor of Science in Ceramics

at the

MASSACHUSETTS INSTITUTE OF TECHNOLOGY

February 1995

Author .....
Department of Materials Science and Engineering
January 13, 1995

Certified by .....
Bernhardt J. Wuensch
Professor of Ceramics
Thesis Supervisor

Accepted by .....
Carl V. Thompson II
Professor of Electronic Materials
Chair, Departmental Committee on Graduate Students

Secondary Ion Mass Spectrometric Analysis of Oxygen Grain Boundary Diffusion in Magnesium-Oxide Bicrystals

by

Michael James Liberatore

Submitted to the Department of Materials Science and Engineering
on January 13, 1995, in partial fulfillment of the
requirements for the degree of
Doctor of Science in Ceramics

Abstract

Chemical vapor transport by HCl gas, a procedure that has been used successfully in the past for the growth of MgO single crystals has been adapted to the growth, for the first time, of high purity MgO [001] tilt boundaries of controlled orientation.

Oxygen-18 bulk diffusion has been measureded in MgO as a function of temperature from 1250 - 1500°C and as a function of partial pressure from 10^{-12} - 10^{+1} kPa. Oxygen grain boundary diffusion has been measured in low energy coincidence site ($\Sigma 5$, (310), $\Sigma 13$, (510)) and high energy (asymmetric 16°) [001] tilt grain boundaries in MgO. Diffusion coefficients were evaluated from ^{18}O concentration gradients measured with the aid of secondary-ion mass spectroscopy with a Cs^+ primary ion beam. The bulk diffusivity of oxygen over the given temperature is given by the following Arrhenian relation:

$$D = 2.9 \times 10^{-4} \exp \frac{-4.0eV}{kT} \quad \frac{\text{cm}^2}{\text{sec}} \qquad 1250 - 1500°C$$

The partial pressure dependence of oxygen diffusivity can be expressed as:

$$D \propto P_{O_2}^{0.11} \qquad 10^{-12} - 10^{+1} kPa \qquad 1500°C$$

On the basis of this and other data available for the isotope effect and the change in anion self-diffusion with aliovalent cation doping, it was concluded that transport was most likely due so some form of interstitial mechanism.

Structural analysis of a $\Sigma 13$ boundary revealed that the grain boundary region in was no more than 1 nm thick and that facets form to accommodate small deviations from the ideal misorientation. Grain boundary diffusion analysis was also done. The product of the grain boundary diffusion coefficient and boundary width, δD_b, for the $\Sigma 13$ boundaries is given by the Arrhenian expression:

$$\delta D_b = 2.8 \times 10^{-8} \exp \frac{-3.9eV}{kT} \quad \frac{\text{cm}^3}{\text{sec}} \qquad 1250 - 1500°C$$

Enhanced diffusion of oxygen was also observed in the $\Sigma 5$ boundaries. The oxygen diffusivities in the $\Sigma 5$ and $\Sigma 13$ boundaries at 1300°C were found to be equal to within experimental error ($\Sigma 13$ - 6.1×10^{-21} cm^2/s, $\Sigma 5$ - 9.2×10^{-21} cm^2/s, 1.4×10^{-20} cm^2/s). In the general, 16° boundary, diffusivities were enhanced by 1 - 2 orders of magnitude over the low energy boundaries. This is in accord with the empirical Borisov relation for metals which observed that the logarithm of the quotient of the grain boundary and bulk diffusion coefficients is proportional to the boundary energy.

Thesis Supervisor: Bernhardt J. Wuensch
Title: Professor of Ceramics

Acknowledgments

I am indebted to so many people that it is impossible to fully express my gratitude in mere words. Firstly I would like to thank Prof. Bernie Wuensch for his patience and guidance over the last five years. Never one to criticize, he always seemed to find something positive to say in even the most trying of circumstances. Some of my favorite Bernie'isms': "Don't be so apologetic, no one has ever done this before!", and "A thesis is just part of your education, it should not be your whole life". I would also like to thank Profs. Tuller, Chiang, and Vander Sande for being on my committee. Some of their suggestions/improvements were ones I would never have been able to come up with myself.

I would like to thank all of those people, too numerous to mention, who made my life at MIT a little easier, especially Dr. A.N. Sreeram for all of his help and his friendship and Mr. John Martin, MIT SIMS guru, who was taken from us, without warning, August 15, 1994. Without his patient help most of the work in this thesis would not have been possible.

Contents

List of Figures

List of Tables

Chapter 1

Introduction

The relative importance of grain boundary phenomena in the processing and operation of ceramic and electronic materials and devices has increased dramatically in recent years. The enhanced diffusion of oxygen in grain boundaries is of particular interest in ceramic oxides as it can be the controlling factor in kinetic processes and is also important in device applications.

Understanding the diffusion of oxygen in grain boundaries is essential if one is to understand processes such as sintering. One mechanism of densification of a powder agglomerate or polycrystal is diffusion of material from the surface to internal voids in the body through grain boundaries. If grain boundary diffusion of oxygen is significantly faster than lattice diffusion then it can be rate controlling; (diffusion of cations is generally not rate controlling as they usually have higher diffusivities than the larger anions). For similar reasons grain boundary diffusion can be the rate controlling step in a solid state reaction. In a heterogeneous reaction, where the reaction occurs at an interface, two possible rate controlling mechanisms are diffusion of reactants to the interface or diffusion of products away from the interface, the so called "janatorial effect". By a simple LeChatelier analysis we can see that if reactants are depleted or products allowed to accumulate the rate of the reaction will drop. If the solid has a sufficient amount of grain boundary the reaction rate will be enhanced by the transport of reactants and / or products along grain boundaries. [1]

Other phenomena such as ionic conductivity in polycrystalline oxides can have a

large grain boundary component. In a dense polycrystal, with a large grain boundary area / total volume ratio migration of ions along grain boundaries can have a significant contribution to the total conductivity, σ, which is given by $\sum_i c_i q_i \mu_i$ where c, q, and μ are the concentration, charge, and mobility of ionic species i. The total concentration of ions in the grain boundaries will be less than in the bulk since the "thickness" of a grain boundary is only a few atomic spacings, but if the diffusivity (and hence mobility, as $\mu = D(\frac{q}{kT})$ by the Nernst Einstein relation) of the ions is higher in the grain boundaries (as is often the case) a significant fraction of the conductivity can be attributed to grain boundaries.

Grain boundary diffusivity is also important in device applications. The critical phase in the processing of PTCR thermistors is an oxidative anneal which takes place after the device is sintered. This step is necessary to form the potential barriers at the grain boundaries which give the device its characteristic high resistivity at temperatures above the Curie point. The reason it is possible to achieve this is because oxygen diffuses in through the grain boundaries more quickly than into the bulk. If bulk diffusion was comparable to grain boundary diffusion then the oxidizing atmosphere would significantly alter the position of the Fermi level in the grains, which is undesirable. [2]

From the previous discussion one can see the importance of grain boundary diffusion. In spite of the importance, little is known about the structure-property relations of grain boundaries in oxides. Studies of grain boundary diffusion have been done in polycrystals but these give averages over many boundaries of different orientation. When diffusion has been studied in individual boundaries impurity segregation has made the results difficult to interpret. Thus it would be desirable to study individual boundaries of controlled orientation in the absence of segregation in more detail. It is the purpose of this thesis to study grain boundary diffusion in a representative ceramic oxide, MgO. There have been many diffusion studies in MgO due to the fact that it is a stable, high melting compound with a simple structure and little deviation from stoichiometry. Moreover, large single crystals have been available for many years. The first quantitative study of oxygen diffusion in MgO was performed

by Oishi and Kingery [3]. Crushed MgO single crystals that had been annealed in an ^{18}O atmosphere were subsequently reduced to CO_2. The relative amounts of the stable isotopes ^{16}O and ^{18}O in the CO_2 vapor produced were determined by gas phase mass spectrometry. This method was not precise, however, as it required assumptions about the size and shape of the particles to make the mathematics of analysis tractable.

Systematic studies of grain boundary diffusion in MgO are both scarce and at present not well understood. Two early studies of oxygen grain boundary diffusion done by Condit [4] and McKenzie [5] used the techniques of proton activation and audioradiography to examine the penetration of the stable isotope ^{18}O along the grain boundary in Fe doped MgO bicrystals. The crystals were grown from the melt and annealed in an atmosphere of ^{18}O. In both cases the audioradiography revealed ^{18}O penetration along the grain boundary to be much deeper than in the bulk region. A study of Ni^{2+} diffusion in MgO polycrystals and pressure sintered bicrystals by Wuensch and Vasilos [6] revealed enhanced transport at the boundaries. A subsequent study of Ni^{2+} and Co^{2+} grain boundary diffusion in pressure sintered bicrystals was done by the same authors [7]. As in the previous study, fast diffusion was observed along the grain boundaries. In both cases, though, the enhanced transport was correlated with the presence of impurities segregated from the bulk, most notably Ca, Si and Fe. In two more recent studies of oxygen grain boundary diffusion performed by Dolhert [8] and Roshko [9], doped and undoped polycrystals and deformed single crystals of MgO were analyzed with secondary-ion mass spectrometry after annealing in an atmosphere of ^{18}O. Both studies confirm enhanced diffusion of oxygen along grain boundaries but the results are again clouded somewhat by the mitigating presence of segregated impurities and second phases at triple junctions.

High purity boundaries are clearly needed to permit elucidation of structure-property relations of grain boundaries. High purity MgO single crystals have been prepared by Gruber [10] and Yoo [11] using chemical vapor transport. It was the goal of this study to adapt this technique to the growth of bicrystals of MgO with high purity boundaries, well-characterized in terms of atomic scale structure and impurity

distribution; the bicrystals were used in a study of oxygen grain boundary diffusion in MgO.

Chapter 2

Theory and Literature Review

2.1 Grain Boundary Structure and Energy

2.1.1 Description of a General Grain Boundary [12]

A grain boundary is a disturbance in the crystalline structure of a material between two regions of the same composition but different orientation. A general grain boundary requires 9 parameters to describe it. If we imagine making two parallel cuts through a single crystal, removing the slab of material between the cuts, putting the grains back together (not necessarily in exactly the same place) and twisting, as in figure 2-1 then we have "created" a general grain boundary. Three of the 9 parameters are required to describe the translation (if any) of one grain with respect to the other. A single vector is enough as it is a rigid body translation. Three parameters are needed to locate the grain boundary plane (recall the equation for a plane in 3-space is $\frac{x}{A} + \frac{y}{B} + \frac{z}{C} = 1$). The final three parameters are needed to describe the crystal misorientation. This is can be done by specifying a unit vector as a rotation axis and a rotation angle through which one crystal will be rotated with respect to the other. The rotation axis only needs two parameters to describe it since it's magnitude is irrelevant (it is usually taken to be a unit vector). A boundary in which the rotation vector is parallel to the boundary plane is called a tilt boundary. Furthermore if the boundary plane is a mirror plane of the bicrystal then the boundary is

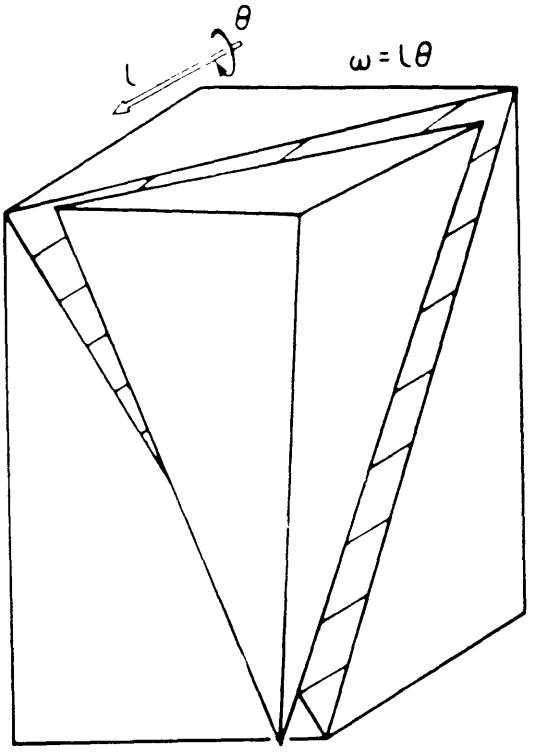

Figure 2-1: Creation of a General Grain Boundary

a symmetric tilt (or twin) boundary. If the rotation axis is normal to the boundary plane, the boundary is a twist boundary. In a mixed boundary the rotation axis lies in an intermediate position.

Different grain boundaries will have different energies. The grain boundary energy, γ, or more properly the excess interfacial free energy is defined in basic thermodynamics for a system containing a grain boundary as the incremental change in the internal energy (E) of the system with the change in interfacial area (A) at constant entropy (S), volume (V) and number of solute atoms (N_i). Alternate definitions are also possible in terms of the the Gibbs free energy, G, the Helmholz free energy, F, and the system temperature and pressure, T and P respectively.

$$\gamma = (\frac{\partial E}{\partial A})_{S,V,N_i} = (\frac{\partial G}{\partial A})_{T,P,N_i} = (\frac{\partial F}{\partial A})_{T,V,N_i}$$

If there is local relaxation of the structure adjacent to the boundary the rigid body translation and the position of the boundary normal to itself will assume values depending on the crystal misorientation and boundary inclination so as to minimize the interfacial free energy. In this case the number of parameters necessary to describe the boundary is reduced from 9 to 5. The rigid body translation is eliminated and the boundary plane requires only two parameters to define it since only the inclination can be specified; this can be done by a unit normal to the boundary plane. This remains a large number of parameters which can be varied independently. To simplify matters experimentalists often study special boundaries which require one or two geometrical parameters to describe them. In this work symmetric tilt boundaries have been studied. They require only one parameter to describe them, the misorientation angle, θ.

2.1.2 Dislocation Models for Grain Boundaries

For many years it was postulated that a grain boundary consisted of an amorphous layer several hundred angstroms thick (the so called "Beilby layer") separating two perfect crystals of different orientation. It is now known that the thickness of a grain boundary is on the order of Angstroms, corresponding to only a few atomic spacings,

and that they do have a definite periodic structure depending on the orientation of the grains on either side of the boundary. A convenient method for describing the structure of boundaries involves the use of dislocations.

Primary Dislocation Models

A primary dislocation model describes a grain boundary as a collection of lattice dislocations (dislocations whose Burgers vector is a lattice translation). A general grain boundary can be created by introducing a set of lattice dislocations into a single crystal and gathering them into a planar array. An example for the symmetrical tilt boundary is shown in figure 2-2. If edge dislocations are introduced on each successive lattice plane and collected into a planar array the result will be a rotation of the crystal on one side of the dislocation array with respect to the other. The rotation occurs to keep the boundary lattice planes on either side of the dislocation array straight, causing the resultant "bad material" to be restricted to small core region around the dislocations. By making a Burgers circuit construction in the bicrystal which contains the grain boundary, the dislocation content can be seen. When the same circuit is drawn in the single crystal the closure failure obtained is the vector sum of the Burgers vectors of the dislocations which comprise that segment of the boundary which the circuit enclosed. An examples for the $\Sigma 5$ and symmetric tilt boundary is shown in figure 2-3.

A primary dislocation description of a grain boundary is not unique. A particular boundary structure can be achieved by introducing several different sets of lattice dislocations. The higher the symmetry of the crystal the more primary dislocation descriptions exist for a boundary in that crystal. Consider the boundary in figure 2-4. A set of lattice dislocations parallel to [001] was introduced so as to produce a rotation around [001] of 126.9°. The same boundary can be produced by causing rotations of 53.1° or 36.9°. For cubic systems there exist 24 equivalent axis angle pair descriptions for a general grain boundary [12]. The primary dislocation content of each of these descriptions is different, which begs the question: Are some descriptions better than others? Is there a best way to describe a particular grain boundary in terms of its pri-

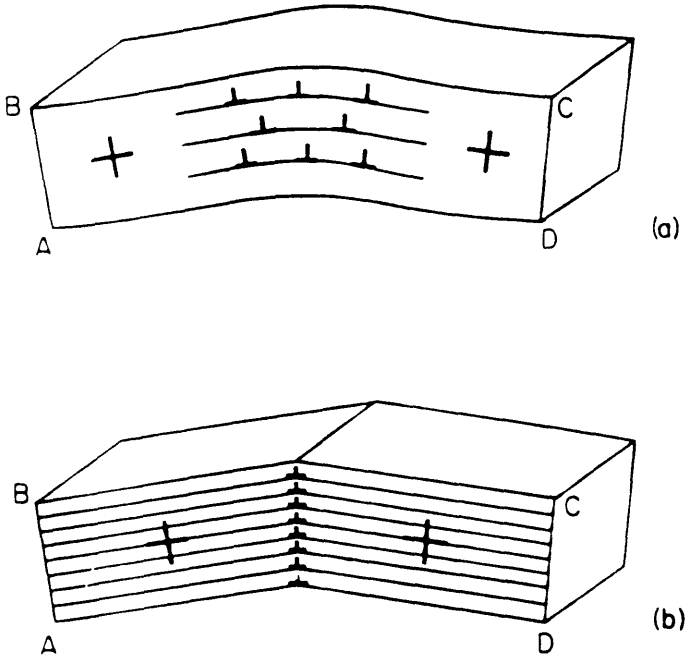

Figure 2-2: Formation of a symmetric tilt boundary by introduction and polygonalization of lattice dislocations.

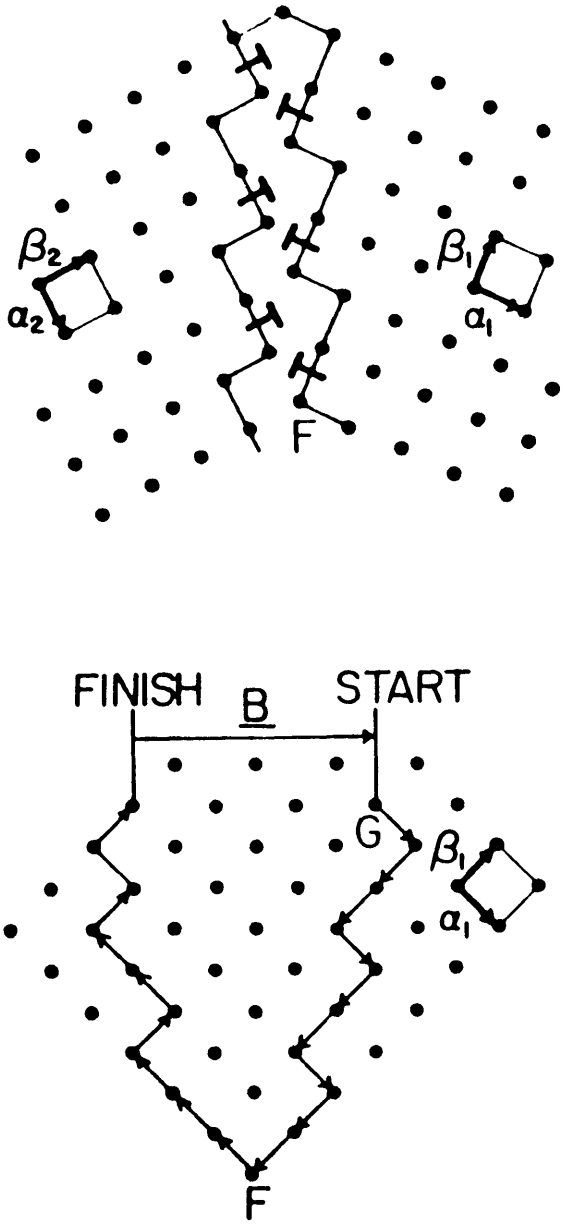

Figure 2-3: Burgers circuit for $\Sigma 5$ and symmetric tilt boundary.

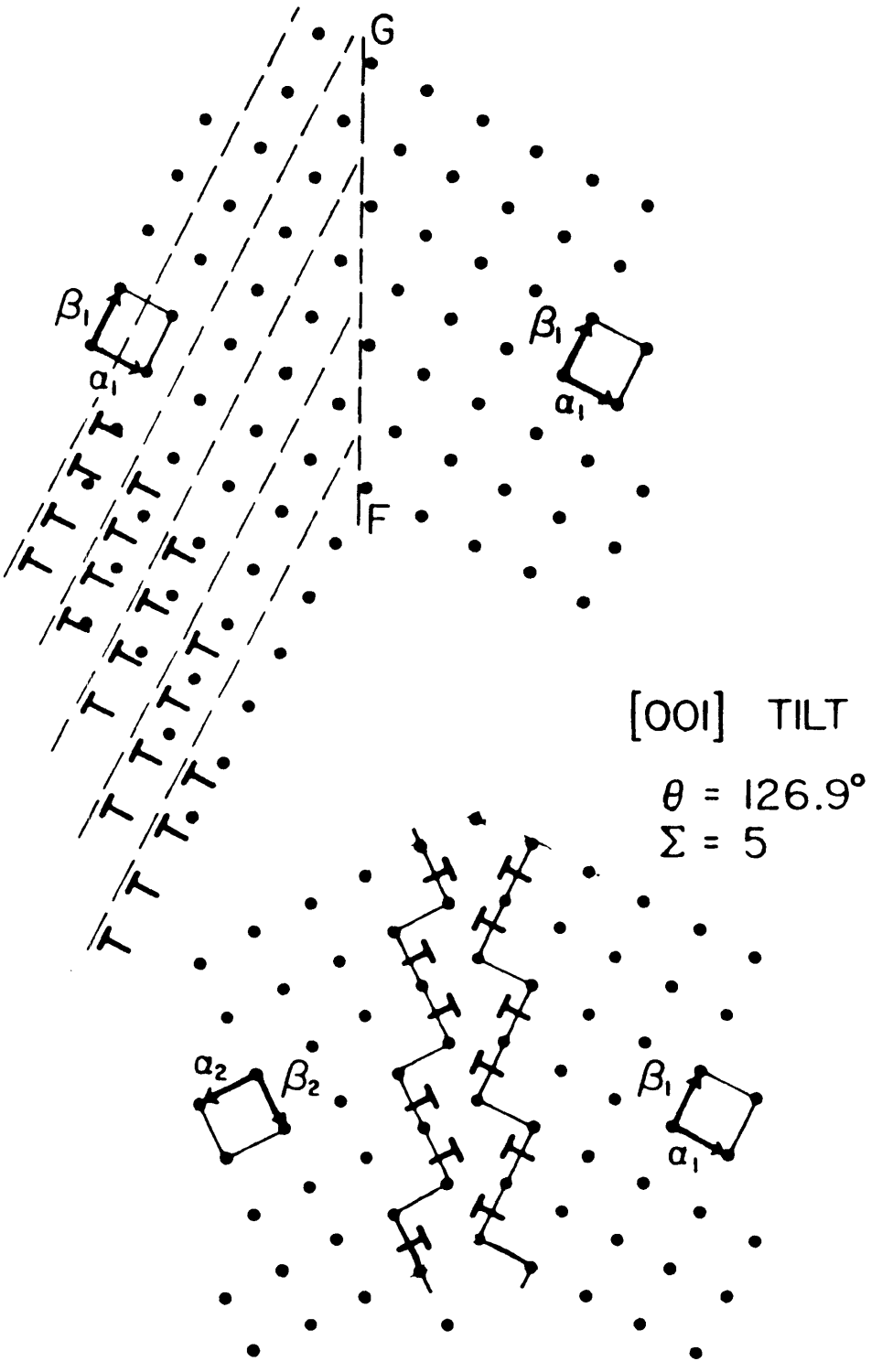

Figure 2-4: One of the primary dislocation descriptions for the Σ5 boundary

mary dislocation content? In theory, for a static boundary any description will suffice as long as it is used consistently. In practice it is usually easier to describe a boundary in terms of a relatively simple array of dislocations. Furthermore, observations of boundary dislocation structure by diffraction strain contrast in the transmission electron microscope [13] always reveal simple (low dislocation content) rather than complex (high dislocation content) boundary structures. The preferred description is the one where the dislocation spacing is the largest. This frequently is the one which corresponds to the axis/angle pair in which the rotation angle is the smallest. This description is often referred to as the disorientation. More importantly, no significant problems arise from the fact that there is no unique description of static boundary structure in terms of primary dislocations. [12]

The dislocation spacing in a symmetric tilt boundary can be determined via a simple geometrical construction as shown in figure 2-5. Consider the portion of the bicrystal enclosed by ABCD. AB and BC are (100) surfaces and BD is the symmetric tilt boundary. All the lattice planes which initiate at the surfaces AB and BC terminate as dislocations at the boundary BC. The length AB + BC is equal to the number of lattice planes which initiate in that portion of the surface, n_p, times the interplanar spacing, which is equal to b, the magnitude of the Burgers vector of the primary boundary dislocations. From the figure it can also be seen, using simple trigonometry, that the distance AB is equal to the length of the boundary considered in the figure, h, times the sine of the angle opposite AB, which is equal to half of the tilt angle, θ. Noting that AB + BC = 2AB and combining these observations yields the following:

$$n_p = \frac{2h}{b} \sin \frac{\theta}{2}$$

The dislocation spacing D, is then the length of the boundary, h, divided by the number of dislocations, which is equal to n_p, the number of planes which terminate at the boundary.

$$D = \frac{h}{n_p} = \frac{b}{2 \sin \frac{\theta}{2}}$$

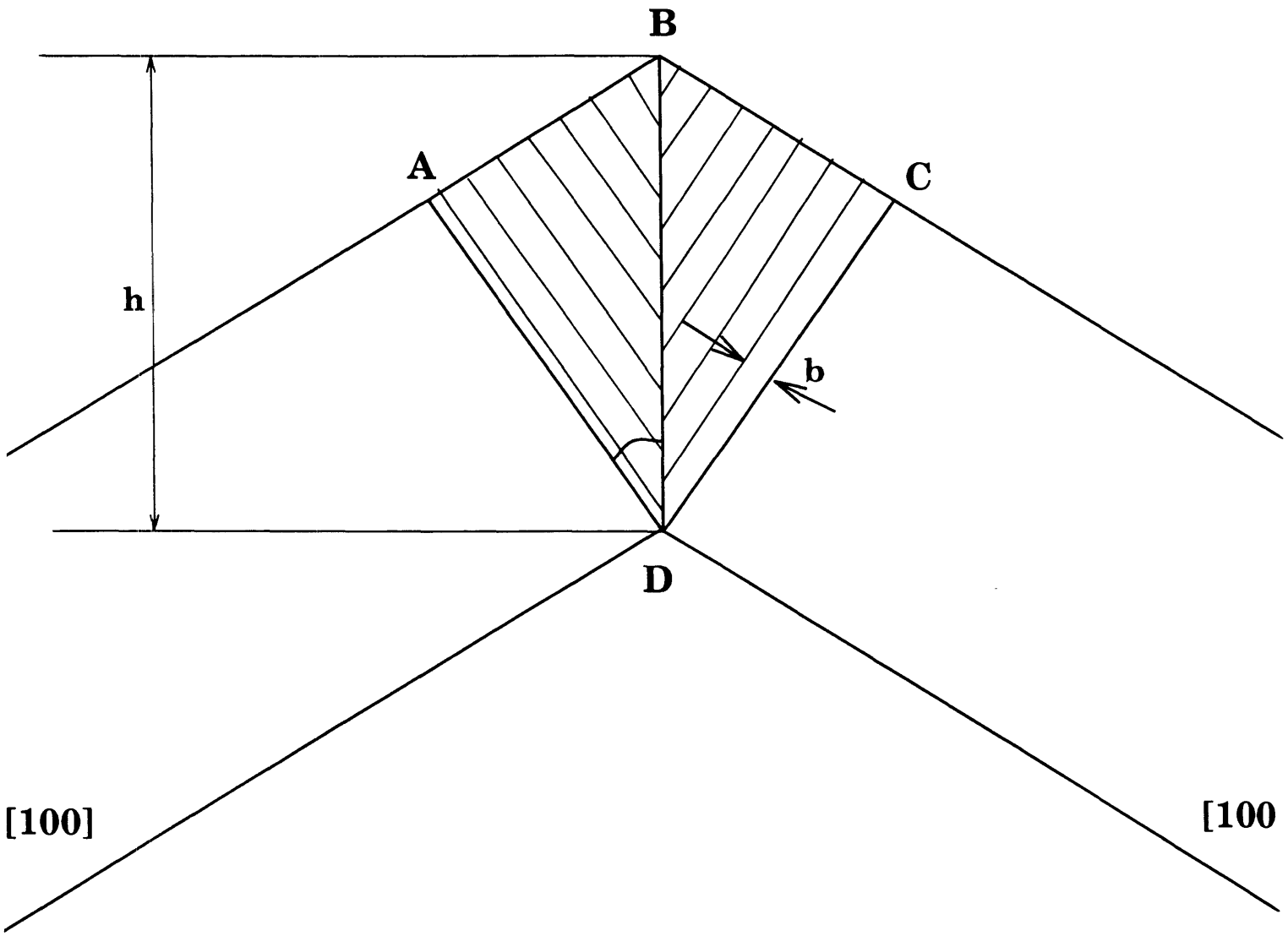

Figure 2-5: Determining the dislocation spacing in a symmetric tilt boundary

which for small tilt angles simplifies to:

$$D \approx \frac{b}{\theta}$$

A relation which can be used to determine the dislocation content of a general grain boundary consisting of i sets of equally-spaced dislocations is the Frank formula [14] which can be expressed as:

$$\vec{V} \times \vec{a} = \Sigma\, \vec{b_i}(\vec{N_i} \cdot \vec{V}) \tag{2.1}$$

where $\vec{V}$) is any vector in the boundary plane, $\vec{a}$ is a unit vector along the axis of rotation of crystal B around crystal A, $\vec{b_i}$ is the Burgers vector of dislocation set i, $\vec{N_i}$ is a vector perpendicular to dislocation set i with magnitude equal to $\frac{1}{2D_i \sin(\theta/2)}$, where D_i is the average spacing between dislocations of type i, and θ is the angle of rotation of crystal B around crystal A. Three sets of dislocations are required to describe a general grain boundary [14]. If one pictures a general grain boundary as a twist orientation superimposed on a tilt orientation then this becomes evident as a pure tilt boundary can be described as a set of parallel edge dislocations whereas a pure twist boundary can be described as a grid of 2 sets of parallel screw dislocations. Given a rotation axis $\vec{a}$, a unit vector $\vec{n}$ normal to the boundary plane and three independent $\vec{b_i}$ equation 2.1 can be solved for the dislocation spacings D_i. A solution, as derived by Read and Shockley [35], is:

$$N_i = \vec{a} \times \vec{b_i^*} - \vec{n}[\vec{n} \cdot (\vec{a} \times \vec{b_i^*})]$$

where $\vec{b_i^*}$ are the reciprocal Burgers vectors defined by

$$\vec{b_i^*} = \frac{\vec{b_j} \times \vec{b_k}}{\vec{b_i} \cdot (\vec{b_j} \times \vec{b_k})} \qquad i, j, k = 1, 2, 3$$

Burgers vectors are referred to a perfect reference crystal to avoid ambiguity. If fewer than three sets of dislocations are required to describe a boundary it must be a special one. Some examples are: symmetric tilt (1 set of edge), asymmetric tilt (2 sets of

edge), pure twist (2 sets of screw).

Another way of describing the structure of grain boundaries, especially useful in describing special boundaries, is by using the coincidence site lattice (CSL) model. In this model the lattices of crystals A and B of the bicrystal are imagined to extend beyond the boundary and throughout all space. A point where atoms of each lattice coincide is chosen as the origin. The coincident site lattice is then comprised of all points in space where the atoms of lattices A and B come into coincidence. They do form a regular array (hence the designation coincidence site *lattice*). The reciprocal of the fraction of lattice sites which come into coincidence is an important quantity in CSL theory and is denoted by the symbol Σ; thus if 1 in 5 lattice sites come into coincidence for a particular boundary it is denoted a $\Sigma 5$ boundary. Examples for two of the MgO boundaries used in this study are shown in figures 2-6 and 2-7. In figure 2-6 grains A and B are rotated about (001) by 36.9° and the boundary is chosen to be a [210] plane perpendicular to the plane of the paper. The boundary plane is thus a plane of symmetry of the bicrystal. By counting atoms in one of the two-dimensional unit cells it can be seen that there are a total of 4 Mg atoms inside the unit cell plus 4 on the corners, each of which is shared amongst 4 neighboring cells, for a total of five atoms per cell. In this schematic the corner atoms are the CSL points. One in five of the Mg atoms are in coincidence. The same is true for the oxygen sublattice, therefore this is a $\Sigma 5$ symmetric tilt boundary. The boundary of figure 2-7 is a $\Sigma 13$ symmetric tilt boundary; this can be verified by a similar procedure. Closer examination will reveal that the angle of rotation is 22.6° and the boundary plane is [510]. It is a fact that the Σ values for both pure tilt and twist boundaries of the same angle of rotation are the same. This can be seen by further examination of figures 2-6 and 2-7. If the boundary is not chosen to be a plane perpendicular to the paper but rather the plane of the paper itself we have a pure twist boundary. All else is the same. The crystals have still been rotated by the same amount with respect to each other and both lattices still extend beyond the boundary and throughout all space. The CSL's are thus exactly the same for the tilt and twist boundaries, only the boundary plane has changed. The Σ values must also then be the same.

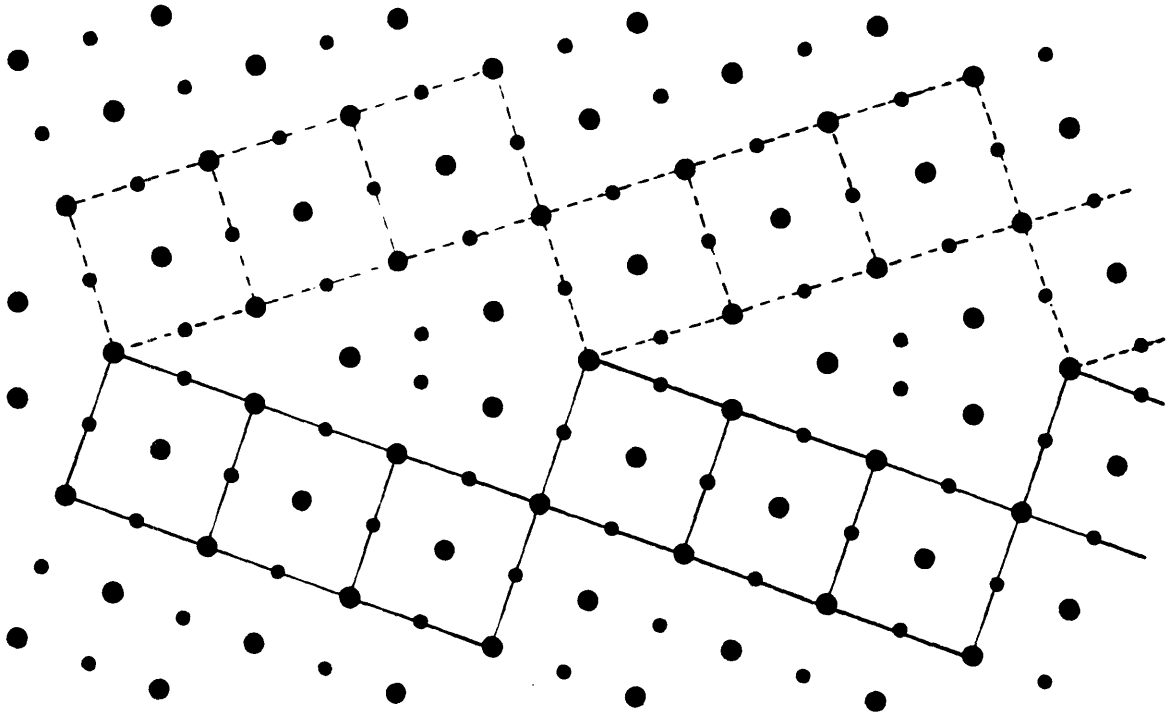

Figure 2-6: The $\Sigma 5$ [210], 36.9° boundary in MgO.

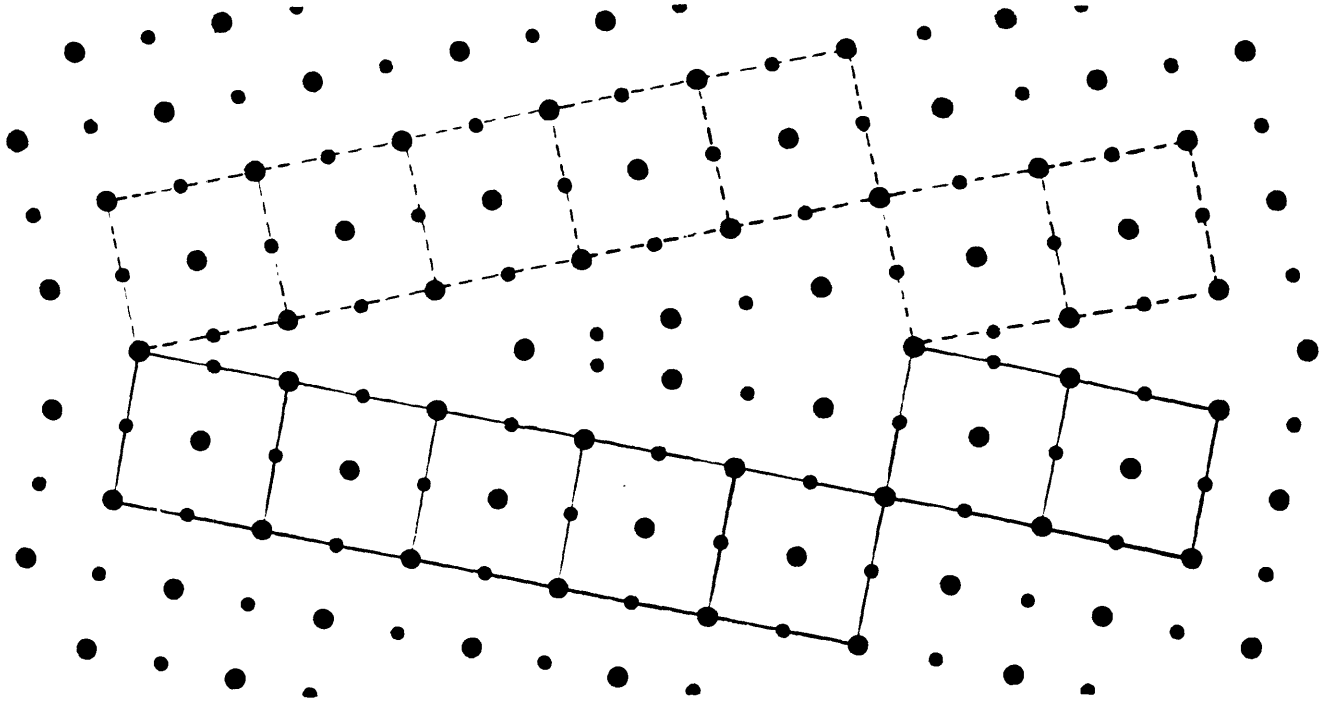

Figure 2-7: The $\Sigma 13$ [510], 22.6° boundary in MgO.

There are an infinite number of CSL's which can be generated by rotations around (001). The Σ values and rotation angles, θ, may be generated by the functions:

$$\Sigma = r^2 + s^2 \quad \text{for } r^2 + s^2 + \text{odd}$$
$$\Sigma = \tfrac{1}{2}(r^2 + s^2) \quad \text{for } r^2 + s^2 \text{ even}$$
$$\theta = 2 \ \text{Arctan} \ \tfrac{s}{r}$$

The Σ values and misorientation angles are generated by substituting positive integers for r and s. These formulas are useful in that they simplify the task of deriving the lattices with the highest degrees of coincidence (lowest Σ values). The lowest Σ values are produced by (r,s) = (2,1), $\Sigma = 5$ and (5,1), (3,2), $\Sigma = 13$ and (4,1), $\Sigma = 17$. When r = s, $\theta = 90°$ which for cubic lattices returns the perfect single crystal; these values are therefore not considered. The $\Sigma 13$ boundary is produced by two sets of r,s pairs. The 5,1 pair produces the smallest rotation angle, 22.6°, and is taken to be the disorientation. It should be fairly obvious from the generation formulas that Σ varies in a highly discontinuous manner with θ. Note also that in the case of (001) tilt boundaries in cubic crystals the r,s notation reveals the identity of the grain boundary plane, the Miller indices being (rs0). For example the $\Sigma 5$ boundary plane is (210) and the $\Sigma 13$ (510) or (320).

The rigid lattice grain boundary produced by rotation of crystals A and B may not in actuality represent the structure of the boundary region. In real crystals the rigid boundary structure will relax to a structure of minimum energy. Boundaries of high coincidence (low Σ), though, have been shown by both theory and experiment (as will be discussed in a later section) to be orientations which correspond to relative minima in plots of grain boundary energy versus misorientation angle. Furthermore, any rigid body translation of crystal A with respect to crystal B will not change the periodicity of atoms across the boundary. It is generally assumed that the relaxed pattern of atoms in the "real" boundary has the same periodicity as those of the CSL boundary, though this has never been proven. [12]

Secondary Dislocation Models

Primary dislocation models are useful in describing grain boundary structure but they have their limitations. At misorientations greater than roughly 15° the spacing of typical primary dislocations becomes small enough that their cores begin to overlap. The boundary can no longer thus be treated as an array of isolated dislocations. For this reason secondary dislocation models have been developed. These are based on perturbations in the primary dislocation spacing. The perturbations are more widely spaced than the primaries and therefore the associated dislocations are discrete. If one considers the $\Sigma 5$ boundary depicted in figure 2-8 it is clear that the array of primary dislocations is uniform. The $\Sigma 17$ boundary shown in figure 2-9 contains in its array of primary dislocations a periodic perturbation on the spacing thereof, indicated by the arrows. It can be shown that the $\Sigma 17$ (61.9°) tilt boundary can be derived from the $\Sigma 5$ (53.1°) tilt boundary by introducing secondary dislocations with Burgers vectors equal to twice the (210) interplanar spacing into the Σ 5 boundary structure, thus causing the extra rotation from 53.1° to 61.9°. This analysis is analogous to viewing a low angle tilt boundary as a perturbation in the perfect crystal by introducing primary dislocations at regular intervals, the difference being that secondary (or grain boundary) dislocations do not usually have lattice translations as their Burgers vectors. In general they have smaller Burgers vectors. They are detectable, however. With the aid of transmission electron microscopy, secondary grain boundary dislocations have been observed at near coincidence boundaries in metals [13] and ceramics, even MgO [15]. In all cases the spacing of secondary dislocations increases as the high coincidence (low Σ) orientations are approached.

An alternate way of describing such boundaries is the structural unit description. As has been mentioned previously and has been observed experimentally, certain low Σ boundaries ($\Sigma 5$ for example) consist of only an array of primary dislocations with no irregularities (i.e., no secondary dislocations). Boundaries of this type are considered to consist of a singular "structural unit" (a small group of atoms arranged in a characteristic configuration). In this light all boundaries can be considered to be

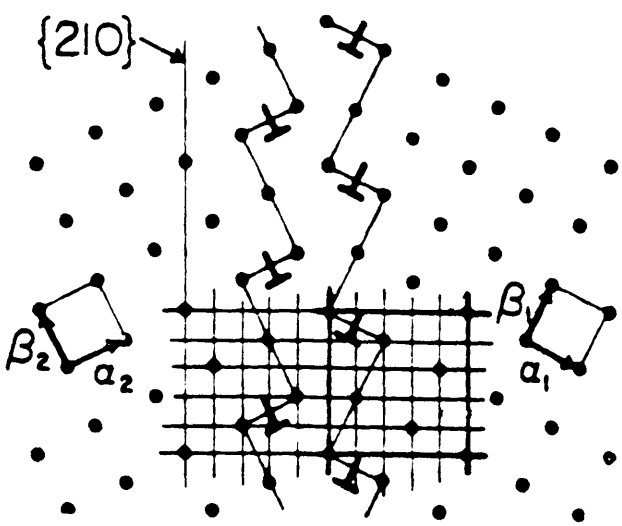

Figure 2-8: Uniform primary dislocation spacing in $\Sigma 5$ boundary.

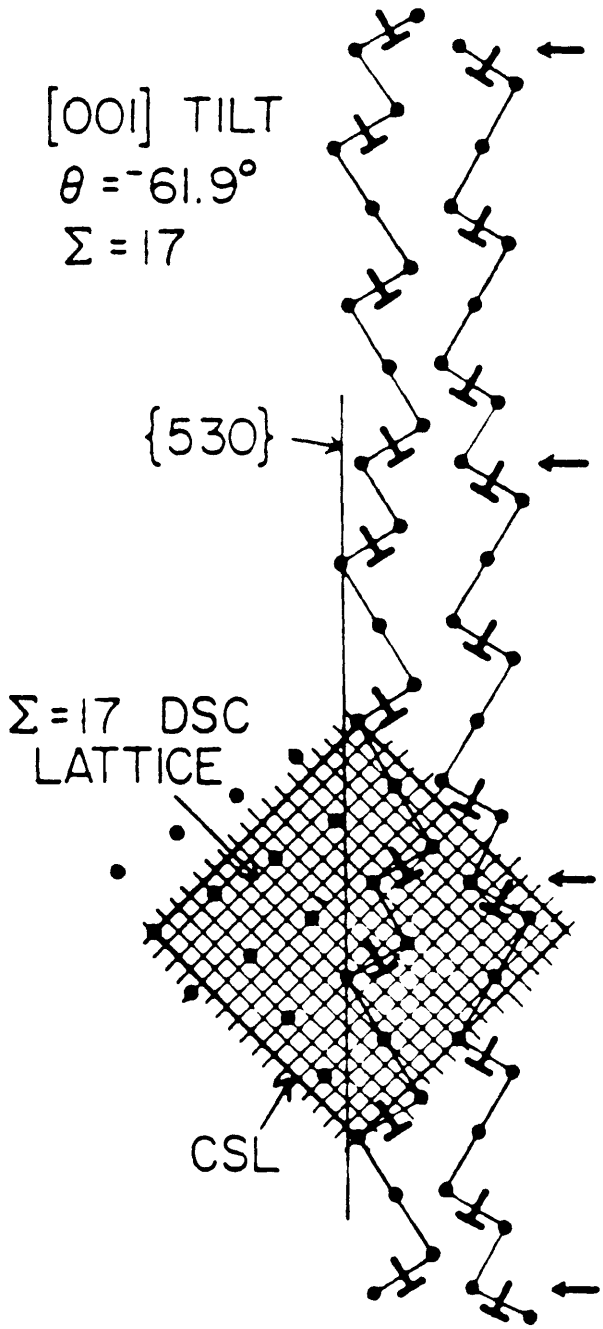

Figure 2-9: Periodic perturbation of primary spacing in Σ17 boundary (indicated by arrows)

composed of mixtures of the structural units of the nearest delimiting (low Σ) boundaries on each side [16]. The number of each type of structural unit is proportional to the nearness of the boundary to that particular orientation. This description is equivalent to the secondary dislocation model.

Literature Review - Grain Boundary Structure

The literature on grain boundary structure centers around two main areas, one being calculation of atomic positions in grain boundaries via molecular statics computer simulations, the other being direct imaging of grain boundaries using transmission electron microscopy and other techniques. Earlier work concentrated on imaging the dislocation structure of boundaries but, as the resolution of electron microscopes improved, atomic resolution imaging of grain boundaries became possible. Most early work was done on metals since bicrystals are easily fabricated and specimens are easily prepared for TEM analysis. Low angle twist boundaries were among the first to be examined because the dislocations are spaced fairly widely and can be observed without the need for a high resolution instrument. A study of the primary dislocation structure in (001) twist boundaries in gold was done by Schober and Balluffi [17]. In this study (001) twist boundaries of gold were prepared by welding (001) oriented gold single crystals together at twist angles varying from 0 - 9°. They observed, using TEM, a crossed grid of screw dislocations, as predicted by the model of Read and Shockley, with spacing $d = b/\theta$ where b is the magnitude of the Burgers vector and θ the misorientation angle (see figure 2-10). The study was extended to high angle grain boundaries [18, 19]. In this study the authors prepared (001) twist boundaries of gold with misorientations ranging up to 45° using the same technique as in ref [17]. The boundaries were analyzed by electron diffraction and imaging in the transmission electron microscope. Primary screw dislocation grids were observed directly by diffraction strain contrast imaging at twist angles up to approximately 25° and again their spacing was found to correspond with that predicted by the Frank formula (valid at high angles) $d = b_o \sin(\theta/2)$. At twist angles greater than 25° contrast became too poor to observe the dislocation grids directly. In these cases the d spacings

Figure 2-10: Crossed grid of screw dislocations in Gold twist boundary. From Schober and Balluffi, 1970

were obtained indirectly by use of the boundary reflections in the bicrystal electron diffraction patterns. They were again found to obey the Frank law. Secondary grain boundary dislocations were also observed at high angles using TEM imaging. This was possible since their spacing is much greater than primaries (especially close to low Σ boundaries). Secondary grain boundary dislocation networks were observed at misorientations very close to the three highest periodicity, shortest wavelength boundaries (special boundaries) possible for (001) twist boundaries, the Σ 5, Σ13, and Σ 17. The results again agree very closely with theory. At misorientations very close to the special boundaries the secondary dislocations were found to be quite far apart; their spacing decreasing as the departure from the special orientation, $\Delta\theta$, increased, according to the relation $d_s = b_s 2\sin(\Delta\theta/2)$ where d_s is the secondary dislocation spacing and b_s the Burgers vectors for the secondary grain boundary dislocations which were $\frac{a}{10}< 310 >$, $\frac{a}{26}< 510 >$, and $\frac{a}{34}< 530 >$ for the Σ 5, Σ 13, and Σ 17 boundaries respectively (a = lattice parameter). The same pattern of secondary dislocation spacing was observed for all three special boundaries. Interestingly no reflections which could be attributed to the secondary dislocation network were detected in the bicrystal electron diffraction patterns. The authors suggest possible explanations for this as being that the reflections were too weak to detect or were difficult to distinguish because of double diffraction. In order to obviate these effects the same group did a study of high angle twist boundaries in gold using X-ray diffraction [20] where the multiple diffraction process is much less important. With long exposures of gold bicrystals to CuK_α radiation they were able to detect the same reflections as were observed using electron diffraction minus many of the reflections due to double diffraction because of the smaller Ewald sphere. No reflections corresponding to the secondary dislocation structure were reported.

Tilt boundaries in gold have also been studied by Balluffi and co-workers using electron diffraction and microscopy techniques similar to those used in the study of twist boundaries in gold. Low angle ($\theta = 8.4°$) symmetric tilt, [21] high angle ($\theta = 28.1°$, Σ175) symmetric tilt [22] and mixed boundaries containing a small tilt component [23] have been studied. TEM imaging revealed dislocation structure to

consist of a single set of parallel edge dislocations as predicted by Read and Shockley. Dislocations spacings were deduced from the bicrystal electron diffraction patterns. The details of this analysis are given in ref. [21]. In all cases the dislocation spacings were found to obey the Frank formula as a function of tilt angle.

The task of analyzing the structure of grain boundaries in ceramics is a bit more challenging than is the case for metals. Due to their refractory nature, bicrystals are not easily fabricated, and due to their brittleness, samples thin enough to examine in the electron microscope are difficult to prepare. As specimen preparation techniques for electron microscopy analysis became more sophisticated the study of the structure of ceramic grain boundaries became possible, however.

Several studies of the dislocation structure of twist and mixed twist and tilt boundaries in MgO were done by Sun and Balluffi. An early study [15] focused on special high angle tilt boundaries, namely the Σ 5 and Σ 13. Bicrystals were prepared by pressure welding (4500 psi, 1500°C, argon atmosphere) MgO single crystals with cleaved (100) faces misoriented at the desired tilt angle. Samples were prepared for electron microscopy analysis by mechanical grinding, annealing to remove possible defects caused by the grinding, followed by jet polishing in hot phosphoric acid. TEM examination of a near Σ 5 boundary revealed a square grid of secondary screw dislocations as is expected for a twist boundary plus a superimposed array of edge dislocations due to a small tilt component in the boundary. The Burgers vector of the screw grain boundary dislocations were of the type $\frac{a}{10}$ <310> as was the case in high angle near coincidence twist boundaries in gold. A square network of screw grain boundary dislocations was also observed in the near Σ 13 boundary. Unlike the observed grain boundary dislocations in Σ 13 boundaries in gold, which were of the type $\frac{a}{26}$ <510>, the secondary dislocations in MgO were of the type $\frac{a}{13}$ <320> which are larger than the $\frac{a}{26}$ <510> by $\sqrt{2}$ and at an angle of 45° to them. The authors suggest that core energy effects in grain boundary dislocations may be responsible as these are different in ionic solids as compared to metals.

The study was expanded to study other near coincidence boundaries in MgO [24]. Twist boundaries covering the full range of misorientations $0° < \theta < 45°$ were pre-

pared and examined using the same technique as in ref. [15]. Square grids of screw grain boundary dislocations were observed in the TEM for boundaries near the following CSL misorientations Σ 1, 5, 13, 17, 25, 29, and 53. In the low angle case ($\Sigma = 1$) the observed dislocations were primaries in all the other cases they were secondaries. Edge dislocation arrays were also observed in bicrystals which contained a tilt component. A micrograph showing the square screw dislocation network with superimposed edge dislocation array of a $\Sigma 5$ twist boundary with a small tilt component is shown in figure 2-11. In these cases the dislocation spacings were found to correspond closely with values predicted by the Frank formula $d = b/2\sin[(\Delta\theta/2)]$. $\Delta\theta$ is the angular departure from the special misorientation. No dislocation networks were observed at general misorientations or close to special misorientations where $\Sigma > 53$. In these boundaries the grain boundary dislocations have such small Burgers vectors that they are difficult to detect.

In all of the special boundaries other than the Σ 13 the screw dislocations present in the networks had Burgers vectors identical to those of comparable dislocations in twist boundaries in gold: for example, $\frac{a}{10}$ <310> for Σ 5 and $\frac{a}{34}$ <530> for Σ 17. Only the Σ 13 boundaries, as mentioned previously, were found to deviate from this behavior, having Burgers vectors along <320> rather than <510> as would be expected and was observed in gold. The authors point out that these are only partial grain boundary dislocations. A partial grain boundary dislocation may exist in a boundary when two or more crystallographically equivalent translational positions of crystal A with respect to crystal B have the same minimum energy [24]. This can occur if the boundary contains or has as its normal a symmetry axis of the CSL. Atomistic simulations of [001] twist boundaries in FCC metals by Bristowe and Crocker [26] have found there to be two other low energy, high symmetry states other than the perfect CSL structure in Σ 5, 13, 17 and 25 twist boundaries. These modifications differ only in the the relative translation of crystal A with respect to crystal B. This is just the condition required for partial grain boundary dislocations to exist. This is a possible explanation for the observations of the partial grain boundary dislocations in the Σ 13 boundary in MgO.

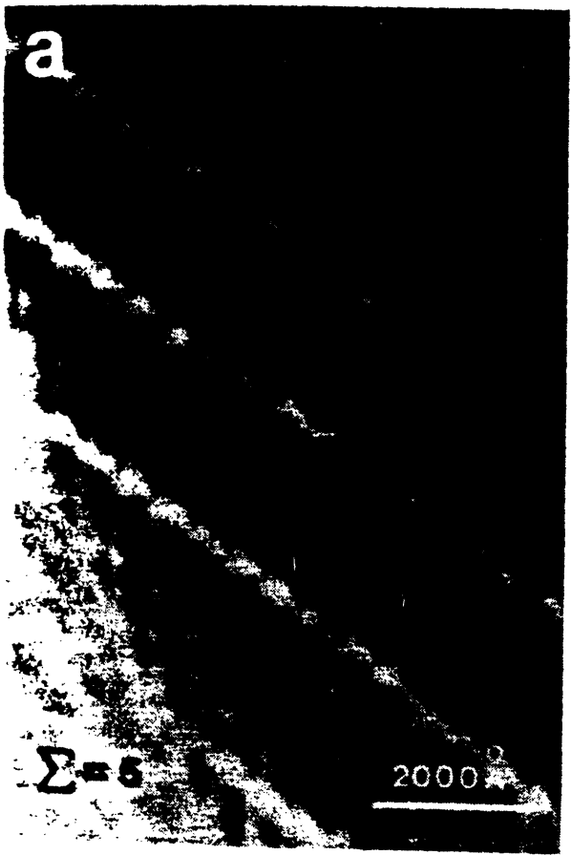

Figure 2-11: $\Sigma 5$ twist boundary in MgO with tilt component, showing screw and edge dislocation arrays.

A concommittant study of extrinsic grain boundary dislocations in MgO [25] was also done. In this study extrinsic grain boundary dislocations were observed. These are lattice dislocations which are attracted to the grain boundary and remain embedded therein as extrinsic grain boundary dislocation structures. They do not serve to accommodate the crystal misorientation associated with the grain boundary. They do not simply accumulate haphazardly at the grain boundary but rather "decompose" into two or more perfect grain boundary dislocations the sum of whose Burgers vectors is equal to the Burgers vector of the original lattice dislocation. The decomposition is accompanied by a decrease in elastic energy which is the driving force for it. These observations are completely consistent with the CSL model for grain boundaries.

The results of these studies provide strong evidence for the applicability of the CSL grain boundary model to MgO and other ionic solids. The ionic nature of the material apparently may be compensated for by suitable ionic relaxations within the framework of the CSL model. This being the case, the core structure of grain boundaries in MgO must bear some resemblance those in metals. This has been corroborated by more recent studies and its implications on grain boundary energy and diffusion will be discussed.

Experimental results concerning the structure of low Σ boundaries in ionic oxides seem to be at odds with various computer simulations [27] which suggest that large angle twist boundaries in ionic FCC materials are only marginally stable with respect to dissociation into two free surfaces. Theoretical analyses done by Wolf [28, 29] indicate that the substitution of Fe^{2+} for Mg^{2+} in the boundary plane or adjacent planes increases the stability of said boundary. The theoretical analyses involved a computer simulation based on energy minimization similar to the Harwell HADES lattice relaxation program. It has been suggested, therefore, that the stability of the MgO twist boundaries prepared by Sun and Balluffi is due to the presence of impurities segregated to the grain boundary.

In the studies of Sun and Balluffi no impurity analysis was done. However in a later study [30] the structure of small angle twist boundaries in MgO was examined as a function of impurity (Fe specifically) content. Bicrystals were prepared in a manner

similar to the previous studies using single crystals which were nominally pure and which contained 310, 4300, and 11900 ppm Fe. The bicrystals were annealed in either an oxidizing or reducing atmosphere to regulate the amount of Fe present as Fe^{2+} or Fe^{3+}. In the nominally pure MgO, square dislocation networks with Burgers vectors of the type $\frac{a}{2}$ <110>, whose spacing corresponded to that predicted by the Frank formula, were observed. These results are in accord with the observations of Sun and Balluffi. Analysis of the 4300 ppm Fe doped MgO bicrystals was performed on both as pressed and annealed (in oxidizing and reducing atmospheres) samples. In all cases, regardless of the annealing treatment, almost all of the samples analyzed contained two distinct boundary structures. One was identical to that found in nominally pure MgO, and the other a distorted hexagonal dislocation network consisting of three sets of dislocations. The dislocation line directions for the three sets were along $[1\bar{1}0]$, [210] and [120]. Distorted hexagonal dislocation networks were never observed in the pure [001] twist boundaries. The authors conclude that this effect is, therefore, a result of the presence of the Fe solute. Further examination of these dislocation structures revealed the presence of a large number of subgrain boundaries (small angle grain boundaries produced usually as a result of deformation or strain) in the Fe doped bicrystals. No such sub-boundaries were observed in the undoped MgO bicrystals. In order to determine when the sub-boundaries were formed, several as-received Fe doped single crystals were examined in the electron microscope; no sub-boundaries were present. Re-examination of the Fe doped bicrystals revealed that almost all of the sub-boundaries were within 20μm of the manufactured boundary, leading to the conclusion that the sub-boundaries formed either during the hot pressing or subsequent annealing only in the Fe doped MgO. These sub-boundaries interacted with the intrinsic twist-boundary dislocation structure, locally altering the rotation axis and angle causing the formation of regions with the distorted hexagonal dislocation network observed in the Fe doped bicrystals. The 11900 ppm Fe doped bicrystals contained the same dislocation structures as the 4300 ppm bicrystals in roughly the same quantity. The 310 ppm doped bicrystals contained boundary structures which were identical to the undoped bicrystals, suggesting that there is a transition in boundary structure

somewhere between 310 and 4300 ppm Fe.

Due to the fact that substantial segregation has been observed in bicrystal specimens with similar compositions given similar heat treatments [31] the authors conclude that the change in boundary structure is due to solute segregation. The authors propose that the boundary decomposition in the presence of Fe is due to thermodynamic rather than kinetic reasons. They believe that the dissociation is due to the fact that, in the presence of segregated Fe, the boundary can lower its free energy by forming sub-boundaries and dissociating into the distorted hexagonal dislocation structures. This is in contrast to a kinetic interpretation wherein it is assumed that the boundary is unstable, even in nominally pure MgO bicrystals, but that the Fe lowers the activation barrier to the grain-boundary phase transformation. The authors make this claim based on prior work which had shown that Fe solute impeded rather than enhanced the motion of grain boundaries in MgO, thus making it unlikely that the presence of Fe would improve the kinetics of grain boundary dissociation. One would think that the results of this study would support the results of Sun and Balluffi over the theoretical computations of Wolf, which claimed that twist boundaries in pure MgO are unstable unless stabilized by the presence of Fe. This is not necessarily the case, though. It is still possible that the twist boundaries are stabilized by the presence of Fe, but that they are still further stabilized by dissociation of their intrinsic dislocation structure into the aforementioned distorted hexagonal network.

Atomic scale detail has also been observed in grain boundaries in ceramics. A study of low- and high-angle symmetric tilt boundaries in NiO has been done by Merkle and Smith [32, 33] using atomic-resolution electron microscopy. Boundaries near the Σ 5 and Σ 13 orientations as well as several low angle boundaries were fabricated using the Verneuil technique. (Oriented single crystals were used as seeds and the bicrystals were grown in an arc-image furnace using ultra pure NiO powder as a source material) The high-resolution electron microscopy of the boundaries confirmed several predictions of the geometrical (CSL) theory. Firstly the structure of each crystal is preserved virtually up to the boundary plane. The boundary layer is no more than one or two atomic spacings thick. In the case of the special boundaries

Σ 5 and Σ 13, in particular, the repeat units are small, that is the boundaries have a high periodicity. Facetting was observed in the Σ 5 boundaries; symmetric (210) and asymmetric facets were detected. In the case of the asymmetric facets the boundary was usually parallel to a (100)/(340) plane on opposite sides of the boundary. This can be thought of as being brought about by a translation of the boundary parallel to itself. Not surprisingly, different core structures were observed in the different facets. Figure 2-12 shows a structural image of the Σ 5 tilt boundary along with close-ups of the different core structures. The images show a somewhat open structure at the boundary; linear expansions are 0.4 Å and 0.3 Å perpendicular to the boundary for the two facets shown in figure 2-12. This is in sharp contrast to the molecular statics calculations of Duffy and Tasker [34] which predict huge openings at the cores, corresponding to an expansion of roughly 1.1 Å. It is worth noting, however, that the simulations are generally done at a temperature of 0 K where there are no entropy effects. The fabricated bicrystals are quenched from the growth temperature of 1400 K, essentially freezing in the high temperature structure where entropy effects may be significant. In the case of the Σ 13 (320) boundary, close agreement was observed between the experimental and calculated images. In particular, the prediction of an asymmetric core structure of the boundary was confirmed. The NiO grain boundaries also showed strong Fresnel contrast effects as a function of defocus in bright field images, suggesting a reduction in atomic density at the grain boundary which the authors suggest might be as a result of the presence of Schottky pairs in and around the boundary cores. This is in accord with the molecular statics calculations of Wolf [28] which predict that high angle grain boundaries are stabilized by the presence of Schottky pairs. The implications on grain boundary diffusion will be discussed in a later section.

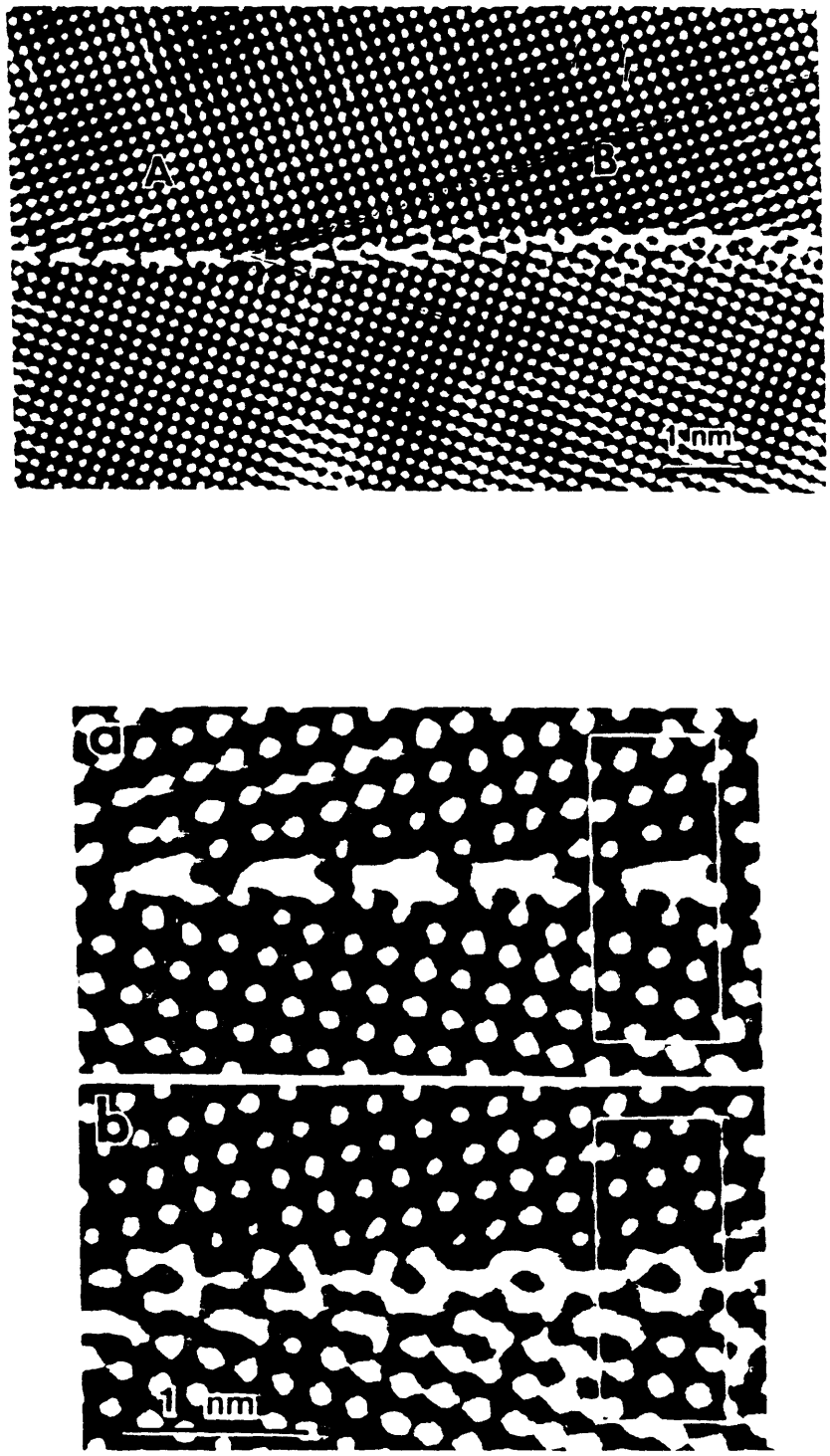

Figure 2-12: High resolution micrograph of $\Sigma 5$ tilt boundary in NiO with close-ups of core structures. From Merkle and Smith, 1987

2.1.3 Grain Boundary Energy

Read-Schockley Expression for Energy of Low Angle Grain Boundaries

An expression for the interfacial energy of a low angle grain boundary was derived in the early 1950's by Read and Shockley [35, 36] using the known elastic energy of a discrete dislocation and the fact that a low angle grain boundary can be thought of as an array of dislocations. The shear stress $\sigma_{\theta z}$ on the slip plane in the slip direction of a single straight dislocation in an isotropic material is given by :

$$\sigma_{\theta z} = \frac{Gb}{2\pi r}$$

where G is the shear modulus, b the magnitude of the Burgers vector and r the distance from the dislocation. For the purpose of the analysis, the boundary is divided into strips normal to itself and parallel to the dislocation line such that one dislocation is at the center of each strip. The width of each strip is equal to the dislocation spacing $D = b/\theta$ for small angle boundaries. The energy in a strip E_s, is divided into three parts. E_I is the energy of atomic misfit in the dislocation core (radius = r_l) where linear elasticity does not apply. E_{II} is the elastic energy in the good material outside the dislocation core extending out to a radius R = KD where $\frac{b}{D} << K < 1$. The values of K (and hence R) are somewhat arbitrary but must be small enough that the stress field within R is approximately equal to the stress field of the the enclosed dislocation alone. E_{III} is the remaining energy of the strip (see figure 2-13) thus

$$E_s = E_I + E_{II} + E_{III}$$

If θ changes by a small amount $d\theta$ the change in E_s, dE_s is

$$dE_s = dE_I + dE_{II} + dE_{III}$$

If θ decreases by $d\theta$ R and D will increase according to :

$$-\frac{d\theta}{\theta} = \frac{dD}{D} = \frac{dR}{R}.$$

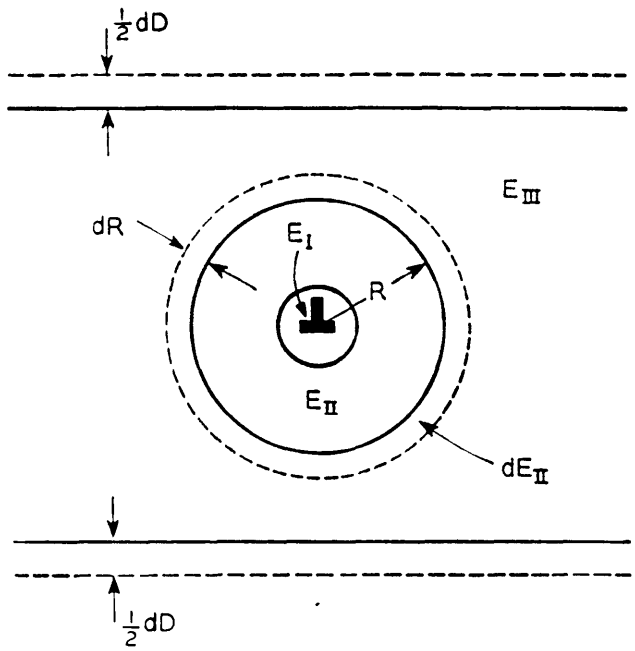

Figure 2-13: Geometry used for computation of strain energy in and around dislocation core

This can easily be verified using the fact that $\theta = \frac{b}{D}$ and R = KD. If the strip width is increased by dD the change will be as follows. E_I is only concerned with the energy of the core. Therefore, as long as the cores don't overlap (which they do not, by definition, in a small angle grain boundary) it is unchanged. E_{II} increases since D increases. The increase in E_{II}, dE_{II} is the energy in the ring bounded by R [=KD] and R + dR [= K(D + dD)]. E_{III} is unchanged. The area of each strip increases but the elastic strain energy/area decreases because the dislocations are spaced further apart. The effects exactly cancel each other out. Since E_I and E_{III} are unchanged, the incremental change in total energy $dE_s = dE_{II}$, the energy in the ring bounded by R and R + dR. In that ring the stress is due entirely to the enclosed dislocation and can thus be calculated. If the ring is imagined to be unconstrained by the surrounding material and then cut and allowed to relax (see figure 2-14) the strain is relieved and the dislocation eliminated. The energy in the ring is equal to the work done on the cut which is $\frac{1}{2}\sigma dR$ times the offset which is equal to b, the magnitude of the Burgers vector. If the cut is along the slip plane $\sigma_{\theta z} = \frac{Gb}{2\pi r}$ and thus

$$dE_s = \frac{1}{2}\sigma b dr = \frac{Gb^2}{4\pi}\frac{dr}{r}$$

since

$$\frac{dR}{R} = -\frac{d\theta}{\theta}$$

then

$$dE_s = -\frac{Gb^2}{4\pi}\frac{d\theta}{\theta} E_s = \frac{Gb^2}{4\pi}\int -\frac{d\theta}{\theta} \quad = \quad \frac{Gb^2}{4\pi}[-ln\theta + c] \quad = \quad \frac{Gb^2}{4\pi}[c - ln\theta]$$

The total grain boundary energy / area is the energy / area per slab, E_s times the density of dislocations 1/D = θ/b.

$$E \quad = \quad \frac{E_s\theta}{b} \quad = \quad \frac{Gb\theta}{4\pi}[c - ln\theta]$$

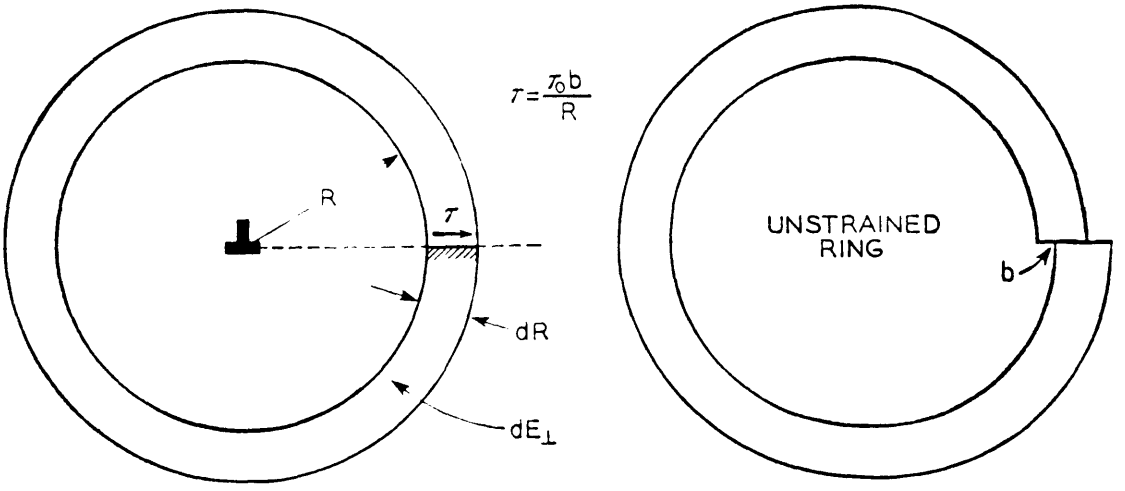

Figure 2-14: Computation of E_{II}.

generally written as

$$E = E_o\theta[A - ln\theta]$$

where $E_o = Gb/4\pi$ and A is an undetermined constant of integration which depends on the atomic misfit in the dislocation cores. A curve of this form has several interesting properties. First, as expected, E goes to zero as θ goes to zero. This is not immediately obvious as the equation becomes indeterminate if one substitutes 0 for θ. However, application of L'Hopitals rule reveals that this is indeed the case. This is an important result since it is required that in the limiting case of $\theta = 0$ (no boundary) the boundary energy would be zero. It is also worth noting that there is a cusp at $\theta = 0$ ($dE/d\theta = +\infty$). The significance of this fact will become apparent in the discussion of energies of high angle boundaries. This derivation is only valid for low angle grain boundaries since it was assumed that the crystal could be cut into slices and the energies of the individual dislocations could be summed. This breaks down when the dislocation cores begin to overlap which is the case when θ is more than about 15 °. The formula agrees well with experimental data for low angle grain boundaries in metals if the quantities E_o and A are used as fitting parameters [35]. Recall that they are theoretically calculable, but are only useful if absolute boundary energies are measured.

As has been previously mentioned, the Read-Shockley formula is only valid at low angles where the individual dislocations comprising the boundary are discrete. As the misorientation increases the boundary becomes a continuous slab of bad material and the boundary energy remains roughly constant at higher angle misorientations. This has been confirmed experimentally in metallic [35] as well as in ceramic/ionic systems [37]. It has also been verified theoretically using the dislocation models of Read and Shockley by Li [38]. There are deviations in this behavior at misorientations corresponding to twin boundaries and low Σ CSL boundaries. The good fit of these boundaries manifests itself as as cusps in the E versus θ plots. This result should not be surprising as it was pointed out previously that there is always a cusp in the E versus θ plot at $\theta = 0$ corresponding to the $\Sigma = 1$ orientation, the ultimate in good

fit. A physical argument for the presence of these cusps is as follows. Dislocations cannot always be evenly spaced. Since they can only occur on a horizontal plane intersecting the grain boundary they are only evenly spaced when D/b $(1/\theta)$ is an integer. When this is not true there will be a perturbation in the spacing of the dislocations. For example if a boundary had θ corresponding to a dislocation every six atomic planes it would have an energy of, say, $E(\theta)$. Let θ be increased slightly so the average dislocation spacing would decrease to 5.9 planes. There cannot, of course, be a dislocation every 5.9 planes. What happens is that the structure would remain such that there was a dislocation every six planes and occasionally there would be a dislocation every fifth plane so that the average spacing was 5.9. This contributes an energy term of the order $-(E_0/6)\delta\theta \ln\delta\theta$ far from the grain boundary; the effective strength of the perturbation is b/6. A similar cusp will occur whenever dislocations are spaced at exactly an integral number of planes. Minor cusps will also occur at n/2 planar spacings, where n is an integer At 6.5, for example, the configuration will be a regular alternation between 5 and 6 plane spaced dislocations. In fact, there should be cusps at least theoretically, at every θ which gives a rational value for D/b [35]. Practically though, this fine structure is never observed as it will always be smoothed out by statistical fluctuations. Only the prominent cusps (twin boundaries, low Σ boundaries) are ever observed.

An alternate explanation for the presence of cusps in terms of a secondary grain boundary dislocation model has been offered by Balluffi. [12] According to CSL theory, and as has been discussed previously, high coincidence (low Σ) boundaries may formally be described by an array of primary dislocations giving them a characteristic high periodicity. As the misorientation changes from these highly periodic boundaries, there are perturbations in the primary dislocation spacing which can be described as secondary dislocations. As the misorientation of the boundary increases from the low Σ orientation, those secondaries become more closely spaced. If the secondary grain boundary dislocations possess local stress fields they should produce cusps in the E versus θ plots. If it is assumed that the elastic fields are restricted to cylinders of radius D/2 around each secondary dislocation, D being the spacing of the secondary

dislocations, and that the field can be treated in the same manner as the field around an isolated dislocation (recall that the secondary dislocations are actually buried within the primary dislocation grid) then the energy stored therein is given by [14]

$$E = \frac{Gb^2}{4\pi(1-\nu)} \ln(\frac{\alpha D}{2b})$$

where most quantities are as defined previously, and ν = Poisson ratio, $\alpha = b/r_0$, r_0 = dislocation core radius, $\alpha \approx 1$. The change in surface energy ΔE is given by this energy, E, multiplied by the reciprocal of the dislocation spacing D, (the closer the spacing the greater the energy contribution of the secondaries). The spacing of the secondaries can be expressed in a manner analogous to primaries as:

$$D = \frac{b}{2\sin\frac{\Delta\theta}{2}}$$

where $\Delta\theta$ is the deviation from the special orientation. When $\Delta\theta = 0$ the secondaries are infinitely spaced, i.e. there are none, as is expected in a special boundary. Presumably $\Delta\theta$ is small, so we can use the approximation

$$D = \frac{b}{\Delta\theta}$$

This has been shown to be the case experimentally. The cusps are centered in a narrow band around the special orientation. An expression for ΔE is thus:

$$\Delta E = E \cdot \frac{1}{D} = \frac{Gb^2}{4\pi(1-\nu)} \cdot [\frac{\Delta\theta}{b}] \cdot \ln[\frac{\alpha}{2\Delta\theta}]$$

Rearranging and grouping parameters together gives

$$\Delta E(\Delta\theta) = (A \cdot \Delta\theta)[B - \ln\Delta\theta]$$

$$A = \frac{Gb^2}{4\pi(1-\nu)} \qquad B = \frac{\alpha}{2}$$

This expression is exactly analogous to the expression for the energy of a low angle tilt boundary, and thus is similarly cusped at $\Delta\theta$=0, the special orientation.

Measurements of grain boundary energy are generally done by dihedral angle measurements at boundary triple junctions or boundary-surface intersections. A view of three boundaries meeting at a junction is shown in figure 2-15. Each boundary can reduce its energy by shrinking to reduce its area or rotating to an orientation of lower energy. The relationship between the boundary energies E_1, E_2, and E_3 and the angles Ψ_1, Ψ_2,and Ψ_3 is equivalent to the triangle of forces problem for three forces acting on a point. If each boundary is represented by a vector whose length is equal to the energy of that particular boundary then the relationship between the boundary energies and angles is given by the law of sines [35, 39].

$$\frac{E_1}{\sin(180-\Psi_1)} = \frac{E_2}{\sin(180-\Psi_2)} = \frac{E_3}{\sin(180-\Psi_3)}$$

which is equivalent to :

$$\frac{E_1}{\sin\Psi_1} = \frac{E_2}{\sin\Psi_2} = \frac{E_3}{\sin\Psi_3}$$

This is an approximation since it does not take into account the "torque terms" which would cause the boundaries to rotate. An exact expression taking into account the torque terms ($\frac{\partial E_i}{\partial \varphi_i}$), φ = misorientation parameter, was derived by Herring [40]. This solution is not often used in practice, though, as the quantities ($\frac{\partial E_i}{\partial \varphi_i}$) are not easily measured.

When a boundary intersects a free surface at normal incidence as in figure 2-16 a similar analysis is possible yielding: [39]

$$E_b = 2E_s \sin\frac{\Psi}{2} \tag{2.2}$$

This geometry is particularly useful to experimentalists as it allows for absolute boundary energy determination if the surface energy is known, and, unlike the triple junction method, it allows the experimenter, by making appropriately oriented bicrystals, to specify the boundary orientation. This allows for systematic investigations

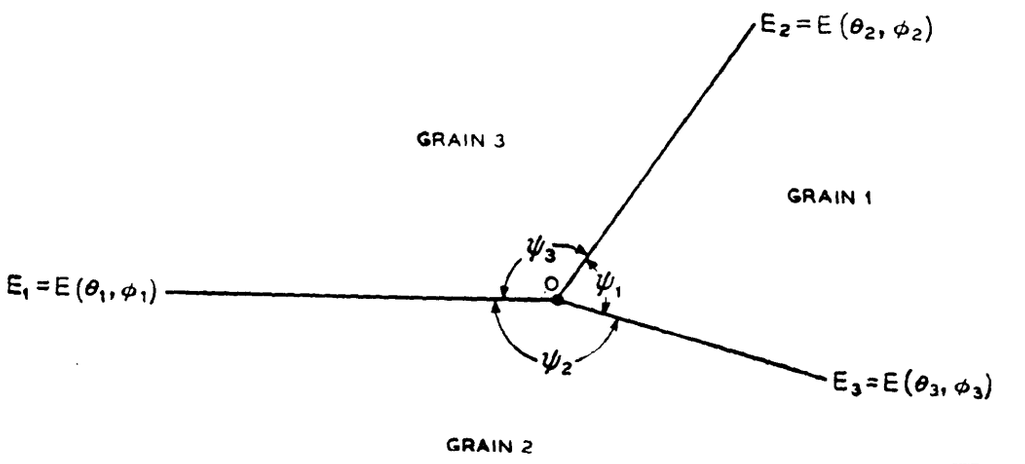

Figure 2-15: Triple junction method for measuring boundary energies. - Three boundaries meeting at a junction.

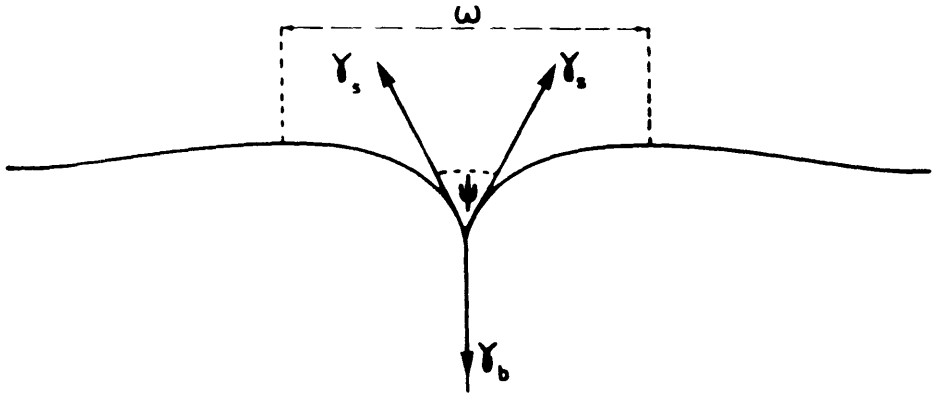

Figure 2-16: Calculation of boundary energy by boundary/surface dihedral angle measurement

of boundary energy as a function of orientation . The triple junction method only allows for the determination of the boundary energies relative to one another, and control of boundary orientation is difficult if not impossible.

Experimental measurements of grain boundary energy have been performed on a number of metals. The data for ceramics is much less extensive. However, several studies have been done in recent years. Also, numerous molecular statics / computer simulations of grain boundaries have been done.

Several studies of the energies of [001] tilt boundaries in NiO have been done. All of these studies employed the bicrystal/thermal grooving technique. NiO bicrystals were all grown from the melt using various techniques including the Verneuil and floating zone methods. The general procedure followed is that the single crystals are cut, oriented and clamped together to be used as seeds. The growth is then carried out and the bicrystals are annealed to relieve stresses and cut into samples. Flat surfaces were prepared perpendicular to the boundary by mechanical polishing.

Boundary energies were determined via dihedral angle measurements. Bicrystals were thermally grooved by annealing in air, thus the need for the initial flat surface. Actual surface contours were measured by either surface profilometry or interference microscopy. From these contours the dihedral angles could easily be measured and the boundary energies calculated

In studies by Ready and Jech, and Dhalenne [41, 37] [001] symmetrical tilt boundaries of NiO were studied. The results of the studies are in fair agreement with each other and agree qualitatively at least with the Read-Shockley expression for grain boundary energy at low misorientation angles. In both studies the grain boundary energy increased rapidly at low values of θ, reached a maximum around 20° and remained roughly constant after that, figure 2-17. In the study by Dhalenne [37] several special misorientations corresponding to low Σ values were also examined, among them the $\Sigma 5$ (36.9°), $\Sigma 13$ (22.6°) and the $\Sigma 17$ (28.1°). Oddly no energy cusps were measured at these misorientations. The result is disturbing since cusps have been predicted at these misorientations by CSL theory, and since secondary dislocation networks have been observed to obey the Frank expression for their spacing near these

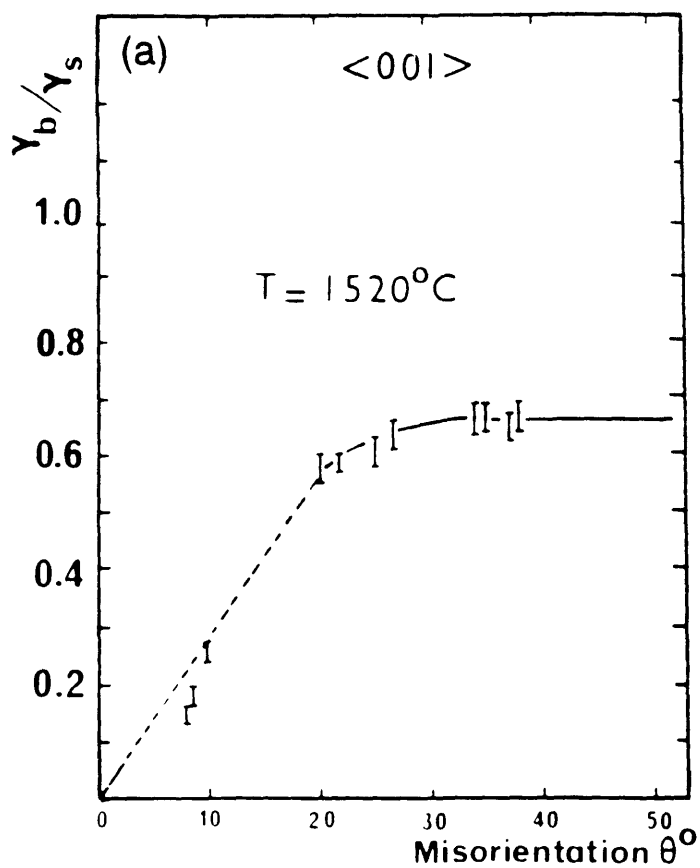

Figure 2-17: Energy of [001] symmetric tilt boundaries in NiO, as a function of misorientation parameter, θ. From Dhalenne, 1984

orientations in both metals and ceramics. The authors claim to have viewed these boundary structures themselves by transmission electron microscopy. The authors believe that cusps do exist in the E vs. θ curve at these misorientations but are not deep enough to be measured by thermal grooving. The authors of both studies also point out that segregation also plays a role in determining the energy of boundaries. This is not accounted for in the CSL/dislocation models of grain boundaries. This was observed directly by Ready and Jech [41] who also measured boundary energy as a function of annealing temperature from 1300 - 1550°C. They noticed a strong dependence of boundary energy on anneal temperature. Higher boundary energies were observed at lower temperatures which is consistent with a boundary stabilized by segregated impurities. The more segregation present, the lower the boundary energy is expected to be. More segregation would occur at higher temperatures where segregating species are more mobile, resulting in lower boundary energies.

The same authors have studied [011] symmetric tilt boundaries in NiO [42, 43]. Grain boundary energy was measured as a function of tilt angle at two different anneal temperatures, using a method identical to their previous study of [001] boundaries. The results show a marked difference in behavior from the [001] tilt boundaries. At low tilt angles there is a rapid increase in the relative energy up to about 20° where a plateau is reached. This result is similar to the behavior of the [001] boundaries, however unlike the [001] boundaries the plateau is interrupted by three distinct cusps in the grain boundary energy versus misorientation plot at the (221), (111), and (113) twin orientations. These cusps correspond to the $\Sigma 9$ (39°), $\Sigma 3$ (70.5°), and $\Sigma 11$ (129.5°) CSL designations respectively. Also the relative grain boundary energies are higher for the [011] tilt boundaries as compared to the [001] tilt boundaries by a factor of 1.5 - 2. This result has more recently been corroborated for MgO in a study by Handwerker et al. [44] In this study dihedral angle measurements were done on large numbers of randomly oriented grain boundary/surface junctions in polycrystalline MgO and undoped and MgO-doped Al_2O_3. MgO samples were prepared by calcining high purity $MgCO_3$ to MgO, cold pressing at 700 MPa and sintering at 1600°C for 48 hours to 99% of theoretical density. Samples were polished after sintering to a

final grit size of 0.25 μm and were packed in MgO powder for annealing to avoid excessive evaporation. Grooving was done at 1250°C in air. Dihedral angles were measured using the metal reference line (MRL) technique and conventional scanning electron microscopy. For MgO the values of measured dihedral angles ranged from 97 - 123° with a median of 112° and a roughly uniform distribution (no particular value favored). This corresponds to a relative grain boundary energies E_b/E_s of 0.95 - 1.33 the extremes corresponding to the lowest and highest energy tilt boundary orientations (the [001] and [011] respectively). Dhalenne et al. obtained the values of 0.7 and 1.2 for [001] and [011] symmetric tilt NiO boundaries grooved at 1520°C. These though were the "plateau values", the highest values in the plot of E versus θ corresponding to general, aperiodic boundaries. In that study low energy boundaries were also detected at special misorientations (for the [011] case) since boundary orientations were varied systematically. In the Handwerker study of randomly oriented boundaries presumably some <011> as well as <001> boundaries were measured but no low energy boundaries ($\Psi > 160°$) were detected. This result is surprising because it means that not only were no special high angle boundaries present, but also no low angle grain boundaries. There should have been some present for reasons of sheer probability alone. Low energy boundaries were detected in the undoped Al_2O_3.

There is not much literature on grain boundary energy in MgO, the above study being one of the few that exist. There is, however, one rather well known study which is indirectly related to grain boundary energy. Chaudhari and Matthews studied coincidence twist boundaries in MgO smoke particles [45]. The investigators measured misorientation angles of MgO twist boundaries using transmission electron microscopy. Samples were prepared by burning a magnesium rod in air and collecting the smoke particles on carbon covered grids, the idea being that the cubic smoke particles would be free to rotate and settle into low energy orientations when they came together. Results showed that often (001) surfaces did come into contact, most of these were in parallel contact (i.e. $\theta = 0$) as expected since this is the lowest energy orientation, but among the non parallel bicrystals there was a distinct preference was apparent for low Σ orientations, providing indirect evidence for the low relative energy

of these boundaries. Specifically, relative maxima were present at 16.5°, 22.6°, and 37.3° in the histograms of frequency versus misorientation angle, corresponding to the $\Sigma 25$, $\Sigma 13$, and $\Sigma 5$ boundaries respectively. The absence of a peak corresponding to the $\Sigma 17$ boundary seems to suggest a relatively high energy for this boundary.

A more systematic study of grain boundary energy in MgO bicrystals was done by Kimura et al., [46] who prepared bicrystals by hot pressing cut, polished MgO single crystals. They examined low and high angle [001] symmetric tilt boundaries as well as one high angle [111] tilt boundary. Thermal grooving was done at 1500°C for times of 10 - 80 hours. Boundary groove widths and depths were measured by means of optical interferometry. Presumably relative boundary energies were computed using equation 2.2 The authors did not specify the relation that was used. The results were similar to those of the (more complete) study of [001] symmetric tilt boundaries in NiO by Dhalenne et al. The boundary energy (E_b/E_s) was cusped at $\theta = 0$ and rose to a maximum around $\theta = 23°$, behavior in accordance with the Read-Shockley equation for energy of low angle grain boundaries. Above 23° the boundary energy reached it's plateau value, $E_b/E_s = 0.65$, which is virtually identical to that measured by Dhalenne for NiO. Also, similarly, no low energy boundaries were measured at the expected angles for the low Σ orientations. The measured energy of a given boundary did not change with anneal time.

2.2 Grain Boundary Segregation

The presence of impurities segregated from the bulk is a mitigating factor in virtually all studies of grain boundary diffusion, and will be examined further in this section. Diffusion in solids, be it bulk or grain boundary diffusion, is dictated by point defect concentrations. In ionic ceramics, due to their high defect formation energies, bulk point defect concentrations are often determined by the amount of aliovalent impurities present. This is always the case in MgO. If segregation exists then defect chemistry (and hence the concentration of point defects) in the vicinity of the grain boundary will be different from the bulk, obscuring the intrinsic properties of the

grain boundary, and diluting our ability to measure structure-property relations of grain boundaries. In cases where the extent of segregation is great, there may exist continuous second phases along grain boundaries in which case our ability to measure properties of the grain boundary are totally muted.

Impurity segregation is usually the result of one or both of the following: insolubility or boundary electrostatic potential. The first case is the simplest, impurities insoluble in the bulk either form second phase inclusions or are rejected to the grain boundaries where they can accumulate to any extent. Segregation due to insolubility occurs in both metals and ceramics and is mainly due to size differences between host and impurity ions. By having impurity ions segregate to the boundary the total elastic energy of the system is reduced, this reduction in energy is the driving force for the segregation. An expression for the tendency of a particular species to segregate has been derived by McLean: [47]

$$C_b = \frac{C_\infty \exp(\frac{-F_a}{kT})}{1 - C_\infty \exp(\frac{-F_a}{kT})}$$

where C_b is the concentration of that particular species in the grain boundary region, C_∞ is the bulk concentration, and F_a is the free energy of adsorption which is low for solutes with a small degree of misfit and large for solutes with a high degree of misfit. An often-used estimate of F_a is the energy of an elastic inclusion in an elastic continuum, where the host material is the continuum and the solute ion is the inclusion. The elastic energy U, (due to Eschelby [48]) is:

$$U = \frac{6\pi r^3 (\frac{\Delta r}{r})^2 B}{1 - (\frac{3B}{4\mu})}$$

where r is the radius of the host ion for that particular lattice site, Δr is the difference in radius between the solute and host ion, B and μ are the bulk modulus and shear modulus, respectively, of the host material.

The effect of grain boundary electrostatic potential on segregation behavior is more difficult to model, but several approaches have been proposed. Surfaces and

grain boundaries can be thought of as infinite sources and sinks for point defects. The formation of point defects, vacancies and interstitials, can be thought of as a process of equilibration with a surface or grain boundary. Vacancies are formed at surfaces and move into the bulk crystal by exchange with lattice ions. Interstitials can be formed by the motion of surface ions to interstitial positions in the bulk crystal. Vacancies and interstitials can also be formed in the bulk crystal in pairs (Frenkel defects) by the migration of an ion from a lattice site to an interstitial position. Given that a surface can generate point defects individually (and not in pairs as in the bulk) their concentrations need not be equal at or near surfaces or grain boundaries. In fact the concentrations of point defects are dictated by the individual defect formation energies g_i and g_v for interstitials and vacancies respectively. These energies are functions of surface orientation or grain boundary misorientation and of course differ depending on whether the defect is cationic or anionic. Taking vacancies as an example, if the free energy of formation of cation vacancies is less than the free energy of formation of anion vacancies then there will always be an excess of cation vacancies near the surface resulting in a positively charged surface. A negative space charge cloud is thus formed adjacent to the surface or grain boundary. This distribution of charge will retard the further formation of cation vacancies and while enhancing the formation of anion vacancies the result being that in equilibrium the bulk concentration of anion and cation vacancies is equal (as is required by charge neutrality) [49, 50]. This is the case in an intrinsic ionic crystal. In the case of an extrinsic material the bulk point defect concentrations are determined by the concentration of aliovalent impurities rather than by the intrinsic free energies of formation. There is still an equilibrium between the surface and the generated point defects and thus the surface potential and space charge layer are still present in an extrinsic material.

Surface and grain boundary potentials induce segregation of mobile charged impurities. Attempts to model and calculate the magnitude and spatial variation of the surface potential have been made by many different authors for different materials, most notably Kliewer and Koehler [50, 51, 52, 53] who modeled surface potential in materials where Schottky and Frenkel disorder predominated (NaCl and AgCl re-

spectively) and Yan, Canon, and Bowen [54] who applied both the space charge and elastic contributions to the calculation of solute segregation. In MgO and other ceramic oxides segregation of impurities is common and over the years many studies of grain boundary segregation have been done using a variety of techniques. Several reviews of grain boundary segregation in ceramics, oxides in particular have been done by Kingery [55, 56, 57].

Before the availability of modern surface analytical techniques much of the evidence for grain boundary segregation came from empirical observation. For example it has long been known that LiF and NaF additions aid in the densification of hot pressed MgO polycrystalline ceramics [58]. It was thought that these phases accumulated at the grain boundaries and aided in material transport and slippage during hot pressing by a liquid phase mechanism. This hypothesis turned out to be correct.

With the dawn of modern surface science though, many systematic studies of surface and grain boundary segregation have been done. A study which confirmed the above observation was done by Johnson et al. [59] who studied hot pressed MgO using Auger electron spectroscopy. The authors hot pressed a series of polycrystalline MgO samples at varying temperatures/times with varying LiF/NaF concentrations both with and without subsequent annealing. Additives ranged from 0.3 to 2 weight percent LiF or NaF. Pressing times varied from 15 minutes to 2 hours; pressing temperatures ranged from 1000°C to 1260°C. Samples were fractured and analyzed by inert ion beam sputtering coupled with Auger analysis so as to obtain concentration profiles as a function of distance from the grain boundary. All fractures were determined to be intergranular by scanning electron microscopy. Analysis revealed all samples to contain grain boundary segregation. Even the nominally pure MgO sample (20 minutes 1260°C) contained Ca and Ti in excess at the grain boundaries which disappeared within 10 atomic layers of the grain boundary. Both the LiF and NaF-doped MgO showed a considerable amount of fluoride present at the grain boundaries (30 - 40 atomic % estimated) of the as-pressed material. As was the case with the Ca and Ti, the species were located within 10 atomic layers of the grain boundary with steep concentration gradients. As the anneal temperatures of the hot-pressed

samples increased, the amount of fluoride present in the grain boundaries decreased while the amount of calcium increased, see fig. 2-18. This can be attributed, no doubt, to the volatility of the fluoride phases at the anneal temperatures used (1315 - 1540°C). The calcium oxide, not being volatile at those temperatures, can diffuse faster to the grain boundaries during the annealing than during the generally shorter, lower temperature hot pressing runs, thus the higher Ca concentration as annealing temperature increased. These results demonstrate unequivocally the presence of segregation of impurities localized to grain boundary regions and confirm the proposed liquid phase sintering mechanism responsible for the densification of NiF and LiF doped MgO ceramics.

Studies of aluminum segregation (spinel precipitation) in polycrystalline MgO were done by Berthelet et al. [60] and Kingery et al. [61]. In the study by Berthelet, MgO samples with 0.43% and 0.031% by mass of Al were prepared. The former were prepared by adding α-alumina to reagent grade magnesium carbonate and hot pressing. The latter sample was prepared by evaporating alumina onto a substrate of nominally pure hot pressed MgO and annealing to achieve homogeneity. All heat treatments were done at 1850°C. After heat treatment, samples were either air quenched to room temperature or crucible cooled at a rate of roughly 100°C per minute. Samples were thinned to electron transparency and observed under a 100kV transmission electron microscope. Segregation was revealed at grain boundaries and dislocations by the presence of macroscopic precipitates. Electron diffraction analysis of the precipitates revealed that aluminum did not segregate in the form of Al_2O_3 as it was incorporated into the MgO, but rather as the ternary phase spinel, $MgAl_2O_4$. This is not a surprising result since spinel is a stable phase consisting of equal molar ratios of MgO and Al_2O_3. Extensive precipitation was observed at boundaries in the 0.43 weight percent sample. Precipitates were fewer in number in the air quenched samples as compared to the crucible cooled ones, which is reasonable because in the slower cooled samples more time was spent at the kinetically-favored undercooling temperature at which nucleation is most likely. In low angle grain boundaries an orientation relationship was observed between the precipitate and matrix; [110] and

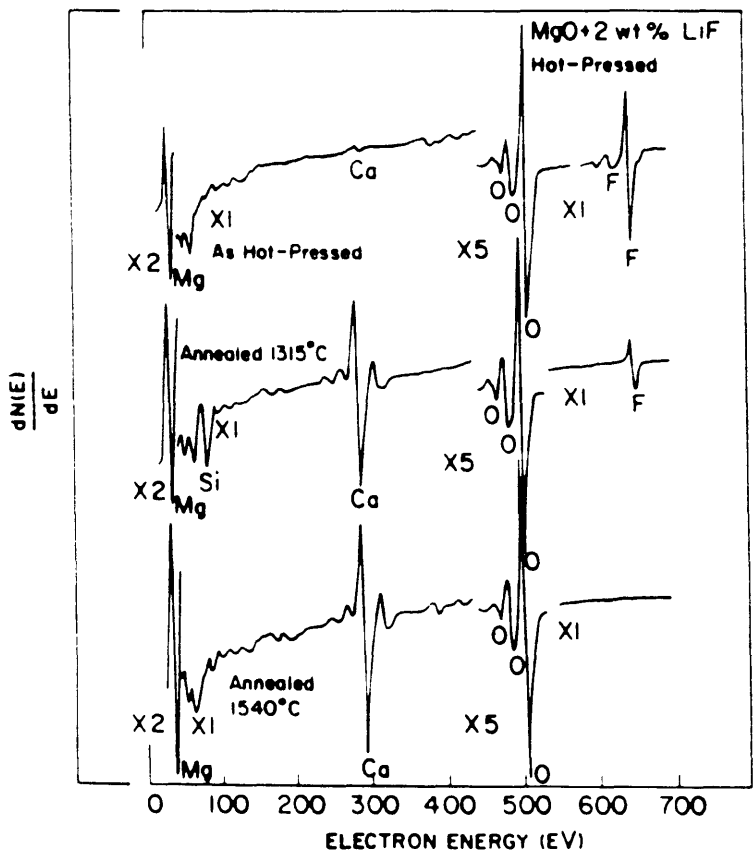

Figure 2-18: Auger spectra of grain boundary fractures in MgO doped with 2% LiF for as pressed samples, and samples annealed at 1315 C and 1540 C showing the decrease in fluoride concentration and the increase in calcium concentration. From Johnson et al., J. American Ceramic Society, 57 [8] 342-44 (1974).

[112] planes in MgO were parallel to the identical planes in spinel. In a system with such substantial precipitation, segregation can almost assuredly be attributed to insolubility/strain energy minimization. Grain boundaries and dislocations served as sites for heterogeneous nucleation of precipitates. This conclusion is supported by the observation of bulk precipitation in the quenched samples. None was observed in the crucible-cooled samples. This is consistent with a heterogeneous nucleation mechanism. In the more slowly-cooled samples, spinel would have time to diffuse to the grain boundaries where it could nucleate at lower undercoolings. However, in the quenched samples there was insufficient time for diffusion to the boundaries, so homogeneous nucleation occurred in the bulk, at much larger undercoolings no doubt. No precipitates were observed in the 0.031 weight percent Al_2O_3 sample at grain boundaries or dislocations. This is not to say that there was no segregation. It cannot be expected not to find segregation even in nominally pure MgO heated to 1850°C much less in MgO that has been doped, but the TEM technique can only detect segregation if it is present in the form of macroscopic precipitates. For the 0.031% Al samples at the high cooling rates used there was insufficient driving force for precipitation even at favored sites such as grain boundaries and dislocations.

The study by Kingery et al. [61] was a bit more thorough. Knowing that segregation need not be accompanied by precipitation they used ion microprobe mass spectroscopy to detect the presence of Al close to the surfaces of MgO single crystals doped with two different concentrations of Al_2O_3 . The crystals were prepared by vapor phase deposition and doped by hydrostatically packing in Al_2O_3 and heating at 1800°C. The crystals were then removed from the Al_2O_3 and heated at 1870°C to achieve homogenization. Fresh surfaces were then prepared by cleaving and etching in 150°C phosphoric acid to remove surface damage. These samples were then annealed in air for several hours at 1800°C to induce segregation. As in the previous study half of the samples were air quenched and the other half furnace cooled (35°C/minute) to determine the effect of cooling rate. Bulk Al concentrations, revealed by wet chemical analysis, were 0.187 and 0.006 weight percent. Samples were first etched in 50°C sulfuric acid and examined using scanning electron microscopy to search for precipitates.

Sulfuric acid etched the bulk MgO leaving behind the spinel precipitates, making them easier to detect. Precipitates were only observed in the 0.187 weight% sample which had been furnace cooled; this is seemingly inconsistent with the results of the previous study. Recall that in the previous study there were a small number of precipitates detected in the quenched sample but these samples had a much higher bulk concentration of Al (0.43 wt%). Thus the driving force for precipitation was higher. The results are, in fact, not at all inconsistent. Furthermore, some segregation was detected in the quenched sample in the subsequent ion microprobe analysis. The concentration of Al did vary in a region of 100 Å from the surface (roughly the width of a typical space charge region in a ceramic) first decreasing, reaching a minimum then increasing, indicating that the near surface region was depleted by Al segregating to the surface. This is exactly the behavior expected in segregation due to space charge effects, which would be more prominent in the quenched samples. No precipitates were observed in the 0.006 wt% sample, but the ion microprobe analysis did reveal surface segregation of aluminum in both the quenched and slow cooled samples as is expected. Segregation is much more pronounced in the slow cooled sample (Al concentration at the surface 1.5 orders of magnitude higher) which is reasonable since the diffusion time was longer. In both samples the depth of the segregation layer was about 1 μm.

To further examine segregation without precipitation Kingery and Black did a study of Fe, Cr, and Sc segregation to surfaces in MgO all within a single phase concentration region [62]. Thus precipitation could not be expected as the driving force for segregation. Single crystals of MgO with 3200 and 4600 ppm total of Fe as well as samples with 800 ppm Cr and 3000 ppm Sc were prepared and analyzed using a method similar to the previous study. Annealing temperatures ranged from 1020°C to 1609°C. Some anneals were done in oxidizing (P_{O_2} = 1 atm) and some in reducing ($P_{O2} = 10^{-9}$ atm) atmospheres to determine the effect of oxygen partial pressure. Ion microprobe analysis revealed substantial segregation in all Fe and Sc samples annealed in air or oxidizing atmosphere with enhanced solute concentrations to depths of several hundred angstroms. This occurred despite the fact that the bulk concentrations were

well within the regime of solid solubility for the anneal temperatures used, and the fact that of all the solute atoms had comparable sizes to Mg (0.77 Å for Fe, 0.73 Å for Sc, compared to 0.72 Å for Mg). This lead the authors to conclude that segregation was undoubtedly due to the space charge field associated with the surface. Surfaces and boundaries in MgO being negatively charged would thus attract positively charged aliovalent impurities. No segregation was observed in the Fe samples annealed in the reducing atmosphere, but given the previous discussion the reason for this becomes apparent. Under reducing conditions the iron is present almost totally as Fe^{2+} which is isovalent with Mg^{2+}, and thus effectively neutral. No segregation is expected. In the samples annealed in oxidizing atmosphere, however most of the Fe was present as Fe^{3+} which has an effective positive charge thus segregation would be expected and was observed. The opposite was true with chromium. No segregation was observed in the sample annealed in air and, in fact, the surface was depleted of Cr. The authors attribute this to the volatility of chrome oxide at the anneal temperature used, 1275°C.

A similar study of segregation in MgO grain boundaries was done by Chiang et al. [63] who prepared MgO polycrystals doped with Sc by hydroxide coprecipitation from solutions of $Mg(NO_3)_2$ and $Sc(NO_3)_3$ to ensure uniform solute distribution. Sc conentration was determined to be 3000 ppm by atomic absorption analysis. The powder was pressed and sintered at 1600°C and quenched to attain a uniform solid solution. A second heat treatment was done to induce equilibrium segregation at 1200°C for 165 hours, after which the samples were cooled rapidly at a rate of 10°C/s to room temperature. Analysis was done by inert ion-beam sputtering coupled with Auger electron spectroscopy. Samples were fractured in the high vacuum chamber of the Auger spectrometer to expose fresh grain boundary and avoid adsorption of atmospheric impurities to the freshly exposed surfaces. Ca and Si concentrations were monitored in addition to Sc as these are commonly present in hundreds of ppm even in the purest MgO samples. As was the case with MgO surfaces, segregation was also detected at the grain boundaries. Figure 2-19 presents the concentration profiles. Scandium exhibited the most prominent segregation, probably since it was

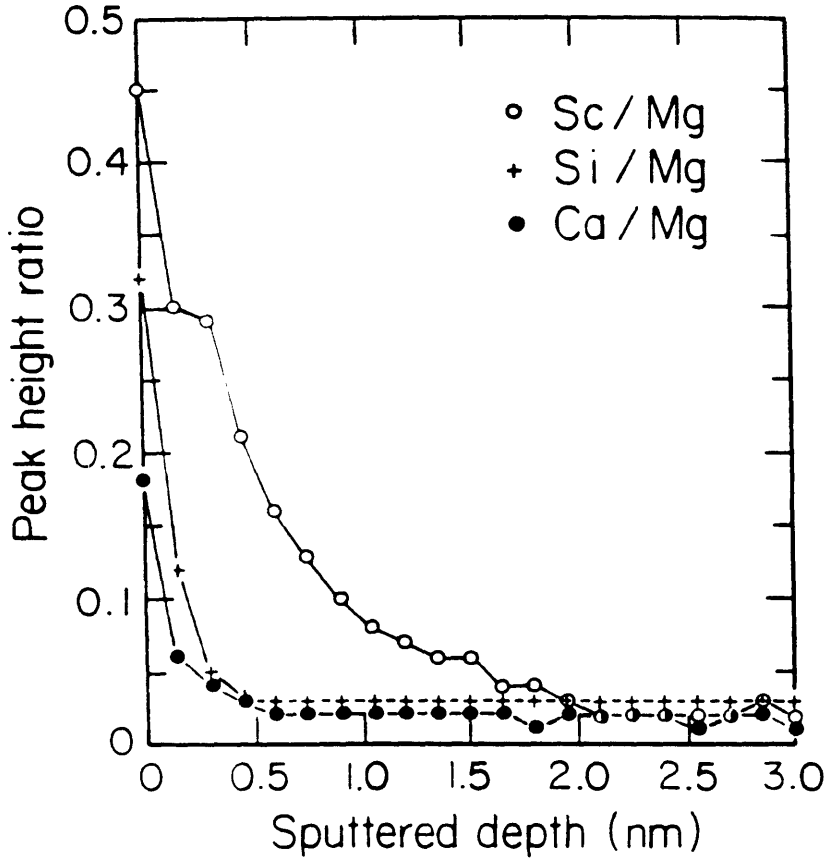

Figure 2-19: Peak height ratios for Sc, Ca, and Si as a function of distance from grain boundary in MgO doped with 3000 ppm Sc, and annealed at 1200 C 165 hours, showing the extent of segregation. From Chiang et al., J. American Ceramic Society, 64 [7] 385 (1981).

present in the highest concentration in the bulk. Enhanced Sc levels were detected to a distance of roughly 2.5 nm from the boundary, while Ca and Si levels dropped to bulk values less than 1 nm from the boundary. This study is interesting because it confirms boundary segregation Mg due to both space charge (for Sc) and elastic effects (for Ca) and, in the case of Si, the combination of the two.

Over the last 10 or so years the method of choice for measuring composition profiles across interfaces has become the use of energy dispersive X-ray spectroscopy (EDS) in the analytical electron microscope (AEM). Using a procedure outlined by Vander Sande [64] and Hall [65], compositional variations can be measured at and near grain boundaries with a spatial resolution of less than 10 nm. This is comparable to the depth resolution of a typical Auger spectrometer or ion microprobe, but offers the advantage of being able to select individual grain boundaries for study by using the imaging capability of the electron microscope. Auger analysis and especially ion microprobe analysis do not have good spatial resolution so, typically, samples are fractured and analyzed with the incident beam perpendicular to the boundary. This does not allow for choice in the selection of individual grain boundaries for study. The AEM/EDS method is done with the beam parallel to the boundary and thus individual boundaries can be identified and selected for study. The ultimate resolution of the technique depends on the material being studied as well as electron beam parameters (beam diameter, gun brightness, accelerating voltage) and was calculated by Hall to be roughly 5nm for MgO in a field emission STEM with a 100 kV accelerating potential and a 2.5 nm beam diameter [65].

Several STEM studies of grain boundary segregation in MgO have been done using this technique, among them Kingery [66], Hall et al. [67], and Roshko [68]. In the study by Kingery et al. "high" purity MgO powder prepared by autoclave oxidation of Mg was doped with 1570 ppm by mass of Fe. The doped powder was pressed and sintered at 1700°C for 5h, then annealed at 1100°C for 19 hours to induce segregation and quenched. Samples were prepared for STEM analysis by mechanical grinding and Ar ion milling to electron transparency. A grain boundary was examined by taking EDS spectra at spatial increments of 20nm on a line perpendicular to the boundary.

The concentrations of Si, Ca, and La were monitored as well as Fe as it is a common impurity. Bulk concentrations were determined to be 20 ppm for Ca and <50 ppm for Si and La by emission spectroscopic analysis. Results, shown in figure 2-20a confirm substantial enhancement in concentration in a region roughly 20nm thick centered on the boundary for all the cations present. The relative enhancement of Si, Ca, and La are greater than of Fe. This is probably due to the strain energy to contribution to segregation present in Si, Ca, and La but not in Fe due to its similarity in size to Mg. The study of Hall, using a similar technique, focused only on segregation of Fe and showed similar results.

The study by Roshko and Kingery [68] attempted to correlate grain boundary structure/energy in MgO with segregation behavior. In this study, bicrystals containing both special and non-special boundaries were prepared and doped with differing levels of impurity content to determine systematically the effect of grain boundary structure/energy on segregation. $\Sigma 5$, $\Sigma 17$ and nonspecial high angle twist boundaries were prepared by hot pressing (001) cleaved MgO single crystals (1500°C, 2-6 hrs, 3.1 $\times$ 10^7 Pa) oriented at the proper twist angle. Samples were cut from these bicrystals such that the boundary was perpendicular to the surface, as is required by the analysis. The samples were doped by encasing them in pellets of MgO powder doped with 2600 ppm Ca and annealing for 158 hours at 1700°C. Concentrations were determined to be $\approx$ 2600 ppm Ca (dopant) and $\approx$ 65 ppm Si (natural impurity). After cleaning samples were annealed again at 1375°C for 2 hours and quenched. Bicrystals were prepared for STEM analysis by mechanical grinding and Ar ion milling. Precipitates containing Ca, Mg, and Si were observed in all of the doped samples. Boundary areas free of precipitates were used for the EDS analysis. EDS analysis revealed segregation of both Ca and Si in all boundaries, but interestingly the amount of segregation (expressed as fraction of monolayer coverage) for each of the species at the non-special boundary was approximately double that of the special boundaries. The results are summarized in figure 2-20b. The results support the theory that non-special boundaries are higher in energy and can be stabilized by the adsorption of impurity ions. If the energy decrease of the non-special boundaries is related to the amount of seg-

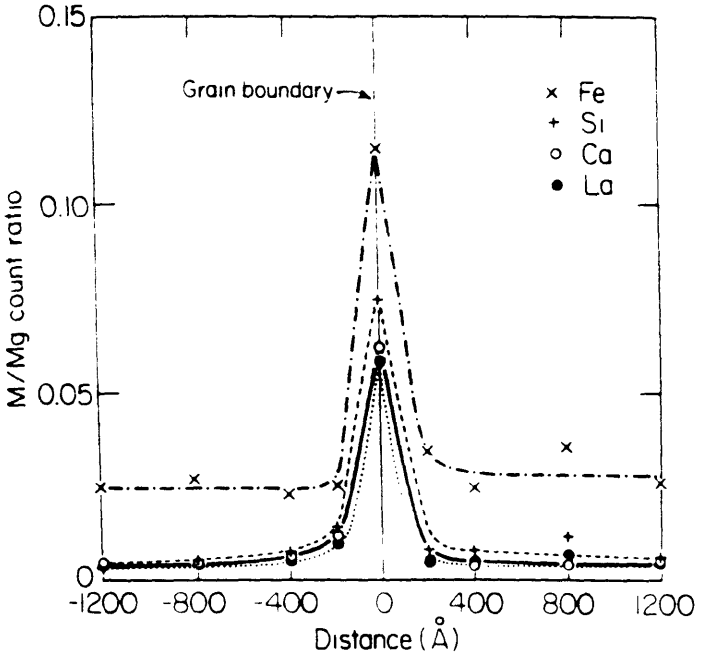

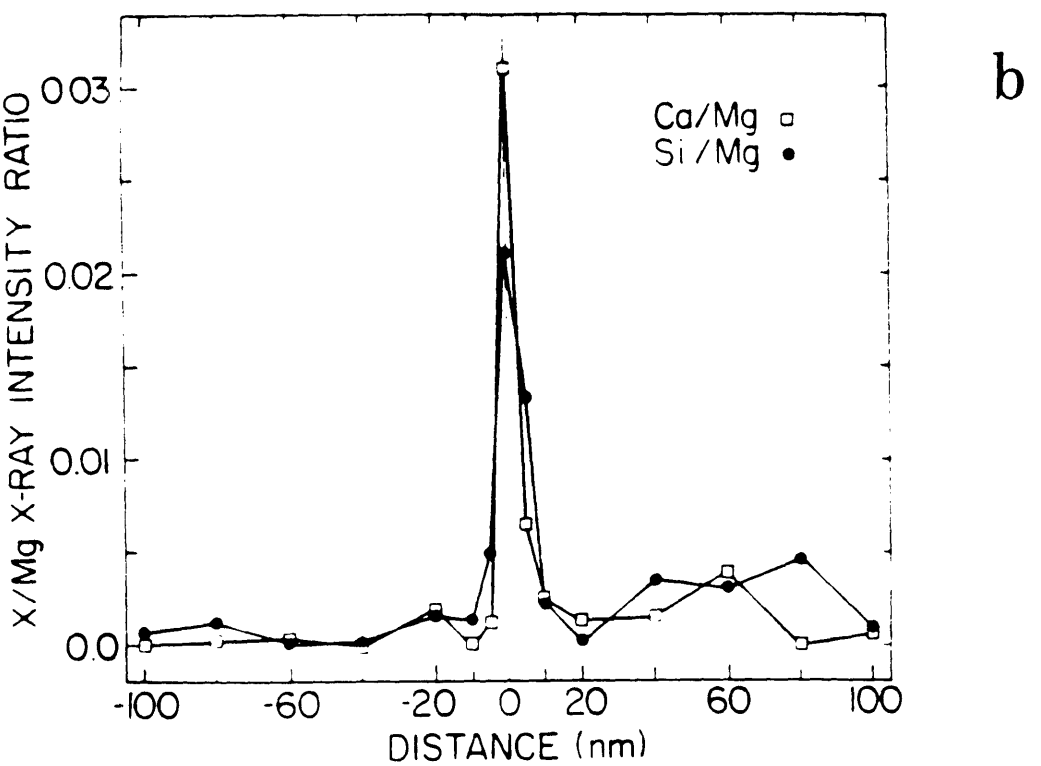

Figure 2-20: Concentration profiles in MgO grain boundaries measured using dedicated STEM technique showing segregation of (a) Fe, Ca, Si, La, Kingery et al., J. Mat. Sci. 14 1766 (1979). (b) Ca, Si, Roshko et al. J. American Ceramic Society, 68 [12] C-331 (1985).

regation, then more segregation should occur at the non-special boundaries, which is what was observed. Thus a correlation has been observed between grain boundary structure/energy and segregation.

All the preceding evidence suggests that we can expect some segregation of impurities even in undoped "high purity" MgO that has been processed at high temperatures. The fact that solutes tend to segregate preferentially to high energy boundaries confuses the issue even more. We cannot expect equal segregation to differently oriented boundaries in MgO bicrystals even if the individual bicrystals have equal impurity concentrations. Thus to establish a relationship between grain boundary structure/energy and grain boundary diffusion a procedure was developed to fabricate MgO bicrystals from high purity MgO without subjecting them to high temperatures for long periods of time which would induce segregation.

2.3 Bulk and Grain Boundary Diffusion

2.3.1 Continuum diffusion

In the study of diffusion, Fick's second law is the controlling equation, and many solutions have been derived for varying initial and boundary conditions. Commonly, radioactive tracers are used to track the self-diffusion of a particular species. This approach is not possible for oxygen, though, as its only radioactive isotope, ^{15}O, has a half life of less than 2 minutes [69] making it unsuitable. Stable isotopes are suitable tracers as the natural abundances of isotopes other than ^{16}O are very low. Hence they are used out of necessity. Their use makes the task of analysis much more difficult than the radiotracer method as some form of mass spectroscopy is usually required. In any macroscopic quantity of oxygen, three stable isotopes exist in the following fractions: ^{16}O, 0.99759; ^{17}O, 0.00037; ^{18}O, 0.00204. In a single crystal of MgO with the fraction of ^{18}O enhanced to a level higher than the natural abundance of 0.00204 ^{18}O will tend to diffuse out of the crystal, replaced by ^{16}O, if a surface of the heated crystal is exposed to air. The process can be speeded up by increasing the

temperature. Using this knowledge we can determine the diffusion coefficient if we have a profile of the concentration of the isotopes ^{18}C and ^{16}C as a function of depth into the sample, x, after a certain time, t.

If we treat the crystal as being infinite, which is justified for short times, and assume that the concentration of each isotope at the surface $^{18}C_s$, $^{16}C_s$ is constant (they are in fact and are equal to the natural abundances) then the solution of the diffusion equation is of the standard error function variety: [70]

$$\frac{^{18}C(x) - ^{18}C_s}{^{18}C_s - ^{18}C_b} = \text{erf}\frac{x}{\sqrt{4Dt}}$$

where $^{18}C_b$ is also a constant, equal to the fraction of ^{18}O in the bulk of the crystal, and D is the diffusivity. Rearranging the above relation:

$$\text{erf}^{-1}\left[\frac{^{18}C(x) - ^{18}C_s}{^{18}C_s - ^{18}C_b}\right] = \frac{1}{\sqrt{4Dt}} \cdot x$$

We see that a plot of $\text{erf}^{-1}[\frac{^{18}C(x) - ^{18}C_s}{^{18}C_s - ^{18}C_b}]$ versus x would be linear with a slope of $\frac{1}{\sqrt{4Dt}}$; t is known; we can calculate D. [11]

There is a complication in the above analysis that does not arise in radioactive tracer methods where the concentration of isotope is vanishingly small. A measurable isotope effect is present. The diffusion coefficient that this experiment would measure is actually a weighted average of the diffusion coefficients of ^{18}O and ^{16}O, ^{18}D and ^{16}D respectively, given by [72]

$$D = \frac{^{18}D^{16}D}{^{18}C^{18}D + ^{16}C^{16}D} \tag{2.3}$$

If the concentration of ^{18}O was negligibly small, as it would be in a tracer experiment ($^{18}C \approx 0$, $^{16}C \approx 1$), the first term in the denominator would vanish and the second would be roughly ^{16}D reducing the equation to D = ^{18}D, the tracer diffusivity, what we expect. Since in the present case ^{18}C and ^{16}C are comparable the measured diffusion coefficient is a hybrid of ^{18}D and ^{16}D that depends on isotopic composition. This difference in the diffusivity of two different isotopes of the same element is known as

the isotope effect. In this case we expect ^{16}D to be greater than ^{18}D since ^{16}O is the lighter isotope. The difference is given by:

$$^{16}D = [1 + f\Delta K(\sqrt{\frac{^{18}M}{^{16}M}} - 1)]\,^{18}D$$

where ^{18}M and ^{16}M are the masses of the isotopes, ΔK is the fraction of the activation energy associated with motion of the diffusing atom at the saddle point (as opposed to motion of the nearest neighbors), and f is the correlation factor. The quantity $f(\sqrt{\frac{^{18}M}{^{16}M}} - 1)$ a.k.a. α is usually no more than 0.05 ($\sqrt{\frac{18}{16}}$ - 1 = 0.061, f $\leq$ 1). Substituting the above expression for ^{16}D into 2.3 gives

$$D = \frac{^{18}D(1+\alpha)}{1 +^{16} C\alpha} \approx^{18} D(1 +^{18} C\alpha)$$

which is a function of C. Fick's second law, from which the solution is derived, assumes concentration independent diffusivities. The previous solution is not rigorously correct. Since α is always small however the error amounts to only a few percent and is usually negligible in comparison to experimental error [73].

We have previously seen that the solution to the diffusion equation in a single crystal yields an error function dependence of the concentration on time and depth. Note that since the crystal is initially homogeneous and isotopic and the only way oxygen can enter or leave the crystal is through the surface, the problem is a one dimensional one spatially, that is C = C(x,t)

A bicrystal contains a grain boundary which can act as a source or sink for matter. Unless the diffusivity of oxygen is the same in the lattice as it is in the grain boundary a second spatial dimension is introduced into the problem. Concentration is now not only dependent on distance from the surface, x, but also distance from the grain boundary, y, C = C(x,y,t). This problem has been solved exactly by both Whipple [74] and Suzoka [75] for different initial and boundary conditions. Their results are similar. Unfortunately the mathematics is extremely complex and the solutions are not analytic. They can only be expressed in integral form. A summary of the method

of solution and results are presented.

The geometry of the problem is shown in figure 2-21. The system is modeled as a semi-infinite crystal with diffusivity D occupying the half space y > 0; y = 0 is the surface. The crystal is bisected by a thin slab of diffusivity D' parallel to the y axis with thickness 2a. This is the grain boundary and presumably D' > D. The initial condition is that ^{18}C is equal to the bulk concentration, C_b, everywhere, that is ^{18}C(x,y,0) = C_b. The surface concentration will at all times remain constant at C_s, the natural abundance of the ^{18}O isotope, ^{18}C(x,0,t) = C_s. Far from both the surface and the grain boundary the concentration remains at the bulk value for all times, ^{18}C(∞,∞,t) = C_b. To make the mathematics more tractable, a substitution will be made to simplify the boundary conditions, redefining the concentration variable as C = ^{18}C - C_b, so that after solving for C the final solution will be ^{18}C = C + C_b. The initial and boundary conditions are now as follows: C(x,y,0) = 0, C(x,0,t) = C_s - C_b, and C(∞,∞,t) = 0. We can now solve Fick's law for the bicrystal.

In the bulk crystal

$$\frac{\partial C}{\partial t} = D\nabla^2 C \quad |x| > a \tag{2.4}$$

In the grain boundary slab

$$\frac{\partial C'}{\partial t} = D'\nabla^2 C' \quad |x| < a \tag{2.5}$$

[note: Quantities with a prime, ′, denote grain boundary quantities.]

At the edges of the slab x = ±a the boundary conditions are that both the concentration and the flux be continuous

$$C(\pm a, y, t) = C'(\pm a, y, t) \tag{2.6}$$

$$J(\pm a, y, t) = J'(\pm a, y, t) \tag{2.7}$$

Applying Fick I:

$$D\frac{\partial C}{\partial x}\bigg|_{x=\pm a} = D'\frac{\partial C'}{\partial x}\bigg|_{x=\pm a} \tag{2.8}$$

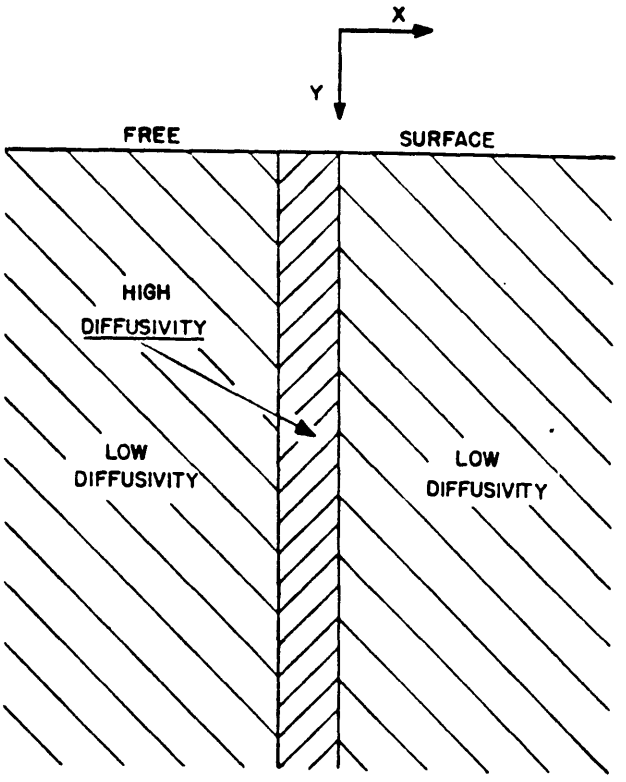

Figure 2-21: Geometry of MgO bicrystal for mathematical analysis

Due to the symmetry of the problem C' will be an even function of x. Therefore we can express it as a power series in even powers of x.

$$C'(x,y,t) = C'_0(y,t) + \frac{x^2}{2}C'_2(y,t) + \cdots \tag{2.9}$$

Substituting this into (2) yields

$$\frac{\partial C'}{\partial t} = D'\left(\frac{\partial^2 C'_0}{\partial y^2} + C'_2 + \frac{x^2}{2}\frac{\partial^2 C'_2}{\partial y^2}\right)$$

substituting x = a

$$\frac{\partial C'_0}{\partial t} + \frac{a^2}{2}\frac{\partial C'_2}{\partial t}D'\left(\frac{\partial^2 C'_0}{\partial y^2} + C'_2 + \frac{a^2}{2}\frac{\partial^2 C'_2}{\partial y^2}\right)$$

Neglecting terms of order a^2 gives

$$\frac{\partial C'_0}{\partial t} = D'\left(\frac{\partial^2 C'_0}{\partial y^2} + C'_2\right) \tag{2.10}$$

Substituting (6) into the boundary conditions (3), (5) yields

$$C(\pm a, y, t) = C'_0(y,t) + \frac{a^2}{2}C'_2(y,t)$$

$$D\frac{\partial C}{\partial x}\bigg|_{x=a} = D'aC'_2(y,t) \tag{2.11}$$

Neglecting terms of order a^2 gives

$$C(\pm a, y, t) = C'_0(y,t) \tag{2.12}$$

Substituting (8) and (9) into (7) yields

$$\frac{\partial C}{\partial t} = D'\frac{\partial^2 C}{\partial y^2} + \frac{D}{a}\frac{\partial C}{\partial x} \tag{2.13}$$

A homogeneous boundary condition satisfied by C at x = ± a

The problem now can be solved using Fourier-Laplace transforms.

The transformation is

$$\psi(x,\mu,\lambda) = \int_0^\infty \exp(-\lambda t)\, dt \int_0^\infty \sin \mu y C(x,y,t)\, dy \tag{2.14}$$

The variable C is being transformed, this transformation transforms t to λ and y to μ.

The inverse transform is then

$$C(x,y,t) = \frac{1}{\pi}\int_{-\infty}^{\infty} \sin \mu y\, d\mu \, \frac{1}{2\pi\imath}\int_{-\imath\infty}^{\imath\infty} \exp(\lambda t)\, \psi(x,\mu,\lambda)\, d\lambda \tag{2.15}$$

Transforming eq. (1) by (11) and employing the boundary conditions we have

$$\frac{\partial^2\psi}{\partial x^2} - \left(\mu^2 + \frac{\lambda}{D}\right)\psi = -\frac{\mu}{\lambda} \tag{2.16}$$

Transforming the boundary condition (10) gives

$$D'\frac{\partial^2\psi}{\partial x^2} - \frac{D}{a}\frac{\partial\psi}{\partial x} - \left(\frac{D'}{D} - 1\right)\lambda\psi = 0 \tag{2.17}$$

The solution of the differential equation (13) which satisfies the boundary condition (14) as well as boundedness can be expressed as the sum

$$\psi = \psi_1 + \psi_2$$

where

$$\psi_1 = \frac{\mu}{\lambda\left(\mu^2 + \frac{\lambda}{D}\right)}$$

$$\psi_2 = \frac{\left(\frac{D'}{D} - 1\right)\mu \exp\left[-\sqrt{\mu^2 + \frac{\lambda}{D}}\,(x-a)\right]}{\left(D'\mu^2 + \frac{D}{a}\sqrt{\mu^2 + \frac{\lambda}{D}} + \lambda\right)\left(\mu^2 + \frac{\lambda}{D}\right)}$$

Computing the reverse transform yields a solution of the form

$$C = C_1 + C_2$$

where

$$C_1 = \operatorname{erfc}\frac{\eta}{2}$$

$$C_2 = \frac{\eta}{2\sqrt{\pi}} \int_1^{\Delta} \frac{d\sigma}{\sigma^{\frac{3}{2}}} \exp\left(-\frac{\eta^2}{4\sigma}\right) \operatorname{erfc}\frac{1}{2}\sqrt{\frac{\Delta - 1}{\Delta + 1}} \left(\frac{\sigma - 1}{\beta} + \xi\right)$$

Where the dimensionless variables ξ, η, β, Δ are defined by

$$\xi = \frac{x - a}{\sqrt{Dt}} \qquad \eta = \frac{y - a}{\sqrt{Dt}} \qquad \beta = \left(\frac{D'}{D} - 1\right)\frac{a}{\sqrt{Dt}} \qquad \Delta = \frac{D'}{D}$$

The solution involves an integral which cannot be determined explicitly, but can be evaluated numerically. C_1 is the contribution of the lattice diffusion and C_2 is the contribution of the grain boundaries. We can see this because, when D' = D, C_2 vanishes and we are left with only C_1. Using SIMS we can obtain a mapping of ^{18}C as a function of x and y for a given t and evaluate D' numerically.

A useful and much more practical approximate solution for the problem has been given by Fisher [76]. In his analysis as in the Whipple/Suzoka analysis the grain boundary is modeled as a thin, high diffusivity slab within a low diffusivity matrix. The geometry and initial and boundary conditions are the same as those for the Whipple solution mentioned previously. If it is assumed that the slab is thin enough that concentration variations across it are negligible (a good assumption for grain boundaries) then the concentration in the slab C' is given by

$$\frac{\partial C'}{\partial t} = D'\frac{\partial^2 C'}{\partial z^2} + \frac{2D}{\delta}\left.\frac{\partial C'}{\partial y}\right|_{y=\pm\frac{\delta}{2}}$$

Note the similarity between this equation and equation 2.13. The first term represents the concentration change associated with diffusion of material along the slab, and the second term represents the flux of material laterally in (out) of the slab. Concentration outside the slab varies according to

$$\frac{\partial C}{\partial t} = D\nabla^2 C$$

which reduces to

$$\frac{\partial C}{\partial t} = D\frac{\partial^2 C}{\partial y^2}$$

in all but a thin layer of material at the free surface, everywhere else in the bulk diffusant is gained (lost) through leakage from (to) the boundary slab. Multiplying by δ^2/D and making the following substitutions:

$$t_1 = \frac{Dt}{\delta^2} \qquad y_1 = \frac{y}{\delta} \qquad z_1 = \frac{z}{\delta(\frac{D'}{D})^{\frac{1}{2}}}$$

transforms these equations into:

$$\frac{\partial C'}{\partial t_1} = D'\frac{\partial^2 C'}{\partial z_1^2} + 2\left.\frac{\partial C'}{\partial y_1}\right|_{y_1=\pm\frac{1}{2}}$$

$$\frac{\partial C}{\partial t_1} = D\frac{\partial^2 C}{\partial y_1^2}$$

If the boundary slab were a free surface with a constant diffusant concentration an expression for the diffusant concentration outside the slab would be:

$$C = C'\mathrm{erfc}\frac{y_1}{2t_1^{\frac{1}{2}}}$$

C' is not a constant, though, but a function of z and t. If it is assumed that concentrations in the slab rise at a rapidly decreasing rate (this has been observed experimentally) then the limiting concentration is approached after a short time and the concentration in the slab can be thought of only as a function of depth, z. The concentration in the bulk can then be expressed as:

$$C = \phi(z)\mathrm{erfc}\frac{y_1}{2t_1^{\frac{1}{2}}} \tag{2.18}$$

where ϕ(z) is the concentration variation in the slab. The condition described above can be mathematically expressed as $\frac{\partial C'}{\partial t_1}$=0 in the slab after a short time. This con-

dition applied to equation 2.18 requires that ϕ satisfy:

$$\frac{\partial^2 \phi}{\partial z_1^2} - \frac{2\phi}{(\pi t_1)^{\frac{1}{2}}} = 0$$

The solution of which with the boundary condition of C' = C_o at $z_1 = 0$ (constant surface concentration) is:

$$\phi = C_o \exp \frac{-2^{\frac{1}{2}} z_1}{(\pi t_1)^{\frac{1}{4}}}$$

giving as the final approximate expression for the bulk concentration

$$C = C_o \exp \frac{-2^{\frac{1}{2}}\ z_1}{(\pi t_1)^{\frac{1}{4}}} \text{erfc}\ \frac{y_1}{2\ t_1^{\frac{1}{2}}}$$

Applying the reverse transformations gives the following expressions for diffusant concentration in the bulk and boundary slab:

$$C(y,z,t) = C_o \exp \frac{-2^{\frac{1}{2}}\ D^{\frac{1}{4}}\ z}{(\pi t)^{\frac{1}{4}}\ (\delta D_b)^{\frac{1}{2}}} \text{erfc}\ \frac{y - \frac{\delta}{2}}{2\ (Dt)^{\frac{1}{2}}} \tag{2.19}$$

$$C'(z,t) = C_o \exp \frac{-2^{\frac{1}{2}}\ D^{\frac{1}{4}}\ z}{(\pi t)^{\frac{1}{4}}\ (\delta D_b)^{\frac{1}{2}}} \tag{2.20}$$

These solutions are analytic and in closed form and are much more useful for analyzing diffusion data than the Whipple/Suzoka integral solutions.

2.3.2 Atomistics of Diffusion

It is well known that diffusion involves atomic exchange with certain types of lattice imperfections such as vacancies and interstitials. The flux of atoms moving from one lattice plane to the next in an isotropic solid under the influence of a concentration gradient in the x direction is given by

$$J = -\frac{1}{6}\alpha^2 \Gamma f \frac{\partial C}{\partial x}$$

where

α is the jump distance (cm)

Γ is the jump frequency (Hz)

f is the correlation factor

From Fick's first law the diffusivity is then $D = \frac{1}{6}\alpha^2\Gamma$. The jump frequency is the probability of an atom acquiring the activation energy needed to jump times the probability of having a vacant adjacent site (at least for a vacancy mechanism). Both are expressible as Boltzmann factors such that

$$\Gamma = z\nu_0 \exp\left[-\frac{2G_m + G_s}{2kT}\right]$$

where

ν_0 is the Debye frequency (Hz)

G_m is the free energy of migration (eV)

G_s is the free energy of formation of a Schottky defect (eV)

The diffusivity is then [73]

$$D = \frac{1}{6}\alpha^2 z\nu_0 f \exp\left[-\frac{2G_m + G_s}{2kT}\right] \tag{2.21}$$

Analogous expressions can be derived for an interstitial mechanism of diffusion. Of course in an ionic crystal we can greatly vary the concentration of point defects, especially vacancies, by varying the processing atmosphere or the concentration of aliovalent impurities.

The atomic packing in a grain boundary is only slightly less dense than in the bulk crystal, therefore we can expect that the motion of point defects such as vacancies and interstitials are responsible for diffusion in grain boundaries as well. An expression for the grain boundary diffusivity can be derived which is analogous to the expression for the lattice diffusivity. [77]

$$D_{gb} = \frac{1}{4}\alpha^2 z\nu_0 f_{gb} \exp\left[-\frac{2G_m + G_s - 2G_s^B}{2kT}\right] \tag{2.22}$$

G_s is once again the Schottky formation energy (assuming vacancy mechanism)

G_m is the migration free energy in the grain boundary

G_s^B is the vacancy/grain boundary association energy

f_{gb} is the correlation factor in the grain boundary

All other quantities are the same as or close to the bulk values. G_m varies depending on the structure of the boundary in question but it is reasonable to assume that it will be higher (and diffusivities lower) in low Σ boundaries where the atomic registry is better. There is usually a positive binding energy between a grain boundary and vacancy, G_m^B, which lowers the enthalpy portion of the activation energy, resulting in higher diffusivity. The physical manifestation of this term is simply that the concentration of point defects is higher in the grain boundary than in the bulk.

2.3.3 Literature Review - Diffusion in MgO

Bulk diffusion

Many studies have been done on diffusion and mobility in MgO under various experimental conditions and using several different techniques. Diffusion experiments in MgO and the alkaline earth oxides in general are not simple in practice as these oxides tend to have high melting points and are notoriously difficult to purify. The alkaline earth oxides all have the rocksalt structure. Point defect formation energies in these close packed structures are extremely high making intrinsic defect populations small compared to those generated by the presence of aliovalent impurities, even at high temperatures. Theoretical estimates of defect formation energies in MgO are available, most having been calculated by the HADES lattice relaxation program Mackrodt [78] Sangster, [79] and Catlow [80] have computed values for the Schottky pair formation and migration energies using different interatomic potentials and. Mackrodt has also estimated the energy of formation of paired oxygen interstitials in MgO (peroxy centers). Table 2.1 summarizes these values. Gourdin and Kingery [81] have estimated, using a similar procedure, a value of ca. 12 eV for the Frenkel pair formation energy in MgO which is quite a bit lower than the 15.2 eV predicted by

	Mackrodt et al.	Sangster et al.	Catlow et al.
Schottky pair formation	7.5	7.72	7.5 - 7.9
Oxygen vacancy migration	2.38	2.11	1.3 - 2.1
Magnesium vacancy migration	2.16	2.07	1.8 - 2.2
Magnesium-oxygen divacancy association	-2.55	-	-2.2 - -2.7 [1]
Frenkel pair formation	15.2	-	-
Oxygen interstitial pair (peroxy center) formation	9.2	-	-

Table 2.1: Calculated defect formation/migration energies for MgO (eV).

Mackrodt. In their simulations this energy dropped considerably with the presence of adjacent cation vacancies as occurs in cluster formation. Using a value of 7.5eV for the Schottky energy to compute the intrinsic vacancy concentration as determined by the Schottky equilibrium

$$[V''_{Mg}][V^{\cdot\cdot}_{O}] = K_s = \exp -\frac{h_s}{kT}$$

$$[V''_{Mg}] = [V^{\cdot\cdot}_{O}] = \exp -\frac{h_s}{2kT}$$

$$h_s = \text{Schottky energy}$$

gives a native vacancy concentration on the order of 50 ppb at the melting point whereas the purest MgO crystals available by any commercial process have several hundreds of ppm total impurities which can result in the creation of point defects if they are aliovalent. Consider the cation impurity M^{3+} as an example:

$$M_2O_3 \overset{3MgO}{\rightarrow} 2M^{\cdot}_{Mg} + 3O_O + V''_{Mg} \qquad [V''_{Mg}] = \frac{1}{2}[M^{\cdot}_{Mg}]$$

It is thus unlikely that intrinsic diffusion is observed in any commercially prepared MgO. Experimental data has in general shown this to be the case.

[1] Values were computed by subtracting Schottky pair formation energies from divacancy formation energies.

It is fairly well established that cationic self-diffusion in MgO proceeds by an extrinsic vacancy mechanism, the vacancy concentrations being impurity controlled by the defect incorporation $2[V''_{Mg}] = [I'_{Mg}]$ where I is the trivalent impurity density. Activation energies for Mg self diffusion have been measured by Wuensch et al. [82] to be roughly 2.76eV. In the case of impurity controlled cation diffusion this activation energy should be equal to the vacancy migration energy. It is slightly higher than the calculated values but not outrageously so. Other results tend to support the conclusion more strongly. Among them are ionic conductivity studies by Sempolinski and Kingery [83] and Dulcot and Deportes [84], which report activation energies for ionic conduction of 2.3eV and 2.2eV respectively. In the regime where cation migration is solely responsible for the ionic conduction this activation energy is once again equal to the cation vacancy migration energy. In these studies the agreement between the experimental and calculated values is excellent, thus the general agreement on the mechanism for cation self diffusion in MgO. That being the case, given the Schottky equilibrium, oxygen vacancy concentrations will be depressed far below their already low intrinsic levels, perhaps lower than native oxygen interstitial concentrations These defects, the oxygen vacanvy and oxygen interstitial, are also related, by the Frenkel equilibrium. Some investigators have surmised that oxygen self diffusion proceeds by interstitial or other mechanisms.

The first to study oxygen diffusion in MgO were Oishi and Kingery [3] who determined the diffusivity of oxygen by annealing crushed sieved particles of MgO in a gas mixture containing $\sim$ 10 % ^{18}O at 150 torr P_{0_2}. Assuming spherical particles of radius a the ratio of the amount of ^{18}O in the particles at time t to the amount of ^{18}O in the particles at infinite time goes as $\frac{\sqrt{Dt}}{a}$. After the anneal the $^{18}O/^{16}O$ ratio in the powder was determined via mass spectrometry. The MgO was reduced to CO by heating with graphite; it was subsequently decomposed to CO_2. The ratio could then be determined via mass spectrometry by measuring the $^{46}CO_2/^{44}CO_2$ ratio. The results obtained over a temperature range from 1300 - 1750 C can be represented by the equation $D = 2.5\times10^{-6}\exp(-2.71eV/kT)$ cm^2/s. Due to the low activation energy, they concluded that the diffusion is impurity controlled. The assumption of an

equivalent spherical radius to fit the mathematical model used is not rigorously correct, though. The crushed crystals were of course irregularly shaped and of varying sizes. The results must be viewed in that light. The same technique was also used by subsequent investigators with similar assumptions and results. Hashimoto et al. [1] reported D = 4.5×10^{-7}exp(-2.61eV/kT) cm^2/s in the temperature range 1050 - 1438°C.

Another early study was done by Rovner [85] who also used the same tracer in technique on crushed single crystals obtained from two different sources. Between 975 and 1150°C there was good agreement between the different MgO crystals. The diffusivities representable by D = 4.3×10^{-5}exp(-3.57eV/kT) cm^2/s D = 2.4×10^{-5}exp(-3.57eV/kT) cm^2/s. Another Arrhenian regime was reported for lower temperatures, 750 - 975°C with considerably lower diffusivity, D = 4.8×10^{-14}exp(-1.32eV/kT) cm^2/s. These results are difficult to interpret. The high temperature results are not in sharp disagreement with those of Kingery and in fact agree quite well with some of the later, more accurate studies. It is unlikely though, given what we know now, that the two regimes represent intrinsic/extrinsic diffusion.

A study done by Ando, Kurokawa, and Oishi [86] involved the measurement of oxygen diffusivity in Fe doped MgO crystals under a partial pressure of O_2 of 150 torr. They used a stable isotope exchange technique and measured oxygen diffusivities from 1400 - 1700 C in crystals doped with 310, 2300, and 12900 ppm Fe. They reported a diffusion coefficient over that temperature range expressible as D = 6.76exp-5.56eV/kT) cm^2/s and to within experimental error insensitive of impurity content. Due to this result they concluded that oxygen diffusion could not be solely due to a vacancy mechanism. They proposed a vacancy pair mechanism in which two free vacancies become associated $V_{\ddot{O}} + V''_{Mg} = (V_{\ddot{O}}V''_{Mg})^{\times}$. The concentration of vacancy pairs would then be $[(V_{\ddot{O}}V''_{Mg})^{\times}] = K_s \cdot K_b$ where K_s is the Schottky equilibrium constant and K_b the defect reaction constant. Note that the concentration is a product of constants and therefore itself a constant at a given temperature, insensitive to impurity concentration. The activation energy would then be the sum $H_s + H_b + H_m$ the Schottky enthalpy plus the defect reaction enthalpy plus the migration enthalpy.

Schmalzried, [87] in a study of high temperature creep in CoO-MgO solid solutions, reported creep rates for coarse grained $(Co_{0.5}Mg_{0.5})O$ under high stresses and high temperatures to be proportional to $P_{O_2}^{+\frac{1}{6}}$ for P_{O_2} above 5 Pa. According to the Nebarro-Herring equation the creep rate is proportional to the diffusivity of oxygen, and finding the creep rate to be independent of grain size they concluded that lattice and not grain boundary diffusion was controlling. Thus
$D_L \propto P_{O_2}^{+\frac{1}{6}}$ the dependence corresponding to interstitial diffusion. The authors conclude from this that lattice diffusion of oxygen in MgO occurs by an interstitial mechanism.

In a more recent study, Yoo and Wuensch [11] measured oxygen diffusivities in high-purity single crystals of MgO through out-diffusion of ^{18}O from a layer of $Mg^{18}O$ epitaxially grown on a normal MgO substrate by the technique of chemical vapor transport. Anneals were done in air atmosphere ($P_{O_2} \sim 150$ torr) at temperatures ranging from 1000 - 1700 C. The tracer-out technique results in erfc-like concentration profiles from which diffusivities can easily be determined. Profiles were obtained using secondary ion mass spectrometry. The diffusivity of oxygen can be represented in the temperature range by $D = 1.8\times10^{-6}\exp(-3.24eV/kT)$ cm^2/s. The author reaches no conclusion as to possible mechanisms for diffusion pointing out that the experimental activation energies are too low for an impurity controlled vacancy mechanism or a vacancy association/migration mechanism.

Measurements by Semken [69] using the same technique under similar conditions gave $D = 9.54\times10^{-17}$ cm^2/s at T = 1400 C and $D = 1.34\times10^{-16}$ cm^2/s at T= 1450 C, not really enough data points to determine either D_0 or the activation energy conclusively, but they do agree with the results of Yoo to within experimental error. He proposes an interstitial mechanism for oxygen diffusion due to the depressed levels of vacancy concentration, even though theoretical estimates of the activation energy for interstitial diffusion are about 8.9eV, more than 2.5 times the value of 3.24eV obtained by Yoo. The author offers the suggestion that theoretical estimates of the Frenkel formation energy have been overestimated.

The most recent work in this area has been done by C.P. Flynn [88, 89] who claims

to see intrinsic and extrinsic regimes of oxygen diffusion. This claim may have merit, though. In this study molecular beam epitaxy was used to grow the MgO single crystals used for the analysis. Molecular beam epitaxy is a form of evaporation that has long been used in the semiconductor industry to produce ultrahigh purity semiconductor materials. Buried tracer layers of $Mg^{18}O \approx 50$ Å thick were grown between high purity $Mg^{16}O$ at depths of 300 to 2000 Å. Anneals were done at temperatures of 1000K to 2400K. At the higher temperatures the crystals were encased in MgO powder to prevent excessive loss of material to evaporation. Tracer profiles were obtained by secondary ion mass spectrometry. Results for oxygen diffusion can be represented by D = 76exp(-6.91eV/kT) cm^2/s for the high temperature 1700 - 2400K intrinsic regime and D = 1.0×10^{-10}exp(-2.66eV/kT) cm^2/s for the low temperature extrinsic regime. The latter regime is in fair agreement with some of the other studies previously mentioned, but the former one with its 6.91eV activation energy is unique; this is the highest activation energy ever reported for oxygen diffusion in MgO. The activation energy of circa 6.9 eV is close to the theoretical estimate of activation energy of diffusion by intrinsic cation-anion vacancy pair migration (7.3 eV). The authors reached this conclusion based on other results [86] which showed oxygen diffusion to be relatively insensitive to impurity concentration, leading them to believe that the migrating defects are uncharged. that the migrating defects are uncharged. More recent experimental results have not borne this out, though, as will be discussed in a later section. The authors tend to attribute this never-before-observed behavior more to the high quality (low dislocation density) of the grown material rather than the purity. They point out the preceding studies of oxygen diffusion were done by a surface exchange technique. The damage caused by surface preparation (polishing etc.) being responsible for the higher observed diffusivities. This seems incongruous with the results of Yoo and Semken who used as-grown surfaces for their exchange experiments. Although it may be that due to the much slower deposition rates of MBE that the native dislocation densities in the MBE grown crystals are much lower than in CVT grown crystals.

Grain Boundary Diffusion

One of the first studies which suggested enhanced values of the diffusivity of oxygen in grain boundaries in MgO was the aforementioned study by by Hashimoto and Hama [1] They studied in diffusion of ^{18}O into polycrystalline MgO at partial pressures of 40 torr O_2 and temperatures from 1050 - 1438 C using a technique similar to that of Oishi and Kingery. Their results for two different particle sizes are $D = 4.5\times10^{-5}\exp(-2.61eV/kT)$ cm^2/s for an average particle size, a, of 70 μm and $D = 1.3\times10^{-5}\exp(-2.61eV/kT)$ cm^2/s for a = 40 μm. They attribute the higher diffusivity at higher average particle size to diffusion along grain boundaries. As further evidence they offer that if the length parameter is normalized to the grain size instead of the particle size (both samples had roughly the same average grain size = 15 μm) the results came into coincidence at $D = 4.5\times10^{-7}\exp(-2.61eV/kT)$ cm^2/s suggesting that grain boundary diffusion was fast and bulk diffusion into each individual grain was rate limiting.

Systematic studies of grain boundary diffusion in MgO are relatively uncommon and studies of oxygen boundary diffusion are particularly rare. One of the first systematic studies of grain boundary diffusion in MgO was done by Wuensch and Vasilos [6], who studied Ni^{2+} diffusion in MgO polycrystals and natural and pressure sintered bicrystals. The authors prepared the samples for analysis by cutting so that the boundary was normal to the surface (for the case of the bicrystal) and polishing. Samples were annealed at temperatures from 900 - 1900 °C as either a sandwich couple (two MgO crystals with a thin layer of NiO between) or as a vapor deposition couple. Boundary conditions were suitably adjusted for the analysis. Concentration profiles were obtained by mechanical grinding to known depths and using X-ray absorption analysis or electron microprobe spectroscopy to obtain concentrations at various distances from the boundaries. Results showed enhanced diffusion at some boundaries but were generally non-reproducible and, more alarmingly, there seemed to be no correlation between boundary misorientation and enhancement of diffusion as enhancement was observed in boundaries with tilt angles as low as 6° and no en-

hancement was observed in boundaries with tilt angles as high as 45°. This seeming paradox was resolved several years later in a study by the same authors of Ni^{2+} and Co^{2+} grain boundary diffusion in MgO. Particular attention was paid to impurity content at the boundaries. Samples were prepared and analyzed in a manner similar to the previous study and once again the results were non-reproducible Some crystals exhibited enhanced diffusion and some did not and, moreover, sometimes within the same sample certain areas of the boundary showed enhancement and others did not. The paradox was solved when the samples were analyzed for impurity content by microbeam probe analysis. In each case where enhanced diffusion was detected impurity segregation was found at the boundary (most notably Ca and Si). Also at each boundary where no enhancement was observed no impurities were detected. These results seem to suggest that enhanced boundary diffusion is an extrinsic phenomenon, despite the more open structure and dislocation networks observed which would seemingly serve to enhance diffusion.

An early study of oxygen grain boundary diffusion was done by Condit and Holt [4] who used the techniques of proton activation and audioradiography to initially locate oxide inclusions in metals and subsequently to examine the penetration of the stable isotope ^{18}O along the grain boundary in MgO bicrystals. In the latter experiment an MgO bicrystal was annealed in 60% ^{18}O for 17 hours at 1610°C. Analysis was accomplished by first bombarding the samples with 2.7MeV protons, wherein the $^{18}O(p,n)\ ^{18}F$ nuclear reaction produces fluorine-18 and a neutron. The ^{18}F has half-life of 112 minutes and decays by positron emission. The positron flux is indicative of the amount of ^{18}O present and can be detected by audioradiography. The energy 2.7MeV is chosen is that this energy is high enough to cause the activation of oxygen yet low enough to minimize unwanted activation. Subsequent audioradiography revealed penetration of the ^{18}O to be much deeper along the grain boundary than in the bulk.

The same technique was applied by McKenzie et al. in a more quantitative study of oxygen grain boundary diffusion [5]. They analyzed bicrystals cut from an originally polycrystalline MgO sample which contained roughly 1100ppm total impurities (mostly Al and Ca). Some samples were doped with Fe (150 and 7000ppm). The

bicrystals were annealed in a 35% ^{18}O atmosphere at temperatures ranging from 1621 - 1743°C. Proton activation was done using 2.8MeV protons. Wedges were ground from the sample surfaces to expose ever increasing depths of boundary. Knowing the wedge angle, depths could be determined. Audioradiographs were taken with a recording microdensitometer at regular intervals along the boundary. Results showed enhanced diffusion along all boundaries in both the doped and undoped materials. The amount of scatter in the data was great but the general trend was that the Fe-doped samples showed greater enhancement than the non-doped ones. Values of the parameter $D'\delta/D^{\frac{1}{2}}$ varied from 1.0×10^{-10} $cm^2/s^{\frac{1}{2}}$ - 24×10^{-10} $cm^2/s^{\frac{1}{2}}$ for the undoped MgO annealed between 1658 and 1705°C and 25×10^{-10} $cm^2/s^{\frac{1}{2}}$ - 81×10^{-10} $cm^2/s^{\frac{1}{2}}$ for the Fe-doped MgO annealed between 1621 and 1679°C. No significant difference was observed between the 150ppm doped and the 7000ppm doped samples. Worth noting is the fact that the audioradiography analysis revealed the presence of activated impurities at some boundaries (not surprisingly) calling into question how reflective the results are of grain boundary structure.

More recent work in this area has been done by Dolhert [8] who studied oxygen grain boundary and dislocation pipe diffusion in polycrystals and deformed single crystals of MgO using secondary ion mass spectrometry. Enhanced diffusion of oxygen was first observed using this technique by Henriksen et al. [90] who studied oxygen diffusivity in MgO single crystals which had been hot forged to give 40% deformation, presumably giving rise to the formation of a large number of subgrain boundaries. A layer of $Mg^{18}O$ was formed on normal crystals by evaporation of Mg metal onto them and subsequent oxidation in an atmosphere of 92% ^{18}O. Annealing was done at 1400°C for 21 hours and depth profiles were obtained from a 150μm $\times$ 150μm area on the sample encompassing a large number of grain boundaries. Analysis of the samples revealed enhancement of diffusion in the deformed samples of approximately four times. Diffusivities ranged from 1.3×10^{-15} cm^2/s - 1.9×10^{-15} cm^2/s for undeformed samples. A value of 5.8×10^{-15} cm^2/s was reported for the deformed sample. This is only an apparent diffusivity, though, as it was determined using the analysis for bulk diffusivity.

The work of Dolhert expanded on this theme. He studied grain boundary diffusion in deformed MgO single crystals and an undoped MgO polycrystal with an average grain size of 11μm. Single crystals were obtained from two different sources, Oak Ridge National Laboratory and Norton Co. The former was deformed to 55% true strain by compression along [100] (10,600psi, 1500°C, 23 minutes). The latter was similarly deformed to 62% true strain (6,660psi, 1700°C, 4 minutes). This treatment induced the formation of subgrain boundaries on (110) planes spaced from 1 to 40μm apart. The polycrystal was prepared under clean room conditions from high purity MgO powder reportedly containing less than 100ppm total impurities. The powder was cold pressed at 200,000psi and sintered in flowing oxygen for 24 hours at 1250°C and 48 hours at 1400°C. Diffusion specimens were cut from the samples and cleaned by rinsing in trichloroethylene, distilled water, acetone, and methanol to hopefully remove cutting fluids before annealing. The specimens cut from the single crystals were also etched in hot phosphoric acid prior to annealing. Annealing was done at temperatures from 1200 - 1500°C in an 80% nitrogen 20% oxygen-18 atmosphere at a total pressure of 765 - 780 torr so leaks would be out instead of in. Diffusion profiles were obtained using secondary ion mass spectrometry with a 9.7keV primary Ar^+ ion beam. The scan area was circular with a 60μm diameter. Grain boundary diffusivities were calculated using the LeClaire analysis assuming "type C" kinetics (volume diffusion negligible); this analysis is appropriate for the analysis of large numbers of randomly oriented boundaries as would be found in a polycrystal or deformed single crystal. The results over the specified temperature range can be summarized by $D'\delta = 3.2\times10^{-7}\exp(-4.06\text{eV/kT})$ cm^3/s, where δ = boundary thickness for grain boundary diffusion and $D = 3.9\times10^{-6}\exp(-3.45\text{eV/kT})$ cm^2/s for bulk diffusion. The author suggests that due to the fact that the diffusion behavior is insensitive to doping that the boundary diffusion is likely controlled by a neutral defect such as neutral oxygen vacancies (F centers) or neutral interstitials which he deemed plausible due to the open structure of ceramic grain boundaries.

A subsequent study by Roshko [9] of oxygen grain boundary diffusion in MgO polycrystals employed class 100 clean room conditions for all processing steps to minimize

contamination. MgO powder was prepared by solution and precipitation from carbonates by dissolving hydromagnesite in semiconductor grade (18 MΩ) water under a CO_2 pressure of 250psi. A metal chelating agent was added and chelate complexes were removed via a combination of centrifuging and filtration. The carbonates were recovered by heating to near boiling and stirring to drive off the water. To convert to MgO the powders were calcined in air in MgO crucibles for 2 hours at 1000°C. To achieve flatness and the fine-grained microstructure desired for SIMS analysis the MgO powder was hot pressed into pellets at 1000°C for 1 hour at 12.5ksi and for an additional hour with no applied pressure to relieve stress. A second anneal was done at 1600°C to fully densify the samples. Grain sizes varied from 2 - 12μm for the samples used. These were cut into diffusion specimens and cleaned in hot phosphoric acid prior to diffusion annealing. Diffusion anneals were done using the exact procedure of Dolhert at temperatures ranging from 1295 - 1515°C. SIMS analysis was also done in a similar manner with a 60μm analysis area but a primary Cs^+ beam of 12.5keV was used because it is more stable than Ar, produces less sputter roughening and is more efficient at producing ionized secondaries. Diffusion coefficients were calculated using the LeClaire analysis and were found to be $D'\delta = 5.0\times10^{-9}\exp(-2.87\text{eV/kT})$ cm^3/s for grain boundary diffusion and $D = 3.2\times10^{-4}\exp(-3.97\text{eV/kT})$ cm^2/s. The 3.97eV activation energy for bulk diffusion seems reasonable but the low 2.87eV activation energy for grain boundary diffusion, although on the order of what would be expected for boundary diffusion, is in disagreement with the previous study. It was discovered by STEM analysis that phosphate precipitates were present at grain boundaries and particularly at triple junctions. This was presumably a result of the H_3PO_4 cleaning. It is suspected that phosphoric acid remained in open pores after the cleaning. Upon second annealing to achieve high density some of these pores became closed, trapping the phosphoric acid, which then decomposed to the phosphate phases detected. These low-melting phosphates were probably liquid at the temperature of the diffusion anneals accounting for the faster diffusivities reported. The bulk diffusivities are reasonable though, which makes sense since the presence of phosphates at the grain boundaries would have a negligible effect on volume diffusion. Thus more credence

is given to the study by Dolhert in which the samples were at least precipitate free if not segregation free.

From this review it should be evident that reliable data on oxygen grain boundary diffusion in MgO is scarce. Attempts to control segregation have usually failed. In fact, in can be said that the amount of segregation present has usually been inversely proportional to the effort expended to avoid it. No attempt to measure the effect of boundary orientation and energy on oxygen diffusion has ever been made. It is the goal of this study to measure the diffusion of oxygen in MgO bicrystals of controlled orientation and purity.

Chapter 3

Sample Preparation and Analysis

From the preceding section it should be apparent that if the relationship between grain boundary structure and diffusion is to be determined. High purity boundaries (comparable to the bulk) will be required. To that end a procedure was developed to fabricate MgO bicrystals from high purity MgO without subjecting them to high temperatures for long periods of time which would induce segregation.

3.1 Preparation of Seed Bicrystals

In order to grow single crystals or bicrystals using chemical vapor transport a seed is required. As a first attempt two MgO single crystals were fastened together with platinum wire and used as a seed. Epitaxial bicrystals were grown using this technique, but since the thin epitaxial layer was all that was holding the two single crystals together they would fracture along the grain boundary after a minimal amount of handling. Clearly, a way to join the single crystals had to be found before any serious work could begin.

Several unsuccessful attempts were made at trying to bond single crystals by embedding them in a powder compact and sintering to provide mechanical stability. Due to the large and nonuniform volume shrinkage of the MgO powder compacts, though, the embedded single crystals would always end up misaligned, separated, or fractured. Early attempts at hot pressing were also unsuccessful. Due to the small

contact area of the single crystals (roughly 10mm × 1mm) they could not easily support any weight. This made hot pressing difficult. An apparatus used for hot pressing is shown in figure 3-1.

Large zirconia bricks were used as weights. These had cylindrical holes bored into them to support the alumina "dies" which had slits cut into them to hold the MgO crystals. This assemblage was loaded into a box furnace, ramped up to temperature (1700°C), and allowed to soak for a time (10 - 15 hours). Inevitably sometime during the run, however, the crystals would buckle and not be in full contact. No bonding therefore occurred. As one might expect these initial trials produced no usable bicrystals. It was decided that in order to bond MgO, large single crystals (for larger contact area), higher pressures and higher temperatures were required.

Large (13mm × 13mm × 20mm) single crystals of (100) cleaved MgO were obtained from Advanced Composite Materials; Greenville, SC. These were cut into slabs approximately 2mm thick at an angle to the normal of one half the desired tilt angle of the bicrystal. A low speed diamond saw equipped with goniometer (South Bay Technology, model 660) was used for this purpose. Two such single crystal slabs could then be pressed into a symmetric tilt bicrystal of desired tilt angle by simply rotating one of them 180° about an axis normal to the cut faces, which will form the grain boundary, and putting them back together, as shown in figure 3-2a. Due to the large surface area in contact (roughly 13 mm^2) and small aspect ratio of the bicrystal, it could support a fair amount of weight without buckling. The crystals were polished to optical flatness before the actual hot pressing to ensure that the contact area between the faces to be joined was a maximum. This was typically done using abrasive SiC and Al_2O_3 paper and powder. The cut faces were successively polished with 320 grit, 500 grit, and 600 grit SiC abrasive paper, followed by 2/0 and 4/0 emery paper and finally 1.0 μm Al_2O_3 paper or powder until optical flatness was achieved. The crystals were washed in reagent grade methanol each time a finer grit paper was to be used to avoid contamination from the coarser grit paper.

The hot pressing was done in a vacuum furnace (Richard D. Brew Inc.; Concord, NH, model 1068) through which a light load could be applied through a port at the

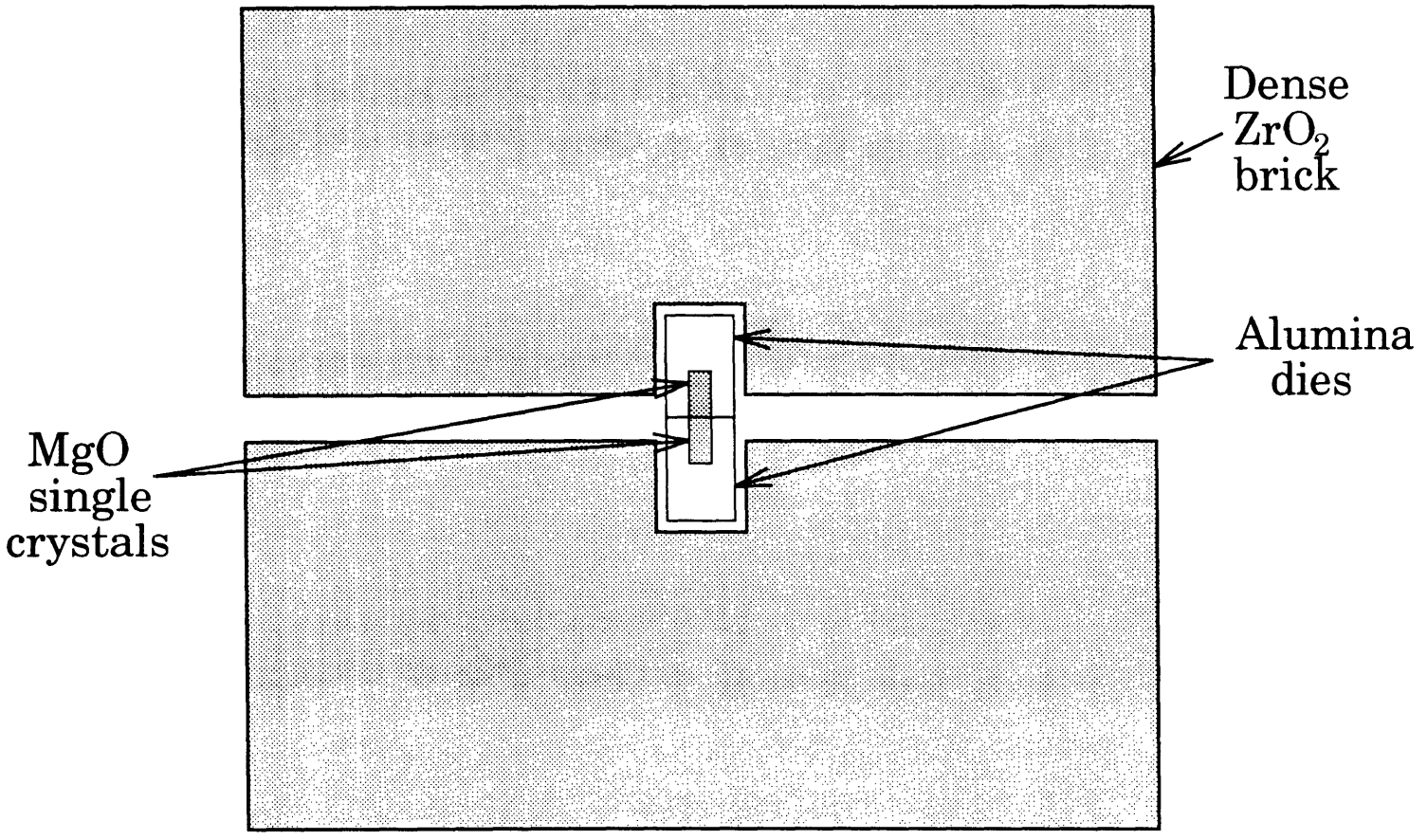

Figure 3-1: Hot pressing MgO single crystals between zirconia bricks

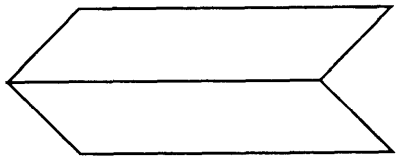

a

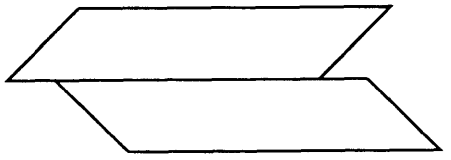

b

Figure 3-2: Crystal Orientation for Hot Pressing (a) normal (b) staggered

top. The crystals to be bonded were sandwiched between two sintered MgO pellets to prevent contact with other parts of the furnace and hopefully avoid contamination. They were also staggered with respect to one another as shown in figure 3-2b. This did not change the orientation of the boundary and facilitated the location of the boundary during the SIMS analysis as will be discussed shortly. The crystals were loaded into the furnace and placed onto a zirconia block which rested on the support rods of the furnace. The configuration is shown in figure 3-3. A graphite rod which supports the load was lowered onto the crystals such that the load was evenly distributed. Care was required to ensure that the crystals remained properly aligned. This required a steady hand and a lot of patience. If the crystals became misaligned during the run they could not be used, and a great deal of time and energy would have been wasted. Once the crystals were properly loaded a weight of about 15 pounds was placed atop the graphite rod, corresponding to a pressure of 100 - 150 psi depending on the size of the cut crystals. This arrangement was quite precarious and it was deemed unwise to to use any more weight. The furnace was closed and evacuated with a combination of mechanical roughing and oil diffusion pumps for a period of 12 - 24 hours until a pressure of at most 10^{-5} torr was achieved. For the last few hours of the pumpdown the furnace was heated to roughly 200°C to outgas any water or organics which might have remained. Once the required vacuum was achieved the heating cycle could begin. From 200°C the temperature was ramped at 10°C per minute to 1200°C and allowed to soak there for one hour to allow the pressure, which would usually rise during this time, to recover to 10^{-5} torr. From this point until the end of the heating cycle the cold trap was filled with liquid nitrogen periodically to maintain as high a vacuum as possible. After the one hour soak the temperature was ramped again at 10°C/minute up to the bonding temperature, 1800°C, where it was held for three hours. Longer runs were not possible because the vapor pressure of MgO is quite high at this temperature. When the soak was continued for longer durations the crystals became rounded due to loss of mass at the peripheries by vaporization; contact area was reduced and the crystals ended up poorly bonded. After the soak the temperature was ramped down to 1500°C by 5°C/minute and the weight

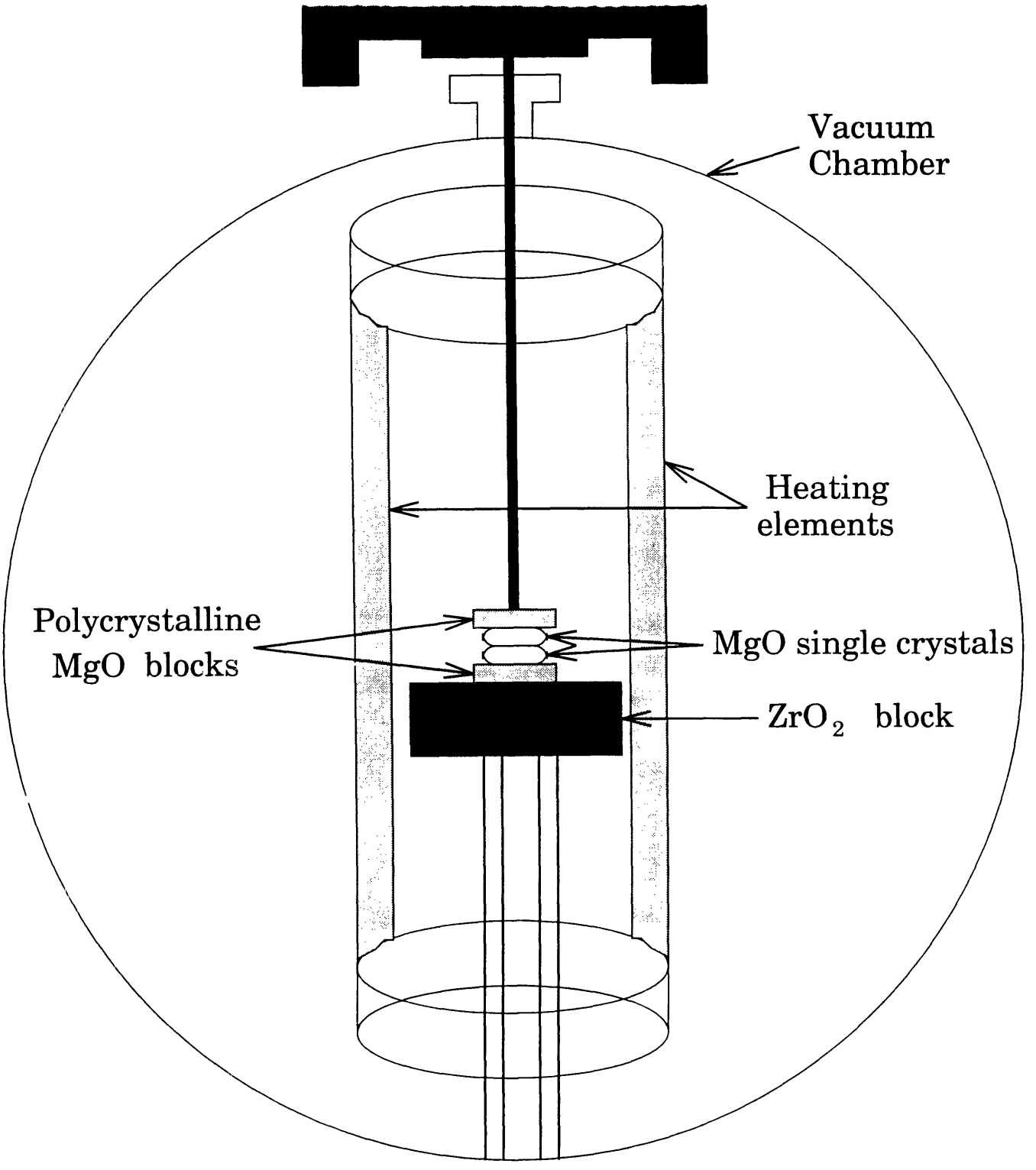

Figure 3-3: Schematic of Hot Pressing Apparatus

was removed. The bicrystal was allowed to anneal there for 1-2 hours before ramping down to room temperature at 20°C/minute. Once cool the furnace was vented and the bicrystal removed.

If the bonding was successful the bicrystal could be cut into substrates for crystal growth. Each hot pressed bicrystal was, in principle, large enough to cut into 5 seeds each between 1 and 2 mm thick. Specimens in which diffusion was to be measured parallel to the tilt axis were cut such that both the boundary plane and the tilt axis were normal to the cut surface, which would be (100) on both sides of the boundary. Thus when the $Mg^{18}O$ was deposited the only driving force for oxygen diffusion would be parallel to the tilt axis. Cutting was done with a low speed diamond wafering saw (Buehler Isomet, Buehler Ltd.; Lake Bluff, IL). This was the most mechanically demanding step in the processing and, typically, half of the potential bicrystal seeds were lost in this step due to fracture at the grain boundary. The surviving bicrystals were polished to optical flatness prior to crystal growth in a fashion similar to the single crystals before pressing (320, 500, 600 grit SiC paper, 2/0, 4/0 emery paper, and 1 μm alumina powder). In the procedures of Yoo [71] and Gruber [10] for the growth of single crystals the substrates were etched in hot phosphoric acid prior to the deposition. This step was omitted in the preparation of bicrystals for two reasons. Firstly, it was reported by Roshko [9] that phosphoric acid became trapped into surface pores during the chemical etching of MgO polycrystals which, upon annealing, decomposed into low melting phosphates that segregated to the triple junctions. Clearly this situation must be avoided if the diffusion data is to have any meaning. Furthermore it was observed that the bicrystals tended to etch preferentially along the grain boundary resulting in a groove along the boundary even after very short etch times. This is also not acceptable so the etching was abandoned. It may not have been necessary in any case as Gruber [10] reports that during the CVT process surface dislocations grow out within the first few microns of deposition, as revealed by etch pit analysis.

3.2 Source Powder Preparation

The source material was labelled with the oxygen-18 isotope. This facilitated the annealing of the bicrystals as it could be done in an air or CO/CO_2 atmosphere and did not need to be done in an ^{18}O atmosphere. The natural abundances of the stable isotopes of oxygen are as follows: ^{16}O, 0.99759; ^{17}O, 0.00037; ^{18}O, 0.00204. By labelling the source powder (and hence the epitaxial MgO deposit) with a higher concentration of the ^{18}O isotope we can simply anneal the bicrystal in air. The ^{18}O diffuses out of the bicrystal, replaced by ^{16}O. The boundary conditions are those for constant surface concentration; the surface concentrations being equal to the natural abundances of the isotopes. If on the other hand, bicrystals with the natural fractions of the oxygen isotopes are used they would have to be annealed in an artificially-enriched atmosphere of ^{18}O. This requires copious amounts of ^{18}O gas which is not only frightfully expensive, but also quite scarce at present. A single pellet of isotopically-enriched MgO can be used to grow several tens or perhaps even hundreds of epitaxial MgO deposits if they are thin enough.

The procedure for preparing the labelled oxide is fairly straight forward. Essentially, Mg turnings are burned in an atmosphere of ^{18}O yielding the isotopically enriched MgO powder. MgO has a free energy of formation, ΔG_f°, of -601 kJ/mole at room temperature [91]; it was therefore expected that it would oxidize readily upon heating, and this was found to be the case. Anyone who has seen magnesium ribbon burned in air also knows this to be true. It burns readily in air giving off a tremendous amount of light and heat drawing a lot of ooh's and aah's from onlookers.

The oxidation apparatus is shown in figure 3-4. Small amounts of Mg were oxidized in a typical run to ensure complete oxidation of the turnings. If oxidation was incomplete (that is, the ^{18}O enriched gas ran out before all of the Mg was oxidized) the oxidation had to be repeated. A typical batch size was 1.0g of Mg in the form of turnings which were washed in reagent grade methanol, allowed to dry and placed in a 1 cm $\times$ 4 cm fused silica boat. This,in turn, was placed in the center of the fused silica tube furnace which was then sealed and evacuated to less than 1.0 Pa by

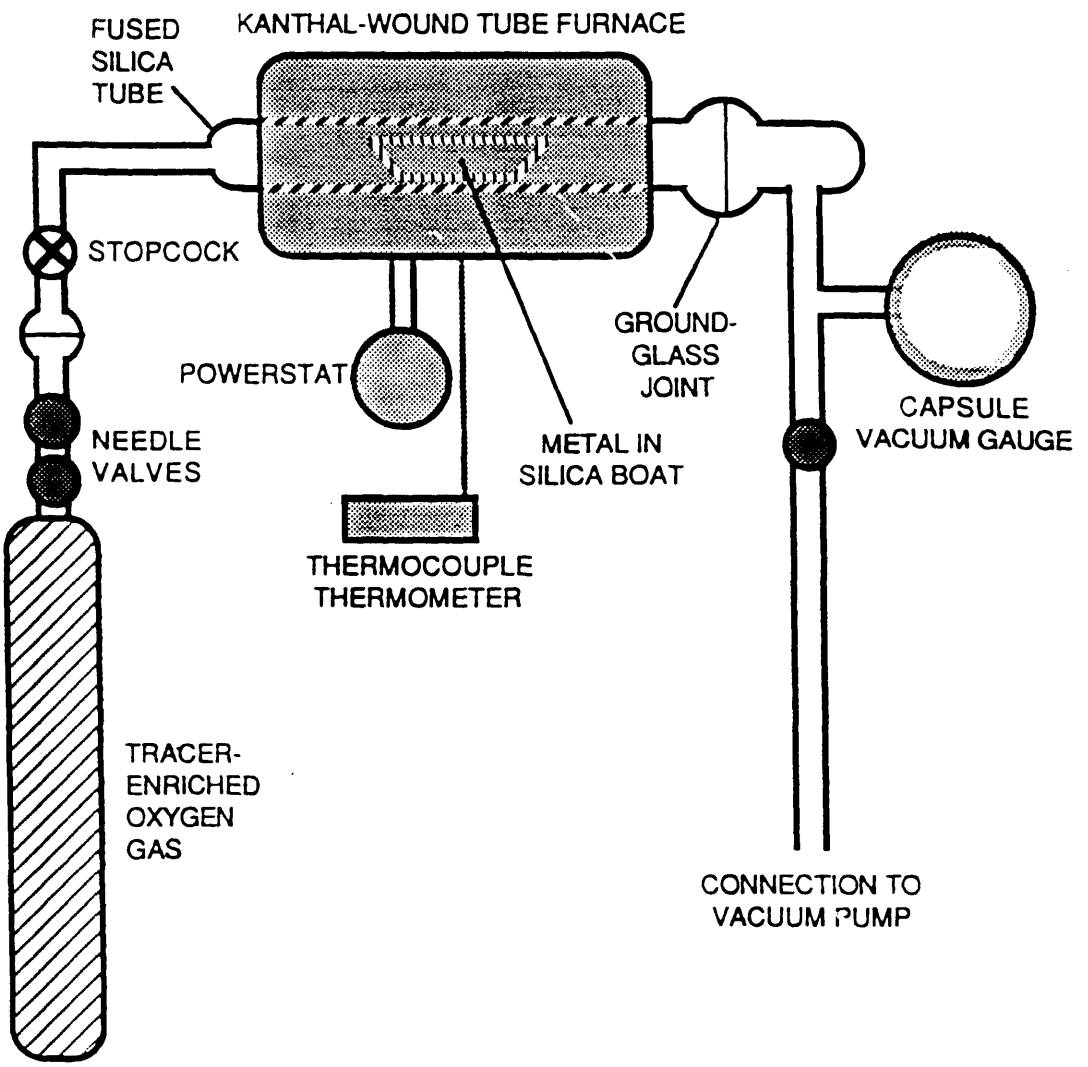

Figure 3-4: Schematic diagram of the Mg Oxidation Apparatus

means of a mechanical roughing pump (*Duo-Seal* Model 1977, Sargent-Welch Scientific Company; Skokie, IL). While the system was pumping down it was also baked out at 200°C and held there for an hour, after which the power was turned down and the system allowed to cool. Once cooled to below 100°C, the valve which led to the vacuum was closed and the pump shut off. The system was then filled to a pressure of 60 kPa with the tracer enriched oxygen gas (30% ^{18}O gas obtained from Cambridge Isotope Laboratories; Woburn, MA) and then sealed. The temperature was then increased at a rate of 20°C until the reaction temperature of 450°C was reached. Slightly below this temperature the power was turned down and the temperature ramped up slowly until the reaction occurred. This was indicated by a bright flash and a drop in pressure. After the reaction stopped due to lack of oxygen the valves to the supply of ^{18}O were opened slightly and the gas was let in slowly until the reaction completed. The power was then turned down and the system allowed to cool to room temperature. Once cool the oxidized product was removed from the silica boat and ground to a fine powder under reagent grade methanol with a mortar and pestile (Coors Ceramics; Golden, CO). The powder was allowed to dry and then cold pressed into a pellet roughly 12 mm in diameter and 2 mm thick. The ram pressure used was about 3000 psi. Pellets were stored in a dessicator when not in use.

3.3 Crystal Growth

3.3.1 Theory and Overview

In most studies of grain boundary diffusion in oxides the results have been clouded to some degree by the presence of segregated impurities. Clearly, in order to elucidate structure-property relations in grain boundaries higher purity boundaries are needed. High purity MgO single crystals have been prepared by Booth [92], Gruber [10], Yoo [11], and Semken [69] using chemical vapor transport (CVT).

Chemical vapor transport is the reaction of a solid or liquid with a gas to form another gaseous compound of limited stability which undergoes the reverse reaction

elsewhere in the system resulting in the reformation of the original material [93] It is a process which has been known for may years. It was mentioned as far back as 1852 in the work of Bunsen [94] who observed the migration of Fe_2O_3 in streams of HCl contained in volcanic gases, presumably by the reaction $Fe_2O_3(s) + 6HCl(g) = 2FeCl_3(g) + 3H_2O(g)$. Significant early work was also done by French mineral chemist H. Saint Claire-Deville [95] who "artificially reproduced" the oxides SnO_2, TiO_2 and MgO through the use of similar vapor transport reactions. More recently such processes have been utilized in the transport and purification of metals, the van Arkel process for purifying zirconium and the Mond process for transporting nickel being two examples. The former is based on the transport of Zr by $I_2(g)$: $Zr(s) + 2I_2(g) = ZrI_4(g)$, the latter based on the transport of Ni by CO(g) : $Ni(s) + 4CO(g) = Ni(CO)_4$.

The theory of CVT has been discussed in detail by Schafer [93], who formulated ten rules which govern the feasibility of vapor transport reactions. The rules are not always easily applied, though. Another approach based on the use of the Ellingham diagram has been discussed by Alcock and Jeffes [96, 97, 98]. The Ellingham diagram is, for a given process, a plot of ΔG°, the standard free energy change for the process, as a function of temperature. In our case, this is the transport of MgO by HCl:

$$MgO(s) + 2HCl(g) = MgCl_2(g) + H_2O(g) \tag{3.1}$$

for which the equilibrium constant K_p can be written

$$K_p = \frac{P_{H_2O}\, P_{MgCl_2}}{P^2_{HCl}} \cdot \frac{1}{a_{MgO}} \quad \text{therefore} \quad a_{MgO} = \frac{P_{H_2O}\, P_{MgCl_2}}{P^2_{HCl}} \cdot \frac{1}{K_p}$$

where P_x is the partial pressure of species x and a_{MgO} is the activity of MgO. In order to effect transport we must disturb the chemical equilibrium in such a way that the activity of MgO, a_{MgO}, is less than unity at the point of removal (forward reaction favored) and greater than unity at the point of deposition (reverse reaction favored). This can be done in one of two ways, by varying K_p or by varying the quantity $P_{H_2O}P_{MgCl_2}/P^2_{HCl}$.

K_p	P_{MgCl_2} (atm)	P_{MgCl_2} - $P^{\circ}_{MgCl_2}$ (atm)
10^{-5}	0.0031	-0.3302
10^{-4}	0.0098	-0.3235
10^{-3}	0.0297	-0.3036
10^{-2}	0.0833	-0.2500
10^{-1}	0.1937	-0.1396
1	0.3333	0
10^{+1}	0.4317	0.0984
10^{+2}	0.4762	0.1429
10^{+3}	0.4922	0.1589
10^{+4}	0.4975	0.1642
10^{+5}	0.4992	0.1659

Table 3.1: $P_{MgCl_2(g)}$ at equilibrium with MgO(s) at varying values of K_p ($\Sigma P = 1$ atm) for the reaction MgO(s) + 2HCl(g) = $MgCl_2$(g) + H_2O(g). $P^{\circ}_{MgCl_2}$ is the partial pressure of $MgCl_2$ at $K_p = 1$.

Varying K_p is accomplished by changing the temperature at which the reaction occurs. The nature of this variance is given by the well known thermodynamic relation $K_p = e^{-\Delta G^{\circ}/RT}$. An Ellingham diagram for reaction 3.1 in the context of ΔH°, the standard enthalpy change of the reaction, ΔS°, the standard entropy change of the reaction and K_p is given in figure 3-5. Recall that $\Delta G^{\circ} = \Delta H^{\circ}$ - $T\Delta S^{\circ}$. It can be seen from this diagram that a constant value of K_p can be represented by a line through the point (ΔG°,T); (0 kcal/mole, O K) the slope of which is -RlnK$_p$. Knowing this it can easily be seen that any reaction with $\Delta H^{\circ} = 0$ (which would pass through the point (0,0) on such a plot) would have a constant K_p at all temperatures, if ΔH and ΔS are independent of temperature; thus it would not be possible to effect transport by varying K_p. Fortunately this is not the case with the transport of MgO by HCl. By changing the temperature we can vary K_p such that the forward reaction is favored at the removal point and the reverse reaction is favored at the deposition point. In the case of MgO this would require that the source be hotter than the seed. It can be seen from table 3.1 that the greatest amount of transport comes from varying K_p only a small amount from unity. For the case of equation 3.1 47.6% of possible transport

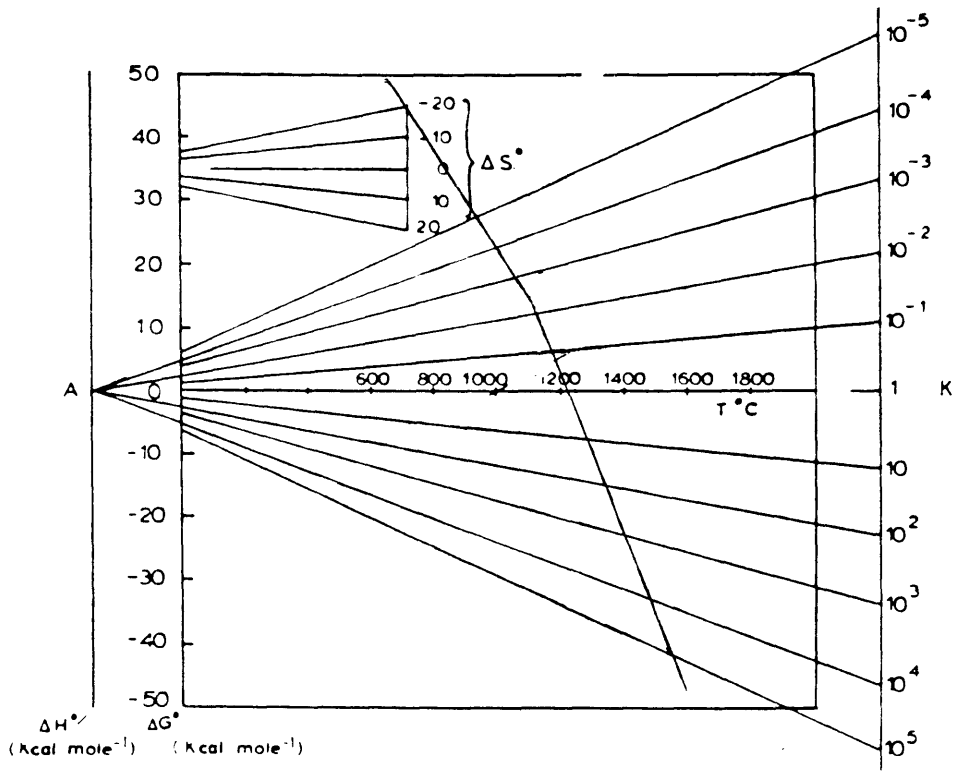

Figure 3-5: Ellingham diagram for the reaction MgO(s) + 2HCl(g) = $MgCl_2$(g) + H_2O(g) in the context of $\Delta H°$, $\Delta S°$, and K_p.

takes place by varying K_p from 10^{-1} to 10^{+1} whereas only 1.4% of possible transport takes place by varying K_p from 10^{+3} to 10^{+5}. P_{MgCl_2} - $P^{\circ}_{MgCl_2}$ (the partial pressure of $MgCl_2$ at $K_p = 1$) is used as a measure of the amount of transport possible. P_{MgCl_2} is actually the number of moles of MgO which will be transported per mole of transport gas and is thus a good measure thereof. Of course for transport to be efficient the temperature at which $K_p = 0$ ($\Delta G^\circ = 0$) must be achievable, For an exothermic reaction this requires that ΔS° be negative. For an endothermic reaction (as is the case with equation 3.1) it must be positive, and it is. For our transport reaction $\Delta H^\circ = 0$ at roughly 1250°C.

K_p can also be varied by changing the total pressure ΣP of the system. For the hypothetical 1:1 reaction X(s) + Y(g) = XY(g), a plot of P_{xy} vs. K_p for a range of ΣP values is shown in figure 3-6. Transport is most efficient where the rate of change of K_p is a maximum (large changes in P_{xy} for small changes in K_p). For a reaction such as equation 3.1 where the number of moles of gas is equal on both sides of the equation (a 1:1 reaction) this always occurs at $K_p = 1$. Alcock and Jeffes have defined a productivity function $PF = P_{xy}\frac{dP_{xy}}{dK_p}$ for the same hypothetical reaction, X(s) + Y(g) = XY(g). Plotting this quantity vs. K_p as in figure 3-7 illustrates this point. This graph applies to all 1:1 reactions thus it is valid for our transport reaction. Transport reactions which are not 1:1 do not see their PF values reach a maximum at $K_p = 1$ for all values of ΣP so this is not an exercise in futility as it may seem. The most efficient transport reactions involve large volume changes. That is, many more moles of gas on one side of the equation. This implies large values of ΔS°. The ΔG vs. T plot will then cross through many decades of K_p with small changes in temperature making large variances in K_p possible with small changes in temperature. As our transport reaction is 1:1 this aspect will not be discussed further.

The activity of MgO can also be changed by varying ΣP within the system, that is transporting a solid across a pressure gradient as opposed to a temperature gradient. This is different from what was just previously discussed. In that case the overall effect of changing total system pressure from one experiment to another was being considered. Here the pressure is being varied within the system in the same exper-

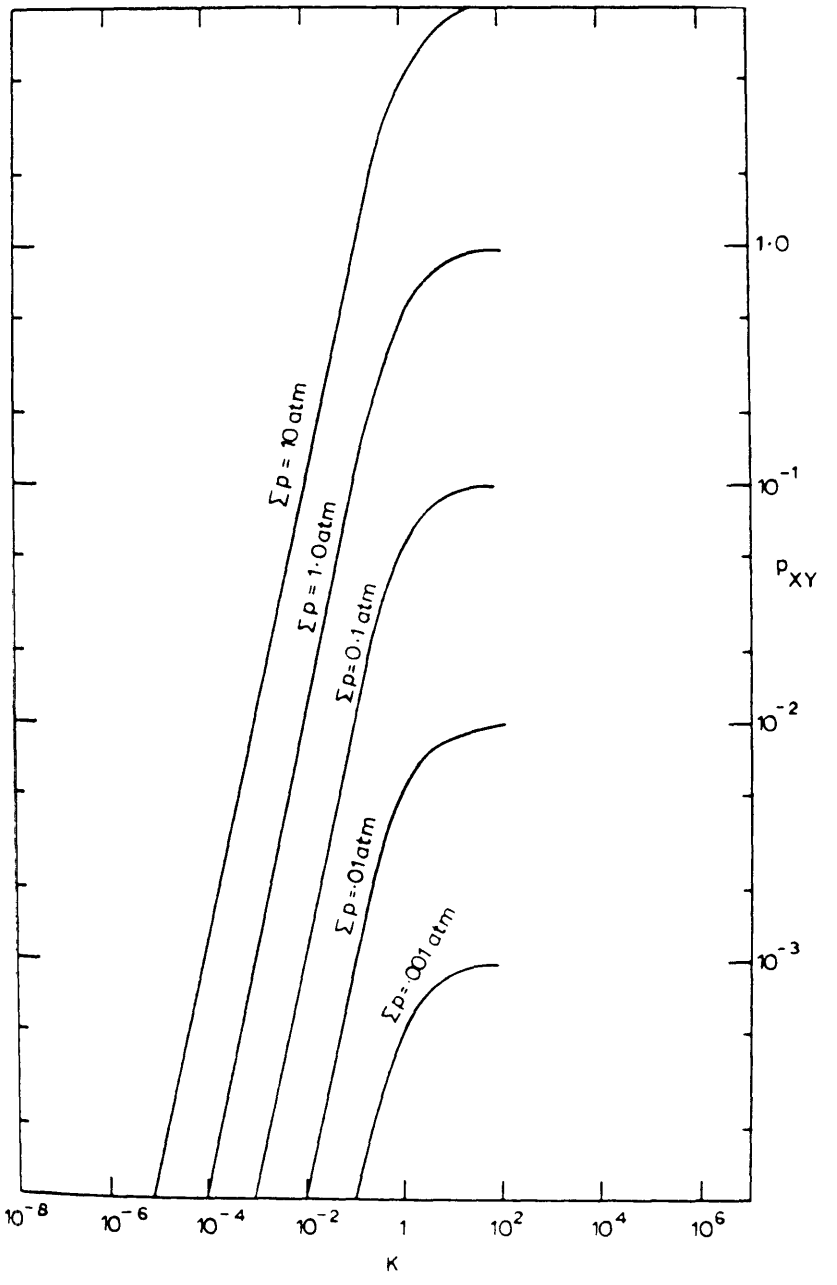

Figure 3-6: Partial pressure of XY(g), P_{xy}, as a function of equilibrium constant, K_p at various total pressures, ΣP, for the hypothetical 1:1 reaction X(s) + Y(g) = XY(g), from Alcock and Jeffes.

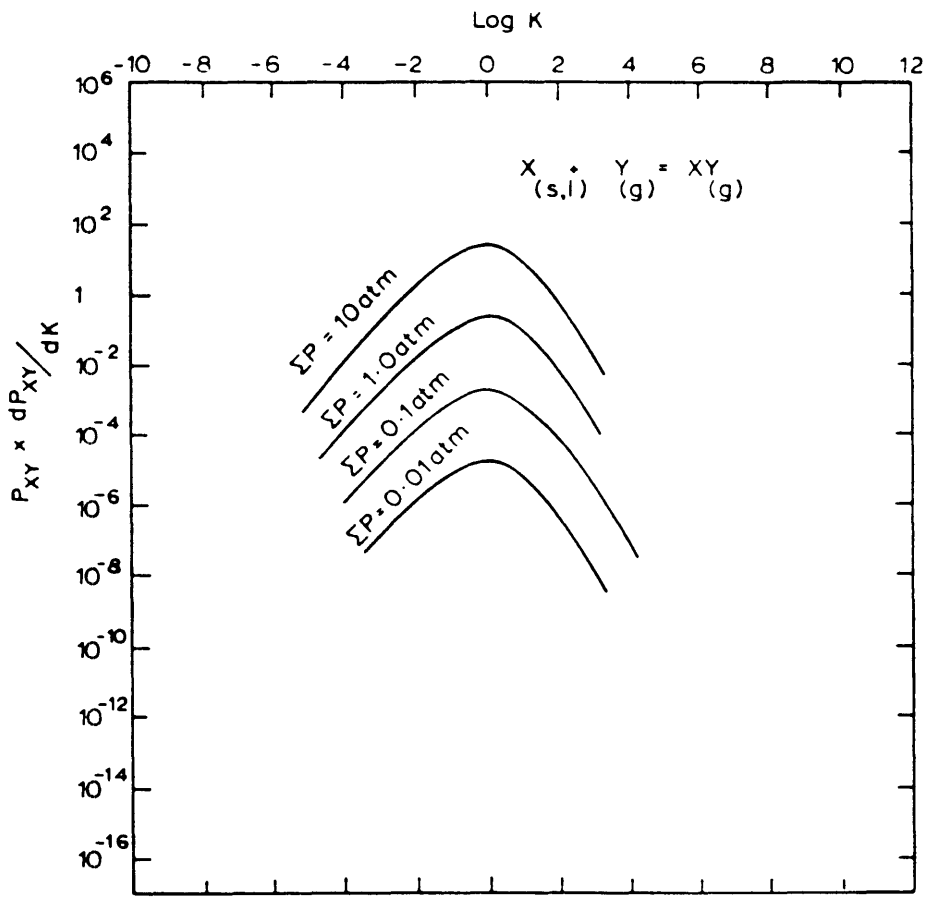

Figure 3-7: Productivity function PF, $P_{xy}\frac{dP_{xy}}{dK_p}$, as a function of K_p for the hypothetical 1:1 reaction X(s) + Y(g) = XY(g) from [17]. This plot applies to all 1:1 reactions.

iment. Once again though, as is probably intuitively obvious, a pressure gradient will have no effect on a reaction with equal numbers of moles of gas on both sides of the equation. This route is therefore not possible for our transport reaction. This is usually not a practical method anyway as the logistics of compressing and rarefying as gas within the same system can be quite inconvenient. Thus the most efficacious transport of MgO by HCl will be achieved by varying K_p as much as possible by placing the source and seed in a temperature gradient about equilibrium.

Two distinct experimental designs have been used to grow epitaxial MgO. Booth and Kingery employed a dynamic forced flow (open system) CVT method [92]. In this process the growth system consists of a gas flow system for producing and delivering the products and a vacuum furnace for deposition and to regulate pressure and dispose of product gases. A schematic of the apparatus is shown in figure 3-8. $MgCl_2$ vapor was generated by passing Cl_2 and CO gases over a bed of MgO powder according to the reaction MgO (s) + Cl_2 (g) = $MgCl_2$ (g) + CO_2 (g). H_2 and excess CO_2 gases were introduced into the furnace through a separate injector to initiate deposition according to the reaction $MgCl_2$ (g) + CO_2 (g) + H_2 (g) = MgO (s) + 2HCl (g) + CO (g). The MgO was deposited epitaxially on single crystal MgO substrates in the furnace. The deposition was conducted at 1600 °C at a total pressure of 5 torr. Gas velocities for both injectors were maintained at 900 cm/sec. Equimolar quantities of Cl_2 and CO were used. Ar(g) was used as a "filler" in order to keep the superficial velocities of both gas streams equal. Deposition temperatures of less than 1600 °C resulted in nucleation of MgO in the gas phase causing powder formation. At still lower temperatures, nucleation of $MgCl_2$ (g) in the form of needles or powder would occur. Growth rates of about 150 μm/hour were achieved. The CVT-grown crystals were far higher in purity than the source material and on par with, or better than, commercially-available MgO crystals prepared by arc melting. The CVT grown were also far superior to arc-melted crystals in terms of dislocation density. Etch pit analysis revealed dislocation densities averaging 5×10^3 cm^{-2} for CVT-grown crystals compared with 2.8×10^5 - 1×10^6 cm^{-2} for the arc melt grown crystals.

Another experimental design was used by Gruber, [10] and subsequently, in our

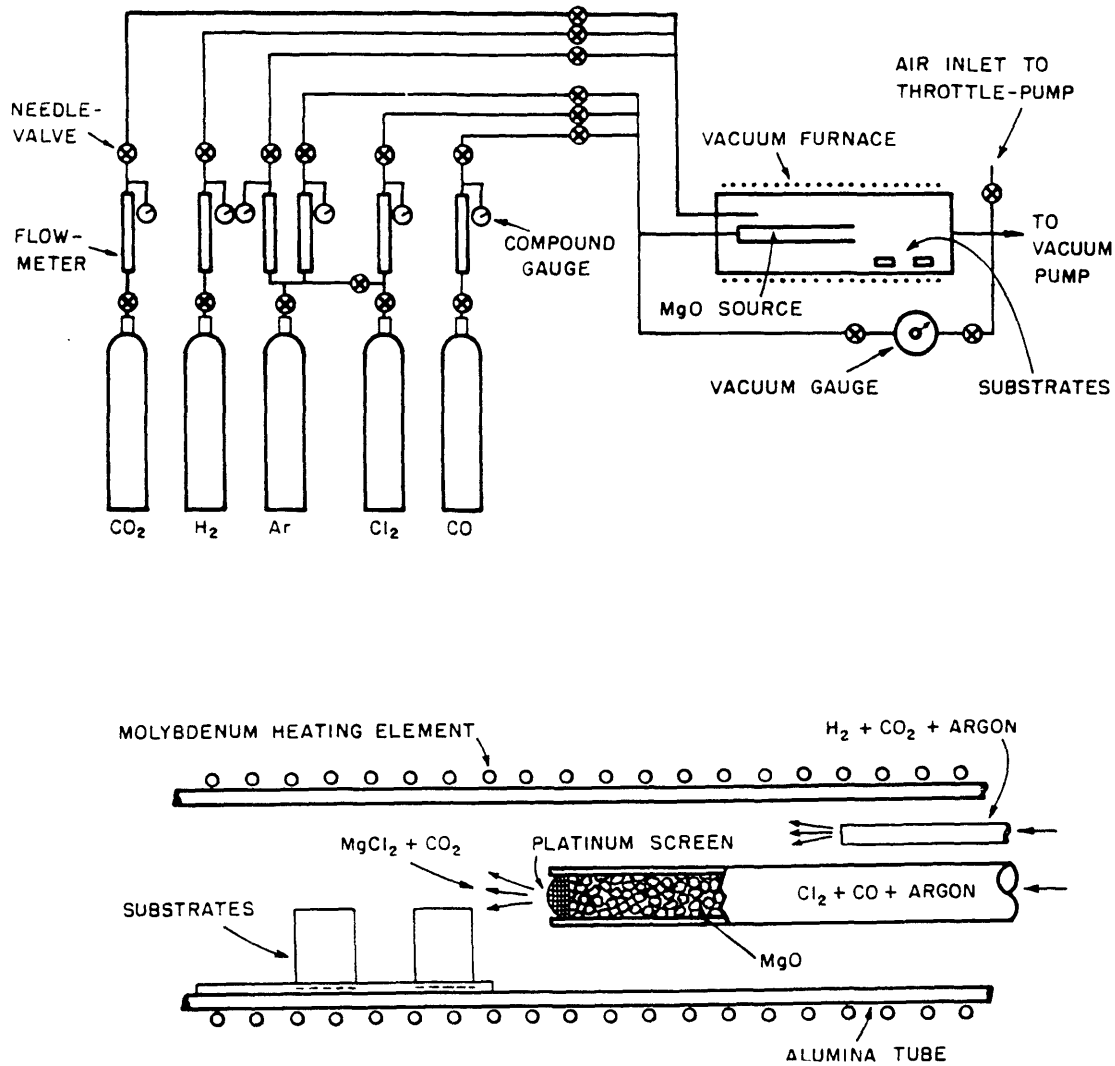

Figure 3-8: Apparatus for growth of MgO crystals by dynamic, open system CVT.

Impurity	Dynamic CVT (ppmw)	Static CVT (ppmw)
Al	100	10
Si	10	50
Fe	10	150
Cl	n.r.	10
Ca	1	< 30
Pt	n.r.	2
CVT / seed crystal dislocation density ratio	0.005 - 0.01	0.01 - 0.1

Table 3.2: Comparison of impurity analyses and dislocation densities for statically and dynamically CVT grown single crystals. Data from [10, 92]. n.r. = not reported

laboratory, by Yoo [71] and Semken [69]. They employed closed system (static) CVT using HCl as a transport gas. In this procedure the source and seed are placed in close proximity in a thermal gradient about 1000°C. After isolation of the growth chamber, HCl gas introduced and the system is sealed. Growth proceeds via the reversible reaction $MgO(s) + 2HCl(g) = MgCl_2(g) + H_2O(g)$, the forward reaction occurring at the source, the reverse reaction at the seed, depositing the MgO epitaxially on the seed. Growth rates were reported to be similar to those for dynamic CVT, purities were similar, and dislocation densities slightly higher. A comparison of results from the two studies is shown in table 3.2. The reason for the high purities of the bulk CVT epitaxial crystals is attributable to the fact that at the growth temperatures only the transport of MgO is favored; transport of most impurities is suppressed. The process can be though of as a chemically assisted distillation. The results of the the studies were similar, however the experimental apparatus is less complicated for static CVT. This was the method used to grow the MgO for this study, with slight modifications to prepare bicrystals rather than single crystals. These will be discussed in the detailed procedure which follows.

3.3.2 Bicrystal Epitaxy

Static chemical vapor transport was used for the growth of MgO bicrystals. Previous authors [10, 11, 69] have used the same technique to grow epitaxial single crystals by using single crystal substrates. Presumably the growth remains epitaxial and bicrystal is produced if the substrate is a bicrystal. This was found to be the case as revealed by transmission electron microscopy of the prepared bicrystals [99]. The seed bicrystals were washed in reagent grade methanol prior to the growth, but other than that were as polished. Gruber [10] has shown that the quality of the substrate has no bearing on the quality of the epitaxial layer. It is invariably lower in dislocation density (and higher in purity) than the seed. It diffusivities are to be measured through the interdiffusion between the ^{16}O and ^{18}O layers (this has been done by Yoo [71]) then the quality of the seed is of extreme importance. The dislocation damage caused by polishing the seed would result in it having a seemingly higher diffusivity than the higher quality epitaxial layer due to the enhancement of diffusion along dislocations (dislocation pipe diffusion). In this study, though, isotopic gradients are produced at the surface of the epitaxial layer by gas exchange with the atmosphere, not by interdiffusion, so the quality of the $^{16}O/^{18}O$ interface is relatively unimportant.

Once the seed bicrystal is ready it is loaded into the crystal growth apparatus for the deposition. A schematic diagram of the apparatus used is shown in figure 3-9; a closeup featuring the growth chamber is shown in figure 3-10. To begin the source pellet is placed at the bottom of a 20 ml platinum crucible. A platinum ring is placed around the pellet to support the seed bicrystal, which is then placed growth side down on the ring. That is to say the polished side is opposite the source pellet. The ring is fashioned such that the source seed distance is approximately 1 mm. It is important to carefully center the seed on the ring to avoid it toppling over during the loading process or the run. If this occurs it is unlikely that the run will be successful. Having done this the crucible is loosely capped with platinum foil and loaded into the fused quartz growth chamber. The crucible assembly rests on a platinum wire mesh which is is strung up by platinum wires. It is suspended from the top of the

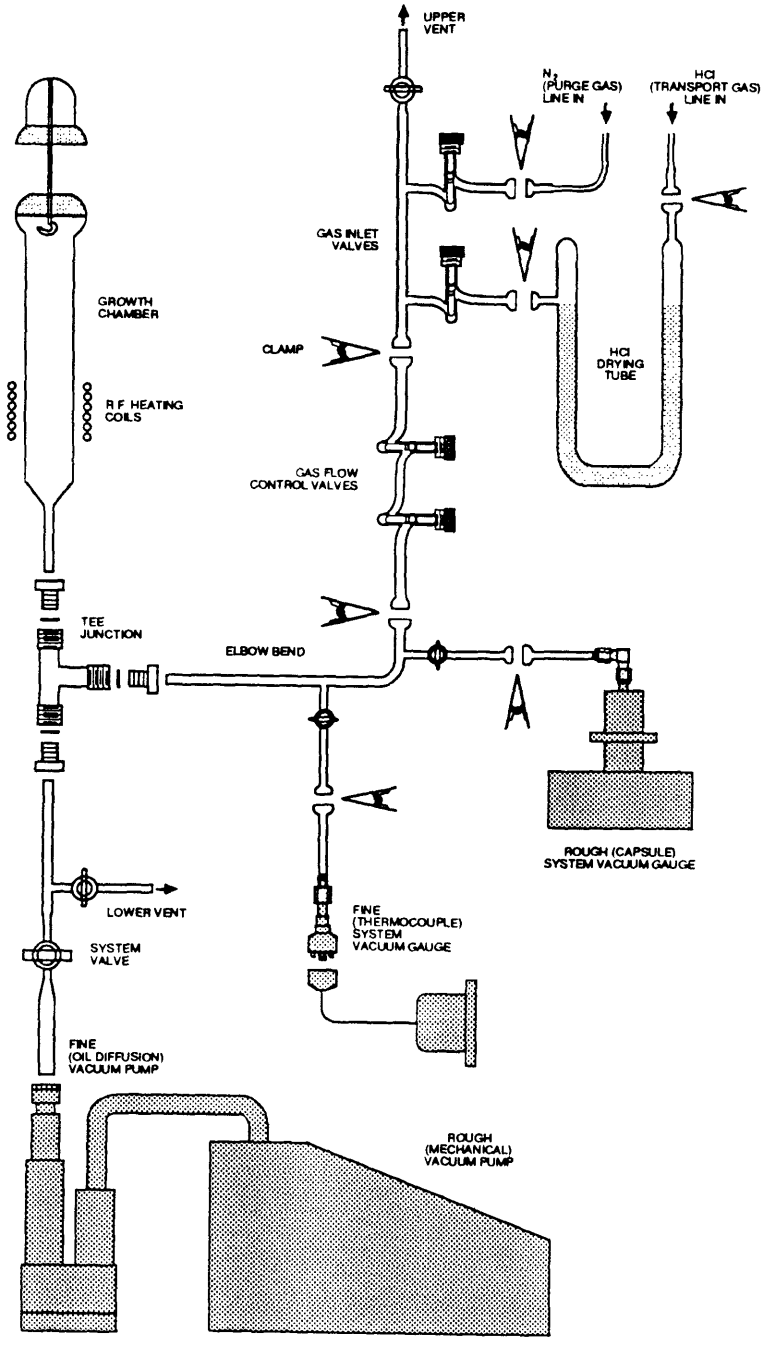

Figure 3-9: CVT crystal growth apparatus used in this study.

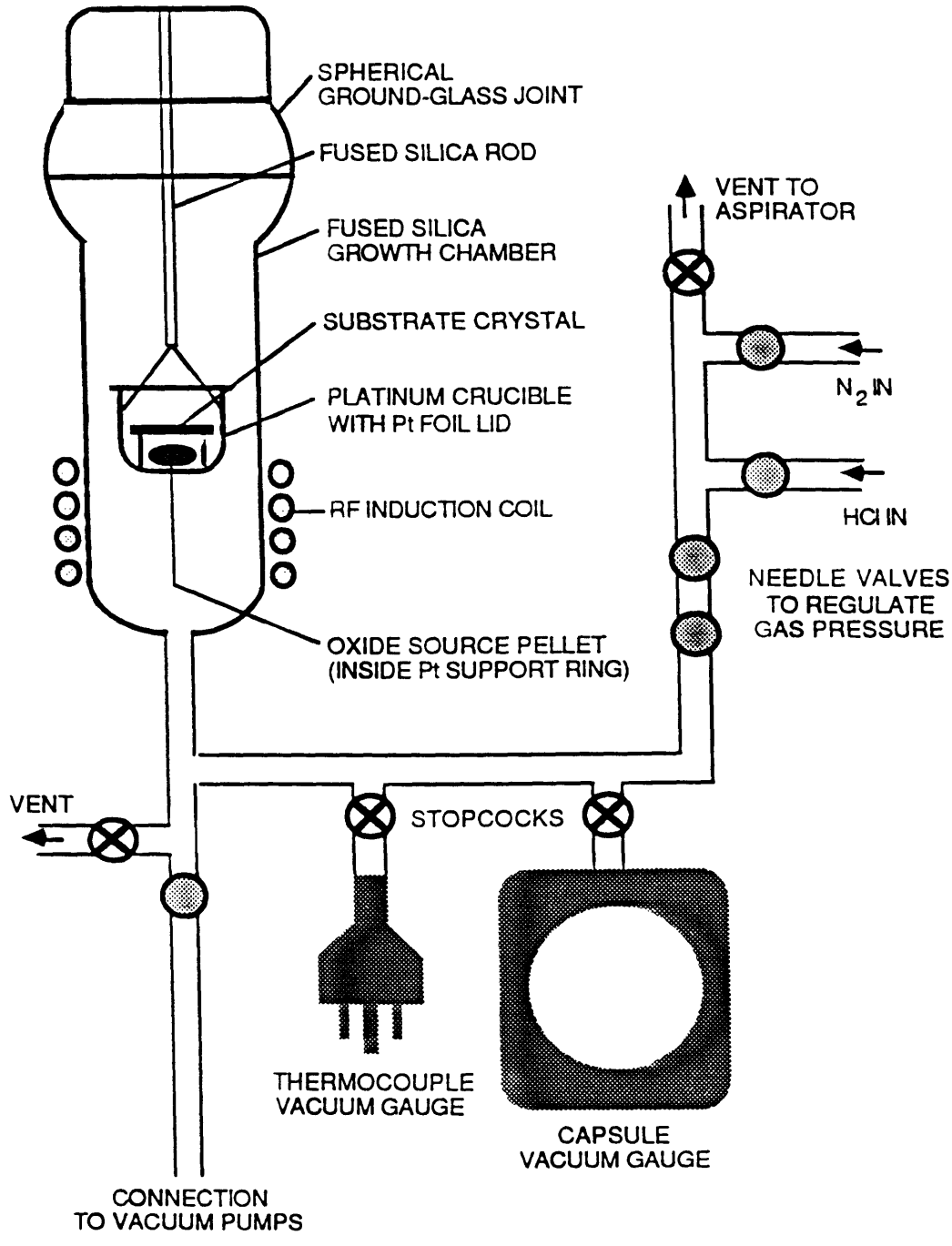

Figure 3-10: Closeup of growth chamber showing placement of crucible assembly in RF induction field.

chamber by the wires which are hung on a fused silica rod emanating from the top of the chamber The temperature gradient necessary for growth is realized by positioning the crucible within the chamber such that it is heated from below. The crucible is heated by a 5kW, kHz frequency induction generator (Model T-5-3-KC-J-B, Lepel High Frequency Laboratories Inc.; New York, NY) the coils of which surround the chamber. The crucible is placed within the induction field such that the bottom is between the first and second coils (see figure 3-10), thus the source will be hotter than the seed as is required.

Having loaded the sample the growth procedure can begin. The system is first evacuated to pressures less than 10^{-4} torr by means of a combination of a mechanical roughing pump (*Duo-Seal* Model 1405, Sargent-Welch Scientific Company; Skokie, IL) and an oil diffusion pump (Model VMF-10, CVC Products Inc; Rochester, NY). Pumpdown is allowed to proceed at room temperature for one hour. Vacuum quality was monitored with a thermocouple vacuum gauge (Model 801, Varian Vacuum Products; Burlington, MA). The system is then baked out at the growth temperature. Following the procedures of Yoo and Semken a growth temperature of approximately 1100° C was used, verified, initially at least, by optical pyrometry of the crucible bottom. This was achieved by operating the generator with a grid current of 0.40 A and a plate current of 0.85 A. This brings the crucible to the growth temperature within two minutes and maintains it with little fluctuation. The bakeout continued for one hour during which time the contents were being outgassed of organics and the like. The final step before the growth run is a system purge using N_2 gas. The system is isolated and dry, low oxygen (< 5ppm) N_2 gas (Airco Inc.; Montvale, NJ) is introduced to a pressure of 400 torr while keeping the crucible at the growth temperature. This is done to eliminate as much O_2 from the system as possible. The N_2 purge lasts from 30 minutes to an hour after which the N_2 gas is pumped out and the system is once again evacuated to pressures less than 10^{-4} torr. The pumpdown is allowed to continue for at least half an hour.

The growth run could then be done. The power on the RF furnace is turned down and the crucible is allowed to cool for a few minutes. The system is then isolated again

and anhydrous, electronic grade HCl (Matheson Gas Products inc.; East Rutherford, NJ) is introduced to a pressure of 20 - 30 torr. Pressure during the run is monitored with a capsule vacuum gauge (Model 16063-T, Leybold-Heraeus Vacuum Products; Weston, MA). The joint leading to the t/c gauge is sealed prior to the introduction of HCl as it would damage the gauge. The crucible is then re-heated to the growth temperature and held there for 2 - 4 hours after which the HCl is evacuated and the furnace power shut off. During typical runs the system pressure has been observed to rise, fall and occasionally remain constant. Successful runs have resulted from all three of these circumstances. Unless there is a severe leak, though, pressure never varies by more than 5 - 10 torr from the initial HCl pressure.

After the system has cooled to room temperature the sample can be removed from the chamber. Before the next run the inner wall of the growth chamber must be cleaned with methanol to remove the MgO which solidified on it. The epitaxial bicrystal is then examined and its thickness is measured with a micrometer. The thickness of the deposit is determined by subtracting off the thickness before the run. A successful run resulted in the deposition of a transparent, rough bicrystal 10 - 150 μm thick full of growth hillocks and etch pits due to the vapor phase growth. The area outside the Pt ring may be covered with a dusting of polycrystalline MgO resulting from more rapid crystallization on these slightly cooler surfaces. Occasionally a similar, thin, white, apparently polycrystalline layer was formed on the entirety of the substrate bicrystal. This was reported by Semken [69] to be the result of a major leakage of air into the system, but is more likely due to bad positioning of the crucible assembly within the induction field, causing the substrate bicrystal being too low in temperature, resulting in the same rapid crystallization phenomenon observed outside the Pt ring in successful runs. Also from time to time a discolored epitaxial layer will be deposited. This apparently is due to small leaks in the system. Minor quantities of air result in the the transport of platinum via oxygen resulting in a Pt contaminated, brownish epitaxial layer. This was also observed and reported by Gruber [10]. This can best be avoided by an adequately long bakeout, thorough N_2 purge, and the use of a high quality vacuum grease (Dow-Corning High Vacuum

Grease; Dow-Corning Inc.) to seal all the glass joints. Actually as of the time of the writing of this thesis a project is underway to replace the multi-piece system depicted in the figures to one consisting of only three distinct glass parts, the growth chamber, a tube leading to the vacuum pumps and the manifold containing the gauges and gas inlets. These would then in turn be connected by a stainless steel Cajon o-ring tee fitting, eliminating all the potentially leaky glass joints.

The major impurities in the epitaxial deposits, reported by Semken [69] are cations, Si and Fe, co-transported with Mg from the source pellet, not Cl as might be expected from the HCl. In fact it was reported by Gruber that the concentration of Cl in the deposit is lower than in the source material [10]. Optimum growth rates were approximately 100 μm per hour, though there was considerable variance, and the average was probably 20 - 30 μm/hour. One can easily see the reason for so much scatter. It is the fact that so many independent variables need to be controlled. The growth temperature, the positioning of the crucible within the induction field (hence the magnitude of temperature gradient), the initial HCl pressure, and the source-seed distance. Each of these may be varied over a considerably wide range just taken separately. When the combinations are considered the number of possibilities is limitless. Also, the quality of the vacuum is most important, as mentioned previously. This cannot be varied independently, though, as it is a consequence of how well the system is sealed. CVT is thus more of a black art than a science and, perhaps needless to say, growth runs were not always successful. The success rate in fact was approximately 50%. That is to say about half the time a transparent bicrystal (presumably) deposit was formed.

A successful run was culminated with the bicrystal being cut into two diffusion specimens for annealing, each approximately 4 mm $\times$ 8 mm. The specimens were annealed as grown, so no further preparation was done prior to annealing. The specimens were stored in a dessicator until needed.

3.4 Annealing

As discussed in a previous section the fact that the tracer is already present in the CVT grown MgO bicrystals makes the diffusion annealing a simple matter as it can be done in an air atmosphere (or in any atmosphere of choice). The ^{18}O diffuses out of the bicrystal upon heating, replaced by ^{16}O. The boundary conditions for the analysis are just those for constant surface concentration, the concentrations being the natural abundances of the three isotopes.

3.4.1 Design of Annealing Experiments

Annealing was done in a horizontal tube furnace designed by Dr. Peter Moon and constructed by Dr. Steven C. Semken, a schematic of which is shown in figure 3-11. The furnace is a 46 × 39 × 36 cm box of alumina refractory brick (K-30 firebrick, Babcock and Wilcox Company; Augusta, GA), containing six resistive SiC heating elements (*Hot Rod XL*, Kanthal Corporation; Bethel, CT). The elements are wired in series and connected to a 220 volt AC power source. The elements surround a 1 in outer diameter alumina tube (McDaniel 998A-3109, McDaniel Refractory Company; Beaver Falls, PA), the ends of which are closed off with Cajon brass O-ring fittings and adaptors (Cajon *Ultra-Torr*, Cajon Corporation; Macedonia, OH). This feature added extra flexibility in that it allowed for a controlled atmosphere inside the tube. CO/CO_2 gas mixtures could be flowed through the tube to control the oxygen partial pressure within, or the ends could simply be left open for air anneals. Exhaust from the furnace was vented to a fume hood. Gas flow was monitored with the aid of a pair of mineral oil bubblers, one where the exhaust gas exits the furnace and the other at the outlet to the fume hood. Temperature was monitored with a type-S (Pt-Pt 10% Rh) thermocouple (Omega SAT-24, Omega Engineering Inc.; Stamford, CT) equipped with a sheath of alumina to protect it from the potential reducing atmosphere of the furnace. Temperature was maintained with a digital temperature controller (Eurotherm 808, Eurotherm Corporation; Reston, VA). The controller offered no progamability, only a single setpoint and ramp were available,

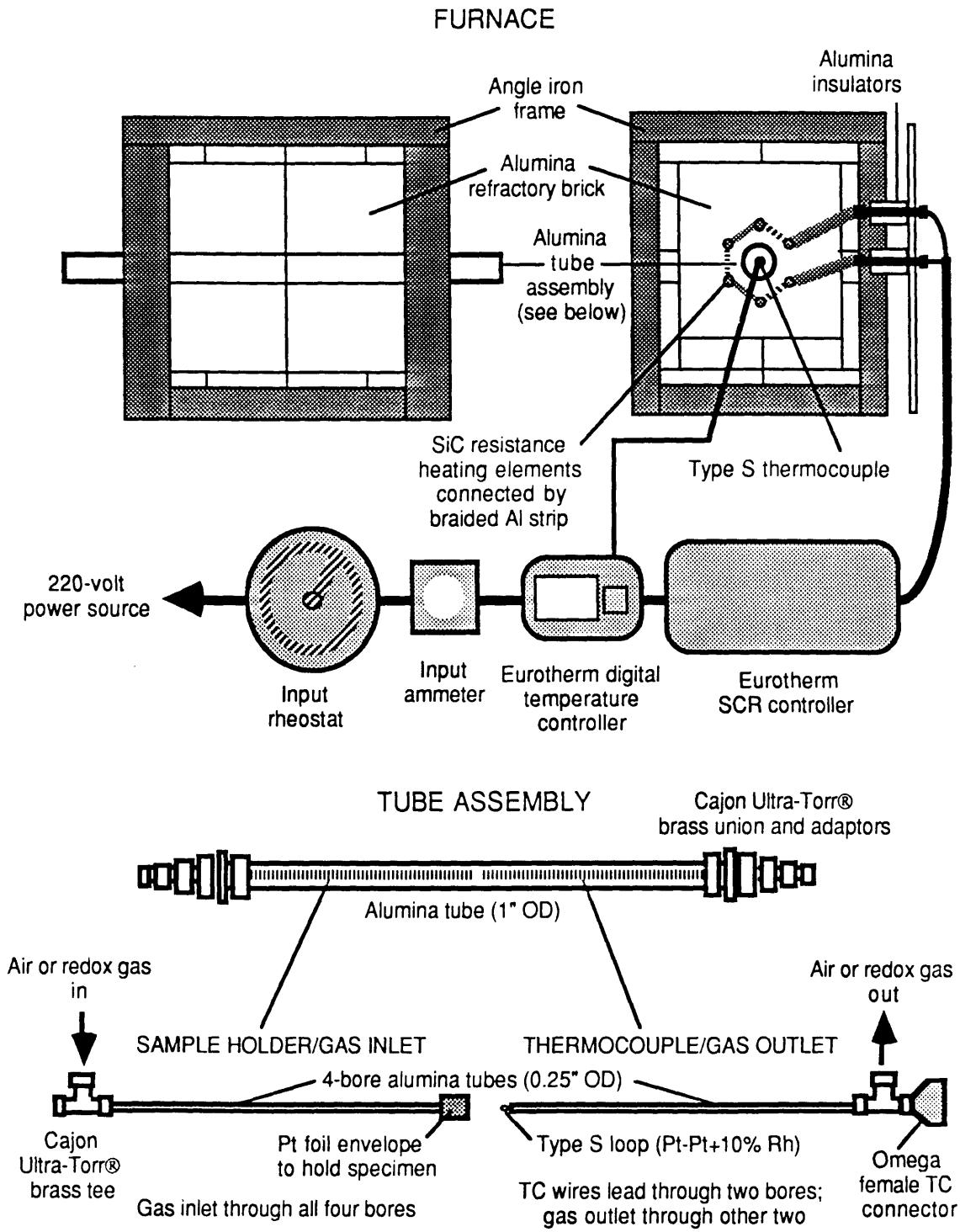

Figure 3-11: Controlled atmosphere tube furnace used for annealing diffusion specimens.

but this was all that was necessary as for diffusion anneals the sample must be brought to the annealing temperature as quickly as possible to minimize error in the timing of the anneals. Likewise when the anneal is over they must be cooled as quickly as possible. Samples to be annealed were loosely enveloped in a foil of platinum to prevent contamination from the furnace as much as possible without restricting the flow of gas around the specimen.

Annealing times were chosen so as to be able to obtain concentration profiles which had not only a contribution from grain boundary diffusion but also a measurable bulk diffusion component. This required anneals much longer than would have been necessary to detect grain boundary diffusion alone. A benefit of longer anneals is that they allow for the grain boundary diffusion profiles to extend further in space laterally from the grain boundary making them easier to detect with the SIMS probe which has a poor lateral resolution of 1 μm at best. Another benefit of long anneals was a reduction in the uncertainty of the anneal time itself. Typically anneals were timed with an uncertainty of one minute, so the longer the anneal the less the percent error in measured annealing time. This is only a minor consideration, however. The main source for uncertainty in the anneal time was the fact that it took time for the annealing furnace to heat from room temperature to the anneal temperature. During this time diffusion is occurring. Fortunately, since diffusivities are exponentially dependent upon temperature any diffusion that occurs during the heat up is negligible until very close to the annealing temperature. The highest heating rate (25 °C / minute) was used, therefore, to minimize this effect. Unfortunately, though, for most of the anneal temperatures used, the furnace could not heat up this rapidly as the temperature got close to the desired anneal temperature. The higher the temperature got the slower the heating rate became. This combined with the shorter times of the anneals at higher temperatures made the longer anneals for all temperatures all the more important. The same concern also applied to the cool down; it too could potentially add some uncertainty to the measured anneal time. In practice, though, this did not turn out to be the case. When the anneals were done the furnace power was shut off and the temperature dropped rapidly (several hundred degrees within

Anneal time	temperature °C
3 hours	1500
4.5 hours	1450
7 hours	1400
3 days	1300
6 days	1250

Table 3.3: Diffusion anneal times and temperatures used in this study

the first few minutes). Thus the cooling phase was not a major contributor to error in measurement of annealing time.

Annealing temperatures were chosen at the high end by the limits of the furnace (SiC elements, 1550 °C maximum temperature), and at the low end by time constraints. Six days at 1250 °C was semi-arbitrarily chosen as the longest anneal time. The regularity of power outages and the desire to anneal all the specimens in the same furnace (for obvious reasons) made longer anneals at lower temperatures impractical. A summary of diffusion times and temperatures for bicrystal specimens is shown in table 3.3; these times yielded grain boundary diffusion profiles of 700 - 1000 nm in depth and bulk diffusion profiles 100 - 300 nm in depth.

Partial pressure dependence of oxygen diffusion was determined by annealing bicrystals in atmospheres of oxygen partial pressure ranging from 10^{-11} to 10^{+1} kPa. This was accomplished by means of flowing mixtures of CO/CO_2 gas (Matheson Gas Products; East Rutherford, NJ and Airco New England; Medford, MA) through the furnace at atmospheric pressure. The corresponding oxygen partial pressure for a given CO/CO_2 mixture at a given temperature can be calculated from the standard Gibbs free energy of the reaction

$$CO(g) + \tfrac{1}{2}O_2(g) = CO_2(g) \quad \text{for which} \quad K_p = \frac{P_{CO_2}}{P_{CO}P_{O_2}^{1/2}}$$

An expression for the Gibbs free energy change of this reaction is given by: [100]

$$\Delta G°(T) = -282400 + 86.81\ T \quad (J/mol)$$

Since ΔG° = -R T ln K_p we can solve for the oxygen partial pressure as a function of the other variables.

$$\text{-RTln } \frac{P_{CO_2}}{P_{CO}P_{O_2}^{1/2}} = \text{-282400 + 86.81 T}$$

$$\frac{P_{CO_2}}{P_{CO}P_{O_2}^{1/2}} = \exp(\frac{282400}{RT} - \frac{86.81}{R})$$

$$P_{O_2}^{-1/2} = \frac{P_{CO}}{P_{CO_2}} \exp(\frac{282400}{RT} - \frac{86.81}{R})$$

$$P_{O_2} = (\frac{P_{CO_2}}{P_{CO}})^2 \exp(\frac{67934}{T} - 10.441)$$

Since the gas mixtures are allowed to flow freely through the system the total pressure is one atmosphere. The ratio of partial pressures P_{CO_2}/P_{CO} is equal to the ratio of volume percentages of the gas mixtures which are known. Thus for a given temperature and gas ratio the oxygen partial pressure can be computed. A plot of oxygen partial pressures versus temperature for a gas mixtures ranging from 0.1% CO to 99.9% CO calculated from the above equation is shown in figure 3-12.

3.5 Secondary Ion Mass Spectrometry

Once the bicrystals had been annealed, the oxygen isotopic gradients had to be measured to determine the diffusivities. In traditional radiotracer experiments diffusant concentrations are obtained indirectly by mechanical grinding of the sample followed by measurement of the sample thickness (to determine depth) followed by activity measurement, the activity being proportional to the diffusant concentration. In order for this technique to be employed the diffusion profiles must be at least several tens of microns long. For slowly diffusing species (such as O^{2-} in MgO) this would require impracticably long diffusion anneals. Also it almost goes without saying that this method requires that the diffusing species have a suitable radioactive isotope. Unfortunately this is not the case for oxygen. Its only radioactive isotope ^{15}O has a half life on the order of minutes making it unsuitable for traditional radiotracer experiments. This is why stable isotopes must be used in oxygen diffusion studies. A

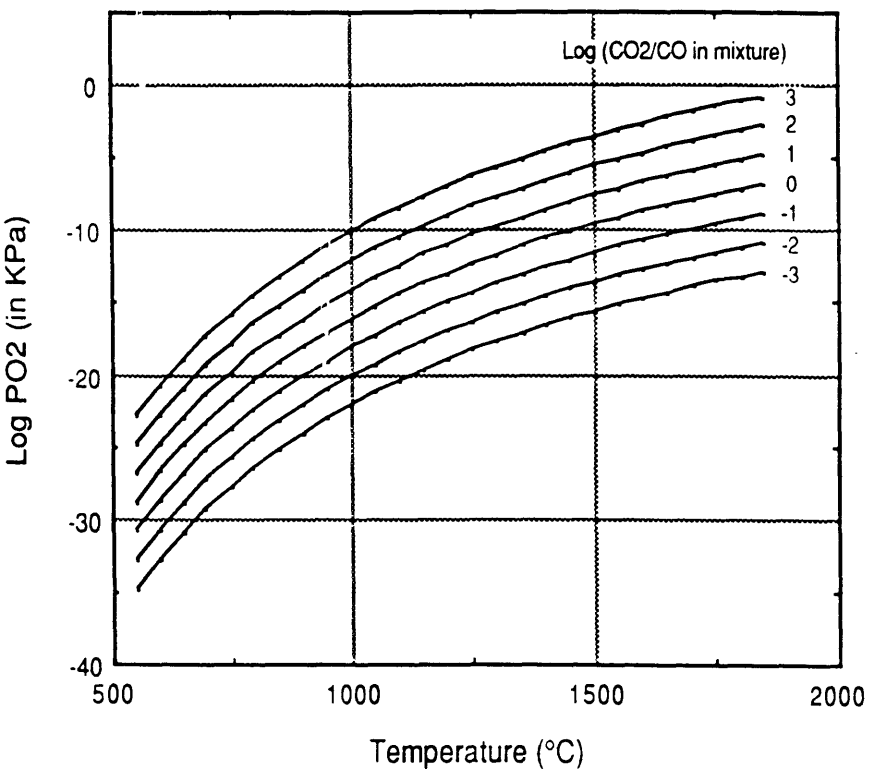

Figure 3-12: Oxygen partial pressure as a function of temperature for a range of CO/CO_2 mixtures.

technique which could measure small diffusion profiles as well as be able to distinguish between different isotopes of oxygen was necessary. Secondary ion mass spectroscopy (or SIMS) is well suited for this type of analysis. SIMS is a combination of two processes, ion beam sputtering and mass spectroscopy. Analysis is accomplished by bombarding the sample surface with energetic, moderate to high mass particles. As a result surface atoms become dislodged and are ejected as secondary particles. These secondary particles are directed to the mass spectrometer where they are sorted according to mass and counted. In the sputtering process surface atoms are "peeled off" virtually layer by layer. This is the reason for the technique's high depth resolution (on the order of a few tens of angstroms). This feature makes the measurement very short diffusion profiles quite routine. The mass analysis capability means that it can easily distinguish among different elements or different isotopes of the same element. This makes it quite useful in studying diffusion in general and oxygen self-diffusion in particular since as just mentioned only stable oxygen isotopes can be used in oxygen self diffusion experiments. For these reasons SIMS was chosen as the technique to use to obtain oxygen diffusion profiles in this study.

3.5.1 Principles of Operation

As mentioned previously SIMS is a combination of two techniques, mass spectroscopy and sputtering. Mass spectroscopy is a well understood analytical technique and will not be discussed further here. The phenomenon of sputtering is less well understood. It was Sir J. J. Thompson who first identified the effect in 1910 when he observed the emission of positive secondary ions by a metal surface in a discharge tube which had been bombarded by "primary" ions. [101] The mechanics of the sputtering process are fairly well agreed upon. A sample surface is bombarded by a beam of energetic particles (ions, neutral atoms, electrons, or photons). When this primary beam impinges on the sample primary particles impact the surface, penetrate it, and eventually are brought to rest, initiating a myriad of collisions between atoms in the near surface region. Incident primary particles can displace lattice ions to a depth of 10-25 nm [101] causing collision cascades. If a cascade reaches the surface the emission of

secondary particles (sputtering) may result. These particles may be electrons, ions, neutral atoms, and / or atomic / ionic clusters. Most of the energy of the primary particles is lost through hard sphere atomic collisions subsequent collision cascades, (this is termed nuclear stopping) though some energy is lost to electronic excitations. These excitations are non collisional and inelastic and drain energy from the primary particle continuously from the time it penetrates the surface until it comes to rest. This is called electronic stopping. In conductive materials the electronic excitation energy will immediately be dissipated as heat as the excited electrons return to the ground state. In insulators, however, the lifetimes of the excited states may be long enough to cause some atomic motion, introducing an electronic contribution to the total sputter yield. Nonetheless most models of sputtering only take into account the hard sphere elastic collisions (knock-on sputtering). The theory of knock-on sputtering is primarily due to Sigmund. [102] Three types of knock on sputtering have been proposed. Single knock-on or prompt sputtering, depicted in figure 3-13, involves, as the name implies, direct impact between the incident particle and the sputtered particle. Slow collisional sputtering occurs due to the collision cascade caused by the incident particle, reaching the surface (see figure 3-14). It happens on a small scale spatially and is thought to be the process which causes the majority of sputtering. Slow thermal sputtering also results from the motion of atoms in the cascade, but it occurs on a longer timescale (10^{-12} seconds after primary impact as opposed to 10^{-14} seconds for collisional sputtering and 10^{-15} seconds for prompt sputtering). It also occurs over a larger volume. It is not thought to be a major contributor to the total sputter yield. The actual sputtering rate, defined as the number of secondary particles removed per primary particle, varies from about 0.1 to 10 and depends on several factors, the most obvious of which is, of course, the material being analyzed. Sputter yields do vary by a factor of three to five throughout the Periodic Table for elemental solids and are related to the surface binding energies of the elements. In the case of this study, however, the material to be analyzed is not a variable, hence this effect will not be discussed further. Sputtering rate increases, not surprisingly, with primary beam energy and primary particle mass. It is also a function of impact

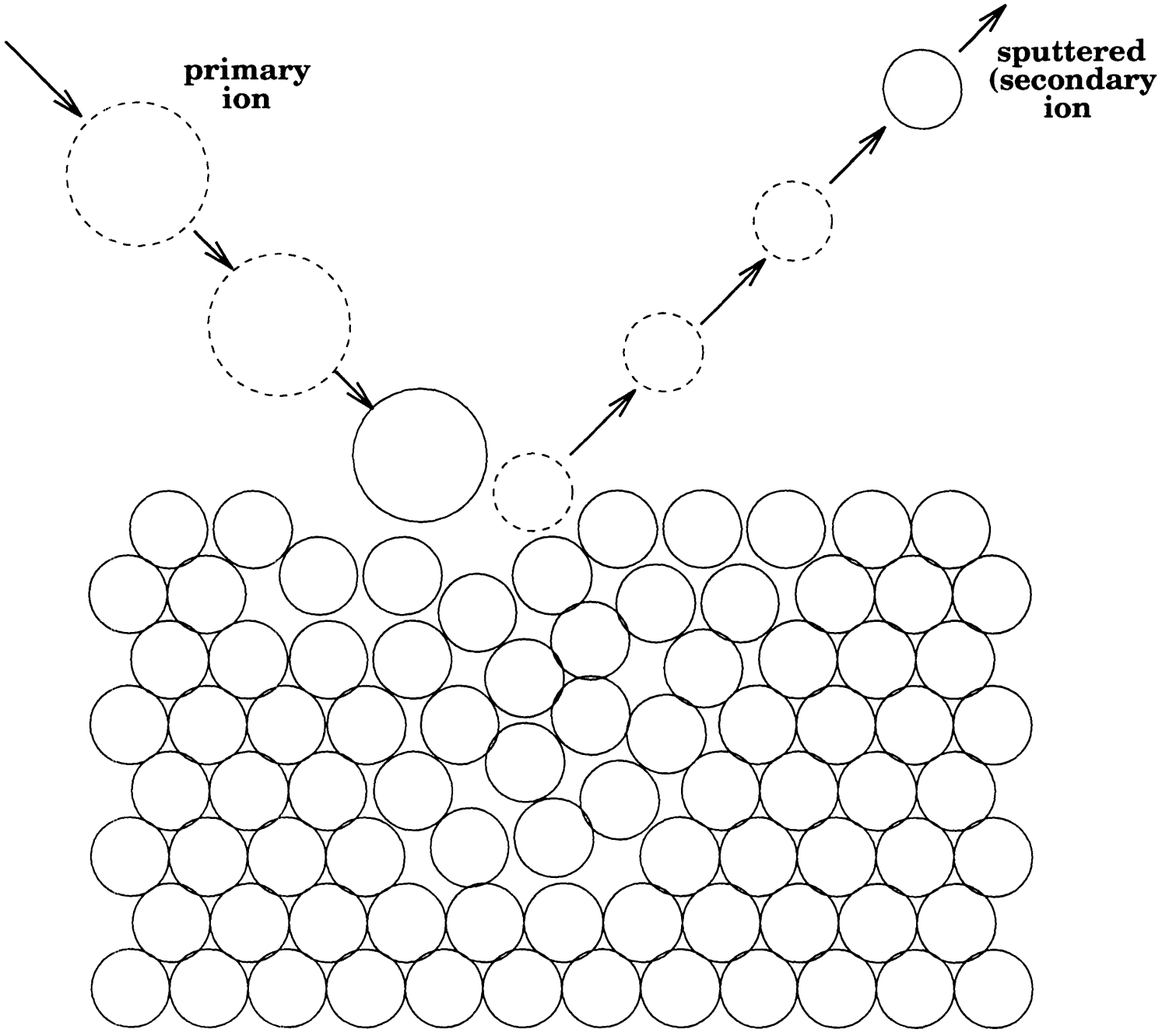

Figure 3-13: Depiction of atomic collisions in single knock-on (prompt) sputtering.

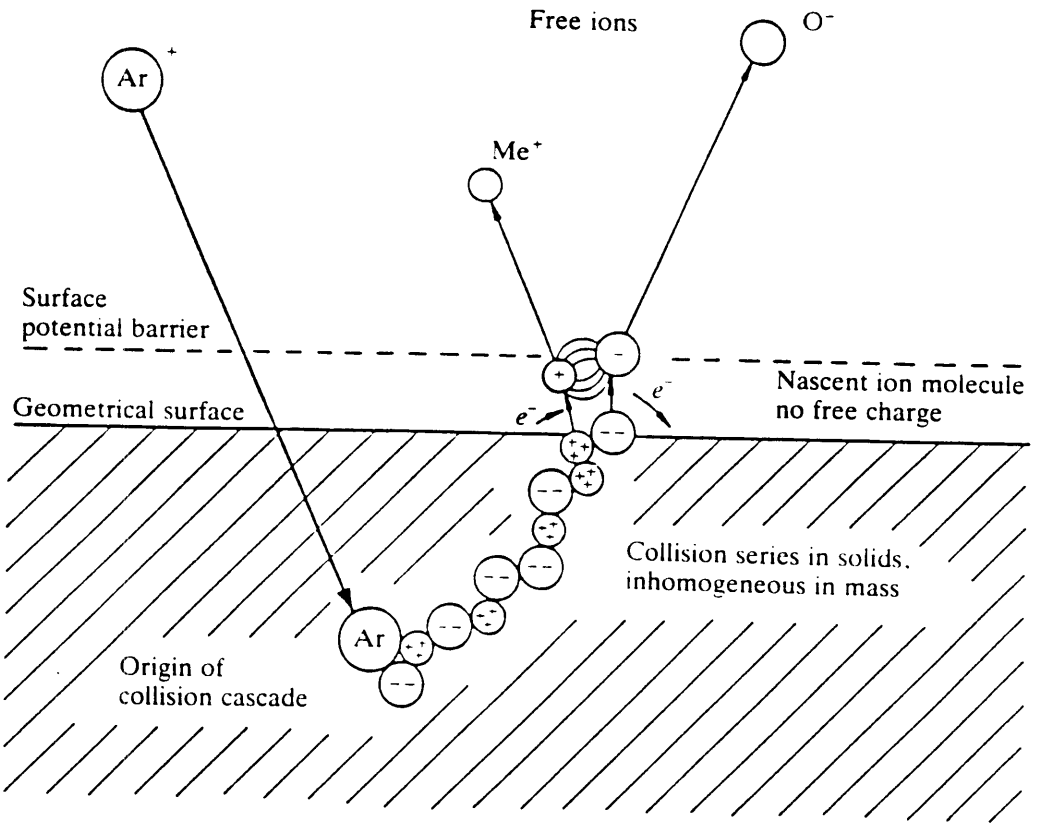

Figure 3-14: Sputtering as a result of a collision cascade (slow collisional sputtering), from Vickerman.

angle, reaching a maximum around 70° to the surface normal presumably due to the fact that most of the impact is felt by atoms close to the surface. It has also been observed in insulating samples that the sputter yield is larger when the primary particles are ions rather than neutrals. Crystal orientation also has an effect on yield. Close packed surface planes can yield twice to thrice as much as non-close packed planes at optimum incident particle energies.

3.5.2 Experimental

The secondary ion mass spectrometer at MIT (VG IX70S, VG/FISIONS Ltd.; Manchester, UK), depicted in figure 3-15 offers three distinct primary ion species $^{16}O_2^+$, $^{67}Ga^+$, and $^{133}Cs^+$. Naturally the oxygen beam could not be used as that is the species being analyzed and this would totally distort the ratio of isotopes being measured. In this study both Ga^+ and Cs^+ were used as primary species. Both produced satisfactory concentration profiles; Cs^+ was chosen early on, however, to do all the subsequent depth profiling for the sake of consistency as well as for other reasons which will be discussed shortly. In this study the beam parameters were as follows, beam energy 10KeV, total current 2.5 nA, impact angle 60° to the surface normal (this is a machine parameter and cannot be varied). Depth profiles were obtained by rastering the beam over a 25 μm $\times$ 50 μm area on the sample surface. This corresponds to a magnification of 500 $\times$ in the imaging mode. Grain boundary diffusion profiles were obtained by scanning an area centered on the grain boundary. This was more easily said than done, as it was often difficult to locate the grain boundary with the primitive optics of the SIMS. Even boundaries which were easily visible in a light microscope or by the naked eye were often difficult to find under the illumination of the SIMS probe. A technique that was developed to remedy this situation was to stagger the MgO crystals prior to hot pressing. The resultant discontinuity would serve as a marker as to the location of the grain boundary. Other tricks such as tilting the sample stage (so as to get views from different angles) as well as scoring the sample surface with a carbide pencil (far from the area to be analyzed of course) were also tried. The boundary was eventually located in almost every case, with the

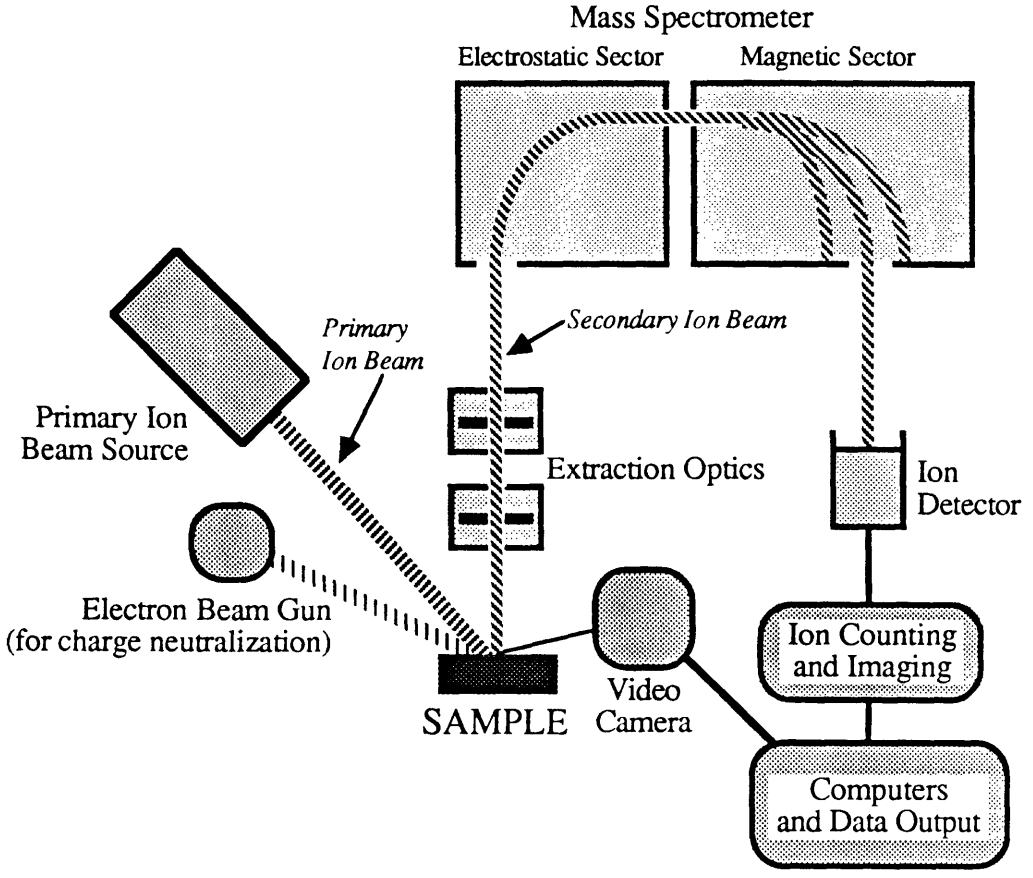

Figure 3-15: The VG IX70S secondary ion mass spectrometer, after Semken

aid of these techniques as well as a lot of trial and error and patience. Scans were performed with the beam oriented such that the long dimension of the crater was parallel to the grain boundary. This was done so as to maximize the contribution to the overall concentration profile by the grain boundary. Further steps needed to be taken, though so that the grain boundary contribution to the overall profile was not lost in the background. To that end the secondary ion signal was gated to the central 2 percent of the rastered area. The gate is a mechanical aperture which physically restricts all but the the central part of the secondary ion signal from entering the detector. These considerations reduced the total analyzed area to less than 1 μm on each side of the boundary. This is still much larger than the dimension of the grain boundary which is presumably only a few atomic spacings wide, but was sufficient to obtain profiles which clearly contained enhancement due to the grain boundary. The procedure for the extraction of the grain boundary diffusivities from these profiles is discussed in another section. Bulk diffusion profiles were obtained by sputtering at a location at least 50 μm removed from the grain boundary. Values for beam magnification and gate reduction are not nearly as important as in scanning the grain boundary. A gate is still recommended to obviate edge effects such as reprecipitation along crater walls and detection of material sputtered from shallower depths, as well as to make crater depth measurement as accurate as possible. For the sake of consistency the same beam parameters were used as in scanning the grain boundary.

In the analysis of conductive materials these are the only factors that need to be considered. The species to be detected can be selected and the analysis can proceed. In the analysis of insulating materials, however, there is another factor to consider. Bombarding an insulating material with a positive ion beam will result in the buildup of a positive charge on the sample surface. If not neutralized the charge will interfere with the emission and detection of secondary species. Positive ions will be given further energy, accelerating them beyond the point where they can be captured by the analyzer. In the case of negative secondary ions (such as oxygen) emission will be suppressed or completely inhibited. One might argue that in the case where only one species is being scanned for (as is the case in this study) this suppression should

not make a difference. The number of ions which make it through to the detector should be proportional to the amount of said ion in the sample at a particular depth which is fine for the analysis to be performed in this study (for the computation of diffusivities on the ratios of the concentrations of the oxygen isotopes are necessary not the absolute values). Unfortunately the process of charging is a dynamic one. The surface is initially uncharged, charges as it is exposed to the ion beam until it reaches a critical point where the charge is dissipated through arcing to ground, indicated by a bright flash on the crt in imaging mode. The process then begins again. As a result profiles obtained from charged samples are unusable for any type of quantitative analysis. See figure 3-16 for an example of such a profile.

Thus surface charge must be eliminated before analysis can be done. This can be done in one of two ways. The first is to avoid it altogether by using a neutral species to bombard the sample surface. The other method, and the one used in this study, is to neutralize the surface charge by concurrent electron bombardment of the sample surface. The VG IX70S is equipped with an electron gun, which was used in obtaining all concentration profiles. In order to effect charge neutralization the electron beam must be focused onto the same spot as the ion beam and the accelerating potential and total beam current must be optimized; more is not always better. This is a tedious process which invariably takes as long as the analysis itself, and must be done for each sample analyzed, though in practice the first is always the most difficult. Fortunately once the procedure has been accomplished for a particular sample it is usually not necessary to readjust the parameters each time a different spot on the sample is to be scanned. Beam parameters for the electron gun did vary somewhat from sample to sample and from day to day but generally fell into the following ranges: accelerating potential 8-10 kV, total beam current 10 - 15μamps. The procedure for focusing the electron beam is highly machine specific and not worth discussing in detail. Furthermore, in order to be able to view the sample inside the analysis chamber the surface must be grounded, else the constant charging and discharging interferes with the image displayed on the crt, making it useless. This occurs due to the fact that in imaging mode the beam is rastered over a much

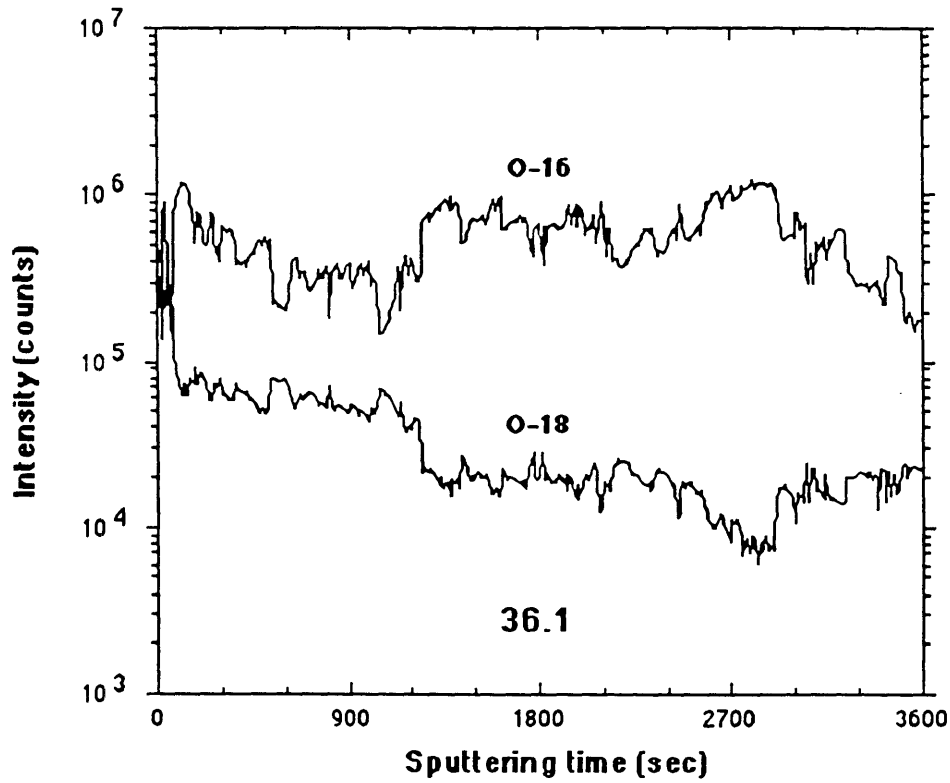

Figure 3-16: SIMS diffusion profile obtained without the use of surface charge neutralization.

larger area than during analysis so the resultant charge buildup would not be fully compensated by the electron beam. To accomplish this grounding, a coating of gold was applied to the samples before loading into the SIMS. Coating was done by means of thermal evaporation in vacuum. Typical coatings were 100 - 300 Å thick. These proved sufficient to be able to view the samples in the analysis chamber. In imaging mode the beam erodes the surface at a very slow rate so the gold coat remains intact throughout the analysis. In analysis mode the beam erodes the gold coat at the point of analysis in a matter of seconds thus introducing only a small error in the measurement of crater depths. These techniques combined to eliminate the problem of charging for the MgO samples. Profiles could then be obtained.

As mentioned earlier profiles were obtained by sputtering at the desired location; secondary ions were extracted by a 6 kV potential and focused electrostatically into a beam which was directed into the magnetic-sector mass spectrometer. The ions were sorted by mass by means of a tunable magnetic field. The detector was programmed to scan for masses 16 and 18 corresponding to $^{16}0$ and $^{18}0$. Of course being a mass spectrometer only a mass value can be tuned; the detector is oblivious to the chemical nature of the species it is detecting. Thus it cannot tell the difference between, say, a ^{16}O ion and a ^{15}OH radical or between a ^{18}O ion and a ^{17}OH radical. It is common for clusters such as OH^- to be ejected as a single secondary particle. This is potentially a problem for a hygroscopic material such as MgO, but as ^{15}O is nonexistent and $^{17}0$ has a miniscule natural abundance of 0.038% this did not prove to be a problem in practice. The cycle time for analysis was approximately 10 seconds; each of the two masses were counted for five seconds and the intensities are stored along with the sputter time as ordered pairs in the RAM of the CPU. These can later be downloaded in ascii format for computational analysis.

The sputter time is stored because the SIMS itself does have the capability to measure crater depths during sputtering. The sputtering rate for a given material in a given orientation for a given set of primary beam parameters must be determined experimentally. It has been shown that for a chemically homogeneous material the sputtering rate is roughly constant for a primary beam of constant energy and current

density [101]. Using the same magnification for each measurement ensured this. As grown epitaxial crystals were too rough to be used in crater measurements, so instead a (100) oriented MgO single crystal which had been polished optically flat was used instead. It was assumed that the lack of isotopic enrichment would not affect the sputtering rate. Using the same beam parameters as during analysis four craters were sputtered for durations of 10, 20, 30, and 40 minutes. This gives 5 data points with which to determine the sputtering rate (using (0,0) of course). Crater depths are typically measured by interference microscopy or surface profilometry. In this study a surface profilometer was used (*Dektak 8000*, Sloan Technology Corporation; Santa Barbara, CA). As MgO tends to hydrate, measurement was done as soon as the crystal was removed from the analysis chamber. Depth measurements were done along the long and short axes of the craters along a path which approximately bisected them. All the measured profiles are shown in figures 3-17, 3-18 For each scan the depth was taken to be the integrated average of the depths at each point where a measurement was recorded, within the central part of the crater where it was the flattest. The averaged region is shown by the shaded areas in the figure. For each sputter duration the depths measured in both directions were averaged to give the depth used in computing the sputtering rate. As can be seen they did not differ by much (as was hoped). A plot of crater depth vs. sputter time is shown in figure 3-19. Fitting a line to these points yields the equation

$$\text{depth} = 2.422 \times \text{time} - 60.4 \text{ Å}$$

with a Pearson linear correlation coefficient of 0.99. Thus a sputtering rate of 2.422 Å/sec was used to convert sputter times into depths.

3.6 Transmission Electron Microscopy

Bicrystals for TEM analysis were prepared by coarse grinding with abrasive SiC and Al_2O_3 paper to a thickness of 100 - 125 μm, followed by fine polishing and dimpling with 1 μm diamond paste down to a thickness of roughly 30 μm. All grinding and

polishing was done on the substrate side of the bicrystal. The samples were then thinned to electron transparency by Ar^+ ion milling from both sides at an angle of 12° to perforation, followed by further milling at 15° to increase the area possible for analysis. Milling had do be done from both sides to prevent redeposition of milled material on the side not being milled. The samples were analyzed in a 200 keV ISI-Akashi EM-002B transmission electron microscope; the analysis being done by Dr. I. Guillermo Solorzano.

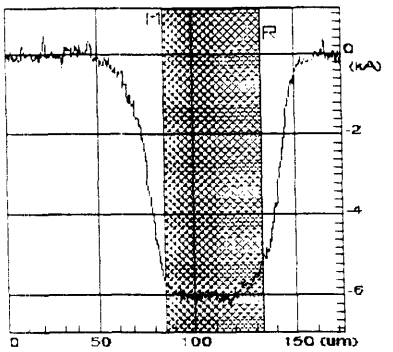


```
DEKTAK 8000  Version 3.00.1
PROGRAM NAME: CALSTD.mp
DESCRIPTION: calstd
SCAN ROUTINE #: 1
TIME  OF  SCAN: 20:04:00 Tue Nov 23 1993
DATA FILE NAME: c:\dektak\data\mapdata.001
Scan ID........ 1123
Location....... 93212um,170983um,-97.129997
Scan Length.... 173um
Resolution..... 0.012 um/sample
Stylus Force... 20mg
R. Cursor...... -5018A @ 133.66um
M. Cursor...... -5615A @ 85.52um
*Vert. Delta... -597A
Horiz. Delta... -48.14um
Filters........ No
ANALYTIC FUNCTIONS:        R:(um); M:(um)
Avg_ht =    -5895A         133.66     85.52
```

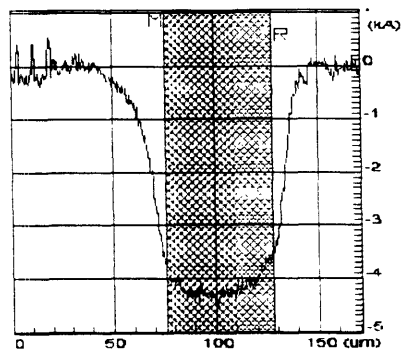


```
DEKTAK 8000  Version 3.00.1
PROGRAM NAME: CALSTD.mp
DESCRIPTION: calstd
SCAN ROUTINE #: 1
TIME  OF  SCAN: 19:55:32 Tue Nov 23 1993
DATA FILE NAME: c:\dektak\data\mapdata.001
Scan ID........ 1123
Location....... 93166um,170816um,-97.129997
Scan Length.... 171um
Resolution..... 0.011 um/sample
Stylus Force... 20mg
R. Cursor...... -3551A @ 128.25um
M. Cursor...... -3931A @ 76.27um
*Vert. Delta... -380A
Horiz. Delta... -51.98um
Filters........ No
ANALYTIC FUNCTIONS:        R:(um); M:(um)
Avg_ht =    -4161A         126.31     76.76
Avg_ht =    -4138A         128.25     76.27
```

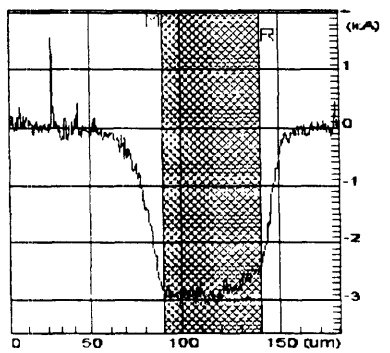


```
DEKTAK 8000  Version 3.00.1
PROGRAM NAME: CALSTD.mp
DESCRIPTION: calstd
SCAN ROUTINE #: 1
TIME  OF  SCAN: 19:48:47 Tue Nov 23 1993
DATA FILE NAME: c:\dektak\data\mapdata.001
Scan ID........ 1123
Location....... 93151um,170709um,-97.129997
Scan Length.... 181um
Resolution..... 0.012 um/sample
Stylus Force... 20mg
R. Cursor...... -2388A @ 140.22um
M. Cursor...... -2896A @ 89.99um
*Vert. Delta... -508A
Horiz. Delta... -50.24um
Filters........ No
ANALYTIC FUNCTIONS:        R:(um); M:(um)
Avg_ht =    -2801A         140.22     89.99
```

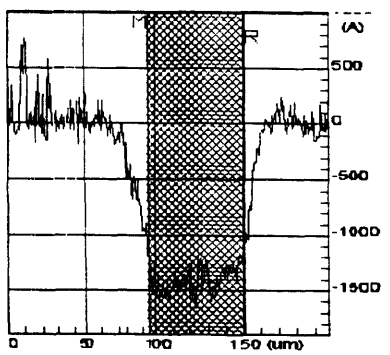


```
DEKTAK 8000  Version 3.00.1
PROGRAM NAME: CALSTD.mp
DESCRIPTION: calstd
SCAN ROUTINE #: 1
TIME  OF  SCAN: 19:42:22 Tue Nov 23 1993
DATA FILE NAME: c:\dektak\data\mapdata.001
Scan ID........ 1123
Location....... 93145um,170601um,-97.129997
Scan Length.... 198um
Resolution..... 0.013 um/sample
Stylus Force... 20mg
R. Cursor...... -1196A @ 149.44um
M. Cursor...... -1306A @ 93.94um
*Vert. Delta... -110A
Horiz. Delta... -55.50um
Filters........ No
ANALYTIC FUNCTIONS:        R:(um); M:(um)
Avg_ht =    -1414A         146.63     18.44
Avg_ht =    -1396A         149.44     13.94
```

Figure 3-17: Crater depth profiles obtained using Dektak 8000 profilometer

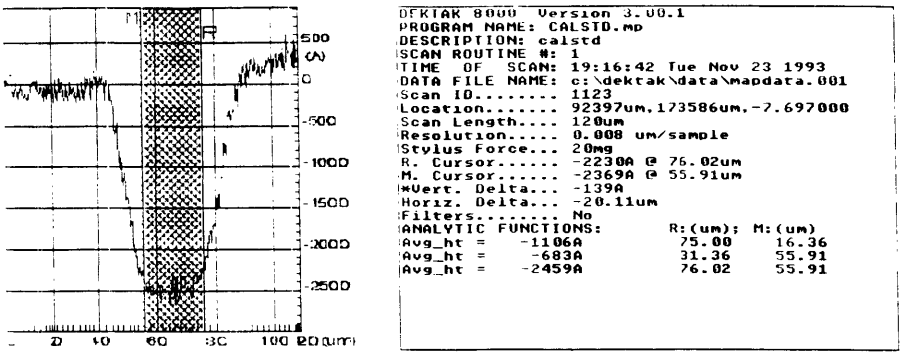

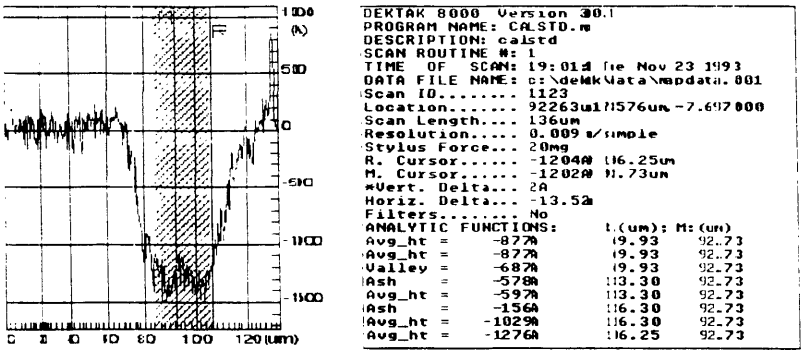

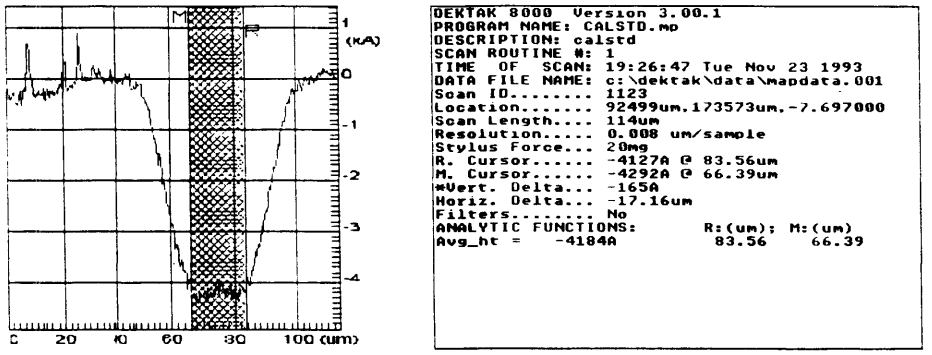

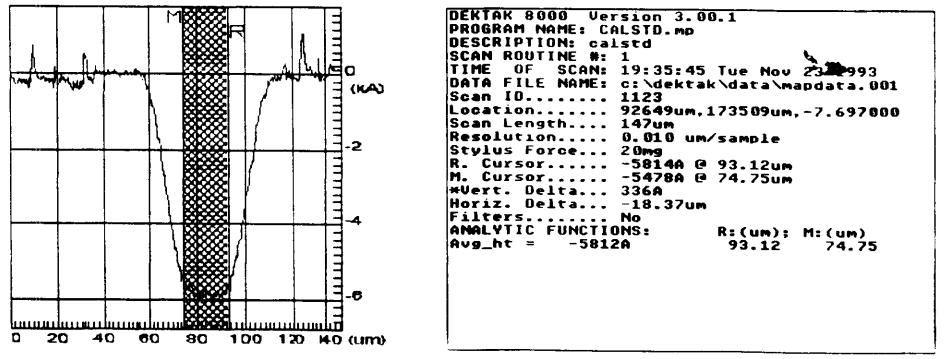

Figure 3-18: Crater depth profiles obtained using Dektak 8000 profilometer, continued

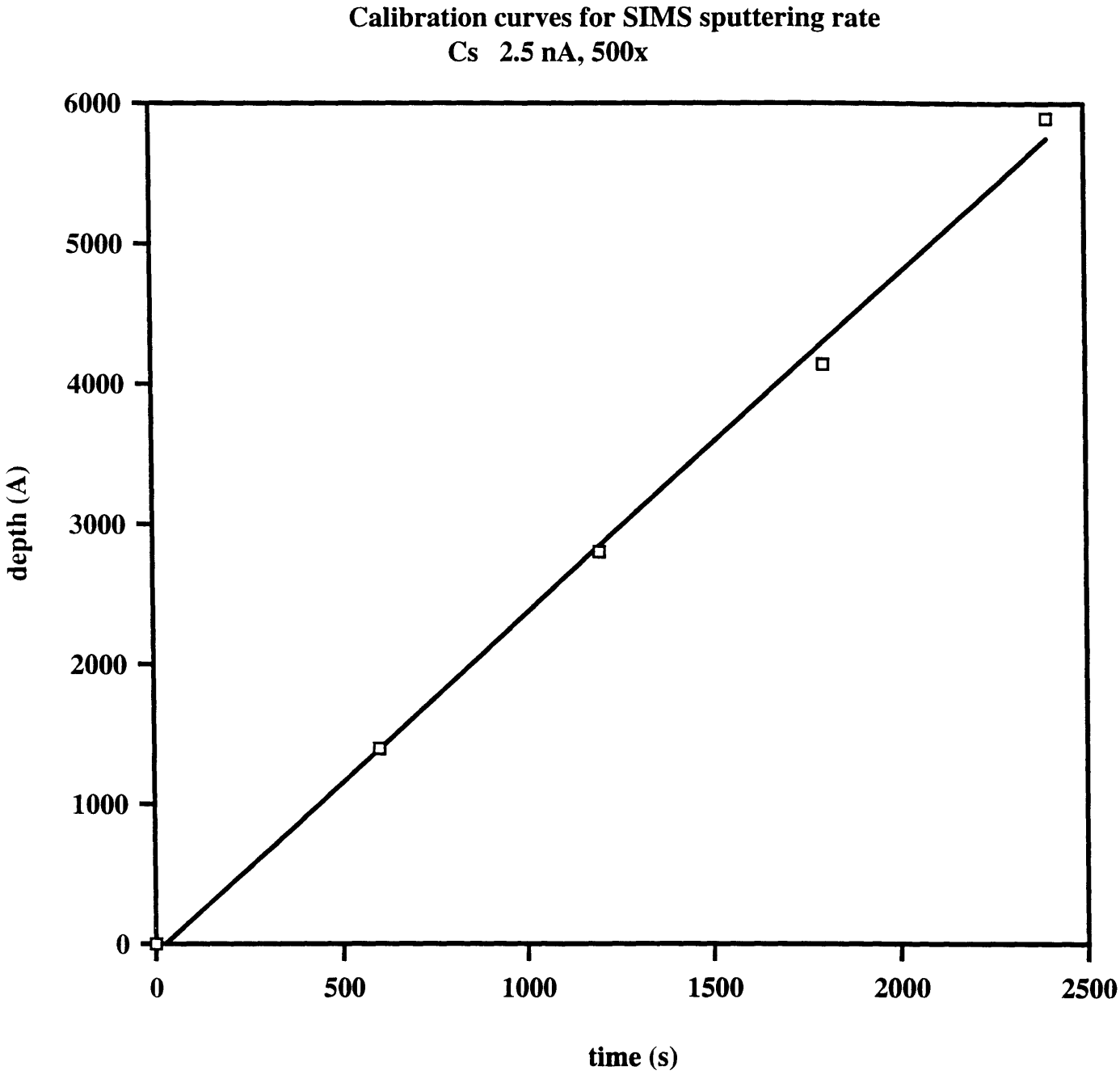

Figure 3-19: Measured crater depths as a function of sputtering time for determination of sputtering rate

Chapter 4

Results and Discussion

4.1 Bulk diffusion of Oxygen

Bulk diffusion coefficients of oxygen in MgO were determined both as a function of temperature and of oxygen partial pressure. Bulk diffusion profiles were obtained as a function of temperature from 1250 - 1500°C from bicrystal specimens annealed in air. Bulk profiles were obtained by sputtering far from the grain boundary. These values, aside from aiding in determining the mechanism of bulk diffusion, are necessary in the computation of the grain boundary diffusion coefficients as has been discussed previously. The fraction of ^{18}O, ^{18}C(x), should vary as follows as a function of depth, x:

$$\frac{^{18}C(x) - ^{18}C_s}{^{18}C_s - ^{18}C_b} = \mathrm{erf}\frac{x}{\sqrt{4Dt}}$$

where $^{18}C_s$ is the fraction of ^{18}O at the surface, equal to the atmospheric concentration of ^{18}O, 0.00204; $^{18}C_b$ is the fraction of ^{18}O in the bulk of the crystal which is roughly 0.3. The bulk fraction of ^{18}O, ^{18}C was computed by dividing the SIMS signal intensity in counts for the ^{18}O isotope by the sum of the signal intensities for the ^{16}O and ^{18}O isotopes. Thus a plot of ^{18}C(x) as a function of depth would be erf-like. A plot of ^{18}C(x) versus depth is shown in figure 4-1 for the bicrystal annealed at 1300°, 72 hours. It is indeed erf-like. Diffusivity is computed by plotting the quantity $\mathrm{erf}^{-1}[\frac{^{18}C(x)-^{18}C_s}{^{18}C_s-^{18}C_b}]$ as a function of depth. A linear plot is thus obtained whose slope is equal to $\frac{1}{\sqrt{4Dt}}$.

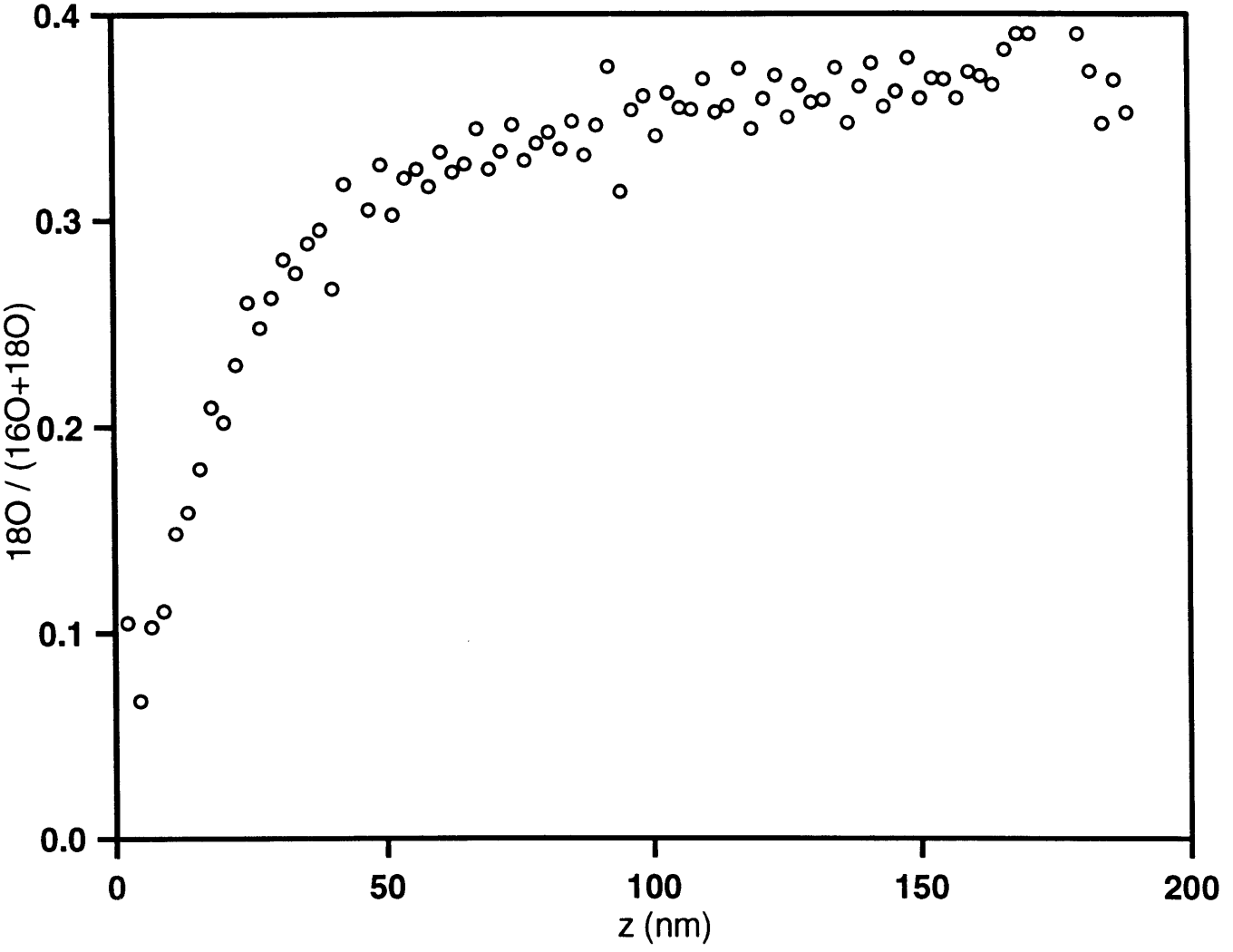

Figure 4-1: Sputter depth profile of $^{18}C(x)$ versus depth in bulk region of bicrystal annealed at 1300°, 72 hours.

Such a plot for the 1300°C data is shown in figure 4-2. Knowing the slope and anneal time, D is easily calculated. An Arrhenius plot of the data from 1250 - 1500°C is given in figure 4-3. Fitting the diffusivities to an Arrhenian type relation for temperature dependence by least-squares regression yields:

$$D = 2.9 \times 10^{-4} \exp \frac{-4.0eV}{kT} \quad \frac{\text{cm}^2}{\text{sec}} \qquad 1250 - 1500°C$$

The 4.0eV activation energy agrees well with the more recent studies of oxygen diffusion (Dolhert 3.45eV, Roshko 3.97eV Yoo 3.24eV) considering the limited temperature range over which measurements were performed. In fact, if one considers the data of Yoo between 1300 - 1500°C only, and does a linear fit to that data, the Arrhenian relation for the temperature dependence of the diffusivity, D = 4.8×10^{-4}exp(-4.0eV/kT) cm^2/s, is in excellent agreement with the present results. This suggests that the CVT technique reproducibly produces crystals of high quality and comparable high purity. Figure 4-4 presents a comparison of the diffusivities obtained in some of the more recent studies. The similarity of the results is not surprising as the crystals used in these studies were all of high purity (in the bulk at least).

The effects of oxygen partial pressure were also investigated by annealing several single crystal specimens at a fixed temperature (1500°C) in various CO/CO_2 gas mixtures. The following fractions of CO/CO_2 were used: 100/1, 1/1, and 1/100 as well as air. Corresponding oxygen partial pressures range from roughly 10^{-12} kPa to 22kPa. Analysis of the isotopic gradients was identical to that used for the analysis of the air-annealed single crystals. A plot of the diffusivities obtained as a function of partial pressure is shown in figure 4-5. A summary of the bulk diffusivities obtained for the temperature range 1250 - 1500°C is shown in table 4.1 Fitting a line to the data obtained yield a partial pressure dependence of:

$$D \propto P_{O_2}^{0.11} \qquad 10^{-12} - 10^{+1} kPa \qquad 1500°C$$

In studies of this type, where the effect of oxygen partial pressure on material properties are measured, the samples should ideally be "pre-annealed" for relatively long

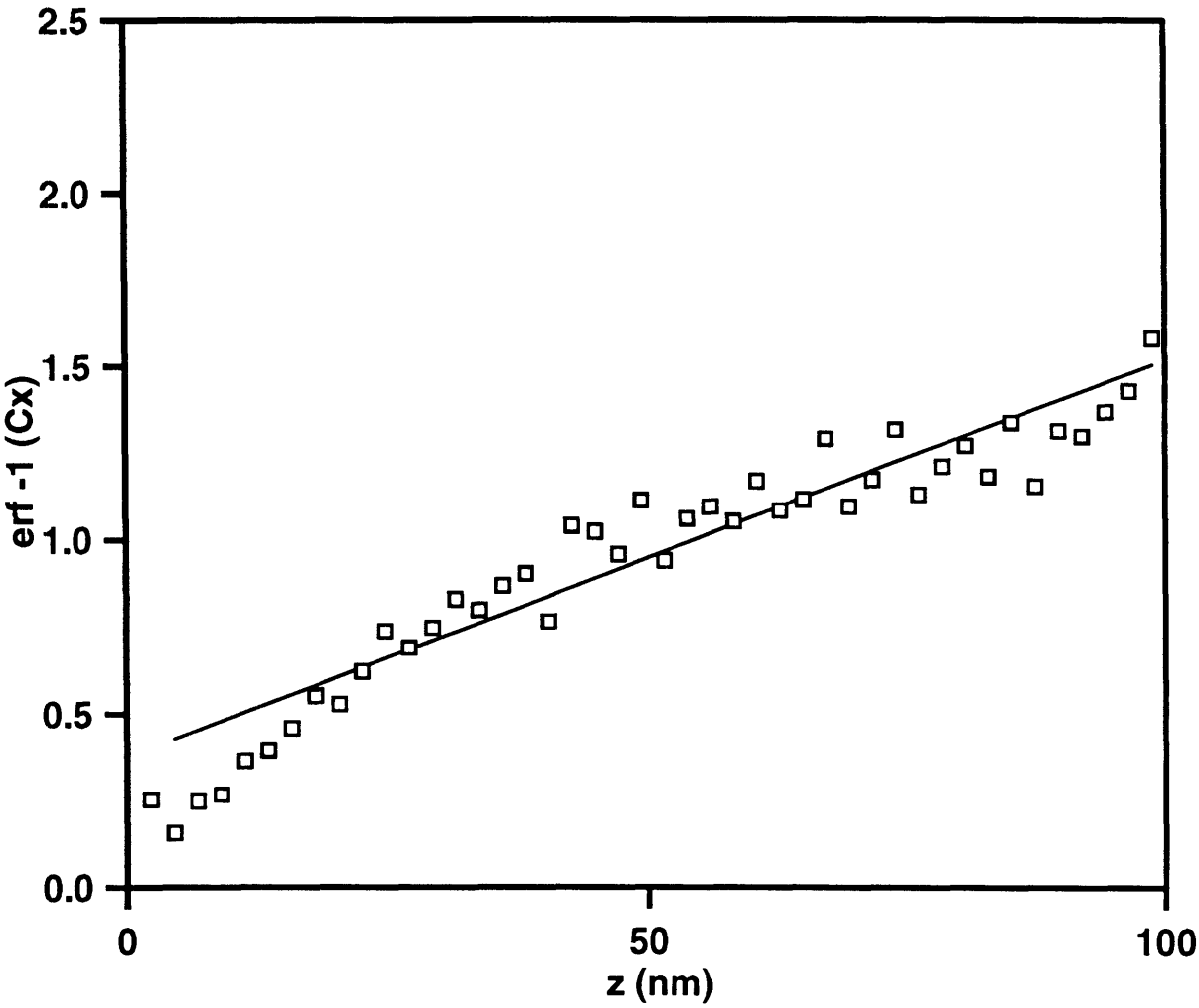

Figure 4-2: $\text{erf}^{-1}[\frac{^{18}C(x)-^{18}C_s}{^{18}C_s-^{18}C_b}]$ versus depth plot for slope determination.

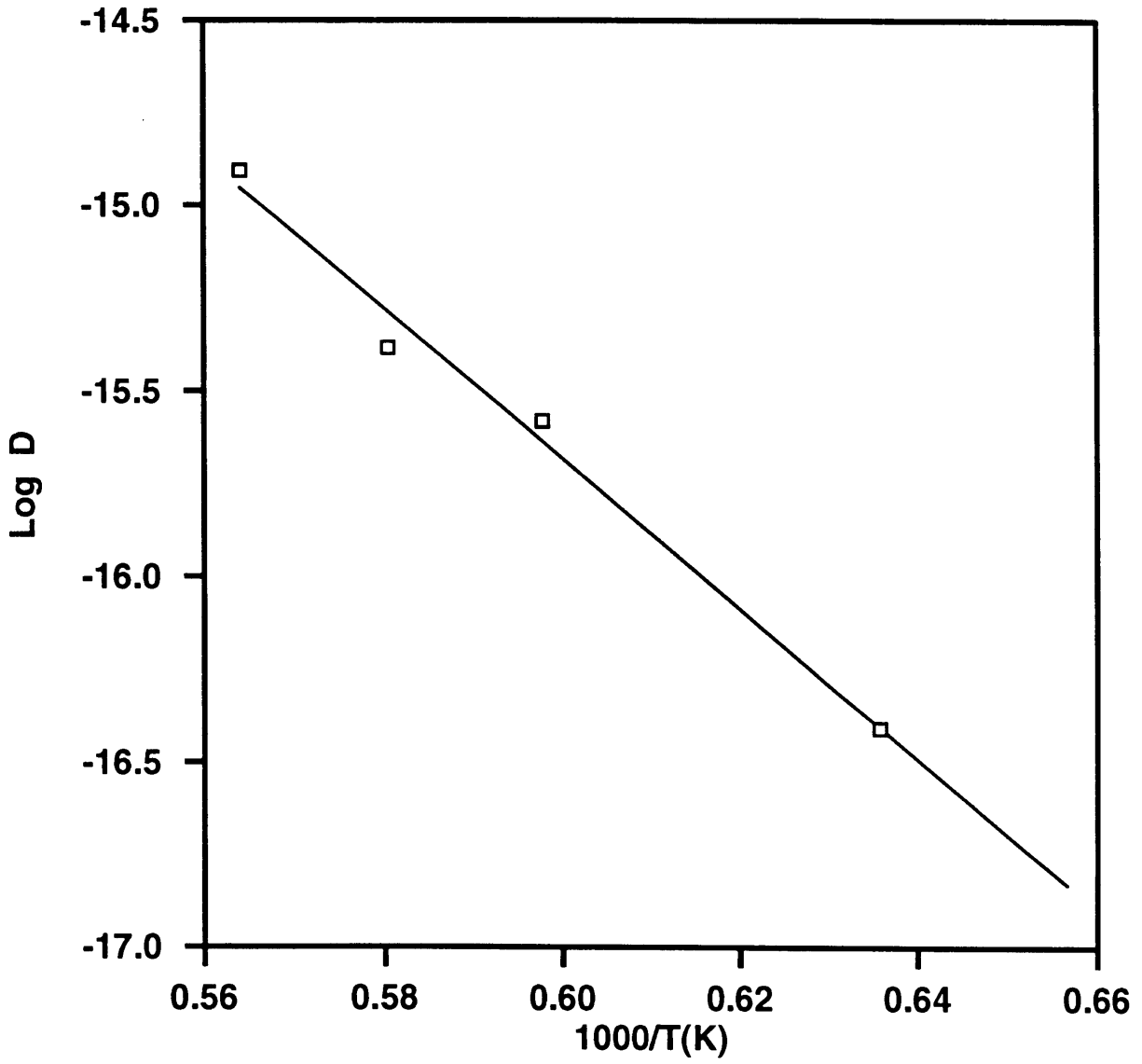

Figure 4-3: Arrhenius plot of D versus 1/T for oxygen bulk diffusion data.

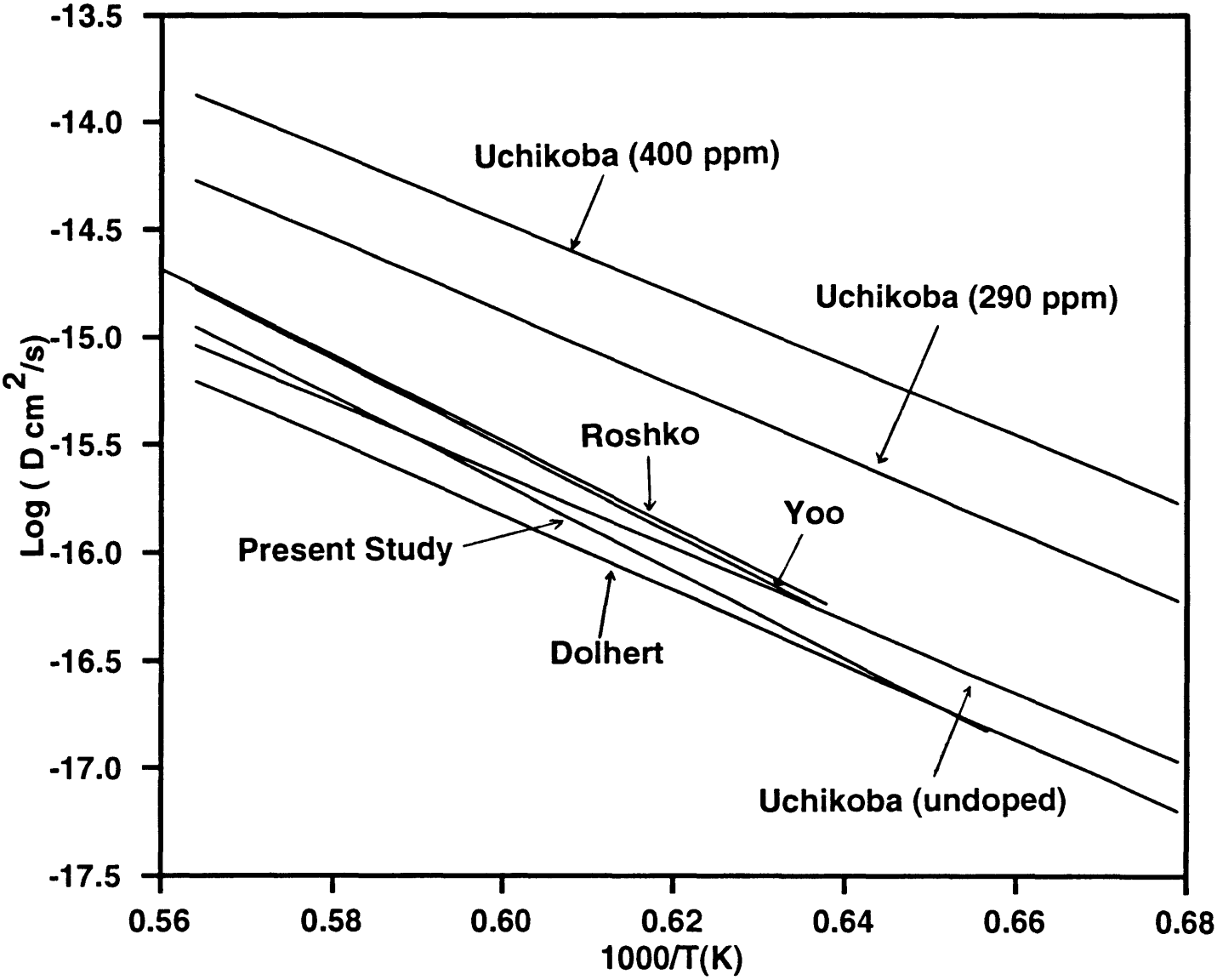

Figure 4-4: Comparsion of arrhenius plots for recent oxygen diffusion studies.

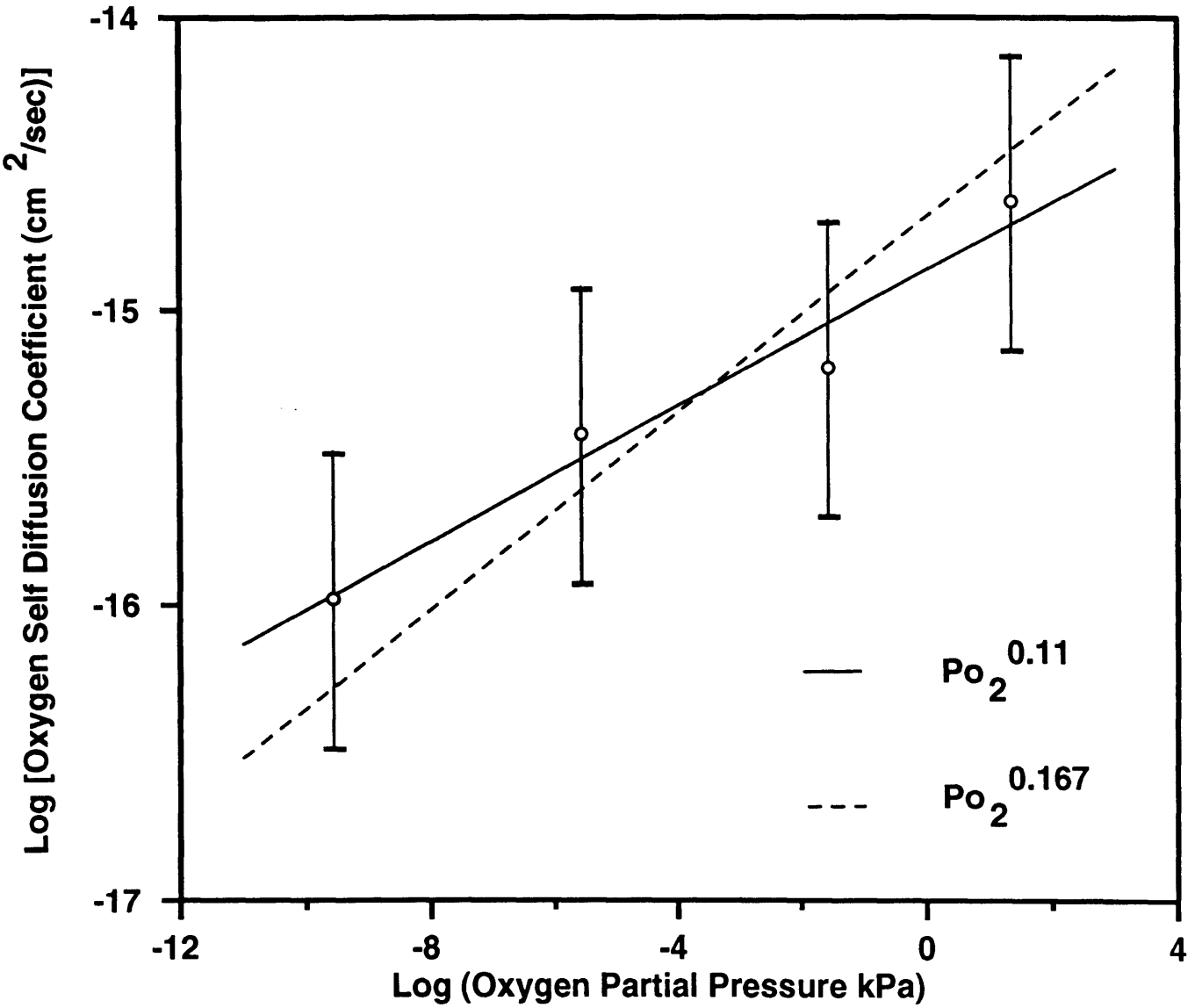

Figure 4-5: Partial pressure dependence of oxygen diffusivity in MgO at 1500°C.

D cm^2/s	T °C.	CO_2/CO
3.9×10^{-17}	1300	air
2.6×10^{-16}	1400	air
4.1×10^{-16}	1450	air
1.2×10^{-15}	1500	air
2.3×10^{-15}	1500	air
6.4×10^{-16}	1500	100/1
3.8×10^{-16}	1500	1/1
1.0×10^{-16}	1500	1/100

Table 4.1: Summary of bulk diffusion data.

times at the temperature and oxygen partial pressure of interest. This allows the defect structure to equilibrate to that characteristic of the partial pressure in question. This could not be done in this study as pre-annealing the specimens would cause them to be depleted of ^{18}O. Essentially a diffusion experiment would be going on. Instead, samples were heated to the anneal temperature in the flowing gas mixture. It is then valid to ask, "Is the diffusivity measured a true tracer diffusivity?". It is possible that it is a chemical diffusion coefficient and may reflect a change in the diffusivity of another species as a function of partial pressure. To answer this question it is useful to examine possible defect reactions associated with atmospheric equilibration. A likely process for equilibration of oxygen with the atmosphere is:

$$\frac{1}{2}O_2 \rightarrow V''_{Mg} + O_O + 2h^{\cdot}.$$

The reason this is the most likely process is that magnesium vacancies and holes have been shown to be the dominant ionic and electronic defects, respectively, in MgO whose defect structure is controlled by supervalent impurities [83, 103]. If equilibration takes place by diffusion on the magnesium sublattice then it is likely that the oxygen diffusivity measured by these experiments is very close to the tracer diffusivity. The reason is because magnesium diffusion is several orders of magnitude more rapid than oxygen diffusion. Results of this study and other studies of magnesium self-diffusion in MgO have shown the difference to be about three orders of magnitude

[104]. Oxygen diffusion thus is taking place in material which has already been equilibrated by the diffusion of magnesium and holes and by the associated Schottky and Frenkel equilibria which relate the magnesium and oxygen point defect concentrations. To illustrate this one can do a hypothetical double tracer experiment, simultaneously examining the relative penetrations of Mg and O tracer into MgO. This has been done in figure 4-6 for T = 1500°C, 10 minutes. Diffusivities used were as follows D_{Mg} = 5×10^{-12} cm^2/s [83], $D_O = 2\times10^{-15}$ cm^2/s from table 4.1. As can be seen from the figure the labeled Mg has already penetrated deep into the crystal after 10 minutes while the labeled oxygen has just barely begun to penetrate. The equilibration front is thus always far ahead of the diffusion front. The oxygen diffusion experiment can be considered as being done in material whose defect structure has been equilibrated to the ambient atmosphere. The oxygen diffusivity thus measured can be considered to be a tracer diffusivity within the limits previously discussed.

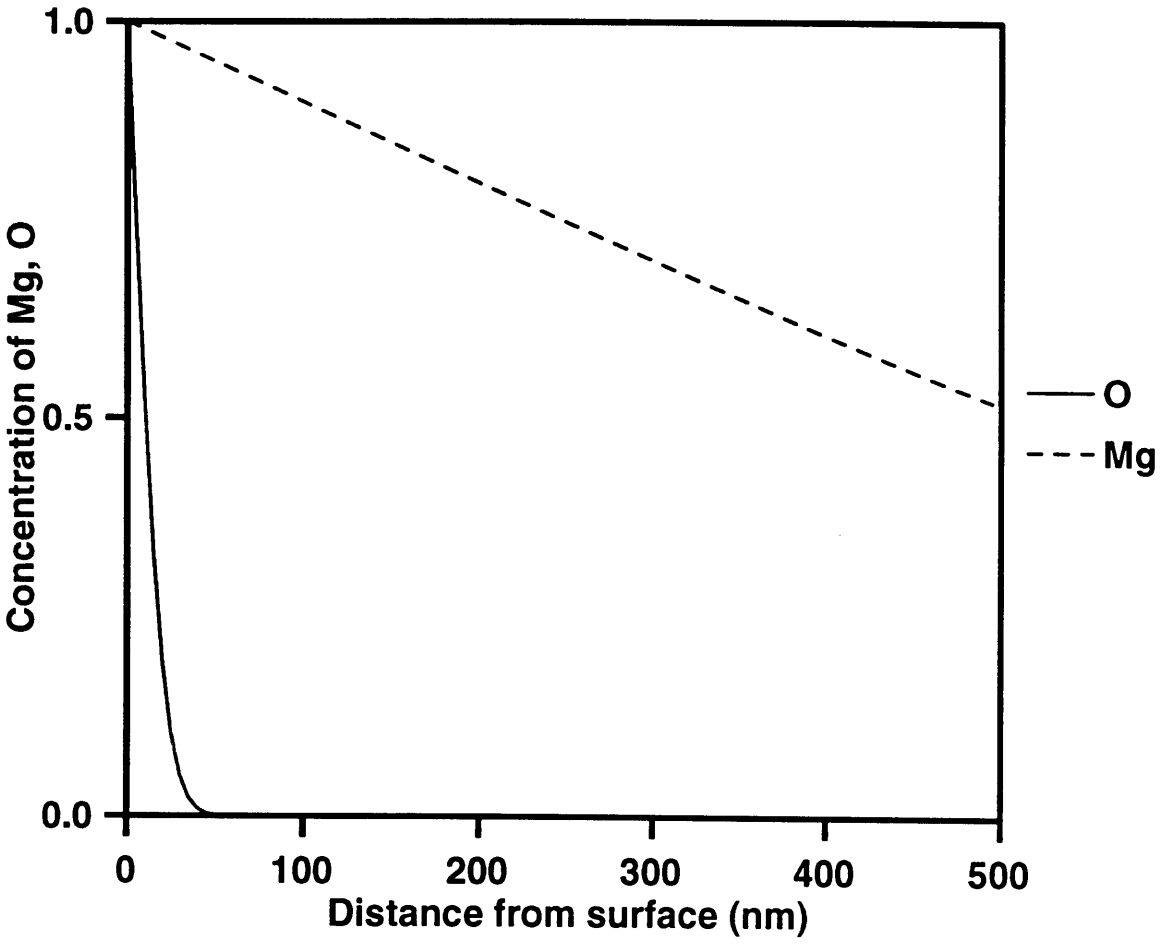

Figure 4-6: Comparison of relative penetration distances for Mg and O tracer (constant surface concentration) - 1500°C.

These results are difficult to interpret given the theoretical estimates of defect formation/association/migration energies listed in table 2.1. The two most plausible mechanisms for oxygen diffusion put forth to date have been the uncharged vacancy pair model of Ando et al. and the paired interstitial (peroxy center) model of Semken. Computed activation energies for the vacancy pair mechanism are closer to those measured experimentally although agreement is not particularly good with calculated activation energies for either mechanism. In the case of extrinsic MgO, where the magnesium vacancy concentration is determined by the aliovalent impurity content, the concentration of oxygen vacancies is depressed far below the intrinsic level by the Schottky equilibrium, as has been discussed. If the magnesium vacancy concentration has been fixed by the trivalent impurity concentration $[M_{Mg}^{\cdot}]$, where M is a trivalent cation,

$$M_2O_3 \overset{3MgO}{\rightarrow} 2M_{Mg}^{\cdot} + 3O_O + V_{Mg}'' \qquad [V_{Mg}''] = \frac{1}{2}[M_{Mg}^{\cdot}] \tag{4.1}$$

the concentration of oxygen vacancies is

$$[V_O^{\cdot\cdot}] = \frac{K_s}{[V_{Mg}'']} = 2\frac{K_s}{[M_{Mg}^{\cdot}]} = 2[M_{Mg}^{\cdot}]^{-1} \exp \frac{h_s}{kT}. \tag{4.2}$$

The formation of the vacancy pair is by the following quasi-chemical reaction:

$$V_{Mg}'' + V_O^{\cdot\cdot} \rightarrow (V_{Mg}'' V_O^{\cdot\cdot})^{\times}. \tag{4.3}$$

The concentration of the vacancy pairs would be given by the product of the formation and association reaction constants [86].

$$[(V_{Mg}'' V_O^{\cdot\cdot})^{\times}] = K_s \cdot K_a$$

Where K_a is the equilibrium constant for the divacancy association, equation 4.3, h_a is the enthalpy of association. Thus we can express the divacancy concentration as

$$[(V_{Mg}'' V_O^{\cdot\cdot})^{\times}] = \exp -\frac{h_s + h_a}{2kT}$$

The divacancy concentration would thus be insensitive to both aliovalent impurity content and oxygen partial pressure. The activation energy for this mechanism of diffusion would be equal to the sum of the activation energies for formation and association of the defects plus the migration enthalpy, $E_a = h_s + h_a + h_m$. Whereas the activation energy for diffusion by the aforementioned extrinsic oxygen vacancy mechanism would be $E_a = h_s + h_m$. Using the values of Mackrodt from table 2.1 the activation energy would be approximately be $E_a \approx 7.3$eV for the vacancy pair mechanism and 9.9eV for the extrinsic anion vacancy mechanism, which are considerably higher than the 3-4 eV obtained in recent diffusion studies (including the present work). The energy for the vacancy pair mechanism, though, does agree to within experimental error with the activation energy obtained by Flynn in his study of MBE grown MgO crystals. It is possible that this is the controlling mechanism in ultrahigh purity, though still extrinsic, MgO. The reasoning behind this is as follows. Even in ultrahigh purity MgO the concentration of Mg vacancies is still determined by the aliovalent impurity content. In conventional high purity MgO this is also the case but the aliovalent impurity content is higher, thus the Mg vacancy concentration will be higher, the free oxygen vacancy concentration will be lower due to the Schottky equilibrium and the free oxygen interstitial concentration will be higher due to the Frenkel equilibrium. At some critical value of aliovalent impurity concentration the concentration of free oxygen interstitials will become higher than that of divacancies which are insensitive to impurity content. At that point, the diffusion behavior, being controlled by the interstitial concentration, will no longer be independent of aliovalent impurity concentration or oxygen partial pressure as will be shown in the following discussion.

The preceding discussion is merely speculative. I will now focus on the experimental evidence that points toward an interstitial mechanism for oxygen diffusion in MgO. The value of 0.11 obtained in this study for the partial pressure dependence of oxygen diffusion might point to an intuitively obvious explanation of oxygen transport by an interstitial mechanism via one of the following processes. (1) incorporation of excess oxygen in the lattice on oxygen sites, with simultaneous creation of Mg vacancies and

holes:

$$\frac{1}{2}O_2 \rightarrow V''_{Mg} + O_O + 2h^{\cdot} \qquad K_p = \frac{[V''_{Mg}]p^2}{P_{O_2}^{\frac{1}{2}}}$$

$$p = 2[V''_{Mg}] \text{ thus :}$$

$$K_p = \frac{4[V''_{Mg}]^3}{P_{O_2}^{\frac{1}{2}}} \qquad [V''_{Mg}] = (\frac{1}{4}K)^{\frac{1}{3}}P_{O_2}^{+\frac{1}{6}}$$

$$[V_O^{\cdot\cdot}] = \frac{K_s}{[V''_{Mg}]} = K_s(\frac{1}{4}K)^{-\frac{1}{3}}P_{O_2}^{-\frac{1}{6}}$$

$$[O''_i] = \frac{K_f}{[V_O^{\cdot\cdot}]} = \frac{K_f}{K_s}(\frac{1}{4}K)^{\frac{1}{3}}P_{O_2}^{+\frac{1}{6}}$$

For the interstitial mechanism $D_O \propto [O"_i]$ therefore for this mechanism:

$$D_O \propto P_{O_2}^{+\frac{1}{6}}$$

Alternatively oxygen can be incorporated into the lattice directly as interstitials with simultaneous creation of holes for charge compensation by

$$\frac{1}{2}O_2 \rightarrow O''_i + 2h^{\cdot} \qquad K_p = \frac{[O''_i]p^2}{P_{O_2}^{\frac{1}{2}}}$$

$$\text{in this case } p = 2[O''_i] \text{ so}$$

$$K_p = \frac{4[O''_i]^3}{P_{O_2}^{\frac{1}{2}}} \qquad [O''_i] = (\frac{1}{4}K)^{\frac{1}{3}}P_{O_2}^{+\frac{1}{6}}$$

For this possible mechanism also $D_O \propto P_{O_2}^{+\frac{1}{6}}$. These processes both would lead to an interstitial diffusion mechanism with an oxygen partial pressure dependence of $\frac{1}{6}$ or 0.167. Considering the degree of experimental error (as indicated by the error bars in the diffusion data in figure 4-5) this value is indistingusihable from the 0.11 dependence computed from the data of this study. A plot of with $D \propto P_{O_2}^{0.167}$ is also shown as a dashed line in figure 4-5, from which it should be clear that the value of 0.11 is within the realm of experimental error for the measurements done in this study. Furthermore there are no likeley defect reactions which would give a partial

pressure dependence closer to 0.11 (namely +1/10 or +1/8). All of the other likely defect incorporation reactions give higher values for the partial pressure dependence.

Given tens to hundreds of ppm of aliovalent impurities some of which are transition metals begs the question of whether these impurities are involved in the atmospheric equilibration. A p to n transition in electronic conduction has been observed in Fe doped MgO by Sempolinski and Kingery [103] at around 10^{-5} kPa oxygen partial pressure which would be consistent with reduction of iron as oxygen partial pressure decreased.

Taking Fe as an example since, it is a major source of contamination in MgO, we can perform an analysis. In oxidizing atmospheres most of the Fe present is likely in the form of Fe^{3+}. As the atmosphere becomes more reducing, the amount of Fe present as Fe^{3+} decreases and the amount present as Fe^{2+} increases. This can occur by the following mechanisms, the first being the most likely for reasons already discussed.

$$2Fe_{Mg}^{\cdot} + 2e' \rightarrow 2Fe_{Mg}^{\times}$$
$$O_O + V_{Mg}'' \rightarrow \frac{1}{2}O_2 + 2e'$$
$$---------$$
$$2Fe_{Mg}^{\cdot} + O_O + V_{Mg}'' \rightarrow \frac{1}{2}O_2 + 2Fe_{Mg}^{\times}$$

$$2Fe_{Mg}^{\cdot} + 2e' \rightarrow 2Fe_{Mg}^{\times}$$
$$O_O \rightarrow \frac{1}{2}O_2 + V_O^{\cdot\cdot} + 2e'$$
$$---------$$
$$2Fe_{Mg}^{\cdot} + O_O \rightarrow \frac{1}{2}O_2 + 2Fe_{Mg}^{\times} + V_O^{\cdot\cdot}$$

Examination of these defect reactions reveals that decreasing the oxygen partial pressure should increase the concentration of oxygen vacancies and decrease the number of trivalent Fe cations while increasing the number of divalent Fe cations. Divalent Fe cations are effectively neutral in Mg sites so they do not contribute to the formation of point defects. By the defect incorporation reactions 4.1, 4.2 we can see directly that a reduction in the concentration of trivalent Fe cations will also serve to increase the oxygen vacancy concentrations. This leads one to the conclusion that if oxygen diffusion is through a vacancy mechanism the diffusion coefficient should increase with decreasing oxygen partial pressure. This was not observed, as the diffusivities decreased with decreasing oxygen partial pressure as can be seen in figure 4-5. The concentration of oxygen interstitials, though, would increase by virtue of the Frenkel equilibrium. Thus if oxygen diffusion were by means of an interstitial mechanism the observed behavior would be consistent, diffusivities decreasing with decreasing oxygen partial pressure.

Other experimental evidence favors the interstitial mechanism as well. A study of oxygen diffusion in scandium doped MgO grown using CVT by Uchikoba and Wuensch [104] showed oxygen diffusivity to increase as the concentration of Sc increased in the temperature range 1200 - 1500°C. Sc being trivalent would obey the defect equilibria of equations 4.1, 4.2. Thus increasing the concentration of Sc would decrease the oxygen vacancy concentration. If vacancy diffusion were controlling, a decrease in oxygen diffusivity would accompany an increase in Sc concentration. Increasing the Sc concentration would have the opposite effect on oxygen interstitial concentration; it would increase due to the Frenkel equilibrium. Thus the diffusivity of oxygen would increase with increasing Sc content if an interstitial mechanism were operative. In the same study the isotope effect was measured in $Mg^{17,18}O$. The authors obtained a value of 0.99 ± 0.25 for the correlation factor at 1200°C. A value of 1 is indicative of an interstitial mechanism of diffusion while a value of 0.781 characteristic of vacancy diffusion in a face-centered cubic lattice. Semken [69] also measured the effect and obtained a value of 1.0 ± 0.22 for the correlation factor at 1400°C. These results also tend to favor an interstitial mechanism for oxygen diffusion. The experimental error

is large so this cannot be stated conclusively but a good deal of evidence does point to an interstitial mechanism of oxygen diffusion.

Theoretical evidence also points toward an interstitial mechanism. If one uses theoretical estimates of defect formation energies in MgO to calculate point defect concentrations for MgO of varying degrees of purity, it can be seen that it does not take a large supervalent impurity concentration to depress the native oxygen vacancy concentrations below the oxygen interstitial concentrations. As an example we shall consider MgO containing 100 ppm total trivalent impurity. Values of defect formation energies in MgO have been a source of considerable debate. The values in table 2.1 are among the first reliable values calculated. The value of 7.5eV for the Schottky enthalpy has withstood the test of time, and is still widely quoted as a reasonable estimate of the Schottky enthalpy. The value of 15.2eV reported by Mackrodt and Stewart for the Frenkel enthalpy is now generally believed to be an overestimate. More recent work by Gourdin and Kingery [105] and Cormack [106] have agreed on a value of ca. 12eV for the Frenkel energy. Using these values and equation 4.2 yields $[V_O^{\cdot\cdot}] = 1.8\times10^{-20}$ at 1300°C. Computing the interstitial fraction using $[O"_i]$ $= K_f/[V_O^{\cdot\cdot}]$ yields $[O"_i] = 9.1\times10^{-20}$, almost an order of magnitude difference for an impurity concentration as low as 100ppm and temperatures as low as 1300°C. Since $h_f > h_s$ the differences would only be magnified for higher temperatures or impurity concentrations.

The only evidence which tends to steer one away from the conclusion that an interstitial mechanism of oxygen diffusion is operative is the activation energy data. Most studies of O diffusion in MgO have yielded activation energies for oxygen diffusion between 3.2 - 4.0eV, nowhere near what the theoretical estimates of activation energies of oxygen diffusion by interstitials predict. If the interstitial concentration was controlled indirectly by the trivalent impurity density as in 4.1, 4.2 then the activation energy for diffusion, E_a, would be equal to h_f - h_s + h_m, where h_f, h_s, and h_m are the Frenkel, Schottky, and migration enthalpies respectively. Substituting the calculated values of Mackrodt from table 2.1 gives a value for E_a of 12.1 - 7.5 + 2.4 = 7.0eV using the migration enthalpy of oxygen vacancies. Of course the migration

enthalpy for oxygen interstitials is higher due to the larger lattice distortion accompanying interstitial migration. A suggestion which would remedy this quandary a bit was offered by Semken [69] who proposed an association of oxygen interstitials around an oxygen vacancy (a peroxy center) based on a model of Hobbs [107] for the incorporation of excess O in BaO. There is evidence for the existence of such defects. Electron diffraction and microscopy studies of SiO_2 by Pascucci [108] and Qin [109] have demonstrated that these defects likely form in α-quartz during radiolysis. The association would afford a decrease in the activation energy for diffusion by the association energy, similarly to the cation-anion vacancy association. $E_a = h_f - h_s + h_m - h_a$. Semken suggests a uncharged peroxy linkage of the form

$$[O_i' - V_O^{\cdot\cdot} - O_i']^{\times}$$

but such defects would be insensitive to both aliovalent impurity content and oxygen partial pressure. It is also unlikely that a large quantity of singly ionized oxygen interstitials are present. An alternative would be:

$$[O_i'' - V_O^{\cdot\cdot} - O_i'']''$$

This defect contains the more likely species O''_i and is doubly ionized like the free oxygen interstitial and would thus display the same aliovalent impurity and partial pressure dependence.

If one accepts that interstitials are the controlling species for bulk oxygen diffusion then it is possible to obtain quantitative estimates of the bulk trivalent impurity concentrations for recent diffusion studies by comparing measured diffusivities in nominally pure samples with those obtained by Uchikoba and Wuensch for Sc doped MgO [104]. Recalling that:

$$D_{O_i} \propto [O_i''] \propto \frac{1}{[V_O^{\cdot\cdot}]} \propto [V''_{Mg}] \propto [M'_{Mg}]$$

The ratio of diffusivities should equal the ratio of the impurity concentrations, all

source $[Sc_2O_3]$ wt. %	deposit $[Sc_2O_3]$ wt. %	$[Sc'_{Mg}]$ ppm
1.0	0.07	400
0.1	0.05	290
0	0	"0"

Table 4.2: Bulk scandium concentrations for CVT MgO grown using doped source material.

else being the same. Uchikoba has measured the absolute Sc concentrations in the Sc doped samples in which he studied diffusion [110]. He measured bulk Sc_2O_3 concentrations using electron microprobe spectroscopy. The results are shown in table 4.2 Aside from attesting to the purification effects of CVT, these can be used to extrapolate impurity concentrations by equating the diffusivity ratios with impurity density ratios. To test the accuracy of this method we can compare the ratios of the diffusion coefficients obtained with the impurity ratios:

$$\frac{D_0[400ppm]}{D_0[290ppm]} = \frac{2.74 \times 10^{-5}}{2.11 \times 10^{-5}} = 1.4 \qquad \frac{400ppm}{290ppm} = 1.3$$

Pre-exponential factors were used over the temperature range 1200 - 1500°C rather than the actual diffusivites This could be done since the activation energies for oxygen diffusion for the three different impurity levels were approximately equal, hence the only variation wass in the activation energy. The ratios are in good agreement and thus the method was used to estimate impurity levels in MgO used in some recent diffusion studies. The following proportion was used to do the calculation:

$$\frac{D}{D[290]} = \frac{[M'_{Mg}]}{290}$$

This yields the results in table 4.3, which are quite reasonable when compared to the impurity concentrations reported by Gruber [10] for CVT grown MgO.

Study	Temperature °C	$\frac{D}{D[290]}$	$[M_{Mg}^{\cdot}]$ ppm	avg$[M_{Mg}^{\cdot}]$ ppm
Yoo and Wuensch [11]				
	1200	0.22	64	77
	1300	0.15	43	
	1400	0.37	107	
	1500	0.32	93	
Current work				
	1300	0.11	32	69
	1400	0.26	75	
	1500	0.75	101	

Table 4.3: Extrapolated trivalent impurity levels for CVT MgO used in recent diffusion studies.

4.2 Grain Boundary Structure

A TEM micrograph of the $\Sigma 13$ grain boundary with accompanying selected area diffraction pattern is shown in figure 4-7. In both grains the electron beam is oriented along a [100] direction. On one side of the boundary [100] cross fringes are visible while on the other side only one set of [100] fringes are visible. The resolution is too poor to gain insight into the dislocation structure but several observations can be made. Firstly the grain boundary width is no more than 1 nm which in good agreement with similar studies done on NiO symmetric tilt boundaries [32, 33]. The atomic density in the grain boundary regions does not differ appreciably from the bulk, which is also in agreement with the NiO studies as well as studies of metallic grain boundaries [77]. There is what appears to be an asymmetric facet in the boundary which is not unreasonable as such facets would serve to accommodate deviations from the ideal misorientation angle for the $\Sigma 13$ boundary (the misorientation angle could only be controlled to within $\pm$ 1°). Asymmetric facets have also been observed in $\Sigma 5$ boundaries in NiO [32, 33]. Lastly, the pure tilt nature of the boundary is attested to by the accompanying electron diffraction pattern, as it is just two superimposed [100] diffraction patterns rotated with respect to one another, as would be expected if the selected area contained both grains.

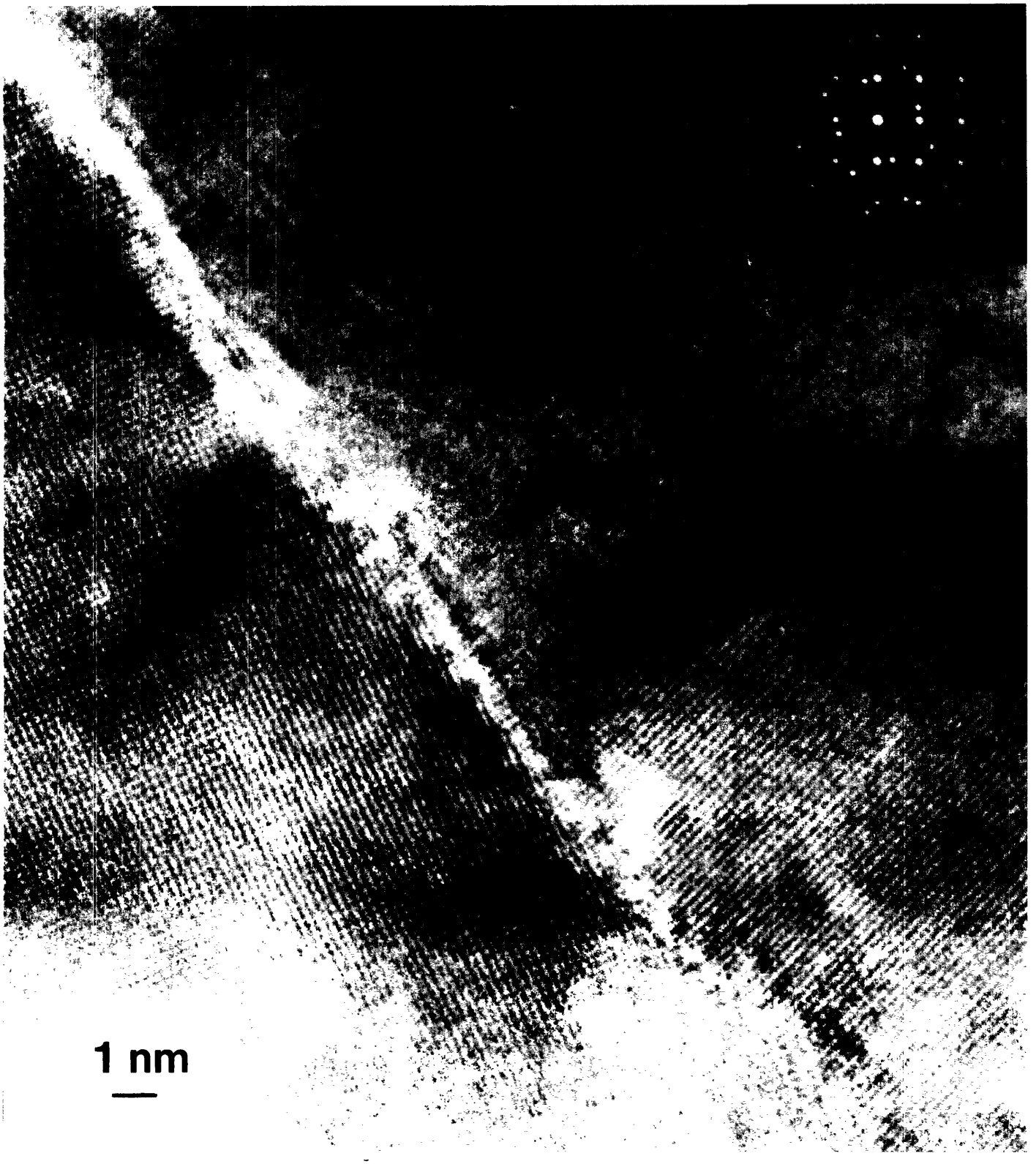

Figure 4.7: TEM micrograph of $\Sigma 13$ (510) tilt boundary in MgO (projection along [100] zone axis). The accompanying electron diffraction pattern contains the diffraction patterns of the individual grains superimposed.

4.3 Grain Boundary Diffusion

The analysis of grain boundary diffusion data is somewhat more complicated than that of bulk diffusion data. The diffusant concentrations in the bulk and grain boundary are given by the Fisher equations 2.19, 2.20, but there is no way of measuring either of these directly. The SIMS profiles yield an average of the two since the probe scans a region including the bulk and the grain boundary. See figure 4-8 for an example of such a profile. A single expression for the average diffusant concentration in the scanned region as a function of depth taking into account the bulk and grain boundary contributions must be derived. To begin, let us review the initial and boundary conditions and sample geometry. In this analysis the diffusant, ^{18}O is initially present in the sample at an atomic concentration of 0.3. The surface concentration of ^{18}O is simply the atmospheric fraction of ^{18}O, or 0.00204 , and it is assumed that deep within the sample the ^{18}O concentration does not vary from its initial value. These conditions can be summarized by:

$\rho(y, 0, t) = C_0$

$\rho(y, z, 0) = C_i \qquad z > 0$

$\rho(y, \infty, t) = C_i$

$\rho(y, z, t)$ = Concentration of ^{18}O in the bicrystal

C_0 = Concentration of ^{18}O at surface = 0.00204

C_i = Initial or bulk concentration of ^{18}O in bicrystal = 0.3

The Fisher solution is written for the case of no diffusant present in the bulk initially so the following transformation was used:

$$C = \rho - C_i$$

yielding the transformed boundary conditions:

$C(y, 0, t) = C_0 - C_i$

$C(y, z, 0) = 0 \qquad z > 0$

$C(y, \infty, t) = 0$

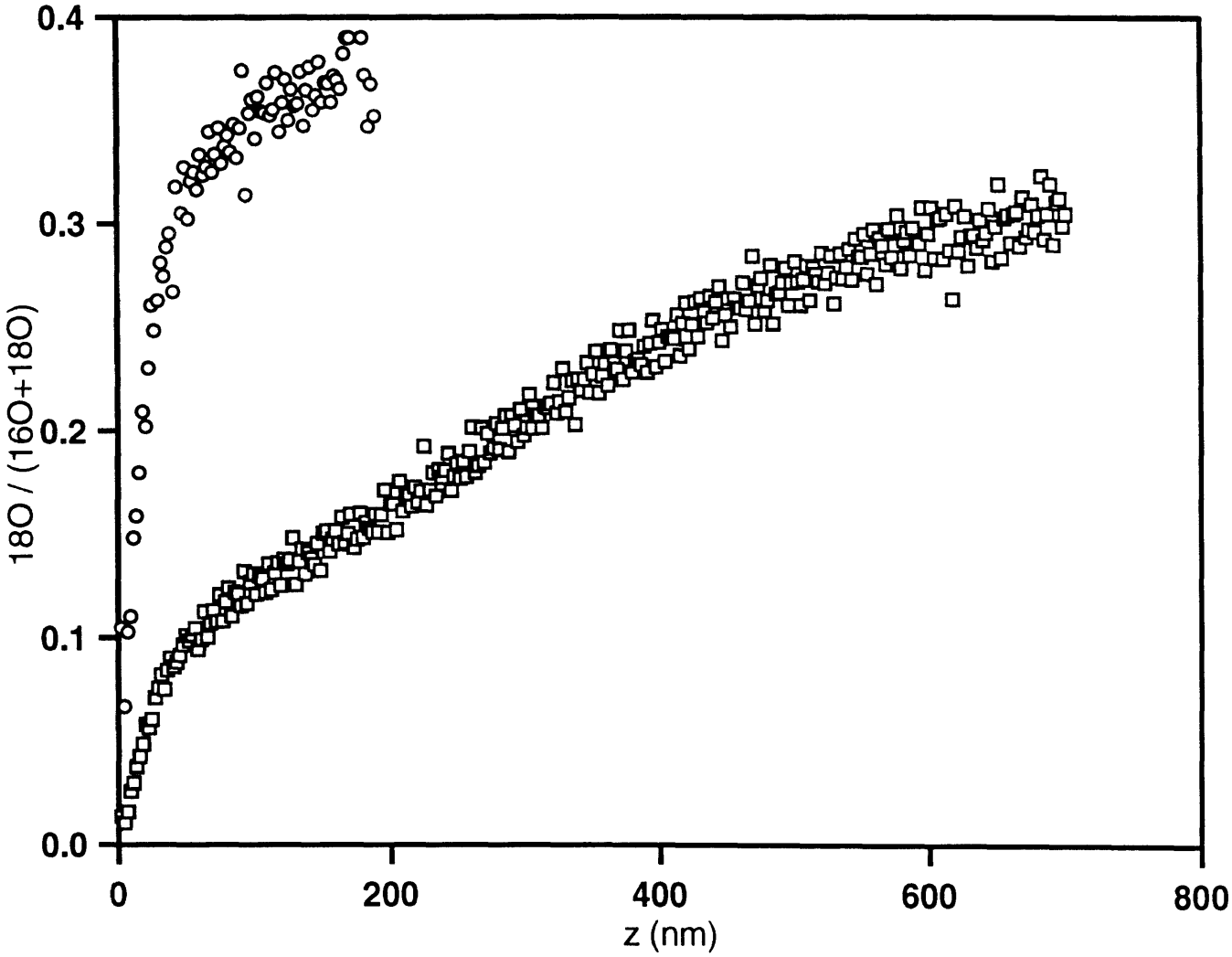

Figure 4-8: Sputter depth profile of $^{18}C(x)$ versus depth in region of bicrystal containing grain boundary. Sample annealed at 1300°, 72 hours.

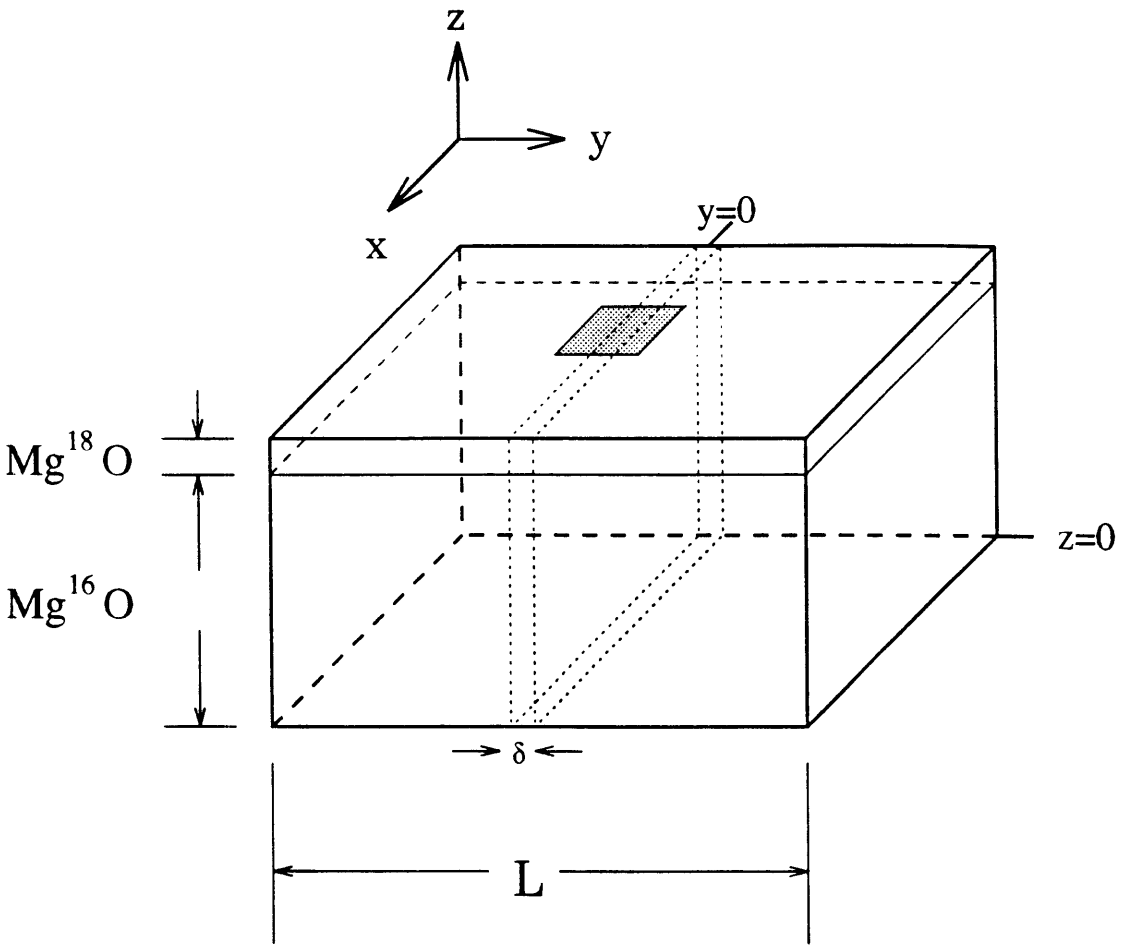

Figure 4-9: Bicrystal specimen geometry showing SIMS analysis area (exaggerated).

The sample geometry is shown in figure 4-9. The grain boundary thickness is δ and the lateral dimension of the SIMS crater is l. The solutions for the bulk and boundary diffusant concentrations are similar to equations 2.19, 2.20 but adjusted for the transformed boundary conditions:

$$C(y,z,t) = (C_o - C_i)\ \exp\frac{-2^{\frac{1}{2}}\ D^{\frac{1}{4}}\ z}{(\pi t)^{\frac{1}{4}}\ (\delta D_b)^{\frac{1}{2}}}\text{erfc}\ \frac{y-\frac{\delta}{2}}{2\ (Dt)^{\frac{1}{2}}}$$

$$C'(z,t) = (C_o - C_i)\ \exp\frac{-2^{\frac{1}{2}}\ D^{\frac{1}{4}}\ z}{(\pi t)^{\frac{1}{4}}\ (\delta D_b)^{\frac{1}{2}}}$$

Thinking of this as a single piecewise defined function we can compute the average value over the analyzed area as a function of depth by the following:

$$\bar{C}(z,t) = \frac{1}{l}\int_{-l/2}^{+l/2} C(y,z,t)\,dy$$

Since the function C is piecewise defined we must compute the integral in a similar fashion.

$$\bar{C}(z,t) = \frac{1}{l}[\int_{-l/2}^{-\delta/2} C dy + \int_{-\delta/2}^{+\delta/2} C' dy + \int_{+\delta/2}^{+l/2} C dy]$$

This computation is not as cantankerous as it appears at first. The only portion of the expressions for concentration which contain any y dependence is the erfc term in the expression for C. Integrating this, we are left only with the exponential terms:

$$\bar{C}(z,t) = K\exp\frac{-2^{\frac{1}{2}}\ D^{\frac{1}{4}}\ z}{(\pi t)^{\frac{1}{4}}\ (\delta D_b)^{\frac{1}{2}}}$$

K is an agglomeration of constants which contains l, but is not a function of z. Knowing this, we can solve for the product of the grain boundary diffusivity and boundary width product. These two quantities are inseparable in the analysis of grain boundary diffusion.

$$\ln\bar{C} = \ln K + \frac{-2^{\frac{1}{2}}\ D^{\frac{1}{4}}\ z}{(\pi t)^{\frac{1}{4}}\ (\delta D_b)^{\frac{1}{2}}}$$

$$\frac{\partial \ln \bar{C}}{\partial z} = \frac{-2^{\frac{1}{2}}\ D^{\frac{1}{4}}\ z}{(\pi t)^{\frac{1}{4}}\ (\delta D_b)^{\frac{1}{2}}}$$

Note that this expression is seemingly independent of K and thus l. Varying the analysis area will only change ln K, the "y-intercept" and not the slope which contains the information about the diffusivity. We know, though, that the value of l is critical in the analysis. If l is too large the grain boundary contribution to the overall diffusion profile will be lost to the background. This seeming paradox is solved if we use the following reasoning. If the SIMS probe were infinitely sensitive, that is to say it could detect the presence of a single diffusant atom, then the size of the analyzed area would be irrelevant as long as it contained the grain boundary, for if it did, the additional diffusant present due to the boundary would be detected by the SIMS probe. Indeed, this is the premise behind the analysis of grain boundary diffusion in polycrystals where the grain boundary area/volume ratio is much higher. In the case of the bicrystal, however, the grain boundary area/volume ratio is very low so we must restrict the analysis to a very small area containing the boundary, such that the extra diffusant present due to the boundary is detectable by the probe. The paradox is then solved. The fact that the parameter l is at all relevant in the analysis is due to a limitation of the experimental technique, not the analysis itself. In this study we have, by trial and error, determined a suitably sized analysis area as has been discussed in a previous section.

Solving for the grain boundary diffusivity gives:

$$\delta D_b = \frac{2D^{\frac{1}{2}}}{(\pi t)^{\frac{1}{2}}[\frac{\partial \ln \bar{C}}{\partial z}]^2}$$

Recall, though, that a transformation of variables was made. Making the reverse transformation $\rho = C + C_i$ gives the following for the concentrations.

$$\rho(y,z,t) \ = C_i - (C_i - C_0)\ \exp \frac{-2^{\frac{1}{2}}\ D^{\frac{1}{4}}\ z}{(\pi t)^{\frac{1}{4}}\ (\delta D_b)^{\frac{1}{2}}} \mathrm{erfc}\ \frac{y - \frac{\delta}{2}}{2\ (Dt)^{\frac{1}{2}}}$$

$$\rho'(z,t) = C_i - (C_i - C_0) \exp \frac{-2^{\frac{1}{2}}\ D^{\frac{1}{4}}\ z}{(\pi t)^{\frac{1}{4}}\ (\delta D_b)^{\frac{1}{2}}}$$

This gives for the average concentration, $\bar{\rho}$:

$$\frac{C_i - \bar{\rho}}{C_i - C_0} = \exp \frac{-2^{\frac{1}{2}}\ D^{\frac{1}{4}}\ z}{(\pi t)^{\frac{1}{4}}\ (\delta D_b)^{\frac{1}{2}}}$$

We can see from this that the correct expression for δD_b can be obtained by substituting the quantity $\frac{C_i - \bar{\rho}}{C_i - C_0}$ for $\bar{C}$. The corrected expression is thus:

$$\delta D_b = \frac{2D^{\frac{1}{2}}}{(\pi t)^{\frac{1}{2}}[\frac{\partial \ln \frac{C_i - \bar{\rho}}{C_i - C_0}}{\partial z}]^2}$$

All the quantities on the right side of the equation can be obtained from the SIMS data except for the annealing time which is known. The slope $\frac{\partial \ln \frac{C_i - \bar{\rho}}{C_i - C_0}}{\partial z}$ may be computed from a plot of $\ln \frac{C_i - \bar{\rho}}{C_i - C_0}$ vs. z as has been done in figure 4-10 for the data of the $\Sigma 13$ sample annealed at 1300°C, 72 hours. A "linear" region must be chosen in which to do the fit because, near the surface, nonlinearity arises from the contribution of bulk diffusion, and deep within the sample scatter in the data becomes large. The criterion for choosing the region is that the largest number of data points be included while still maintaining an acceptable degree of linearity. In our case acceptable linearity meant a value of the Pearson linear correlation coefficient greater than 0.9. Closer inspection of figure 4-10 shows what appears to be an inflection point around 200 nm. Looking at the raw data, figure 4-8, a small change in shape of the curve is visible around 200 nm. It appears to be slightly concave. It appears then that this inflection point is not an artifact of the mathematical manipulations performed on the raw data. Whether or not the change in slope is real is another matter. A change in slope on the lnC vs. depth plot would imply a depth-dependent diffusivity. Such behavior has never been reported but a possible explanation does come to mind when considering the fact that the crystals were grown using CVT. In CVT grown crystals the extrinsic dislocation density increases as the epitaxial interface is approached. Extrinsic dislocations originating in the seed crystal usually grow out within several microns of the epitaxial material. Extrinsic dislocations present can become pinned to a grain boundary and become incorporated into its dislocation structure. This type

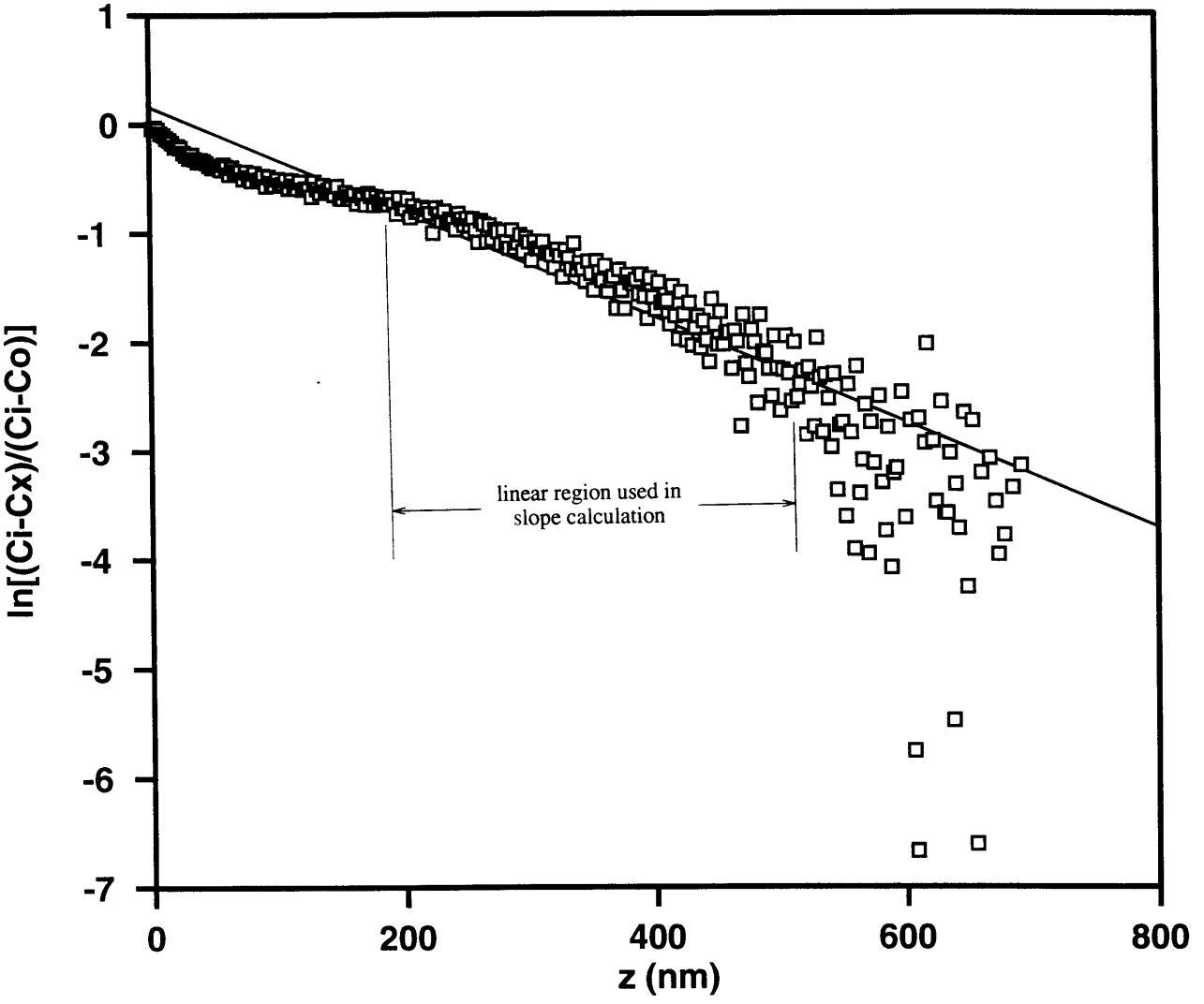

Figure 4-10: Slope determination for grain boundary diffusivity computation.

of behavior is known to occur in ceramics as well as metals, and would probably result in a higher diffusivity at larger depths. This is not what is observed, though. The slope of the lnC versus depth plot is higher at larger depths, corresponding to a lower diffusivity. Considering also that the boundary profiles are usually less than 1μm deep and the epitaxial layers usually more than 30μm thick the epitaxial interface is usually not approached. It could also be possible that this effect is due to some form of volume relaxation towards the surface. This would result in a higher diffusivity at the surface, but this is very unlikely in CVT crystals which are grown under strain free conditions, and furthermore has never been reported to occur even in crystals processed under high stresses. It is most likely that this behavior is an artifact of the SIMS analysis. A charge imbalance could result in repressed or enhanced emission of secondary species depending on the residual charge left on the surface. This is always a potential source of error in the SIMS analysis of insulating materials and requires the operator to monitor the charge balance condition closely during a run. A small imbalance such as this appears to be would hardly be noticeable. To verify that this apparent slope change is not an intrinsic property of the boundary I have plotted several more profiles and displayed them in appendix A. From these curves it appears that the behavior of the curve in figure 4-10 is the exception and not the rule. A summary of the diffusion data for the $\Sigma 5$, $\Sigma 13$, and asymmetric 16° tilt boundaries is shown in table 4.4 and graphically in figure 4-11.

An Arrhenian expression for the quantity δD_b for the $\Sigma 13$ boundaries is:

$$\delta D_b = 2.8 \times 10^{-8} \exp \frac{-3.9eV}{kT} \quad \frac{\text{cm}^3}{\text{sec}} \qquad 1250 - 1500°C$$

Not enough data were taken for the $\Sigma 5$ or the asymmetric 16° tilt boundary to calculate a meaningful activation energy but, if the small amount of data available is to be believed, then a definite trend is apparent. For the one temperature where both were measured, the diffusivities of oxygen in the $\Sigma 5$ and $\Sigma 13$ boundaries were equal to within experimental error. The diffusivity of oxygen in the 16° asymmetric tilt boundary is higher than in the special boundaries by 1-2 orders of magnitude.

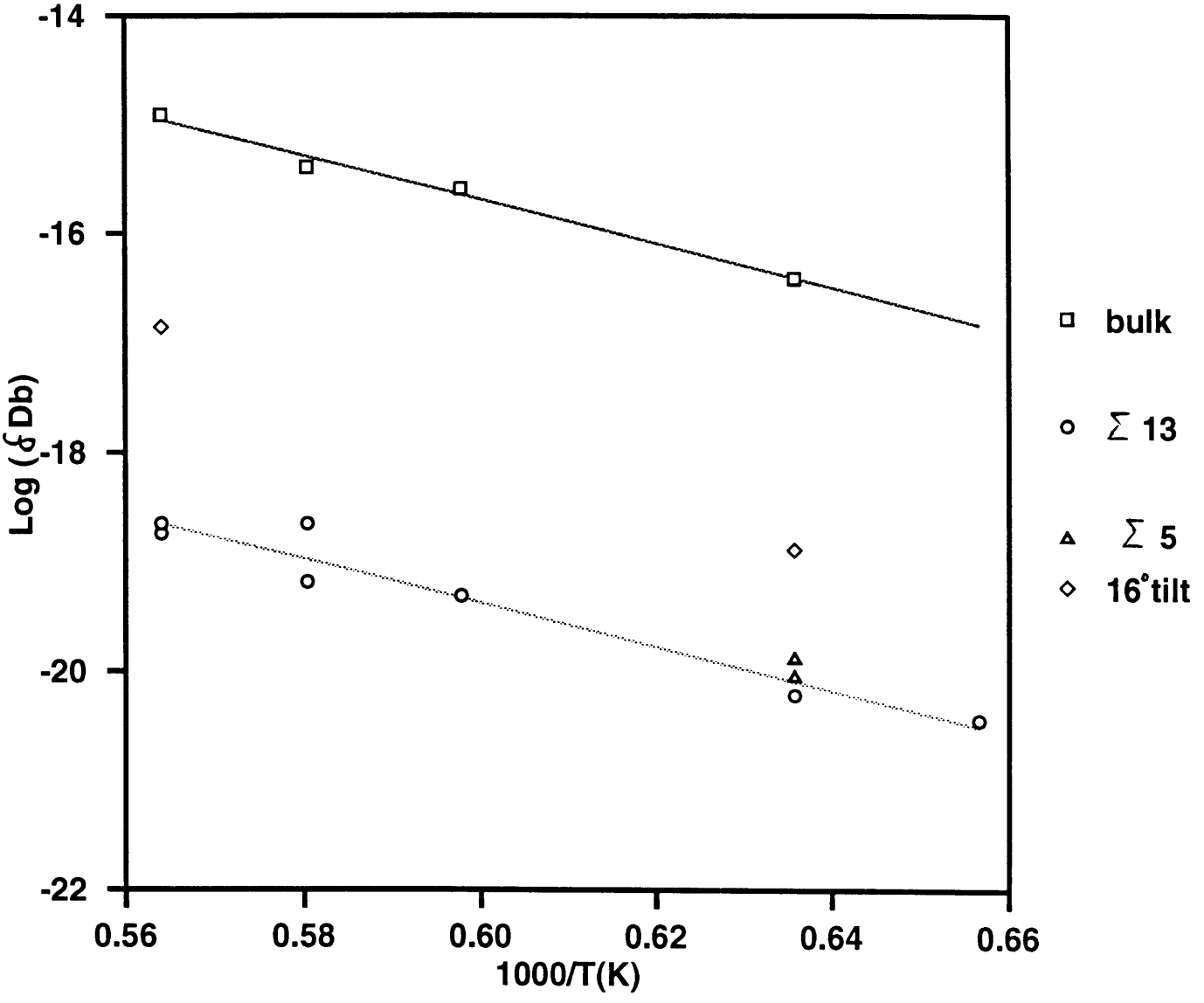

Figure 4-11: Summary of diffusion data, as a function of reciprocal temperature, with best fit line for $\Sigma 13$ boundary.

δD_b cm^3/s	T °C.	Orientation
3.6×10^{-21}	1250	Σ13
6.1×10^{-21}	1300	Σ13
4.9×10^{-20}	1400	Σ13
6.6×10^{-20}	1450	Σ13
2.2×10^{-19}	1450	Σ13
2.3×10^{-19}	1500	Σ13
1.8×10^{-19}	1500	Σ13
9.2×10^{-21}	1300	Σ5
1.4×10^{-20}	1300	Σ5
1.3×10^{-19}	1300	asymmetric 16°
1.4×10^{-17}	1500	asymmetric 16°

Table 4.4: Summary of grain boundary diffusion data.

This suggests a relationship between grain boundary structure and diffusion. While there has been a great deal of work on the relationship between grain boundary structure and energy, and there is a clear relationship between boundary structure and energy, which has been discussed in a prior section, comparatively little work has been done on the relationship between boundary structure and diffusion. It has been theorized that in low Σ, low energy boundaries, due to the good atomic registry between adjoining grains, diffusion (while still enhanced over bulk values) will not be as rapid as in general high angle boundaries, where the degree of fit of the individual grains is not as good, and the interfacial energy is higher. To quantify this effect, Borisov has, on the basis of an empirical correlation of data for metals, postulated that the activation free energy for diffusion in the grain boundary, g_a^b, is reduced from it's bulk lattice value, g_a^l by an amount equal to the interfacial energy γ_{gb} [111].

$$\gamma_{gb} \propto g_a^l - g_a^b = h_a^l - Ts_a^l - (h_a^b - Ts_a^b) = \Delta h_a - T\Delta s_a$$

Since $g_a = h_a - Ts_a$ the decreased activation free energy can be due to a decreased activation enthalpy in the grain boundary or an increase in the activation entropy, or both. Using the above relation and expressions for the bulk and grain boundary diffusivities previously known from atomistic considerations (see equations 2.21 and

2.22) Gupta [112] has derived the following relationship between boundary energy and bulk and grain boundary diffusion:

$$\gamma_{gb} = \kappa RT \ln \frac{D_b}{D_l} \tag{4.4}$$

$$= \kappa RT \ln \frac{\frac{1}{4}\alpha^2 z\nu_0 f_{gb} \exp -\frac{g_a^b}{kT}}{\frac{1}{6}\alpha^2 z\nu_0 f \exp -\frac{g_a^l}{kT}} \tag{4.5}$$

$$= \kappa RT \ln \frac{(\frac{1}{4}\alpha^2 z\nu_0 f_{gb} \exp \frac{s_a^b}{k}) \exp -\frac{h_a^b}{kT}}{(\frac{1}{6}\alpha^2 z\nu_0 f \exp \frac{s_a^l}{k}) \exp -\frac{h_a^l}{kT}} \tag{4.6}$$

$$= \kappa RT \ln \frac{D_b^0 \exp -\frac{h_a^b}{kT}}{D_l^0 \exp -\frac{h_a^l}{kT}} \tag{4.7}$$

$$\kappa = \frac{4.18 \times 10^7}{2a^2 N_A}$$

a = lattice parameter N_A = Avogadro's number

where κ is a conversion factor derived by Guiraldenq [113]. The value of 4.18 $\times 10^7$ was empirically obtained by fitting the above expression to measured diffusivities and grain boundary energies in several different alloy systems. How applicable this value is to ceramics is a matter for speculation due to the dearth of reliable grain-boundary diffusion data in ceramics. From the above equations we can see that the reduced boundary diffusion activation entropy will be revealed by a higher pre-exponential while the reduction in activation enthalpy will be self-evident. Applying equations 4.4 - 4.7 to the results of this study demonstrates the qualitative agreement. A value of 1nm for the grain boundary width, δ, the width of the transition region from the structure of grain 1 to grain 2, was assumed. This is not unreasonable looking at the the electron micrograph, figure 4-7. The grain boundary diffusivity can be represented by D = 0.31exp(-3.9eV/kT) cm^2/s. The pre-exponential term is roughly 4 orders of magnitude larger than for the corresponding bulk pre-exponential. The activation energies appear to be equal to within experimental error, (3.9 - 4.0eV), This equality of diffusion activation energies implies a similar migration enthalpy for oxygen ions in the bulk and grain boundary. The increase in diffusivity is entirely in the pre-exponential which indicates that an increase in point defect concentration is responsible for the increase in diffusivity. If oxygen diffusion in grain boundaries occurs by an interstitial

mechanism as has been proposed for the bulk then this would mean an excess of negative anionic defects in the grain boundary core. If magnesium grain boundary diffusion occurs by a vacancy mechanism as is believed to be the case in the bulk, this would also mean an excess of negative cationic defects in the grain boundary core. Grain boundaries are known to be charged in ionic materials, even in the intrinsic regime due to the difference in the individual formation energies of cationic and anionic defects, as has been discussed in a previous section. The formation energy of cation vacancies is less than the formation energy of anion vacancies. Thus in high purity Schottky materials in the "space charge" region adjacent to the boundary where the bulk charge neutrality condition does not hold, the concentration of negative cation vacancies will be higher than that of positive anion vacancies. This results in a negative space charge layer and a correspondingly positive boundary core. If aliovalent impurities are present, the bulk concentration of point defects will change which can change the sign of the charge in the boundary core and space charge regions. This possibility will now be explored.

An expression for the intrinsic bulk potential, $e\varphi_\infty$, referenced to zero boundary potential has been derived by equating the expressions for the bulk cation and vacancy concentrations [114] which are given by:

$$[V''_{Mg}] = \exp -\frac{g_{V_{Mg}} - 2e\varphi_\infty}{kT} \tag{4.8}$$

$$[V^{\cdot\cdot}_{O}] = \exp -\frac{g_{V_O} + 2e\varphi_\infty}{kT}$$

Equating the two and solving for $e\varphi_\infty$ yields the intrinsic bulk potential:

$$e\varphi_\infty = \frac{1}{2}(g_{V_{Mg}} - g_{V_O})$$

Since $g_{V_O} > g_{V_{Mg}}$ this gives a negative intrinsic bulk potential referenced to zero boundary potential (or a positive boundary potential referenced to zero bulk potential). As has been mentioned previously, though, intrinsic behavior has never been observed in MgO. The defect structure is controlled by the aliovalent impurity con-

tent, the magnesium vacancy concentration usually being fixed by the supervalent impurity density. Since $[V''_{Mg}] = \frac{1}{2}[M^{\cdot}_{Mg}]$ in this case Kingery [114] has given an approximate relationship between the impurity content and the bulk potential by equating $\frac{1}{2}[M^{\cdot}_{Mg}]$ with the right hand side of equation 4.8 yielding

$$\frac{1}{2}[M^{\cdot}_{Mg}] \cong \exp -\frac{g_{V_{Mg}} - e\varphi_{\infty}}{kT}$$

From this approximate relation we can see that the effect of increasing the bulk trivalent impurity density would be to increase the bulk potential, not surprising since these are positive defects. At some point the bulk potential will switch from negative to positive, driving the boundary potential from positive to negative. Thus for a high enough impurity concentration we can expect a negative boundary which would be consistent with enhanced boundary transport via negative defects. To get a quantitative feel of how high the impurity concentrations would have to be, the model of Kliewer and Kohler [50] for the calculation of boundary potentials was applied to MgO. They have derived an expression relating the bulk potential to the impurity concentration, temperature, Schottky enthalpy, and the cation vacancy formation energy.

$$\exp \frac{e\varphi_{\infty}}{kT} = \exp(\frac{g_{V_{Mg}}}{kT})[\frac{C}{2} + [(\frac{C}{2})^2 + \exp(\frac{-h_s}{kT})]^{\frac{1}{2}}]$$

Kliewer and Koehler used this relation (apparently) to compute bulk potentials for NaCl doped with divalent cations. I have done the same using the same parameters as they did, $h_s \approx 2.0$ eV, $g_{V_{Na}} \approx 0.7$ eV, Kingery [114] has suggested similar values. The plot of bulk potential versus temperature for NaCl with 1, 10, 100, and 1000 ppm cation impurity is shown in figure 4-12. This plot resembles closely figure 3 in the paper by Kliewer and Koehler [50] so presumably the calculation was done correctly. The things to note about these curves are that the bulk potential indeed does become positive for high enough impurity levels and that at low impurity levels and high temperatures the intrinsic potential is asymptotically approached. This is reasonable since intrinsic behavior is observed in NaCl at high temperatures due to its low defect formation energies.

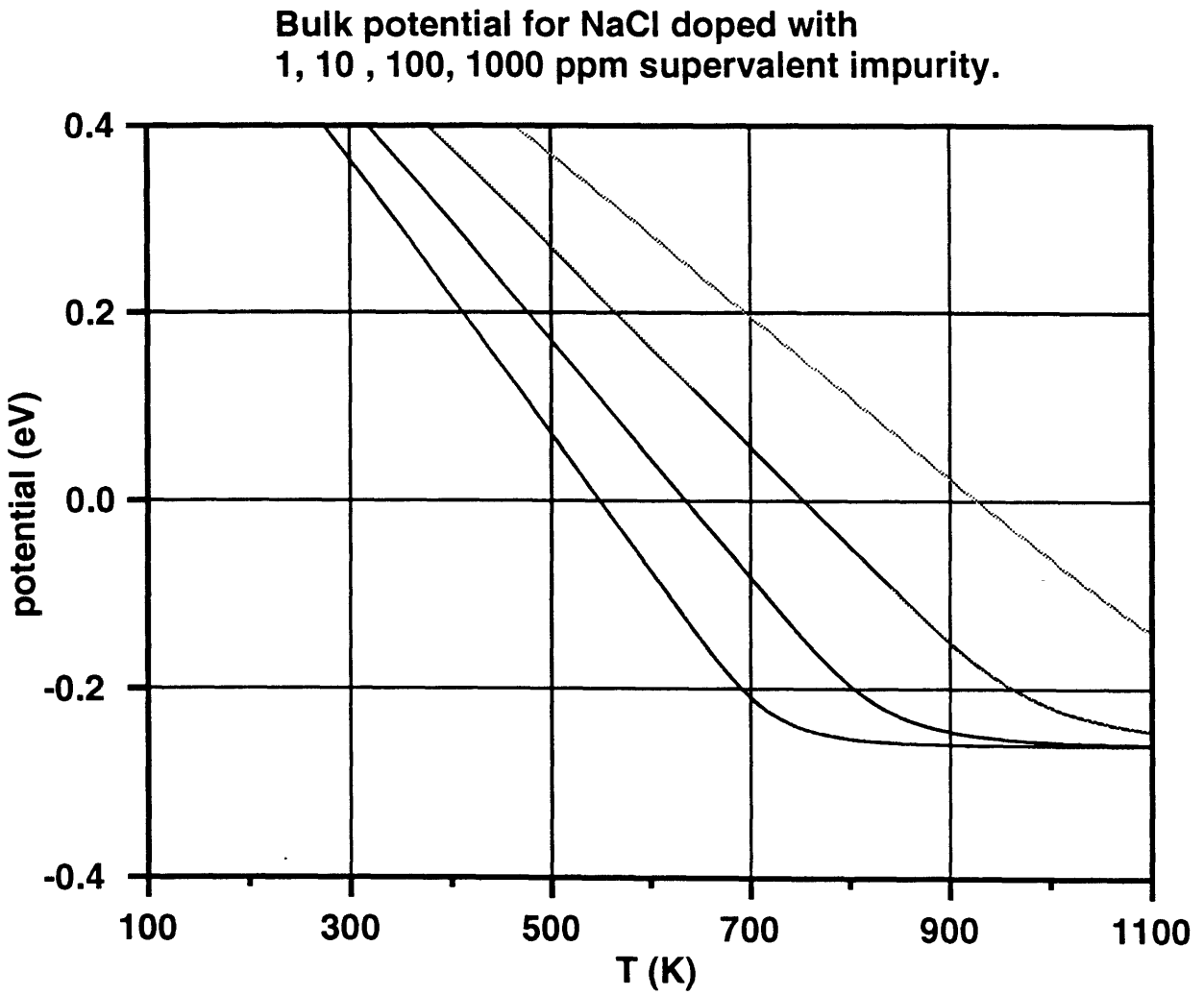

Figure 4-12: Bulk potential for NaCl doped with divalent cation impurity as a function of temperature computed using the method of Kliewer and Koehler.

The same method has been used to compute bulk/boundary potentials for MgO. A value of of 7.5 eV was used for h_s. This value is fairly well agreed upon for the Schottky energy. The vale of $g_{V_{Mg}}$ is open to more debate, though. Chiang [63] has computed a value of 3.0 eV for $g_{V_{Mg}}$ by measuring the boundary charge/potential for MgO doped with 3000 ppm Sc, assuming half of the Sc are associated with a magnesium vacancy forming a neutral complex. Kingery [114] has suggested that the cation vacancy formation energies are on the order of 1/3 of the Schottky energy. This would lead to a value of roughly 2.5 eV for MgO. Figure 4-13 shows the results of the boundary potential computations as a function of temperature up to the melting point (3100 K) for $g_{V_{Mg}} = 2.0$ and 3.0 eV, taking the former as a lower bound and the latter as an upper bound. There are several things to notice about this plot. Firstly the potentials are higher than for NaCl, not surprising since the defect formation energies for MgO are higher. Secondly the intrinsic regime is not as apparent as in the NaCl plot. There is a hint on the 1 ppm curve that the bulk potential is starting to reach its intrinsic value near the melting point. This result is very consistent with the fact that intrinsic behavior is not observed in MgO. If you will recall a value of 0.5 ppm was calculated for the intrinsic cation/anion vacancy concentration at the melting point in a previous section. Thus it is reasonable that we start to see intrinsic behavior at 1 ppm impurity levels at the melting point.

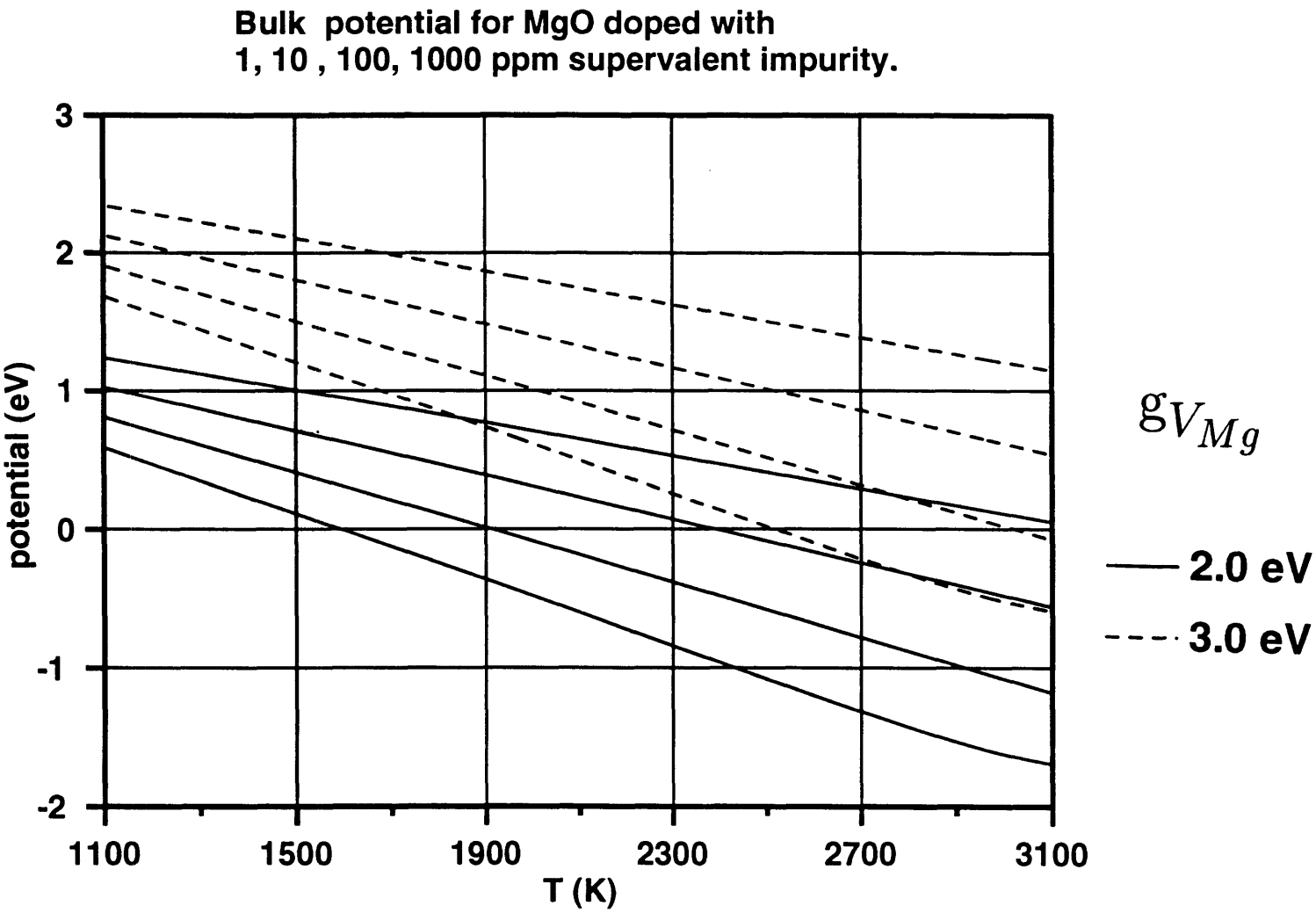

Figure 4-13: Bulk potential for MgO doped with trivalent cation impurity as a function of temperature computed using the method of Kliewer and Koehler.

Of course such low impurity levels in MgO are not presently achievable which is why intrinsic behavior is not observed in MgO. The most significant thing to note is that for the temperatures (1500 - 1800 K) and purities of material (between 10 - 100 ppm trivalent impurity) used in this study the bulk potentials are all positive, corresponding to negative boundary potentials, for all of the values of $g_{V_{Mg}}$ considered. Higher $g_{V_{Mg}}$ values corresponded to higher potentials. Positive bulk potemtials/negative boundary potentials are consistent with an excess of negative defects (magnesium vacancies, oxygen interstitials) at the boundary.

Knowing the bulk potential we can make semi-quantitative calculations of the point defect concentrations as a function of distance from the boundary. It is expected that, since the boundaries are negative for the temperatures and purities of this study, positive defects will be enhanced near the boundary (space charge segregation) and negative defects will be depleted. Following the method of Ikeda and Chiang [115] who employed the formalism of Kliewer and Koehler the spatial variations of trivalent impurity cations, $M_{Mg}^{\cdot}$, and magnesium vacancies V_{Mg}'' were calculated. Representative positive and negative defects were chosen; the behavior of other positive/negative defects would be similar. The trivalent impurity variation is given by:

$$[M_{Mg}^{\cdot}] = C \exp -\frac{e\varphi(x) - e\varphi_{\infty}}{kT}$$

C is a constant which in this case was used to normalize the impurity concentration to 100 ppm in the bulk. The spatial variation of the potential is given by:

$$\varphi(x) = \varphi_{\infty}(1 - \exp \frac{-x}{\delta})$$

δ is the Debye length which is the length scale over which the defect concentrations return to bulk values. It can be computed by:

$$\delta = (\frac{\varepsilon kT}{8\pi[M_{Mg}^{\cdot}]e^2})^{\frac{1}{2}}$$

All quantities are ad defined previously; ε is the permittivity, e the elementary charge. For MgO at 1300°C with 100 ppm supervalent impurity the debye length is 7.3 Å. The magnesium vacancy concentration varies according to equation 4.8. Using a value of 0.5 eV for $e\varphi$ estimated from figure 4-13 for 1300°C 100ppm impurity content gives the spatial variation depicted in figure 4-14 As expected the positive defects do segregate to the boundary while the negative defects are depleted.

As an attempt to confirm this Auger spectroscopy was done on previously annealed MgO bicrystals which had been fractured at the grain boundary in air. Survey scans were done on areas of the boundary corresponding to both the seed crystal and the CVT grown material. A typical survey scan, shown in figure 4-15 for a sample annealed at 1250°C for 6 days, reveals only the presence of Mg and O and some carbon which is typical for samples fractured in air. This rather unremarkable result in reality does not say much about the purity of the material analyzed as in survey mode the technique is not very sensitive. In high resolution mode though the energy analyzer is swept through a much smaller energy window making many more sweeps possible and the analysis more accurate. High resolution sweeps were done for two energy ranges 60 - 100 eV and 275 - 300 eV. The former was to detect the presence of Si which has an Auger peak between 85 - 95 eV. The latter was done to scan for Ca which has an Auger peak between 285 - 295 eV. The results are shown in figures 4-16, 4-17 The high resolution scans reveal the presence of both Si and Ca in the seed bicrystals, indicated by peaks at 90 and 288 eV respectively. The scans done on the CVT grown material show only random noise in the signal. The fact that no segregation was detected in annealed samples is somewhat surprising at first glance but when one considers that the sensitivity of Auger analysis is typically 0.5 - 1 atomic percent depending on the element it is understandable. According to figure 4-14 the maximum concentration of impurity cations (right at the boundary) is less that 2000 ppm (0.2 atomic %) and would thus not be detectable by Auger analysis. Thus the experimental results are consistent with the theoretical calculations.

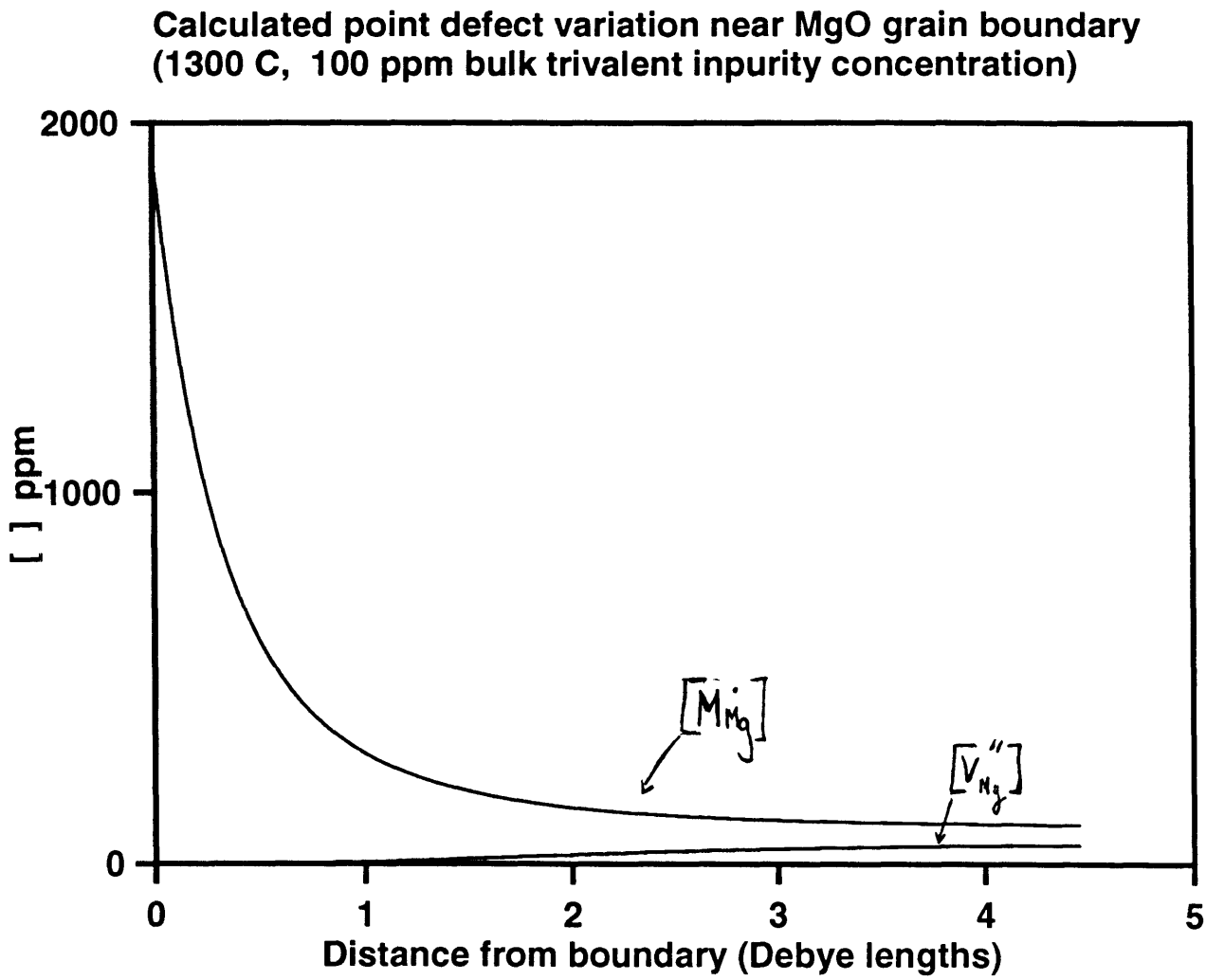

Figure 4-14: Calculated point defect concentrations as a function of distance from grain boundary in MgO with 100ppm trivalent cation impurity at 1300°C, using the method of Ikeda

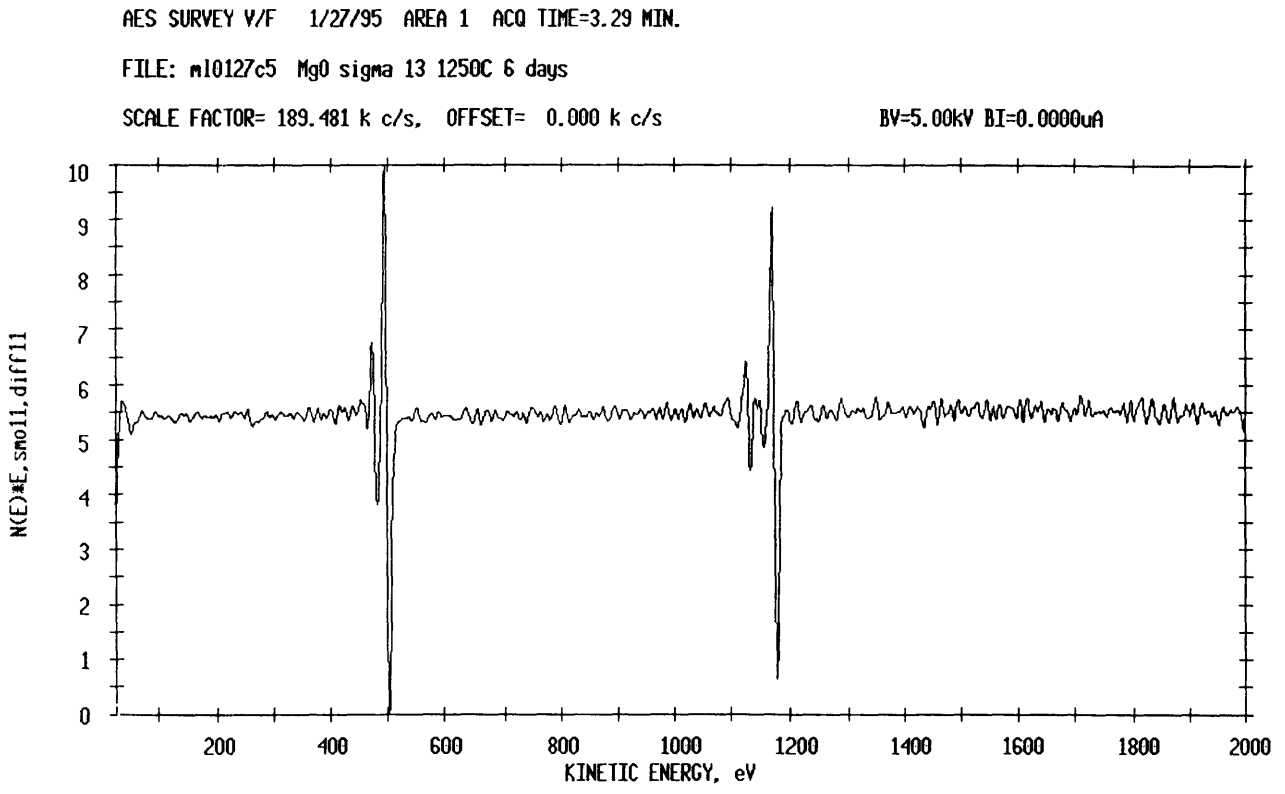

Figure 4-15: Survey Auger spectrum taken on MgO bicrystal annealed at 1250°C 6 days fractured in air at the grain boundary.

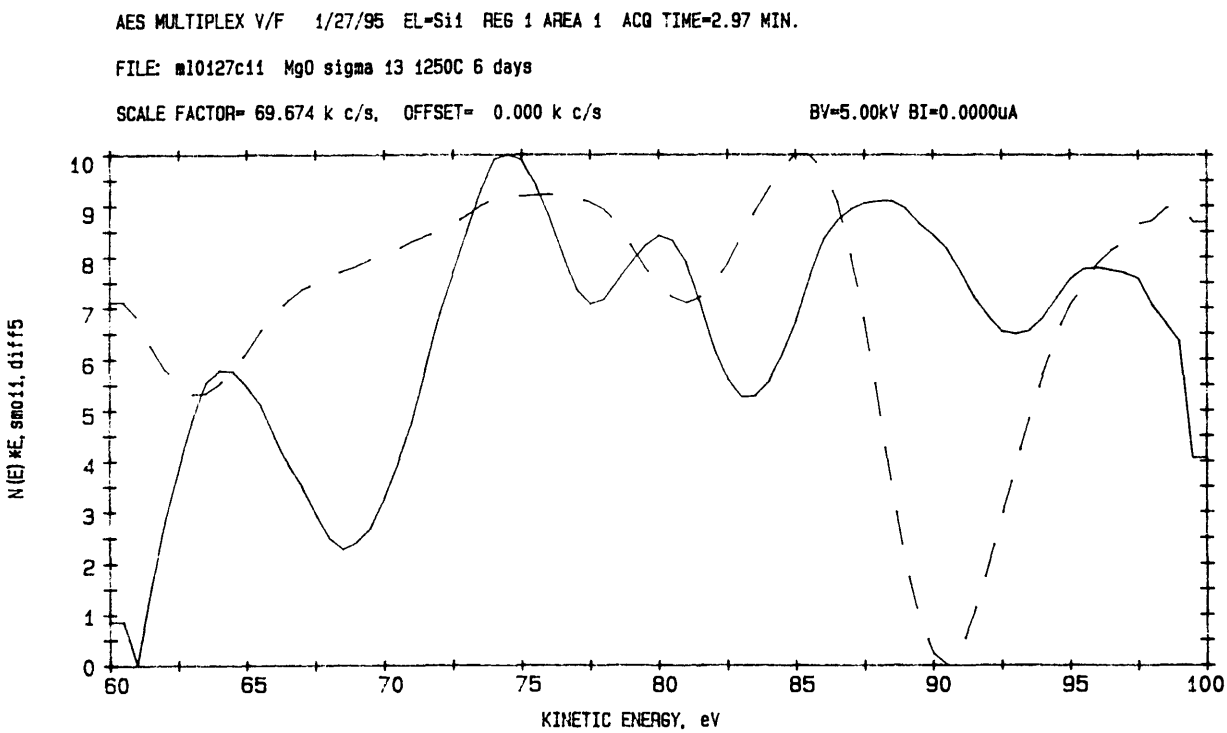

Figure 4-16: High resolution Auger spectrum revealing Si segregation in the seed bicrystal but not in the CVT grown bicrystal. Sold curve = CVT material, Dashed curve = seed crystal.

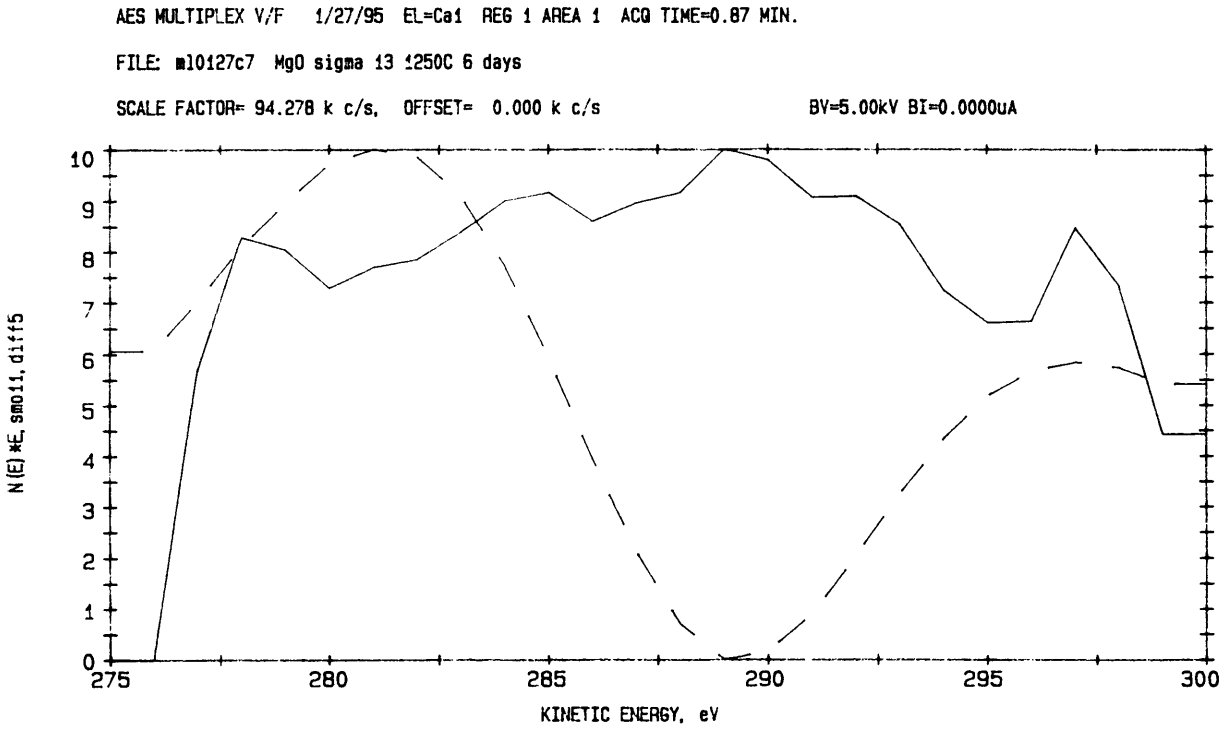

Figure 4-17: High resolution Auger spectrum revealing Ca segregation in the seed bicrystal but not in the CVT grown bicrystal. Sold curve = CVT material, Dashed curve = seed crystal.

Boundary charge densities are also calculable knowing the bulk (boundary) potential by the following relation [63]:

$$\sigma = \frac{\varepsilon kT}{4\delta\pi e}(\exp\frac{z_0}{2} - \exp\frac{-z_0}{2})$$

where z_0 = $e\varphi_0/kT$ = $-e\varphi_\infty/kT$. Performing this calculation yields a value of -1.030×10^{13} cm^{-2}. Converting this to a volume charge density, assuming a uniform charge density in the boundary core, by dividing by the boundary width (1.0 nm) yields -1.03×10^{20} cm^{-3} which would be equal to the point defect concentration in the boundary core if the defects were singly charged, but since we believe they are doubly charged the concentration would be half as much, or $n''_d = 5.1\times10^{19}$ cm^{-3}. The bulk point defect concentration assuming 100 ppm impurity is 5.3×10^{18} cm^{-3} so this does represent an increase of about an order of magnitude. In the bulk, though, the overwhelming majority of point defects are magnesium vacancies, as they are fixed by the aliovalent impurity content. By the Schottky and Frenkel equilibria the oxygen interstital concentration would be $[O''_i] = (k_f/k_s)[V''_O]$. Applying this relation in the grain boundary leads to the following expression for the oxygen interstitial concentration therein:

$$[O''_i] \approx n''_d[\frac{\exp\frac{-h_f}{kT}}{\exp\frac{-h_s}{kT}}]$$

Using the bulk values for the defect formation enthalpies, this yields a value of 1.0×10^5 cm^{-3} for the oxygen interstitial concentration in the boundary core, an enhancement of about 1.5 orders of magnitude over the computed bulk value. Of course the defect formation enthalpies in the bulk and grain boundary are not the same but it is probably not unreasonable to assume that the change from bulk to grain boundary values would be roughly equal on a percentage basis for the Frenkel and Schottky energies, leaving the ratio essentially unchanged.

The interstitial concentrations in the boundary core have been computed by taking the ratio of grain boundary to bulk diffusivities and equating it to the ratio of oxygen

interstitial concentrations:

$$\frac{D_{gb}}{D_{bulk}} = \frac{[O_i'']_{gb}}{[O_i'']_{bulk}}$$

This method is valid because the diffusion activation energies are equal. The increase in diffusivity is due to the increase in point defect concentration. Doing the computations yields values for $[O"_i]_{gb}$ on the order of 10^6 cm^{-3}. While off by roughly an order of magnitude they both represent an enhancement over bulk values.

We can use previous relations (4.4 and 4.7 in particular) to predict the behavior of the special and non-special boundaries. The special ($\Sigma 5$, $\Sigma 13$) boundaries, which have lower γ_b values should also have lower oxygen boundary diffusivities compared to the non special asymmetric 16° tilt boundary. Looking at figure 4-11 we can see that this is exactly the case. Two possible explanations for this result come to mind. The most obvious is that due to the better atomic registry of the special boundaries the defect formation/migration energies are larger than in the non-special boundary where the atomic fit is not as good. This explanation is plausible. Since the activation energies for bulk and grain boundary diffusion in special boundaries are roughly equal, the defect formation and migration energies are also roughly equal. The defect formation/migration energies in the non-special boundary could in fact be lower. There is not enough data to compute a reliable activation energy so it cannot be stated for sure. Another possible explanation lies in the segregation behavior. It has been observed in MgO [68] that there is more segregation in high energy boundaries than low energy boundaries, which is in accordance with the adsorption isotherm of Gibbs. This would require a higher concentration of point defects in the boundary core and thus a higher diffusivity in the high energy non-special boundary. Both of these explanations, though is due to the intrinsic properties of the boundary. Thus the relationship that was surmised between grain boundary structure/energy and diffusion has been established. These results are in accord with observations in metals of lower diffusivities at special boundaries [116]. It also appears safe to conclude from these results that the CVT grown boundaries are low in segregation. If segregation were substantial, precipitation of second phases would occur and no

difference in diffusion behavior would be observed between boundaries of different orientation.

Atomistic mechanisms for grain boundary diffusion are difficult to pin down given the small amount of data available, but some conclusions can be made. Considering the results of the transmission electron microscopy done on MgO boundaries in this work and on NiO boundaries by Merkle and Smith [32, 33] it can be stated that the atomic structure of grain boundaries is not very much different from the bulk and that the atomic density is only slightly less. It is likely, then, that discrete point defects do exist in grain boundaries, and thus the same mechanisms for diffusion are operative. Given the similarity in the activation energies for bulk and grain boundary diffusion it is likely that a similar mechanism is responsible which in this case be some form of interstitial mechanism.

Chapter 5

Summary and Suggestions for Future Work

5.1 Summary

In the present work a new method for the preparation of bicrystals has been developed. The technique of chemical vapor transport, which had previously been applied to the growth of high-purity, high-quality (low dislocation density) single crystals of MgO was successfully applied to the growth of high purity MgO bicrystals by using a hot pressed bicrystal seed. The epitaxial nature of the crystal growth provided a great deal of flexibility in the control of the orientation of the grain boundaries. Different orientations could be achieved by simply varying the orientation of the seed bicrystal. In this study both low energy [001] symmetric tilt coincidence site boundaries ($\Sigma 5$ (310), $\Sigma 13$ (510)) and general high energy boundaries (16° (100)/$\sim$(720) asymmetric tilt) were prepared.

Oxygen grain boundary and bulk diffusion was studied with the following results for the temperature range 1250 - 1500°C:

$$\delta D_b = 2.8 \times 10^{-8} \exp \frac{-3.9eV}{kT} \quad \frac{\text{cm}^3}{\text{sec}} \qquad \Sigma 13$$

$$D = 2.9 \times 10^{-4} \exp \frac{-4.0eV}{kT} \quad \frac{\text{cm}^2}{\text{sec}} \qquad 1250 - 1500°C$$

The partial pressure dependence of oxygen diffusivity was also measured and can be expressed as:

$$D \propto P_{O_2}^{0.11} \qquad 10^{-12} - 10^{+1} kPa \qquad 1500°C$$

Assuming a 1 nm boundary with this corresponds to an enhancement of approximately 3.5 orders of magnitude of $\Sigma 13$ grain-boundary diffusivities over bulk values. Similar behavior was observed in $\Sigma 5$ boundaries. However in the general, 16° boundary, diffusivities were enhanced by 1 - 2 orders of magnitude over the low energy boundaries which is in accord with the empirical Borisov relation.

Previous work on oxygen grain-boundary diffusion in MgO was on randomly-oriented boundaries in a polycrystal making a measurement of misorientation dependence on oxygen diffusion impossible. The CVT-fabricated bicrystals made possible the observation for the first time, of the misorientation dependence of oxygen grain boundary diffusion in a ceramic. Furthermore the scatter in the boundary diffusion data for boundaries of similar orientation was remarkably small. This was due, no doubt, to the high purity and high quality of the CVT grown bicrystals and the fact that they could be annealed and analyzed as grown without any further treatment. These results suggest that structure-property relationships can be measured reproducibly in grain boundaries of controlled orientation and high enough purity. Previous studies of grain boundary diffusion in MgO were highly non-reproducible. This was due partly to the general low quality of the material studied combined with massive amounts of segregation. If poor quality or large amounts of segregation did not completely submerge the intrinsic properties of the boundary being studied then the extensive surface treatments (cutting, polishing, etching) required prior to analysis surely did. For the same reasons, in addition to being irreproducible, previous results of oxygen boundary diffusion studies in MgO also displayed huge amounts of scatter, 3 orders of magnitude of scatter for a single temperature not being uncommon. In the present work there was less than 3 orders of magnitude of variation of oxygen diffusivity over the entire temperature range studied.

Finally an interstitial mechanism for oxygen bulk and grain boundary diffusion in MgO has been proposed. The model is based on the bulk and oxygen partial pressure results of this study, previous results on the isotope effect and the effect of trivalent cation doping on oxygen self-diffusion, and theoretically calculated grain boundary potentials for MgO.

5.2 Suggestions for Future Work

Many further experiments are possible to confirm and expand on the work done in this study. The most evident is a confirmation of the diffusion behavior of low energy boundaries by studying diffusion in the $\Sigma 5$ boundary over a wider temperature range as well as studying other low Σ boundaries and other high energy boundaries. The suggestion that an interstitial mechanism is responsible for diffusion could be tested by studying partial pressure dependence of oxygen grain-boundary diffusion. It can also be verified by studying the isotope effect in the diffusion of ^{17}O, ^{18}O in MgO grain boundaries. This would require the computation of correlation factors for vacancy and interstitial diffusion in grain boundaries which would require knowledge of the atomic structure of the boundaries. This can be accomplished by atomic-resolution imaging of the boundaries. Another interesting experiment to try would be to measure boundary diffusion perpendicular to the tilt axis. This could be done using the procedure developed in this work with only a few modifications. It could thus be determined if there is a difference in the diffusivity parallel to and perpendicular to the tilt axis as is predicted by the dislocation models for grain boundaries.

Bibliography

[1] Hashimoto and Hama, *Preferential Diffusion of Oxygen along Grain Boundaries in Polycrustalline MgO*, J. Applied Physics **43** [11] 4828 1972.

[2] W. Heywang, *Resistivity Anomaly in Doped Barium Titanate*, J. American Ceramic Society **47** [10] 484 1964.

[3] Y. Oishi and W.D. Kingery, *Oxygen Diffusion In Periclase Crystals*, J. Chemical Physics **33** [3] 905 1960.

[4] R.H. Condit and J.B. Holt, *A Technique for Stydying Oxygen Diffusion and Locating Oxide Inclusions in Metals Using the Proton Activation of Oxygen-18*, J. Electrochemical Society **111** 1192 1964.

[5] D.R. McKenzie, A.W. Searcy, J.B. Holt and R.H. Condit, *Oxygen Grain-boundary Diffusion in MgO*, J. American Ceramic Society **54** 188 1971.

[6] B.J. Wuensch and T. Vasilos, *Grain Boundary Diffusion in MgO* J. American Ceramic Society **47** [2] 63 1964.

[7] B.J. Wuensch and T. Vasilos, *Origin of Grain Boundary Diffusion in MgO* J. American Ceramic Society **49** [8] 433 1966.

[8] L.E. Dolhert, PhD thesis, MIT Department of Materials Science and Engineering, 1985.

[9] A. Roshko, PhD thesis, MIT Department of Materials Science and Engineering, 1987.

[10] P.E. Gruber, *Growth of High Purity Magnesium Oxide Single Crystals by Chemical Vapor Transport Techniques*, J. Crystal Growth **18** 94 1973.

[11] H.I. Yoo, B.J. Wuensch and W.T. Petuskey, *Secondary ion Mass Spectrometric Analysis of Oxygen Self-Diffusion in Single Crystal MgO*, **Advances in Ceramics vol. 10, Structure and Properties of MgO and Al_2O_3 Ceramics**, W.D. Kingery, ed., American Ceramic Society, 394-405, 1985.

[12] R.W. Balluffi, **Interfaces in Crystalline Materials**, to be published (1995).

[13] R.W. Balluffi. *Grain Boundary Structure and Segregation*, **Interfacial Segregation**, W. Johnson, J. Blakely, eds., American Society for Metals, 1977.

[14] J.P. Hirth and J. Lothe, **Theory of Dislocations**, (McGraw-Hill, New York 1968).

[15] C.P. Sun and R.W. Balluffi, *Observation of Intrinsic and Extrinsic Secondary Grain Boundary Dislocations in [001] High Angle Twist Boundaries in MgO*, Scripta Met. **13** 757 1979.

[16] R.W. Balluffi, *On the Study of the Structure of Grain Boundaries in Metals*, Ultramicroscopy **14** 155 1984.

[17] T. Schober and R.W. Balluffi, *Dislocation Sub-boundary Arrays in Oriented Thin-film Bicrystals of Gold*, Phil. Mag. **20** 511 1969.

[18] S.L. Sass, T.Y. Tan, and R.W. Balluffi, *The Detection of the Periodic Structure of High-angle Twist Boundaries, I. Electron Diffraction Study.* Phil. Mag. **31** 559 1975.

[19] T.Y. Tan, S.L. Sass, and R.W. Balluffi, *The Detection of the Periodic Structure of High-angle Twist Boundaries, II. High Resolution Electron Microscopy Study*, Phil. Mag. *31* 575 1975.

[20] W. Gaudig, D.Y. Guan, and S.L. Sass, *X-ray Diffraction Study of Large-angle Twist Boundaries*, Phil. Mag. **34** [5] 923 1976.

[21] R.W. Balluffi, S.L. Sass and T. Schober, *Grain Boundary Dislocation Networks as Electron Diffraction Gratings*, Phil. Mag. **26** 585 1972.

[22] T.P. Darby, R. Schindler, and R.W. Balluffi, *On the Interaction of Lattice Dislocations with Grain Boundaries*, Phil. Mag. A **37** [2] 245 1976.

[23] T. Schober and R.W. Balluffi, *Extraneous Grain Boundary Dislocations in Low and High Angle (001) Twist Boundaries in Gold*, Phil. Mag. **24** 165 1971.

[24] C.P. Sun and R.W. Balluffi *Secondary Grain Boundary Dislocations in [001] Twist Boundaries in MgO, I. Intrinsic Structures*, Phil. Mag. A **46** [1] 63 1982.

[25] C.P. Sun and R.W. Balluffi, *Secondary Grain Boundary Dislocations in [001] Twist Boundaries in MgO, II. Extrinsic Structures*, Phil. Mag. A **46** [1] 49 1982.

[26] P.D. Bristowe and A.G. Crocker, Phil. Mag. A **38** 487 1978.

[27] Dieter Wolf, *Energy and Structure of (001) Coincident-Site Twist Boundaries and the Free (001) Surface in MgO: A Theoretical Study*, J. American Ceramic Society **67** [1] 1 1984.

[28] Dieter Wolf, *Formation Energy of Point Defects in Free Surfaces and Grain Boundaries in MgO*, Radiation Effects **75** 203 1983.

[29] Dieter Wolf, *Effect of Fe^{2+} Substitutional Impurities on the Stability of a Σ = 5 (100) CSL Twist Boundary in MgO: A Theoretical Study*, **Advances in Ceramics vol. 6, Character of Grain Boundaries**, M.F. Yan and A.H. Heuer eds., American Ceramic Society, 36-43, 1983.

[30] J.A. Eastman and S.L. Sass, *Influence of Iron on the Structure of Small-angle [001] Twist Boundaries in Magnesium Oxide*, J. American Ceramic Society **69** [10] 753 1986.

[31] T. Mitamura, E.L. Hall, W.D. Kingery, and J.B. Vander Sande, *Grain Boundary Segregation of Iron in Polycrystalline Magnesium Oxide Observed by STEM*, Ceramurgia Int. **5** 131 1979.

[32] K.L. Merkle and D.J. Smith, *Atomic Structure of Symmetric Tilt Grain Boundaries in NiO*, Physical Review Letters **59** [25] 2887 1987.

[33] K.L. Merkle and D.J. Smith, *Atomic Resolution Electron Microscopy of NiO Grain Boundaries*, Ultramicroscopy **22** 57 1987.

[34] D.M. Duffy and P.W. Tasker, *Computer Simulation of (001) Tilt Grain Boundaries in Nickel Oxide*, Phil. Mag. A **47** [6] 817 1983.

[35] W.T. Read, **Dislocations in Crystals**, McGraw-Hill, New York, (1953).

[36] W.T. Read and W. Schockley, *Dislocation Models of Crystal Grain Boundaries*, Phys. Rev. **78** [3] 275 1950.

[37] G. Dhalenne, A. Revcolevschi, and A. Gervais, *Grain Boundaries in NiO, I. Relative Energies of (001) Tilt Boundaries*, Phys. Stat. Sol. (a) **56** 267 1979.

[38] J.C.M. Li *High Angle Tilt Boundary - A Dislocation Core Model* J. Appl. Phys. **32** [3] 525 1960.

[39] J. Friedel, **Dislocations**, Addison-Wesley, Reading, MA, (1964).

[40] C. Herring, The Physics of Powder Metallurgy.

[41] D.W. Ready and R.E. Jech *Energies and Grooving Kinetics of [001] Tilt Boundaries in Nickel Oxide*, J. American Ceramic Society **51** [4] 201 1968.

[42] G. Dhalenne, M. Dechamps, and A. Revcoleevschi, *Relative Energies of (001) Tilt Boundaries in NiO*, J. American Ceramic Society **65** [1] C11 1982.

[43] G. Dhalenne, M. Dechamps, and A. Revcoleevschi, *Energy of Tilt Boundaries and Mass Transport Mechanisms in Nickel Oxide*, **Advances in Ceramics vol. 6, Character of Grain Boundaries**, M.F. Yan and A.H. Heuer eds., American Ceramic Society, 139, 1983.

[44] C.A. Handwerker, J.M. Dynys, R.M. Cannon, and R.L. Coble, *Dihedral Angles in Magnesia and Alumina: Distributions from Surface Thermal Grooves*, J. American Ceramic Society **73** [5] 1371 1990.

[45] P. Chaudhari and J.W. Matthews, *Coincidence Twist Boundaties between Crystalline Smoke Particles*, J. Applied Physics **42** [8] 3063 1971.

[46] S.Kimura, E. Yasuda, N. Horiai, and Y. Moriyoshi, *Boundary Structure Observed in MgO Bicrystals* **Advances in Ceramics vol. 10, Structure and Properties of MgO and Al_2O_3 Ceramics**, W.D. Kingery, ed., American Ceramic Society, 347, 1985.

[47] D. McLean, **Grain Boundaries in Metals**, Clarendon Press, Oxford, U.K., (1957).

[48] J.D. Eschelby, *The Continuum Theory of Lattice Defects*, Solid State Phys. **3** 79 1956.

[49] J.A.S. Ikeda *Grain Boundary Defect Chemistry and Electrostatic Potential in Acceptor and Donor Doped Titanium Dioxide*, PhD thsis, MIT Department of Materials Science and Engineering, 1992.

[50] K.L. Kliewer and J.S. Koehler, *Space Charge in Ionic Crystals I. General Approach with Application to NaCl*, Phys. Rev. **140** [4A] A1226 1965.

[51] K.L. Kliewer, *Space Charge in Ionic Crystals II. The Electron Affinity and Impurity Accumulation*, Phys. Rev. **140** [4A] A1241 1965.

[52] K.L. Kliewer, *Space Charge in Ionic Crystals III. Silver Halides Containing Divalent Cations*, J. Phys. Chem. Solids **27** 705 1966.

[53] K.L. Kliewer, *Space Charge in Ionic Crystals IV. Interstitial Producing Impurities in the Silver Halides* J. Phys. Chem. Solids **27** 719 1966.

[54] M.F. Yan, R.M. Cannon and H.K. Bowen, *Space Charge, Elastic Field, and Dipole Contribution to Equilibrium Solute Segregation at Interfaces*, J. Appl. Phys. **54** [2] 764 1983.

[55] W.D. Kingery, *Plausible Concepts Necessary and Sufficient for Interpretation of Ceramic Grain Boundary Phenomena II, Solute Segregation, Grain Boundary Diffusion and General Discussion*, J. American Ceramic Society **57** [2] 74 1974.

[56] W.D. Kingery, *Segregation Phenomena at Surfaces and at Grain Boundaries in Oxides and Carbides*, Solid State Ionics **12** 299 1984.

[57] W.D. Kingery, *The Chemistry of Ceramic Grain Boundaries*, Pure and Appl. Chem. **56** [12] 1703 1984.

[58] W.C. Johnson, *Grain Boundary Segregation in Ceramics*, Metallurgical Transactions A **8A** 1413 1977.

[59] W.C. Johnson, D.F. Stein, and R.W. Rice, *Analysis of Grain Boundary Impurities and Fluoride Additives in Hot Pressed Oxides by Auger Electron Spectroscopy*, J. American Ceramic Society **57** [8] 342 1974.

[60] C. Berthelet, W.D. Kingery, and J.B. Vander Sande, *Magnesium Aluminate Spinel Precipitation in MgO*, Ceramurgia Int. **2** [2] 62 1976.

[61] W.D. Kingery, W.L. Robbins, A.F. Henriksen, and C.E. Johnson, *Surface Segregation of Aluminum (Spinel Precipitation) in MgO Crystals*, J. American Ceramic Society **59** [5-6] 239 1976.

[62] J.R.H. Black and W.D. Kingery, *Segregation of Aliovalent Solutes Adjacent Surfaces in MgO*, J. American Ceramic Society **62** [3-4] 176 1979.

[63] Y.M. Chiang, A.F. Henriksen W.D. Kingery, and D. Finello *Characterization of Grain Boundary Segregation in MgO*, J. American Ceramic Society **64** [7] 385 1981.

[64] J.B. Vander Sande, A.J. Garratt-Reed, Y.M. Chiang, and T. Thorvaldsson, *Resolving Composition Variations at Interfaces by STEM*, Ultramicroscopy **14** 65 1984.

[65] E.L. Hall, *Compositional Analysis of Interfaces Using X-ray Spectroscopy*, MSA Bulletin **24** [1] 359 1994.

[66] W.D. Kingery, T. Mitamura, J.B. Vander Sande, and E.L. Hall, *Boundary Segregation of Ca, Fe, La, and Si in Magnesium Oxide*, J. Materials Science **14** 1766 1979.

[67] E.L. Hall, D. Imeson, and J.B. Vander Sande, *On Producing High Spatial Resolution Composition Profiles via Scanning Transmission Electron Microscopy*, Phil. Mag. A **43** 1569 1981.

[68] A. Roshko and W.D. Kingery, *Segregation at Special Boundaries in MgO*, J. American Ceramic Society **68** [12] C331 1985.

[69] S.C. Semken, *Epitaxial Crystal Growth and Oxygen Diffusion Studies in MgO and CaO*, PhD thesis, MIT Department of Materials Science and Engineering, 1989.

[70] J. Crank, **The Mathematics of Diffusion**, Oxford University Press, (1975).

[71] Han Ill Yoo, *Isothermal and Non-Isothermal Diffusion of Oxygen in Single Crystal MgO*, PhD thesis, MIT Department of Materials Science and Engineering, 1984.

[72] H. Schmalzried, **Solid State Reactions**, Verlag Chemie Gmbh, 65 (1981).

[73] P.G. Shewmon, **Diffusion in Solids**, The Minerals, Metals, and Materials Society, 2nd ed, 120-122.

[74] R.T.P. Whipple, *Concentraion Contours in Grain Boundary Diffusion*, Phil. Mag. **45** 1225 1954.

[75] T. Suzoka, *Lattice and Grain Boundary Diffusion in Polycrystals*, Transaction of the Japan Institute of Metals **2**, 25 1961.

[76] J.C. Fisher, *Calculation of Diffusion Penetration Curves for Surface and Grain Boundary Diffusion*, J. Applied Physics **22** [1] 74 1951.

[77] Devendra Gupta *Some Formal Aspects of Diffusion: Bulk Solids and Thin Films* (cited) D. Gupta, P. Ho, eds. **Diffusion Phenomena in Thin Films and Microelectronic Materials**, Noyes Publications, (1988).

[78] W.C. Mackrodt and R.F. Stewart, *Defect Properties of Ionic Solids III. The Calculation of the Point-defect Structure of the Alkaline Earth Oxides and CdO*, Journal of Physics C **12** 5015 1979.

[79] M.J.L. Sangster and D.K. Rowell *Calculation of Defect Energies and Volumes in Some Oxides*, Phil. Mag. A **44** 613 1981.

[80] C.R.A. Catlow, I.D. Faux, and M.J. Norgett, *Shell and Breathing Shell Model Calculations for Defect formation Energies in Magnesium Oxide*, J. Phys. C **9** 419 1976.

[81] W.H. Gourdin and W.D. Kingery, *The Defect Structure of MgO Containing Trivalent Cation Solutes: Shell Model Calculations*, J. Materials Science **14** 2053 1979.

[82] B.J. Wuensch, W.T. Steele, and T. Vasilos, *Cation Self-diffusion in Single-crystal MgO*, J. Chemical Physics **58** [12] 5258 1973.

[83] D. Sempolinski and W.D. Kingery, *Ionic Conductivity and Magnesium Vacancy Mobility in Magnesium Oxide*, J. American Ceramic Society **63** [11-12] 664 1980.

[84] M. Dulcot and C. Deportes, *Influence des Impuretes sur la Conductivitie Cationique dans l'oxide de Magnesium Monocristallin*, J. Solid State Chemistry **31** 377 1980.

[85] L.H. Rovner, *Diffusion of Oxygen in Magnesium Oxide*, PhD Thesis, Cornell University Pysiscs Depatment, 1966.

[86] K. Ando et. al. *Oxygen Self Diffusion in Fe Doped MgO Singe Crystals*, J. Chemical Physics **78** [11] 6890 1983.

[87] H. Schmalzried, *High Temperature Creep and Kinetic Demixing in (Co,Mg)O*, J. American Ceramic Society **71** [9] 732 1988.

[88] C.P. Flynn, *Materials Science Through Materials Synthesis*, J. Phys. Chem. Solids, in press.

[89] M.F. Yang and C.P. Flynn, *Intrinsic Diffusion Properties of an Oxide: MgO*, J. Phys. Chem. Solids, in press.

[90] A.F. Henriksen, Y.M. Chiang, W.D. Kingery, and W.T. Petuskey *Enhanced Oxygen Diffusion at 1400°C in Deformed Single Crystal Magnesium Oxide*, **66** C144 1983.

[91] **Janaf Thermochemical Tables** Dow Chemical Company, 1971, 1973, 1975.

[92] J.R. Booth, W.D. Kingery, and H.K. Bowen, *Preparation and Properties of MgO Single Crystals Grown by Chemical Vapor Deposition*, J. Crystal Growth **29** 257 1975.

[93] Harald Schafer, **Chemical Transport Reactions**, Academic Press, New York, (1964).

[94] R. Bunsen, J. prakt. Chem **56** 53 1852, from [93].

[95] H. Saint-Claire Deville, Ann. **120** 176 1861, from [93].

[96] C.B. Alcock and J.H.E. Jeffes, *Application of Thermodynamics to the Selection of Vapor Transport Reactions*, Trans. Institute of Mining and Metallurgy, London **76** C246 1976.

[97] J.H.E. Jeffes and C.B. Alcock, *The Production of Refractory Crystals by Vapor Transport Reactions*, J. Materials Science **3** 635 1978.

[98] J.H.E. Jeffes, *The Physical Chemistry of Transport Processes*, J. Crystal Growth **3,4** 13 1968.

[99] M. Liberatore, B.J. Wuensch I.G. Solorzano, J.B. Vander Sande "Fabrication and Characterization of MgO Bicrystals"; *Mater. Res. Soc. Proc. Vol.* **320** 637 1993.

[100] D.R. Gaskell, **Introduction to Metallurgical Thermodynamics**, 2nd ed., McGraw Hill, New York, (1981), pp. 241-244.

[101] J.C. Vickerman, A. Brown and N.M. Reed, eds., **Secondary Ion Mass Spectrometry Principles and Applications**, Clarendon Press, Oxford, 1989.

[102] P. Sigmund, *Sputtering by Particle Bombardment I*, **Topics in Applied Physics, Vol. 47**, R. Behrisch ed., Springer-Verlag, 1981, from [101].

[103] D. Sempolinski, W.D. Kingery, and H.L. Tuller, *Electrical Conductivity of Single Crystalline Magnesium Oxide*, J. American Ceramic Society **63** [11-12] 669 1980.

[104] B.J. Wuensch, S.C. Semken, F. Uchikoba, and H.I. Yoo, *The Mechanisms for Self-Diffusion in Magnesium Oxide*, **Ceramic Transactions vol. 24, Point Defects**, American Ceramic Society, 79-89, 1991.

[105] W.H. Gourdin, *The Defect Structure of MgO Containing Trivalent Cation Solutes, Calculation and Experiment*, PhD thesis, MIT Department of Materials Science and Engineering, 1977.

[106] Alistair Napier Cormack, Personal communication to B.J. Wuensch of unpublished results, 1991.

[107] L.W. Hobbs, *Secondary Processes in the Environmental Alteration of Insulating Crystals*, **Defects in Insulating Crystals**, K.K. Shvarts, ed., Springer-Verlag, 411-438, 1981.

[108] M.R. Pascucci, PhD Thesis, Case Western Reserve University, Department of Metallurgy and Materials Science, 1980.

[109] L.C. Qin, *Characterization of Metamict Structures by Electron Diffraction and Microscopy*, PhD Thesis, MIT Department of Materials Science and Engineering, 1994.

[110] F. Uchikoba, Personal communucation of unpublihsed work, 1991.

[111] V.T. Borisov, V.M. Golikov and G.V. Scherbedinsky, Phys. Metals Metallogr. **17** 80 1964.

[112] D. Gupta, *The Relationship Between Grain Boundary Structure, Energetics and Diffusion*, Metallurgical Transactions A **8A** 1431 1977.

[113] P. Guiraldenq, *Diffusion Intergranulaire et Energie des Joints de Grains*, J. Physique **36** 10 (colloq. C4) 201 1975.

[114] W.D. Kingery, *Plausible Concepts Necessary and Sufficient for Interpretation of Ceramic Grain Boundary Phenomena I, Grain Boundary Structure and Electrostatic Potential*, J. American Ceramic Society **57** [1] 1 1974.

[115] J.A.S. Ikeda and Y.M. Chiang, *Space Charge Segregation at Grain Boundaries in Titanium Dioxide I. Relationship Between Lattice Defect Chemistry and Space Charge Potential*, J. American Ceramic Society **76** [10] 2437 1993.

[116] N.L. Peterson *The Mechanisms for Grain Boundary Diffusion*, **Advances in Ceramics vol. 6, Character of Grain Boundaries**, M.F. Yan and A.H. Heuer eds., American Ceramic Society, 1983.

Appendix A

Additional Raw Data

In order to confirm that the slight change in slope visible in figure 4-10 is an artifact of the SIMS analysis and not an intrinsic property of the boundaries several more plots of the same kind for different samples have been included. These plots appear in the next few pages.

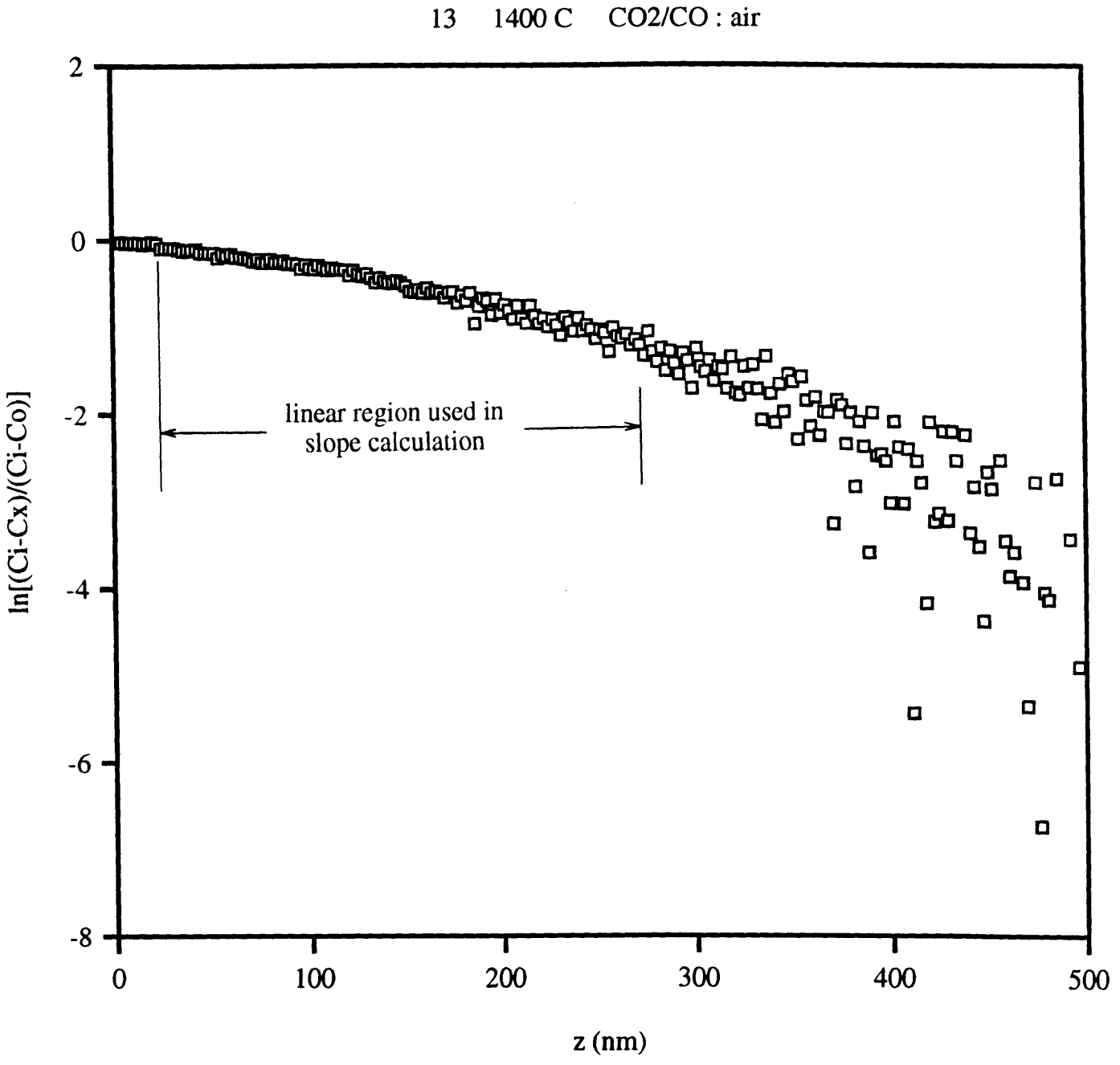

Figure A-1: Slope determination for Σ 13 boundary annelaed at 1400°C, 7 hours.

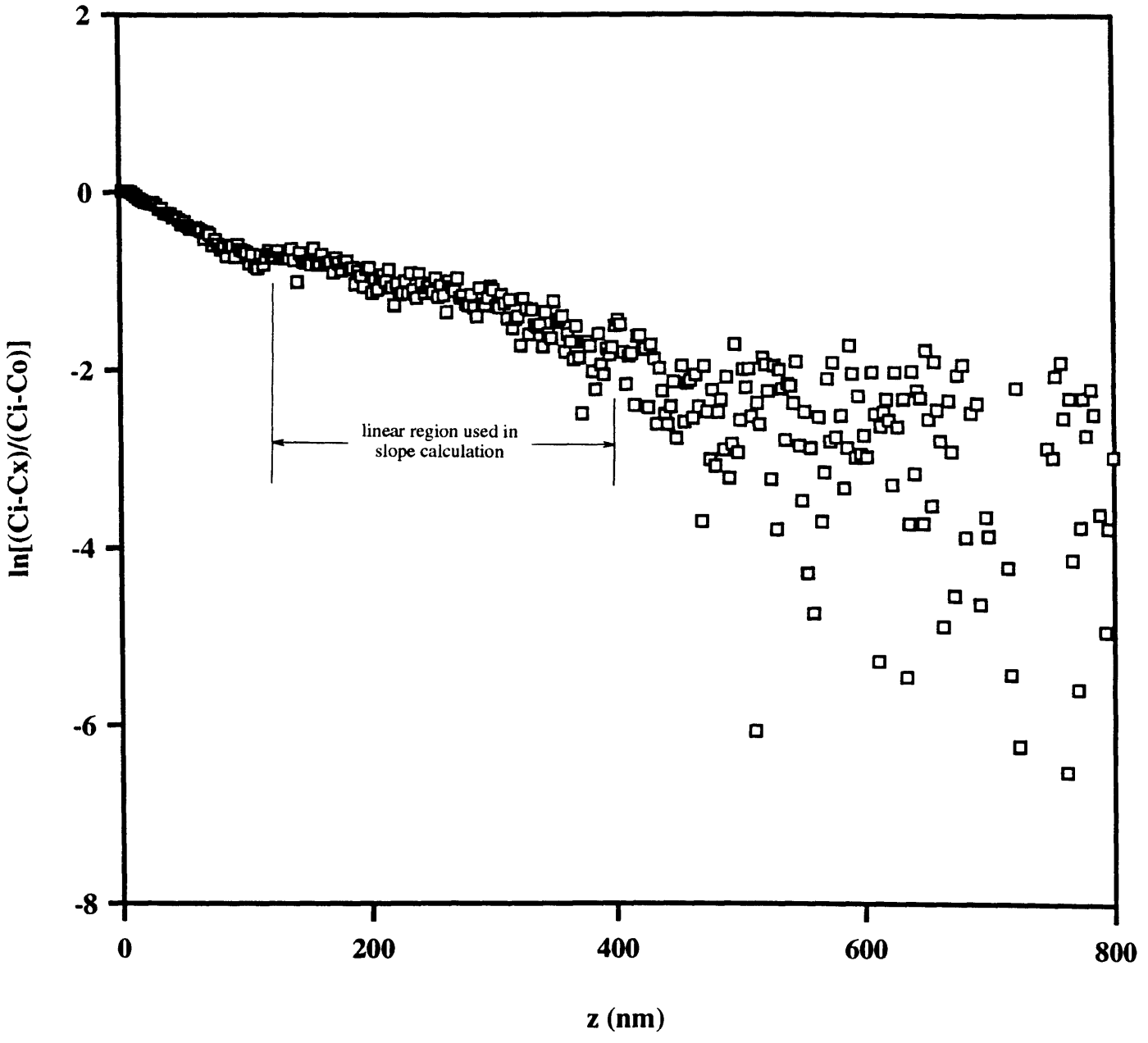

Figure A-2: Slope determination for Σ 13 boundary annelaed at 1450°C, 4.5 hours.

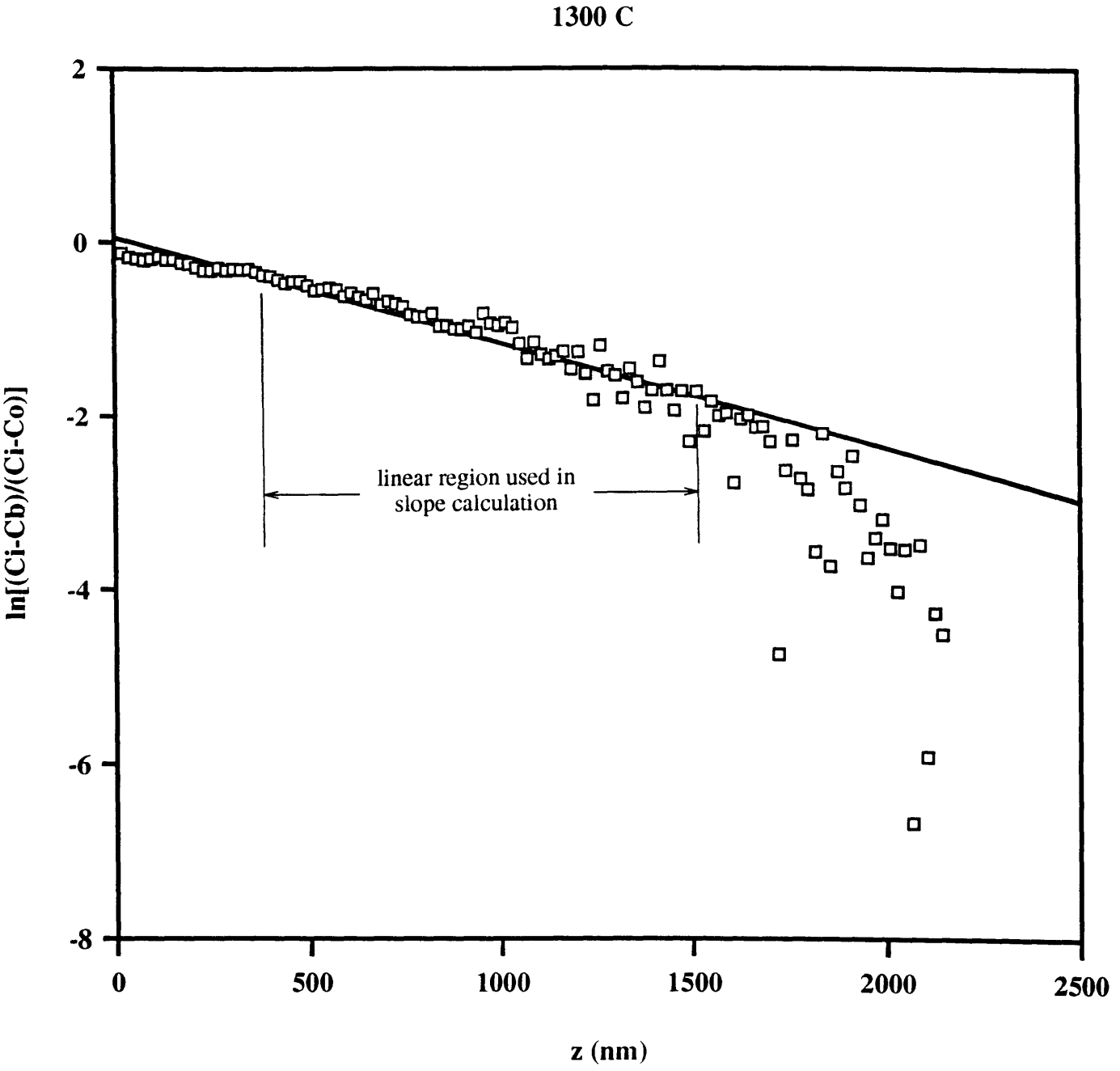

Figure A-3: Slope determination for 16° asymmetric tilt boundary annelaed at 1300°C, 3 days.

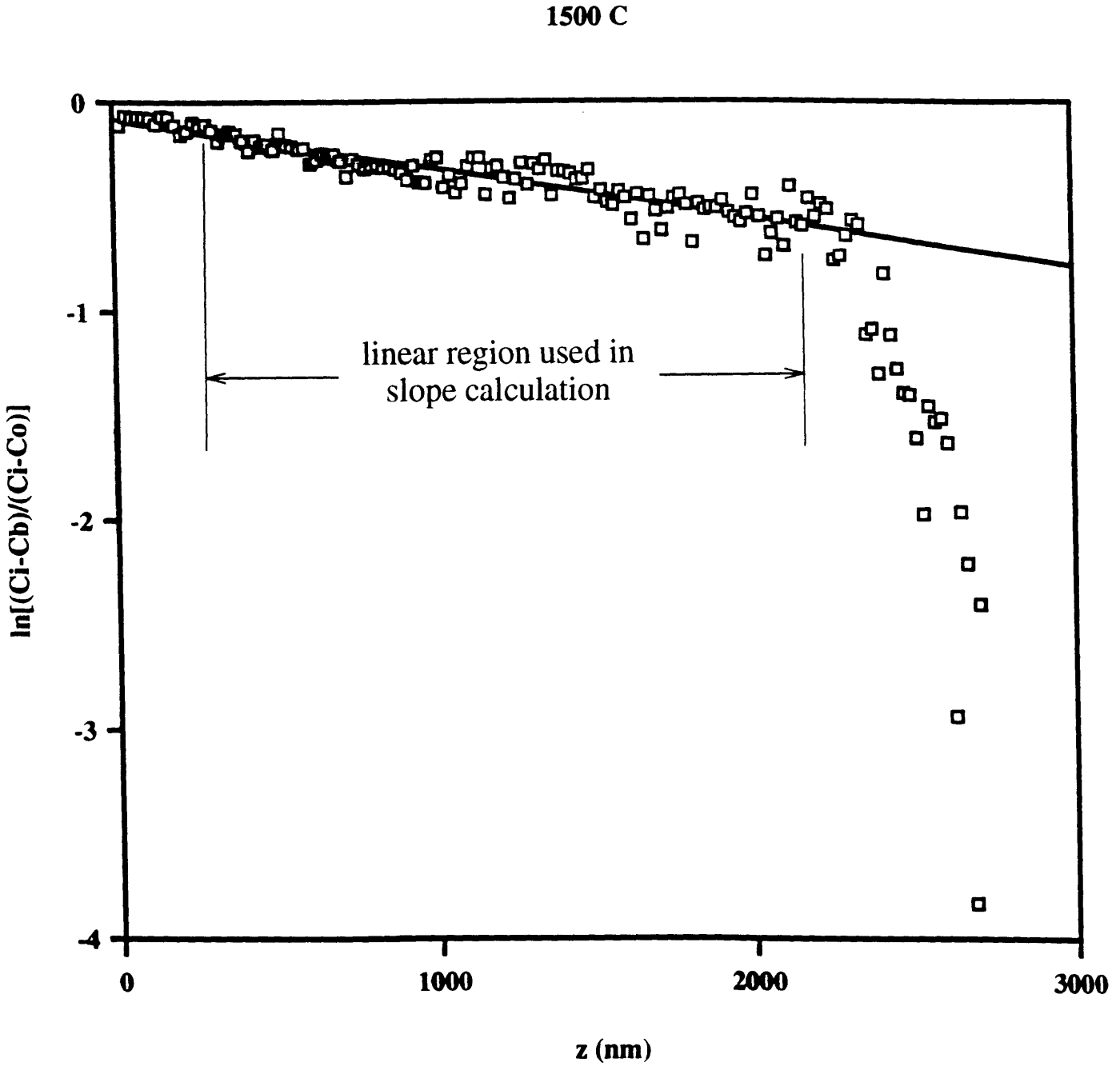

Figure A-4: Slope determination for 16° asymmetric tilt boundary annelaed at 1500°C, 3 hours.